FOSSIL ENERGY

DOE/BC/14897-15
(DE96001269)

ANISOTROPY AND SPATIAL VARIATION OF RELATIVE PERMEABILITY AND LITHOLOGIC CHARACTER OF TENSLEEP SANDSTONE RESERVOIRS IN THE BIGHORN AND WIND RIVER BASINS, WYOMING

Final Report

By
Thomas L. Dunn

April 1997

Performed Under Contract No. DE-AC22-93BC14897

Institute of Energy Research
University of Wyoming
Laramie, Wyoming

Bartlesville Project Office
U. S. DEPARTMENT OF ENERGY
Bartlesville, Oklahoma

DOE/BC/14897-15
Distribution Category UC-122

Anisotropy And Spatial Variation Of Relative Permeability And LithologicCharacter of Tensleep Sandstone Reservoirs In The Bighorn And Wind River Basins, Wyoming

Final Report

By
Thomas L. Dunn

April 1997

Work Performed Under Contract No. DE-AC22-93BC14897

Prepared for
U.S. Department of Energy
Assistant Secretary for Fossil Energy

Robert Lemmon, Project Manager
Bartlesville Project Office
P.O. Box 1398
Bartlesville, OK 74005

Prepared by:
Institute for Energy Research
University ofWyoming
Laramie, Wyoming 82070

ANISOTROPY AND SPATIAL VARIATION OF RELATIVE PERMEABILITY AND LITHOLOGIC CHARACTER OF TENSLEEP SANDSTONE RESERVOIRS IN THE BIGHORN AND WIND RIVER BASINS, WYOMING

Final Technical Report

Reporting Period Start Date:	September 15, 1993
Reporting Period End Date:	October 31, 1996

Thomas L. Dunn
Principal Investigator

Report Issued: October, 1996

D.O.E. Contract No. DE-AC22-93BC14897

Institute for Energy Research
Ronald C. Surdam, Director
Thomas L. Dunn, Associate Director
University of Wyoming
Laramie, Wyoming 82070

ABSTRACT

Objectives: This multidisciplinary study was designed to provide improvements in advanced reservoir characterization techniques. This goal was accomplished through: (1) an examination of the spatial variation and anisotropy of relative permeability in the Tensleep Sandstone reservoirs of Wyoming; (2) the placement of that variation and anisotropy into paleogeographic, and depositional regional frameworks; (3) the development of pore-system imagery techniques for the calculation of relative permeability; and (4) reservoir simulations testing the impact of relative permeability anisotropy and spatial variation on Tensleep Sandstone reservoir enhanced oil recovery.

Concurrent efforts were aimed at understanding the spatial and dynamic alteration in sandstone reservoirs that is caused by rock-fluid interaction during CO_2 enhanced oil recovery processes. The work focused on quantifying the interrelationship of fluid-rock interaction with lithologic characterization and with fluid characterization in terms of changes in chemical composition and fluid properties. This work establishes new criteria for the susceptibility of Tensleep Sandstone reservoirs to formation alteration that results in wellbore scale damage. This task was accomplished by flow experiments using core material; examination of regional trends in water chemistry; examination of local water chemistry trends the at field scale; and chemical modeling of both the experimental and reservoir systems.

Summary of Findings: Reservoir heterogeneity in the Tensleep is primarily controlled by processes of accumulation and preservation of compound crescentic bedforms, which migrated to the south-southwest with superimposed bedforms that migrated to the west. Laterally extensive marine dolomitic units form the boundaries of large-scale flow-units. Sequence stratigraphic analysis indicates that the erosional bounding surfaces capping these dolomitic units are equivalent to sequence boundaries and that the sequence boundary and the overlying eolian sands formed during relative sea level fall. Small-scale heterogeneity (maximum lateral extent of 1000's to a few feet) is caused by grain-packing variation and by erosional bounding surfaces within the eolian units. The erosional bounding surfaces commonly separate stratification types — tightly packed wind-ripple laminae above and loosely packed wind-ripple and grainflow laminae below. These differences in stratification control differences in cementation across the bounding surface as well. Borehole images can be used to identify erosional bounding surfaces in eolian cross-strata. Foreset and bounding surface dip direction and orientation can be used to recreate the dune configuration and model three-dimensional geometry of flow-units.

Tensleep eolian units exhibit anisotropy and heterogeneity of oil-water relative permeability. This anisotropy is seldom predictable from anisotropy of absolute permeability. In general, vertical oil relative permeability (across stratification and surfaces) is lower than horizontal oil relative permeability (along stratification). There are also differences related to stratification type. Wind ripple laminations exhibit greater relative permeability anisotropy than do grainflow laminations. Also, relative permeability is greater adjacent to bounding surface than across it.

The relative permeability anisotropy is demonstrated by differences in the amount of oil produced in the lab measurements, in field behavior, and in simulations where absolute permeability is held constant in the two directions. Vertical cores exhibit more piston-like behavior, producing a greater faction of their total oil before water breakthough. This implies that primary production from horizontal radial flow

should enhance the piston-like displacement across laminations and surfaces, whereas areas past breakthrough may show improved recovery from horizontal wells drilled to penetrate the greatest number of bounding surfaces.

Expressions based on the Kozeny-Carmen equation were developed to derive oil-water relative permeability curves from pore image analysis data (PIA) collected on backscattered electron images of polished thin sections. Oil and water relative permeability predicted from PIA data closely matched the measured values. This approach produces estimates that can reduce the cost of relative permeability analyses by two-thirds.

Regional differences in formation water chemistry of the Tensleep were found to result in differences in susceptibility to formation damage and scale during CO_2 flooding. Fields in the western Bighorn Basin are more susceptible than those in the east. Also risk of wellbore scale increases with higher water saturation.

Differences in connate water chemistry were also considered in calculating potential improvements in waterflood recovery from using injection water that is different from connate water. Using recent University of Wyoming experimental results incremental recovery from the Tensleep from this process was calculated to be over 15 MMBO. This would result in over $11 million to the State of Wyoming in severance tax alone assuming a low oil price of $13/bbl.

Significance to EOR Research Plan: This research, in conjunction with the results of other efforts at the University of Wyoming has identified an additional 15 MMBO of incremental recovery, just in the Tensleep Sandstone alone. Also, this research which has successfully applied an interdisciplinary approach, provides advances in reservoir description in terms of formation water chemistry, and directional relative permeability with regard to sedimentary structures found within eolian sandstone reservoirs.

TABLE OF CONTENTS

LIST OF FIGURES

LIST OF TABLES

EXECUTIVE SUMMARY

BACKGROUND

Permeability variations in reservoirs include the spatial variation (heterogeneity) of the directional variation (anisotropy) of both absolute and relative permeability. Absolute permeability has been extensively studied by other research teams in academia and the petroleum industry. However, relative permeability anisotropy and spatial variations have yet to be considered as to the effects on oil and gas production. The principal focus of this project is to evaluate the importance of relative permeability anisotropy with respect to other known geologic and engineering production concepts.

This research is to provide improved strategies for enhanced oil recovery from the Tensleep Sandstone oil reservoirs in the Bighorn and Wind River basins, Wyoming. The Tensleep Sandstone contains the largest potential reserves within reservoirs which are candidates for EOR processes in the State of Wyoming. Although this formation has produced billions of barrels of oil, in some fields, as little as one in seven barrels of discovered oil is recoverable by current primary and secondary techniques. Because of the great range of °API gravities of the oils produced from the Tensleep Sandstone reservoirs, the proposed study concentrates on establishing an understanding of the spatial variation and anisotropy of relative permeability within the Tensleep Sandstone. This research will associate those spatial distributions and anisotropies with the depositional subfacies and zones of diagenetic alteration found within the Tensleep Sandstone.

The associations between depositional lithofacies, diagenetic alteration, and pore geometry will strongly link relative permeability with the distinct and measurable dimensions of lithofacies and authigenic mineral facies. Hence, the study is to provide criteria for scaling this parameter on a range of scales — from the volume of laboratory investigation to the basin-wide scale of subfacies distribution. Effects of both the depositional processes and the burial diagenesis will be investigated. Image analysis of pore systems will be performed so as to produce algorithms for estimating relative permeability from petrographic analyses of core and well cuttings.

In addition, these studies are being coupled with geochemical modeling and coreflood experiments to investigate the potential for wellbore scaling and formation damage anticipated during EOR processes (e.g., CO_2 flooding). This multidisciplinary project will provide a regional basis for EOR strategies which can be clearly mapped and efficiently applied to the largest potential target reservoir in the State of Wyoming. Additionally, the results of this study have application to all eolian reservoirs through the correlations of relative permeability variation and anisotropy with eolian depositional lithofacies.

RESULTS

Regional Frameworks

Reservoir heterogeneity in terms of barriers and baffles to fluid flow in the Tensleep Sandstone is primarily controlled by the processes that take place during both accumulation and preservation of the eolian system. Accumulation-related small-scale heterogeneity is caused by grain-packing variation associated

with stratification types and erosional bounding surfaces within the eolian units. Laterally extensive marine dolomitic units form the large-scale heterogeneities; they result from fluctuations in relative sea level, which cause preservation of the eolian units. The large-scale heterogeneities present in the Upper Tensleep Sandstone are observed and traceable across portions of the Bighorn Basin. These same units are not traceable south into the Wind River Basin to any credible extent. The smaller scale features have lateral maximum extent ranging from 1000's to a few feet.

A hierarchy of flow-units exists within the Tensleep eolian units. These flowunits are defined by erosional bounding surfaces formed by bedform surface processes during accumulation of the eolian sediments. The erosional bounding surfaces commonly separate tightly packed wind-ripple laminae above the surface from more loosely packed wind-ripple and grainflow laminae below. This results in fluid flow being greater parallel to the boundaries than across the boundaries.

Bedform reconstructions utilizing outcrop foreset orientation and outcrop photomosaics indicate that the compound cross-strata of the Tensleep were produced by compound crescentic bedforms migrating to the south-southwest, with superimposed bedforms on some portions of the lee face migrating to the west.

Well-log cross sections were used to correlate six eolian-marine sequences across the Bighorn Basin. Individual sequences tend to thicken to the west, but they show localized variations in thickness related to local subsidence changes. The Tensleep was placed into a sequence stratigraphic framework such that the erosional bounding surfaces capping the marine dolomitic units are equivalent to sequence boundaries. Correlation to a relative sea-level curve suggests that the sequence boundary and the eolian accumulation formed during the time of falling relative sea level.

Borehole images can be used to identify erosional bounding surfaces in eolian cross-strata and classify them according to the depositional processes that formed them. After structural dip is removed, foreset and bounding surface dip direction and dip orientation data can be used to recreate the configuration of the dunes that formed the Tensleep eolian accumulations. Bedform reconstruction can be used to model the three-dimensional geometry of flow-units enclosed by erosional bounding surfaces. Such models can be used to distribute heterogeneous porosities and permeabilities into reservoir flow models. These models can also be used as input into horizontal drilling and completion designs.

The depth interval of the Tensleep Sandstone interval is relatively small and hence the variation of thermal exposure and therefore the range of extent of diagenesis is small. The variation of diagenesis on spatial variations in relative permeability is confined to the variations of cementation within a given interval and therefore more strongly controlled by either depositional factors (i.e., local operation of preservation and accumulation processes) or related to current outcrop exposure. There is some evidence that indicates that absolute (gas) permeability heterogeneity (commonly examined in outcrop analog) is not always a good indicator of two phase permeability in the subsurface. This may be the result of surface weathering.

Relative Permeability Anisotropy and Heterogeneity

Eighty-four samples of subsurface and outcropping eolian sandstone were measured for directional oil-water relative permeability. Included in the sample set were samples of the lamination types dominant in Tensleep reservoirs. The key sedimentary bounding surfaces were also sampled. This study has made explicit measurements of directional variations in relative permeability, that is anisotropy, in Tensleep reservoir sandstones. The variations in anisotropy and heterogeneity are shown in Figures ES 1 and ES 2.

The measurements show an anisotropy outside or exclusive of variations in gas permeability. The measurements show that, in general, the vertical oil relative permeability is lower than the horizontal oil relative permeability. Comparison of companion gas permeabilities and relative permeabilities indicates that gas permeability anisotropy is not always an indicator of oil-water relative permeability anisotropy. The relative permeability anisotropy is also demonstrated by the differences in the amount of oil produced before water breakthrough. Those cores measured across bounding surfaces and laminations produced a greater faction of their total oil before water breakthough. After breakthrough, those cores tend to rapidly produce water. This piston-like displacement across the fabric and baffles within the reservoirs have implication for effective drainage and development.

To maximize piston-like displacement across the bounding surfaces, primary production through horizontal radial flow should produce the greatest flow across these surfaces. The placement of wells with respect to the orientation of the bedforms is key. Areas that are past breakthrough may show improved incremental recovery from horizontal wellbores drilled such that they penetrate the greatest number of second-order bounding surfaces. This directional approach utilizes the better post-breakthrough recovery properties parallel to laminations and bounding surfaces. These properties are demonstrated in field behavior and in two-phase flow reservoir simulations.

Pore Image Analysis

Expressions were developed to derive oil-water relative permeability from pore image analysis data collected using polished thin sections viewed using a scanning electron microscope (S.E.M.) mounted with a backscattered electron detector. The expressions are derived principally from the Kozeny-Carmen equation.

From this study, water saturation, oil relative permeability and water relative permeability values were predicted and were found to closely follow the measured values. The approach is relatively quick and can be further developed to improve site-specific sensitivity. The approach can easily reduce the cost of relative permeability analysis by two-thirds.

CO_2 Coreflood — Formation Alteration and Wellbore Damage

Regional water chemistry variations of the Tensleep, Bighorn Basin, Wyoming shows four water chemistry types. These four were analyzed for susceptibility to scale and formation damage. Overall, Tensleep oil fields on the western Bighorn Basin have higher susceptibility to wellbore scale and formation damage as a result of CO_2 flooding. Also, risk of wellbore scale increases with higher water saturation.

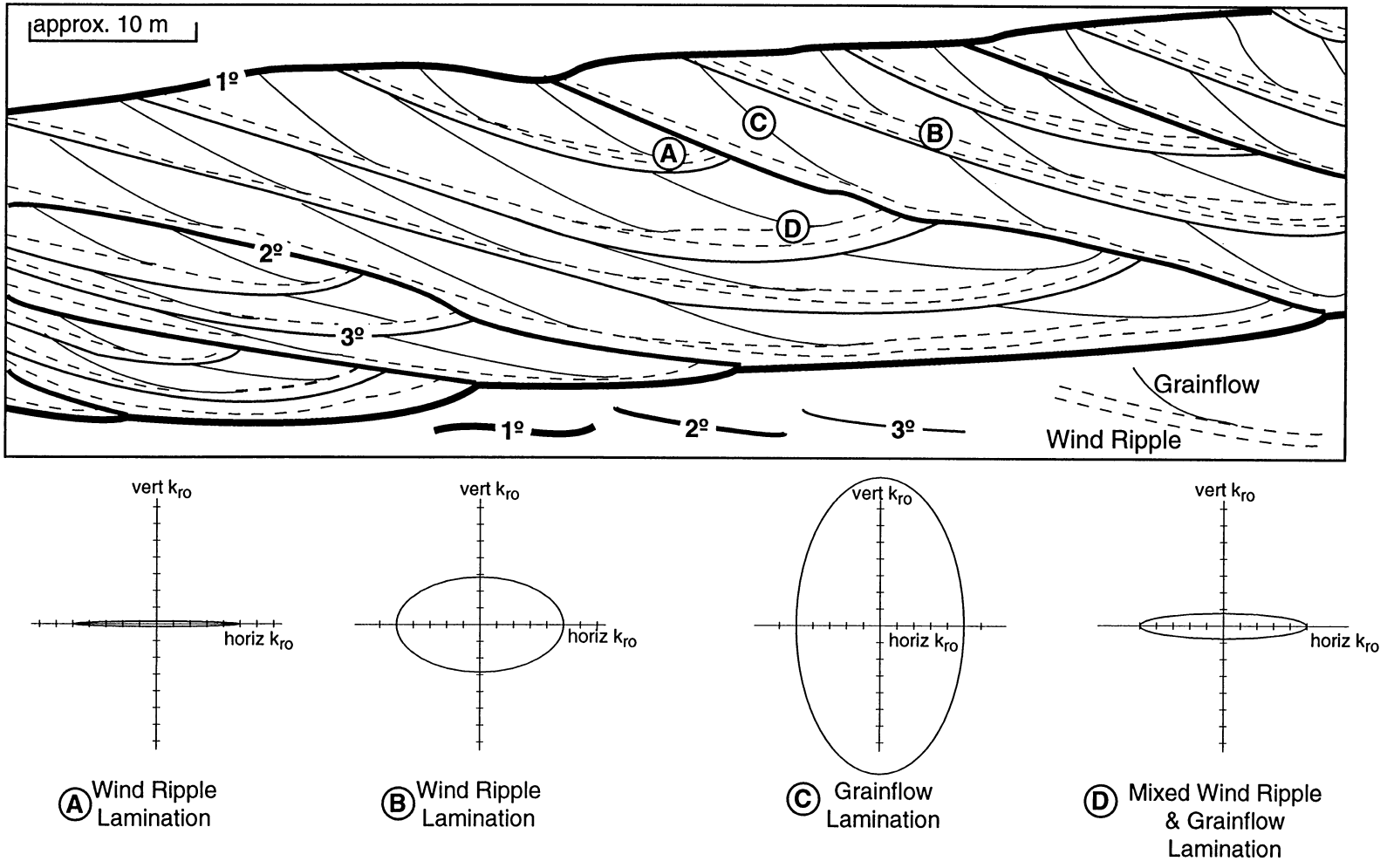

Figure ES 1. Oil relative permeability anisotropy associated with different types of eolian lamination found in the Tensleep. Locations of samples on the schematic drawing of a typical Tensleep outcrop are schematic with respect to types of lamination. Each sample represents a pair of samples - one taken parallel to the lamination and one taken perpendicular to it. The ellipses represent the horizontal and vertical oil relative permeability at each point. A=sample HR75, B=sample NNB3, C= sample MB65, D=sample MB60.

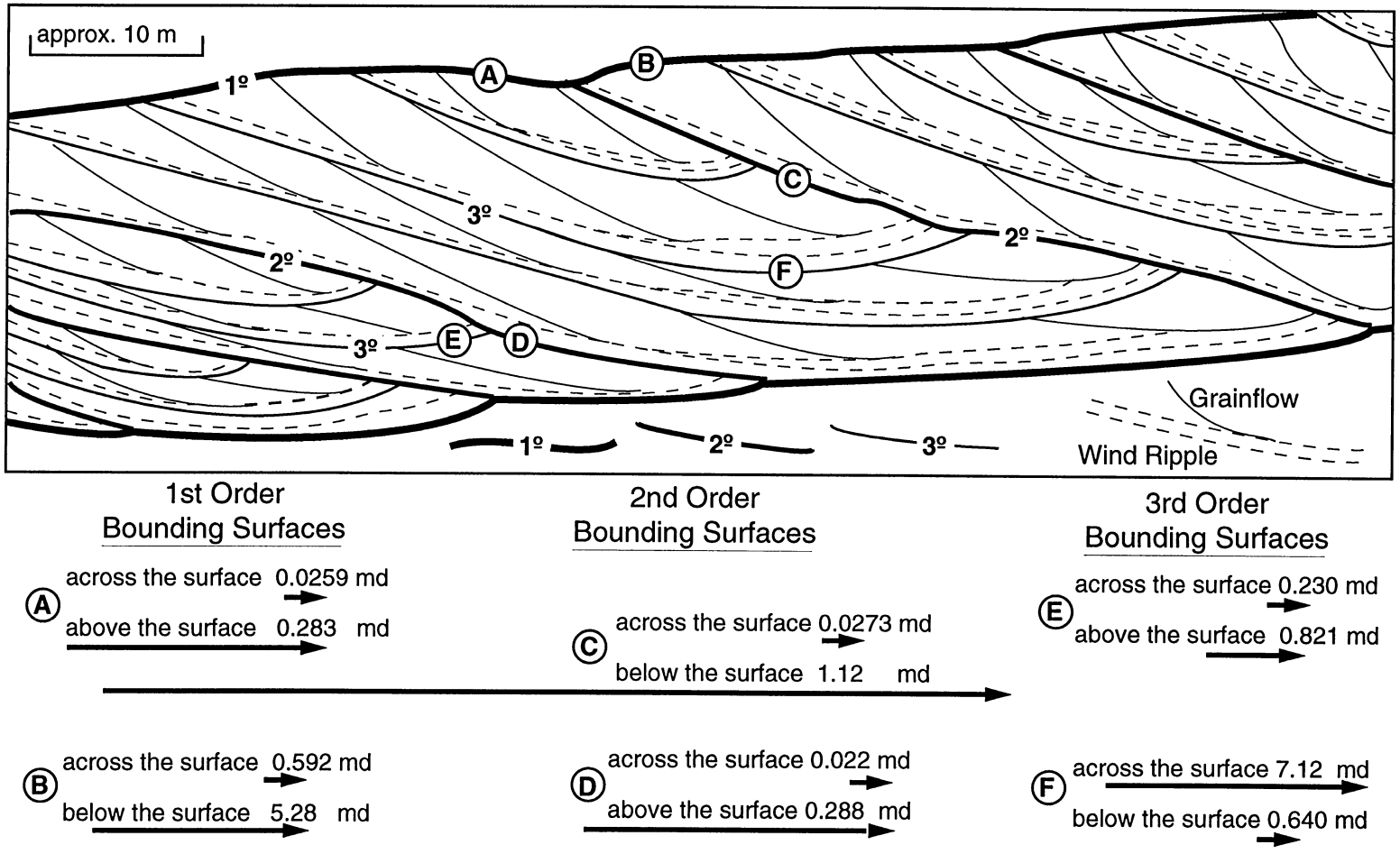

Figure ES 2. Oil relative permeability heterogeneity associated with 1st, 2nd, and 3rd order bounding surfaces. Locations of samples on this schematic drawing of a typical Tensleep outcrop are schematic with respect to types of bounding surfaces. Each sample represents a pair of samples - one taken across the bounding surface and one taken immediately above or below the bounding surface. The length of the arrows are proportional to the differences in the oil relative permeability between the sample pair. A=sample HR75, B=sample NNB3, C=sample MB65, D=sample MB60, E=sample MB20, and F=sample 3B8A.

Improved Oil Recovery from Change in Water Chemistry

Recent work by Tang and Morrow (1996), Yildiz (1995), and Yildiz and Morrow (in press) has shown that oil recovery from waterflooding is sensitive to the composition of the injected brine. Tang and Morrow (1996) showed that injected brine that was more dilute than the connate brine resulted in improved recovery. Typically, Tensleep waterflood projects in the Bighorn and Wind River basins re-inject Tensleep produced water. However, the experiments described above indicate that if a different injection water composition was used, recovery would improve.

Our comprehensive work on the distribution of Tensleep Formation water chemistry was used to estimate potential oil recovery improvement for Tensleep fields in the Bighorn and Wind River basins based on the coefficients derived from the results of the experiments described above. The calculations show that using a waterflood with injection water chemistry that is either more dilute than the formation water for many Tensleep fields may considerably prolong the life of a field. Total incremental recovery is over 15 MMBO. This would result in over $11 million to the State of Wyoming in severance tax alone assuming a low oil price of $13/bbl. Because the Tensleep Sandstone accounts for only 20% of the current oil production in the State, the potential is very large. If this approach was applied and was successful in the other oil producing formations, the gross revenue derived could approach one billion dollars.

TECHNICAL TRANSFER

Technical transfer of the results of this project has covered a variety of media and venues, including the internet. This has allowed us to reach the largest number of people who can benefit from this DOE sponsored research.

In addition to the formal technical transfer items discussed below, numerous informal contacts have been made with industry representatives. Marathon personnel from both the Cody and Littleton offices have made site visits to our offices and have made numerous phone contacts.

The exhibit booth of the Institute for Energy Research which includes highlights of this research has been another important mode of informal technical transfer. Many people in the petroleum industry have learned of this research through this exhibit booth and the researchers who are on hand to discuss it. The booth was displayed at IER's open house in 1994, 1995, and 1996. It was also on display for the 1996 Wyoming legislative session where it was seen by all the legislators, several of whom are in the petroleum industry and most of whom have constituents who are affected by oil revenues. More importantly, the exhibit booth and the results of this research were shown at the Wyoming Governor's Conference on Energy and Minerals in Casper and at a reservoir characterization conference in Denver sponsored by the Gas Research Institute and the Independent Petroleum Association of Mountain States. Attendance at these events resulted in numerous requests for more information and for copies of our annual reports.

World Wide Web Site

We created our www site (//ierultra1.uwyo.edu) to take advantage of the technology enabling people to access our research results from their computer. The site includes our past technical reports and a considerable portion of the data and results of this study. Since May 1996 when we began to collect this type of data, our web site has been visited over 600 times from locations across the United States as well as abroad.

Publications and Theses

This DOE project has resulted in two masters theses, one in petroleum engineering and one in geology. Both of these masters students have gone on to work in the petroleum industry, one with AGAT Laboratories in Canada and the other with Burlington Northern in Midland, Texas.

In addition to the theses, technology transfer has taken place via petroleum industry publications. Several articles have been published, one is in press, and several have been submitted. Additionally, because much of the results were completed late in the term of the contract, several additional publications are in preparation. These will present the latest results as well as pull together the results of the different tasks. Publications are listed below.

Ajdari, I., 1995, Anisotropy of relative permeability within the TensleepSandstone: M.S. thesis, University of Wyoming, 106 p.

Carr-Crabaugh, M., and Dunn, T.L., 1996, Reservoir heterogeneity as a function of accumulation and preservation dynamics, Tensleep Sandstone, Bighorn and Wind River Basins, Wyoming *in* M.W. Longman and M.D. Sonnenfeld, eds., Paleozoic systems of the Rocky Mountain region: Rocky Mountain Section SEPM (Society for Sedimentary Geology), p. 305-320.

Carr-Crabaugh, M., Hurley, N.F., and Carlson, J., 1996, Interpreting eolian reservoir architecture using borehole images: GCS-SEPM Foundation 17th Annual Research Conference on Stratigraphic Analysis, December 8-11, 1996, Houston.

Crabaugh, Mary, and Dunn, Thomas L., 1995, Reservoir heterogeneity as a function of accumulation and preservation dynamics, upper Tensleep Sandstone, Bighorn Basin, Wyoming: (abstract) Program of the Annual Convention of American Association Of Petroleum Geologists, p. 18A.

Dunn, Thomas L., Carr, M., Humphreys, J. D., and Iverson, W.P., Relative permeability anisotropy and heterogeneity of the upper Tensleep Sandstone and implications for oil recovery from eolian reservoirs: *in preparation*, to be submitted to American Association of Petroleum Geologists Bulletin.

Dunn, Thomas L. and Humphreys, J. D., Image analysis applications to estimating relative permeability: *in preparation*, to be submitted to American Association of Petroleum Geologists Bulletin.

Humphreys, J. D., 1996, Determination and geologic interpretation of relative permeability anisotropy and heterogeneity in eolian depositional units of the Tensleep Sandstone, Wyoming: Master of Science Thesis, University of Wyoming, 175 pp.

Iverson, W.P., T.L. Dunn, and I. Ajdari, 1996, Relative permeability anisotropy measurements in Tensleep Sandstone: Society Of Petroleum Engineers, Paper No. SPE 35435; SPE/DOE Tenth Symposium On Improved Oil Recovery.

Shiraki, Ryoji, and Dunn, Thomas L., 1995, Origins of Tensleep formation water chemistry and the prediction of scale formation during CO_2 treatments, Bighorn Basin, Wyoming: (abstract) Program of the Annual Convention of American Association Of Petroleum Geologists, p. 88A.

Shiraki, R., and Dunn, T. L., Experimental study on water-rock interactions during CO_2 flooding in Tensleep sandstone reservoirs, northern Wyoming, USA: *in preparation* to be submitted to Applied Geochemistry.

Shiraki, R., and Dunn, T. L., Experimental study on crude oil-water-rock interactions during CO_2 flooding in Tensleep sandstone reservoirs, northern Wyoming, USA: implications for carbonate scale formation: *in preparation* to be submitted to Applied Geochemistry.

Presentations

Presentations of the research results have been made at national and local meetings. These have included both oral presentations and poster displays. Presentations have also been made to individual oil companies. Additional presentations are planned for later in 1996 and in 1997. All of these presentations are listed below.

Carr, Mary, 1996, Reservoir heterogeneity as a function of accumulation and preservation dynamics, upper Tensleep Sandstone, Bighorn Basin, Wyoming: Rocky Mountain Section of SEPM (Society for Sedimentary Geology), Luncheon, September 22, 1996, Denver, CO.

Carr-Crabaugh, M., 1995, Tensleep reservoir architecture: Presentation to Marathon Oil Co., July, Cody, Wyoming.

Carr-Crabaugh, M., 1995, Tensleep Sandstone reservoir architecture seen in outcrop in the Bighorn Basin, Wyoming: Field Trip for Marathon Oil Co. personnel from Cody, Wyoming office.

Crabaugh, Mary, and Dunn, Thomas L., 1995, Reservoir heterogeneity as a function of accumulation and preservation dynamics, upper Tensleep Sandstone, Bighorn Basin, Wyoming: Poster Presentation at the American Association Of Petroleum Geologists Annual Convention, March 5-8, Houston.

Dunn, Thomas L., John D. Humphreys, and Iverson, W. P., 1997, (submitted), Relative permeability anisotropy and heterogeneity of the upper Tensleep Sandstone and implications for oil recovery from eolian reservoirs: American Association of Petroleum Geologists Annual Meeting, April, Dallas, TX.

Humphreys, J.D., and Dunn, T.L., 1996, Geologic interpretation of relative permeability anisotropy in eolian sandstones, Tensleep Sandstone, Wyoming: Reservoir Characterization Symposium, Denver, CO, Sept. 13, 1996, sponsored by the Rocky Mountain Association of Geologists and the Denver Geophysical Society.

Shiraki, R., and Dunn, T. L., 1997, (submitted), Experimental study on CO_2 coreflooding using dolomite- and anhydrite-cemented Tensleep sandstone from the Bighorn Basin, Wyoming: American Association of Petroleum Geologists Annual Meeting, April, Dallas, TX.

Shiraki, Ryoji, and Dunn, Thomas L., 1995, Origins of Tensleep formation water chemistry and the prediction of scale formation during CO_2 treatments, Bighorn Basin, Wyoming: Poster Presentation at the American Association Of Petroleum Geologists Annual Convention, March 5-8, Houston.

TASK 1.0: REGIONAL FRAMEWORKS

OBJECTIVES

This research characterizes regional trends and variations in the important reservoir and boundary lithofacies of the Tensleep and documents how the reservoir units vary in dimension and character across the productive region. By doing so, this portion of the research links the relative permeability and pore geometry work to distinct and measurable dimensions of eolian lithofacies.

INTRODUCTION

The regional sedimentological framework was the focus of extensive analysis in this study. Our goal was to examine the Tensleep in light of recently advanced concepts of preservation and accumulation. The following two sections are derived wholly from two completed publications reporting on investigations of the large scale features and smaller scale baffles within Tensleep reservoirs.

RESERVOIR HETEROGENEITY AS A FUNCTION OF ACCUMULATION AND PRESERVATION DYNAMICS, TENSLEEP SANDSTONE, BIGHORN AND WIND RIVER BASINS, WYOMING*

MARY CARR-CRABAUGH[1,2] AND THOMAS L. DUNN[1]

[1] Institute for Energy Research
University of Wyoming
P.O. Box 4068
Laramie, Wyoming 82071

[2] Current Address:
Colorado School of Mines
Department of Geology & Geological Engineering
Golden, CO 80401-1887

Abstract

The processes controlling accumulation and preservation of the Tensleep Sandstone eolian units in the Bighorn Basin are distinct, and have different effects on reservoir heterogeneity. Accumulation is the net deposition of sediments within an eolian system, whereas preservation marks the entrance of the sediments into the stratigraphic record. Accumulation of the Upper Tensleep Sandstone in the Bighorn Basin occurred within a dry eolian system, that is, one in which accumulation occurs as a result of aerodynamic controls and is unaffected by the local water table. Conversely, preservation of the Upper Tensleep was caused by the relative rise of sea level that placed the area below the regional base-level of erosion. The orientation and character of the bounding

* *in* M.W. Longman and M.D. Sonnenfeld, eds., Paleozoic systems of the Rocky Mountain region: Rocky Mountain Section SEPM, p.305-320.

surfaces and internal laminations of eolian facies in the Tensleep indicate that the ergs were dominated by large compound bedforms that were affected by annual fluctuations in airflow.

Reservoir heterogeneity can be considered on different scales within the Upper Tensleep Sandstone. Small-scale heterogeneities, such as stratification type, bounding surfaces, and lateral variations in microscopic pore structure, are the result of variations in the character of the bedforms during accumulation. These variations in fabric, along with drive type and fluid mobility ratio, govern sweep efficiency and ultimate recovery. Large-scale heterogeneities, represented by the areally extensive marine dolomites within the Upper Tensleep, are controlled by longer-term variations in preservation space as influenced by relative sea-level fluctuations. These features govern overall reservoir continuity and, along with tectonic fabric, reservoir size. Delineation of these sedimentary processes and the resulting rock fabrics will enhance future incremental production from the Upper Tensleep Sandstone, Wyoming.

Introduction

The Tensleep Sandstone, currently produces more oil than any other formation in the state of Wyoming, and is the largest enhanced oil recovery target in the state. The Tensleep and its equivalents in Wyoming have produced over one billion barrels of oil. Declining recovery and the enormity of the remaining oil-inplace provide motivation for reconsidering the models that drive enhanced oil recovery techniques in the Tensleep Sandstone.

Previous authors have demonstrated that heterogeneity in eolian reservoirs is significantly controlled by the depositional processes that formed the accumulation of sediment (Goggin et al., 1988; Lindquist, 1988; Chandler et al., 1989). Nelson (1985) demonstrated pronounced effects of bedding on absolute permeabilities and porosity-permeability relationships in the eolian sandstone of the Nugget Formation. This paper will demonstrate that the compartmentalization and spatial variations in permeability in the Tensleep Sandstone are largely controlled by the processes taking place during accumulation and preservation of the eolian sediments. Accumulation is the net

deposition of sediments within an eolian system, whereas preservation marks the entrance of the sediments into the stratigraphic record (Kocurek and Havholm, 1993). Because the processes taking place during eolian accumulation can be determined, it is possible to construct accurate depositional models of the Tensleep eolian system and improve prediction of reservoir spatial heterogeneity.

Reservoir heterogeneity can be considered on a number of scales within the Upper Tensleep Sandstone, reflecting the stratigraphic architecture and the controls on accumulation and preservation. The upper Tensleep is composed of a series of eolian sandstone - marine dolostone sequences. Small-scale heterogeneities are delineated by erosional bounding surfaces that subdivide the eolian cross-stratified sandstones. These small-scale heterogeneities reflect the processes taking place during accumulation of the Tensleep Sandstone in a dry eolian system. The largest-scale and most commonly recognized heterogeneities or barriers to flow in the Tensleep are the marine dolomitic units that punctuate and divide the eolian cross-stratified sandstones (Emmett et al., 1971). These marine dolomitic units record marine flooding events that resulted in the preservation of the Tensleep eolian systems.

Methods

Both surface and subsurface data were collected to address both the smallscale features that result from accumulation processes and the larger-scale features associated with preservation processes (Fig. 1.1). Outcrop descriptions and photomosaics were collected to document the internal sedimentary structures of the eolian system that resulted from accumulation processes. Documentation of the dimensions of the larger-scale sandstone - dolomite sequences was produced by the analysis of 168 well logs from the entire Bighorn Basin. Reconstructions of the Tensleep bedforms were performed using the computer program developed by Rubin (1987).

Stratigraphy and Paleogeography

The Tensleep Sandstone is Middle Pennsylvanian (Desmoinesian) to Lower Permian (Wolfcampian) in age, as determined primarily on the basis of

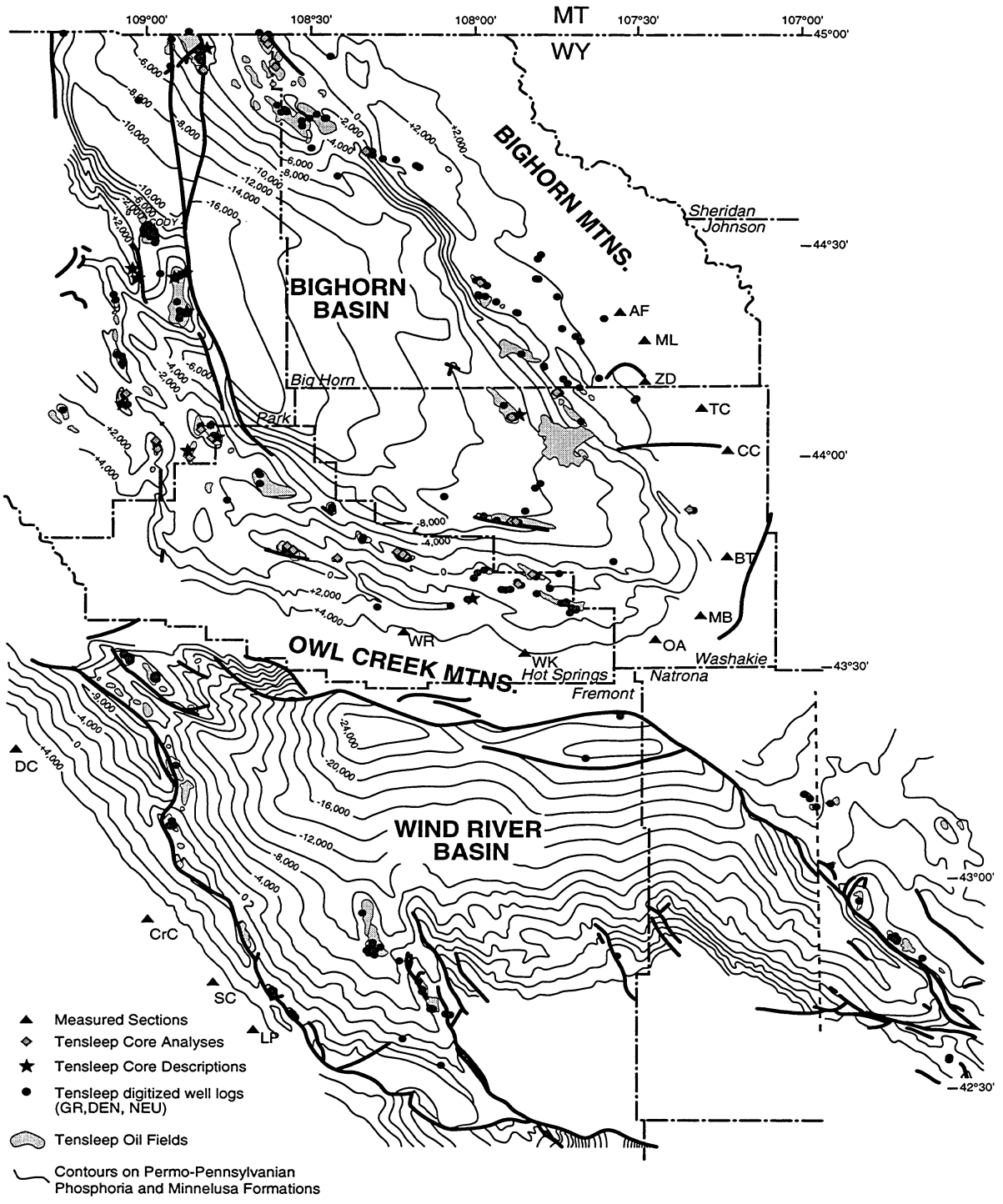

Figure 1.1. Location of Tensleep oil fields and digitized well log and core analyses for the Bighorn and Wind River basins as of October 15, 1995. Section and photomosaic locations north to south: AF=Alkali Flats, ML=Medicine Lodge, ZD=Ziesman Dome, TC=Tensleep Canyon, CC=Canyon Creek, BT=Big Trails, MB=Mohagany Butte, OA=Orchard Anticline, WR=Wind River Canyon, WK=West Kirby Creek, DC=Dinwoody Canyon, CrC=Crooked Creek, SC=Sinks Canyon, LP= Little Popo Agie Canyon. Base map after WGA (1989)

fusulinids (Branson, 1939; Henbest, 1954, 1956; Verville, 1957) and supported by brachiopod (Brainerd and Keyte, 1927; Hoare and Burgess, 1960) and conodont studies (Rhodes, 1963) (Fig. 1.2). Verville et al. (1970) also demonstrated differential truncation of the Tensleep along the eastern flank of the southern Bighorn Mountains, with Wolfcampian strata exposed at the top of the Tensleep in southern areas and Desmoinesian strata exposed at the top in the northern areas. Differential erosion across the top of the Tensleep Sandstone in the Bighorn Basin, resulting in significant variations in unit thickness, has also been demonstrated through physical stratigraphic relationships by Wheeler (1986), Kerr et al. (1986), and Kerr (1989).

The Tensleep Sandstone is composed of a series of eolian sandstones and marine dolomitic sandstones, reflecting cyclic relative sea-level change (Mankiewicz and Steidtman, 1979; Kerr et al., 1986; Wheeler, 1986; Kerr, 1989). Using well-log cross sections, several of the dolomitic units are correlated across the Bighorn Basin (Fig. 1.3). The Tensleep has been informally divided into lower and upper units using the top of a widespread fusulinid, coral-bearing, dolomitic sandstone, following the method of Agatston (1952, 1954) and Wheeler (1986). This sandstone is recognized in well logs as a high-density, low-porosity bed that separates the serrated porosity and gamma-ray log signature of the lower Tensleep from the more blocky signature of the upper Tensleep. Both the lower and upper Tensleep are composed of eolian-marine sequences, but the lower Tensleep is dominated by marine facies and the upper Tensleep is dominated by eolian facies. This paper will concentrate on the eolian

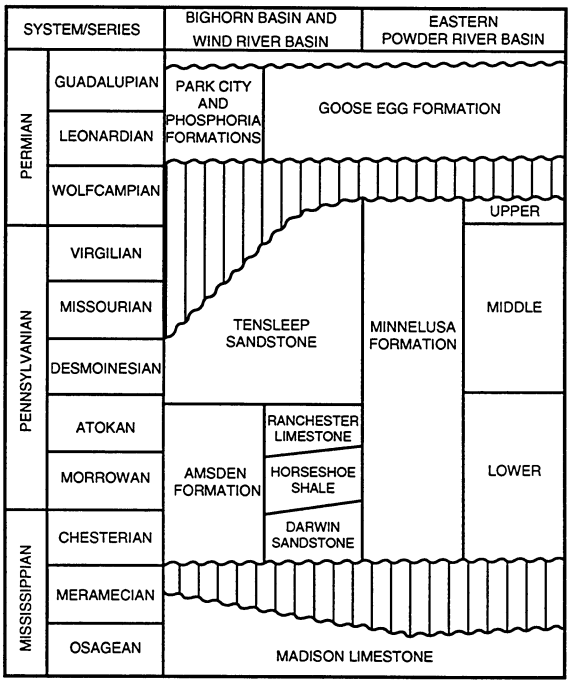

Figure 1.2. Correlation chart showing Mississippian through Permian units in the Bighorn and Wind River basins. After Wheeler (1986)

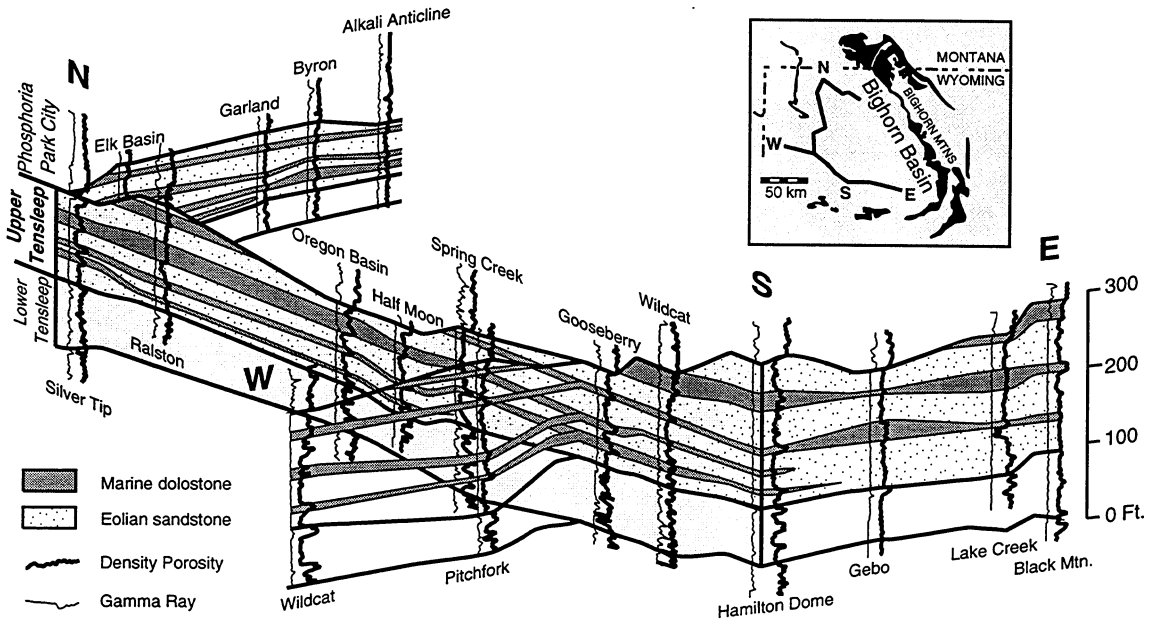

Figure 1.3. Fence diagram illustrating correlatability of individual marine dolomitic units across the Bighorn Basin. Inset map indicates outcrop pattern of upper Paleozoic rocks and the location of wells used in diagram.

dominated facies of the upper Tensleep, which have provided most of the hydrocarbon production.

The upper Tensleep eolian-marine sequences are composed of compound sets of eolian cross-strata gradationally overlain by sandy to fossiliferous dolomites capped by a sharp to erosional contact (Fig. 1.4). The eolian units of the Bighorn Basin are characterized by fine- to very fine-grained, feldspathic quartz arenites with varying amounts of quartz, carbonate, and anhydrite cements.

Figure 1.5 illustrates the general Late Pennsylvanian to Early Permian paleogeography of the United States during a sea-level lowstand. The study area was at approximately 10° north latitude during accumulation of the Tensleep Sandstone (Scotese et al., 1979). Paleocurrent measurements from eolian crossstrata indicate a predominance of southwest dips (Wheeler, 1986; Peterson, 1988; Kerr, 1989). This corresponds well with paleowind flow reconstructions for this time period shown in Figure 1.5, which indicate that winds out of the present-day north and northeast were dominant (Parrish and Peterson, 1988; Peterson, 1988). The global circulation models of Parrish and

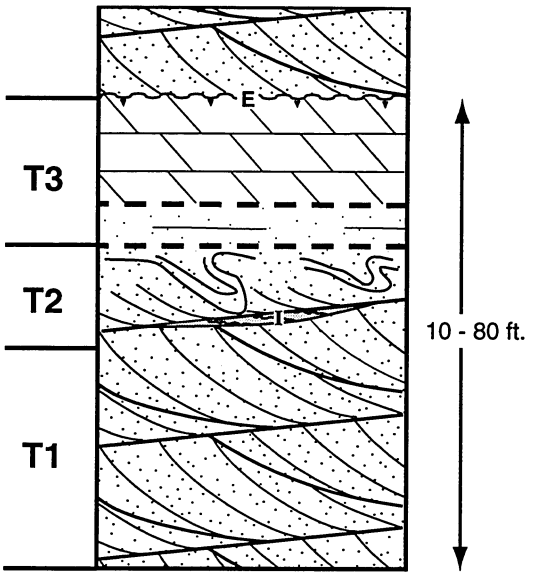

Figure 1.4. Idealized Upper Tensleep eolian-marine cycle. Eolian sandstone accumulation shows a thin, discontinuous interdune accumulation toward the top (I). The uppermost eolian sands are commonly contorted. The eolian sands are gradationally overlain by sandy marine dolomites, which are capped by an erosional surface (E). T1, T2, and T3 correspond to schematic diagrams in Figure 1.7.

resulted from completely independent processes. Accumulation represents the net deposition of sediment through time resulting in a three-dimensional body of sediment (Kocurek and Havholm, 1993). Preservation refers to the placing of an accumulation below some regional baselevel of erosion. Kocurek and Havholm (1993) identified a spectrum of eolian systems as dry, wet, and stabilized, Peterson (1988) indicate a monsoonal climate that had annual fluctuations in wind direction such that the summer winds were northerly and the winter winds were northeasterly.

Tensleep Depositional Model

The accumulation and preservation dynamics of the Tensleep eolian system influenced later fluid migration in the subsurface Tensleep Sandstone reservoirs. In the Tensleep eolian system, accumulation of eolian sediments and their subsequent preservation

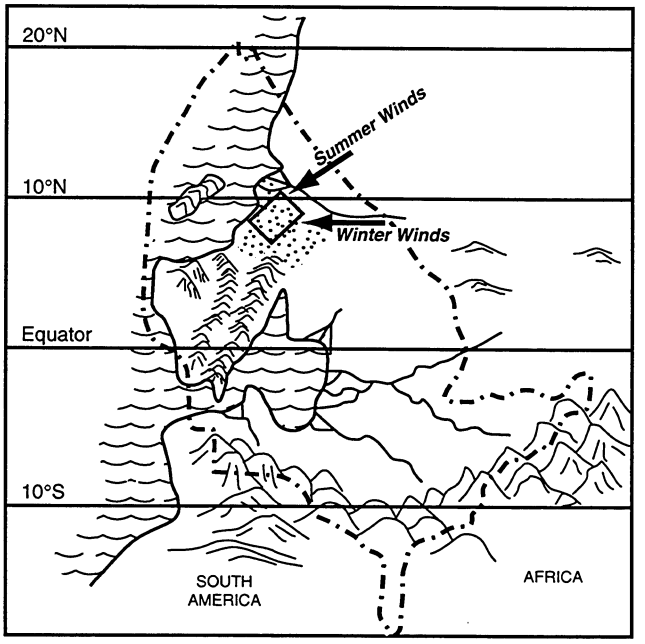

Figure 1.5. Generalized Pennsylvanian to Early Permian paleogeography during a sea-level lowstand. Stipple pattern indicates area of eolian development. Arrows depict paleowind directions from Parrish and Peterson (1988). Box indicates the Bighorn and Wind River basins study area. Modified from Kerr and Dott (1988). Dash-dot line indicates United States border.

depending on the geological processes affecting accumulation. The lack of sedimentary structures normally indicative of a high water table and the paucity of interdune accumulations suggest that the Tensleep eolian accumulations formed in a dry eolian system. A dry eolian system is one in which the water table is at a depth below the sediment surface, such that it has no stabilizing influence on the sediment, and in which accumulation takes place strictly for aerodynamic reasons (Kocurek and Havholm, 1993). Regional relative sea-level rise resulted in flooding of the Wyoming shelf and the formation of marine carbonates. This placed the Tensleep eolian system below the regional base-level of erosion, resulting in its preservation. Figure 1.6 illustrates the accumulation and preservation processes that influenced the formation of the Tensleep Sandstone.

Time 1 in Figure 1.6 depicts a time shortly after an initial sea-level fall and the development of a dry eolian system. This dry eolian system was characterized by large bedforms separated by dry interdune depressions. Data from crossbed orientations, corrected for structure where necessary, indicate that large bedforms were migrating to the south-southwest. As the bedforms migrated and climbed through time, they produced an accumulation of cross-stratified lee-face deposits. The lack of sedimentary structures associated with damp surfaces indicates that the local water table was well below the depositional surface and did not affect accumulation.

Time 2 in Figure 1.6 illustrates the Tensleep at some later time when relative sea level had begun to rise again, causing the local continental water table to rise as well. As the local water table rose, it encountered and flooded the deeper interdune areas. The Tensleep system remained a dry system in which isolated interdune areas were experiencing accumulation under damp conditions. In outcrop, the interdune accumulations tend to occur in the upper one-third of the eolian units. They are characterized by wavy-bedded, very-fine grained sandstones in lens-shaped, laterally discontinuous accumulations. The geometry of the interdune accumulations in outcrop suggests that these interdune areas were not laterally connected (Time 2, Fig. 1.6).

With continued relative sea-level rise the eolian system was flooded and reworked by the marine environment, resulting in a gradational contact between the eolian sandstones and marine fossiliferous sandstones and dolostones (Time 3, Fig. 1.6). Conditions of very low slope and a relatively low-energy shoreline prevented shoreface ravinement from destroying much of the dune-field accumulation. Commonly, the uppermost portions of the eolian units show

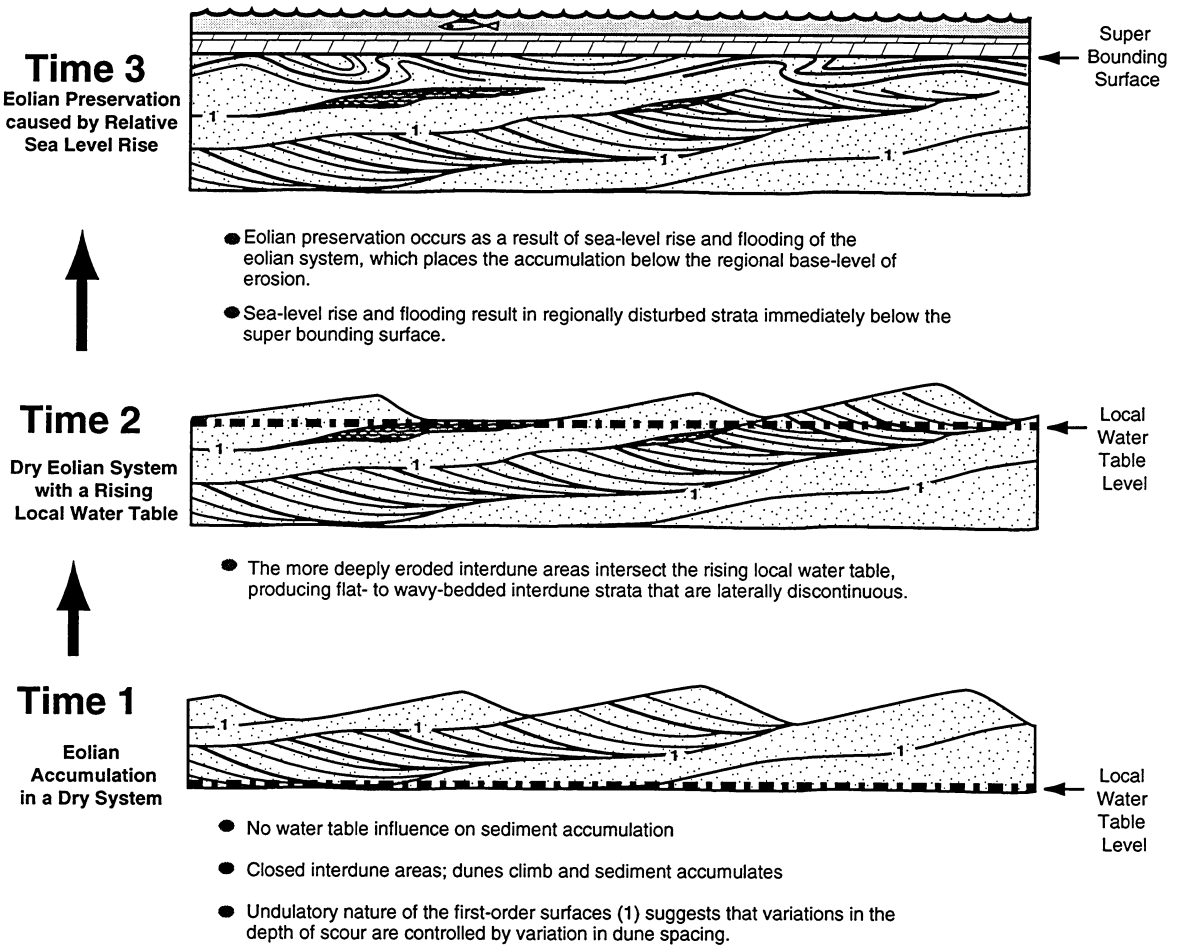

Figure 1.6. Schematic diagrams illustrating accumulation and preservation dynamics of the Tensleep Sandstone parallel to transport direction. Times 1,2, and 3 correspond to T1, T2, and T3 in Figures 1.4 and 1.7. Time 1: Accumulation of sediments in a dry eolian system. The water table is well below the depositional surface and is not influencing accumulation. Time 2: Relative sea-level rise is driving up the coninental water table, causing it to flood the most deeply scoured interdune areas. In outcrop, the interdune accumulations are laterally discontinuous wavy-bedded, heavily-cemented, fine-grained sandstones. Time 3: Relative sea-level rise results in flooding of the area and preservation of the eolian cross-stratified units. Contorted laminae (wavy lines) commonly occur in the upper portions of the eolian sandstone units. Subsequent relative sea-level fall results in the formation of an erosional surface capping the marine carbonates.

softsediment deformation related to flooding of the area and fluid escape, but the exact mechanism of deformation is not well understood. Thus, relative sea-level rise resulted in preservation of the Tensleep eolian accumulations. Subsequent relative sea-level fall resulted in exposure of the marine sediments and the formation of an erosional surface that capped the sequence (Figs. 1.4 and 1.6).

Sequence Stratigraphic Framework

The previous section described the processes occurring in the Tensleep eolian system in response to relative sea-level change; it remains to relate the timing of those processes to a sequence stratigraphic framework. Figure 1.7 illustrates how the Tensleep eolian-marine sequences would be placed into a sequence stratigraphic framework. Two significant bounding surfaces are

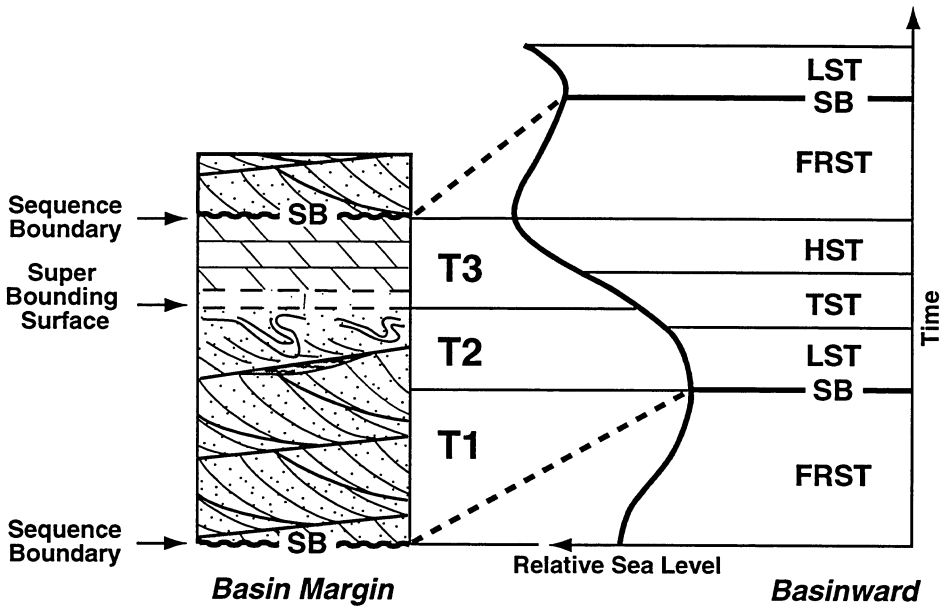

HST Highstand Systems Tract **LST Lowstand Systems Tract**

TST Transgressive Systems Tract **FRST Forced Regressive Systems Tract**

SB Sequence Boundary

Figure 1.7. Idealized Tensleep eolian-marine sequence and its relationship to relative sea-level change. Relative sea level is the combined effect of subsidence and eustatic sea-level change. Relative sea level curve and sequence stratigraphic nomenclature derived from Helland-Hansen (1995).

evident within the Tensleep eolian-marine sequences. The first is the marine flooding surface separating the eolian units from the marine units. This surface is defined as a *super bounding surface* in the terminology developed for eolian depositional systems by Kocurek (1988) and Holland-Hansen (1995) (Fig. 1.7). A super bounding surface marks the cessation of eolian accumulation and in some cases a significant lateral shift in depositional systems.

The second significant surface is the subaerial erosion surface that caps the marine units in the Tensleep sequences. It is a surface of significant basinward shift of environments, and is equivalent to a *sequence boundary* (in the sense of Van Wagoner et al., 1988 and Holland-Hansen, 1995) (Fig. 1.7). As soon as relative sea-level begins to fall, the basin margin accumulations are subject to subaerial erosion, whereas basinward sediments continue to accumulate in the forced regressive systems tract (FRST). According to Helland-Hansen (1995) the erosional sequence boundary continues to form during the entire time of falling relative sea-level and should overlie the deposits of the forced regressive systems tract. This, however, may not be the case in a dry eolian system where sediments can accumulate during relative sea-level fall, because of the absence of traditionally thought of base-level-controlled accommodation space. In the Tensleep Sandstone the erosional sequence boundary is overlain by the accumulations that form during the time of relative sea-level fall (i.e., FRST), and these accumulations are subsequently preserved in the accommodation space formed by the subsequent relative sea-level rise. Accumulation of sediment in a dry eolian system is occurs during relative sea-level fall (rather than during the subsequent rise as would be the conventional interpretation), because of the maximum dryness likely to be induced by the lower water table. This interpretation suggests that the sequence boundary is a time-transgressive surface between the basin margin and the more basinal deposits, in the case of a dry eolian system.

Figure 1.7 places the Tensleep into a regional context from which inferences about the timing of events in the basin can be related to their resultant effects on the basin-margin shelf. The sequence boundary and the dry eolian accumulations that overlie it form consecutively during relative sea-level

fall. It is not possible to determine how much time is represented by each. The eolian accumulations are preserved by flooding of the area during transgression. The transgression is also responsible for the formation of super bounding surfaces and subsequent marine accumulations. This, however, need not be the case for all types of eolian accumulations.

Controls On Reservoir Heterogeneity

With these depositional processes in mind, reservoir heterogeneity within the Tensleep Sandstone can be divided into small-scale heterogeneities formed by accumulation processes and large-scale heterogeneities formed by preservation processes. The small-scale heterogeneities, such as variations in stratification type and bounding surface formation, are directly related to the depositional processes that took place during eolian accumulation. The sea-level-driven sandstone-dolostone sequences represent the large-scale heterogeneities.

Accumulation Processes

As previously stated, the Tensleep is composed of a series of eolian sandstone - marine dolostone sequences (Fig. 1.4). The eolian sandstone units are composed of one to several sets of compound cross-strata. A set of cross-strata is defined as compound if it contains internal erosional surfaces. An individual set of cross-strata represents the accumulation created by the migration and climb of a single large bedform. The erosional surface that separates one set of cross-strata from another is referred to as a first-order surface; it is produced by erosional processes within the interdune area (Brookfield, 1977; Kocurek, 1981; Rubin and Hunter, 1982) (Fig. 1.8). The Tensleep first-order surfaces are commonly undulatory, and show up to 6m (20ft) of relief over a lateral distance of approximately 91m (300 ft) (Fig. 1.9).

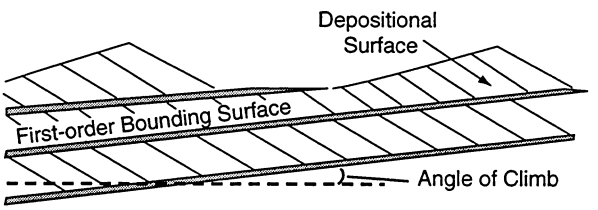

Figure 1.8. Illustration of bedforms climbing through time and space along first-order bounding surfaces. After Kocurek (1988).

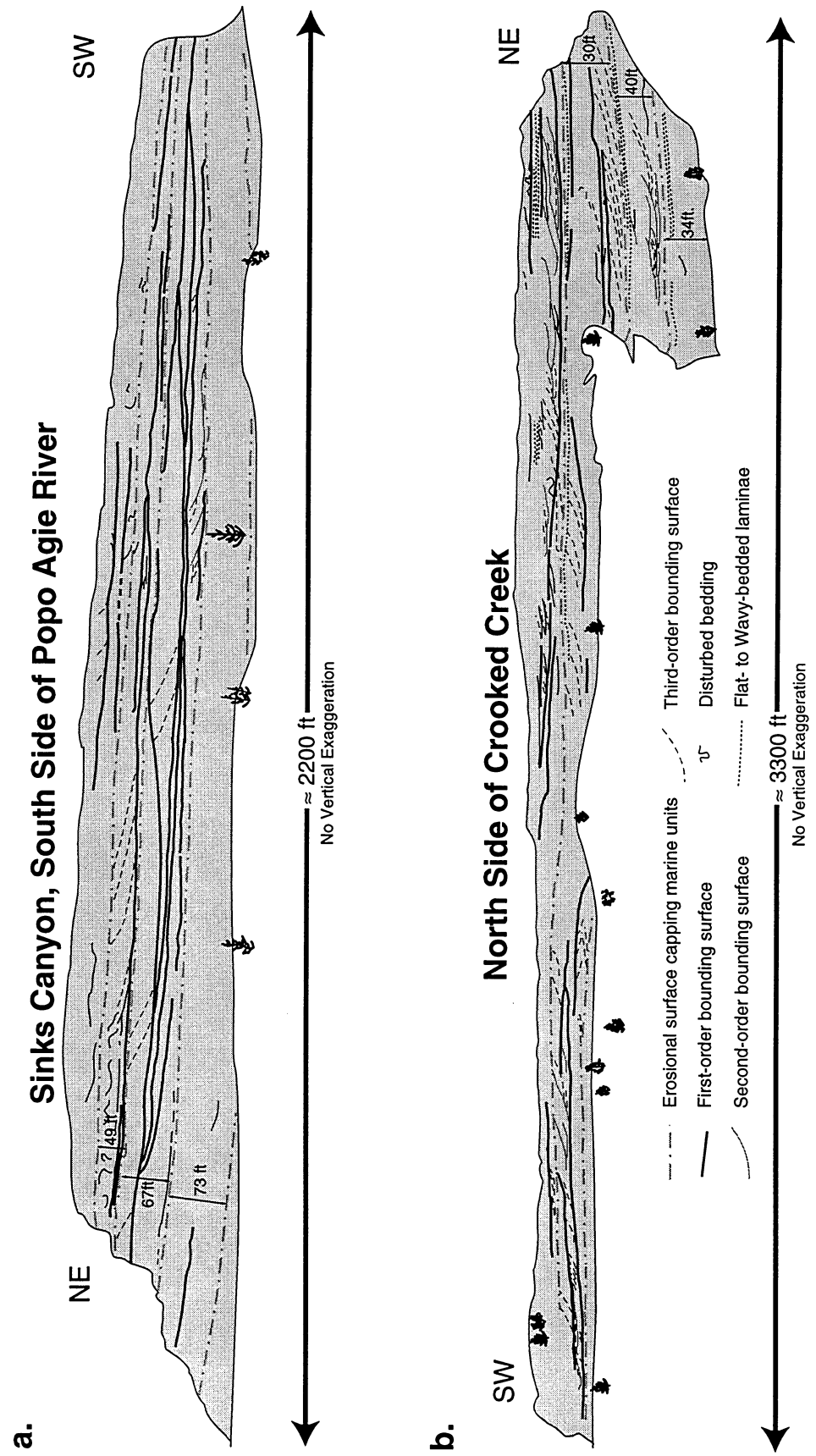

Figure 1.9. Line drawings of outcrop photomosaics, illustrating complexity of stratification within the Tensleep Sandstone. a. Line drawing of outcrop photomosaic from the south side of the Popo Agie River in Sinks Canyon State Park. Note the undulatory nature of the first-order surfaces. b. Scaled drawing of the outcrop of the north side of Crooked Creek, illustrates the abundant second-order surfaces present in some portions of the Tensleep Sandstone.

The undulatory nature of the Tensleep first-order surfaces resulted in the formation of laterally discontinuous, lens-shaped interdune accumulations. The Tensleep eolian system was primarily a dry system in which accumulation processes were unaffected by the local water table. However, as the relative sea level rose, it caused the local continental water table to gradually rise as well (Time 2, Fig. 1.6). As the rising water table encountered the depositional surface in the more deeply scoured interdune areas, the interdune surface became damp, and very fine-grained sand tended to become trapped in the capillary fringe of the water table and resist the erosive effects of the wind. The dampness of the interdune surface also led to the formation of early evaporitic cements (Krystinik, 1990), which were diagenetically altered to dolomite and anhydrite in the subsurface. Biological activity in the form of bacterial and fungal growth also increased. All these factors led to the formation of evaporite-cemented and wavybedded interdune strata. Tensleep interdune accumulations tend to stand out in outcrop relief because they are more heavily cemented than the surrounding cross-stratified sets.

The internal erosional bounding surfaces within the compound sets of crossstrata indicate that erosion was taking place on the lee face of the bedform. According to Rubin and Hunter (1983, p. 407) erosion on the lee face is caused by two processes: "(1) flow changes, such as shifting winds or reversing currents, that change bedform morphology and produce relatively synchronous bounding surfaces that are called reactivation surfaces, and (2) local erosion that may occur continuously in the troughs or on the stoss slopes of small bedforms that migrate across the lee slope of a larger bedform." Reactivation surfaces are also referred to as third-order surfaces, and the erosional surfaces caused by small superimposed bedforms migrating along the lee face of a larger bedform are called second-order surfaces (Brookfield, 1977; Kocurek, 1981). Both of these surfaces have been identified in the Tensleep using criteria set forth in the literature (Brookfield, 1977; Kocurek, 1981; Rubin and Hunter, 1983; Rubin, 1987; Crabaugh and Kocurek, 1993). Figure 1.10 is a composite schematic drawing of the compound cross-strata observed in Tensleep Sandstone outcrops.

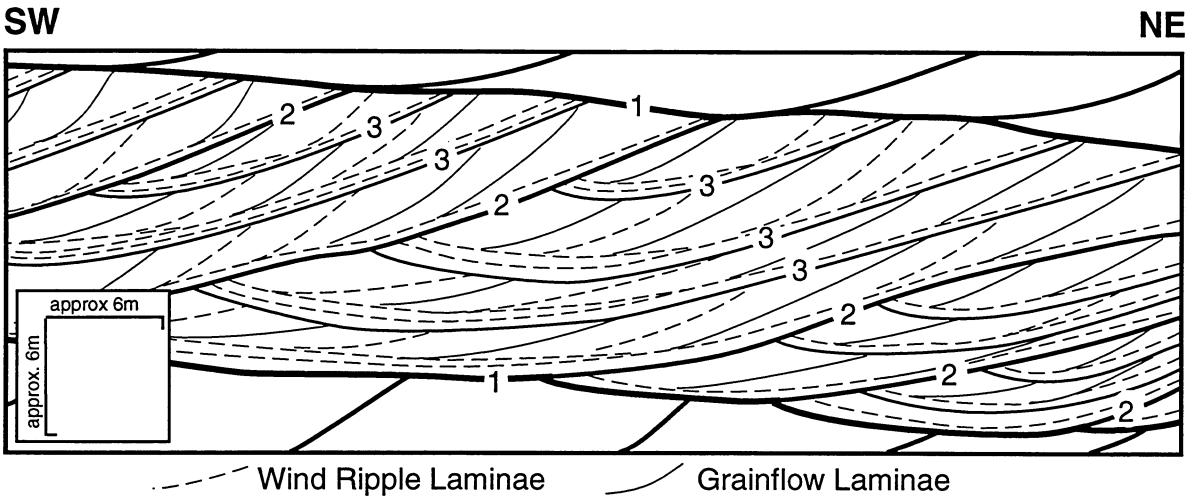

Figure 1.10. Schematic drawing of internal stratification within the Tensleep Sandstone showing the cross-cutting relationships of the first-, second-, and third-order bounding surfaces.

Second-order surfaces have been documented in Tensleep outcrop exposures in both the Bighorn and Wind River basins as well as in Bighorn Basin core. As illustrated in Figures 1.9b and 1.10, second-order surfaces are capped by wind-ripple laminae and truncate third-order bounding surfaces. Second-order surfaces are the erosional surfaces created by the passage of superimposed bedforms along the lee face of the main bedform. Bedform reconstructions using outcrop foreset and bounding surface orientations and following the techniques outlined in Rubin and Hunter (1983) indicate that superimposed bedforms on average were migrating to the west at 271°, while the associated portions of the main bedform were migrating to the south-southwest at 197°, resulting in a net transport of sediment to the southwest.

The most common type of bounding surface in the Tensleep is the thirdorder or reactivation surface. These surfaces bound strata that change upward from low-angle wind-ripple laminae that roughly parallel the bounding surface they overlie (dashed lines in Fig. 1.10), to higher-angle wind-ripple or grainflow laminae, which are in turn truncated by the next third-order surface (Figs. 1.10 and 1.11). These changes in stratification angle indicate cyclic changes in the lee face angle in response to cyclic variations in lee-face flow.

With this hierarchy of stratal surfaces, one can reconstruct the changes that the bedform underwent during a single cycle of bedform migration.

Figure 1.11. Outcrop photograph of reservoir flow-units bounded by third-order bounding surfaces. Dashed lines follow the erosional traces of the third-order surfaces. The surfaces are overlain by tightly packed, low-angle wind-ripple laminae overlain by higher-angle grainflow and wind-ripple laminae. Note the color difference between the grainflow laminae and the wind-ripple laminae. Geologist is 2 meters tall. Photograph taken at the Medicine Lodge measured section (ML, Fig. 1).

Erosional truncation of the higher-angle wind-ripple or grainflow laminae by a third-order surface indicates that the lee face was eroded back by winds moving along or up the lee face. The thin wind-ripple laminae that overlie the third-order surface are at approximately the same angle as the surface, and represent the onset of renewed deposition. These deposits are usually very thin, indicating that the bedform was not undergoing significant southwestward migration. The higherangle wind-ripple or grainflow laminae indicate that the angle of the bedform lee face had increased to the angle of repose for avalanching sediments. This would suggest that winds were once again transverse and that the bedform was actively migrating to the southwest. These fluctuations in airflow are consistent with annual fluctuations in flow expected in a monsoonal setting (Parrish and Peterson, 1988) (Fig. 1.5).

Bedform Reconstruction. In order to reconstruct the Tensleep bedforms, an understanding of the relationship between airflow and bedform surface processes is necessary. Most modern dune fields do not occur in unidirectional wind settings, and they commonly contain compound crescentic bedforms (Breed and Grow, 1979). The bedform sinuosity results in different surface processes occurring on different portions of the same lee face in response to the same wind regime. Secondary airflow direction and resulting surface processes on a bedform lee face are controlled by the incidence angle between the crest of the bedform and the wind moving up the stoss side. When the wind is transverse or strikes the crest within approximately 15° of perpendicular, the result is flow separation along the lee face (Kocurek, 1991). Flow separation and resulting flow deceleration causes grainfall deposition along the upper portion of the lee face and subsequent grain avalanching or grainflow. If the wind strikes the crest more obliquely (> 15° of perpendicular), then airflow is diverted parallel to the lee face, resulting in traction deposits such as wind-ripple laminae (Kocurek, 1991). Oblique airflow is optimum for the formation of superimposed bedforms because of the along-slope deflected airflow. In the Algodones dune field in the southwestern United States, for example, large compound crescentic bedforms have areas with superimposed bedforms migrating along the lee face, where the main crest is oblique while transverse areas of the main bedform are dominated by avalanching processes (Havholm and Kocurek, 1988).

Extensive outcrop exposures of the Tensleep indicate that considerable lateral variability in the character of the cross-strata can occur within a single set of cross-strata. This variability becomes critical when attempting to model both the bedform that formed these accumulations and their subsurface expression. In particular, second-order surfaces show considerable lateral variability. For example, Figure 1.12 shows a single set of cross-strata in the Alkali Flats area. In the northern portion of the outcrop, second-order and third-order surfaces are present, while 91m (300ft) to the south only third-order surfaces are observed (Fig. 1.12). The absence of second-order surfaces within the same set of crossstrata indicates that some portions of the main bedform lee face that formed these accumulations had superimposed bedforms while other

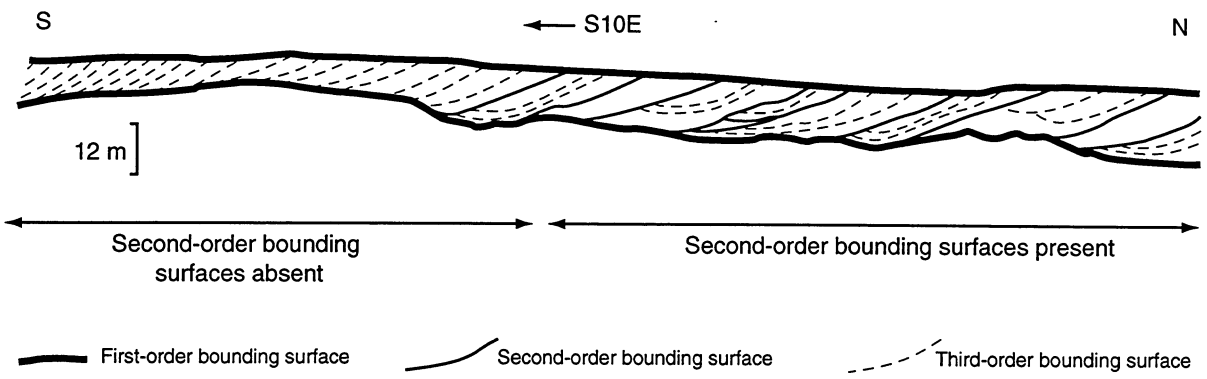

Figure 1.12. Line drawing of a portion of the Alkali Flats outcrop (location AF, Fig.1.1), illustrating the lateral variation in stratification style of a single set of cross-strata. Outcrop distance measures approximately 230m. The section dominated by second-order surfaces corresponds to that portion of the bedform in Figure 1.13 that is oblique to the dominant wind and has superimposed bedforms. The section lacking second-order surfaces and dominated by third-order surfaces corresponds to that portion of the bedform in Figure 1.13 that is perpendicular to the dominant wind.

portions did not. This lateral change within the same set of cross-strata reflects a lateral change in the overall geometry of the bedform that formed the accumulation.

A bedform that illustrates the variations in Tensleep stratification was constructed using outcrop photomosaics and foreset and bounding surface orientations from Tensleep outcrops along the eastern margin of the Bighorn Basin (Fig. 1.13). The compound cross-strata of the Tensleep reflect both transverse and oblique airflow. The areas dominated by second-order surfaces indicate that superimposed bedforms were migrating to the west at 271° under the influence of oblique wind flow. Those areas lacking second-order surfaces were migrating on average to the south at 208° under the influence of a more nearly transverse wind flow. A sinuous crested bedform would allow for both of these conditions to exist simultaneously along the same lee face in response to the same airflow (Fig. 1.13). Photomosaics of laterally extensive Tensleep outcrops indicate that second-order surfaces occur in approximately thirty percent of the Tensleep Sandstone. This percentage is reflected in the bedform reconstruction by the shorter length of those portions of the lee face with superimposed bedforms (Fig. 1.13). Detailed bedform reconstructions have been made for both portions of the main lee face using outcrop foreset and bounding

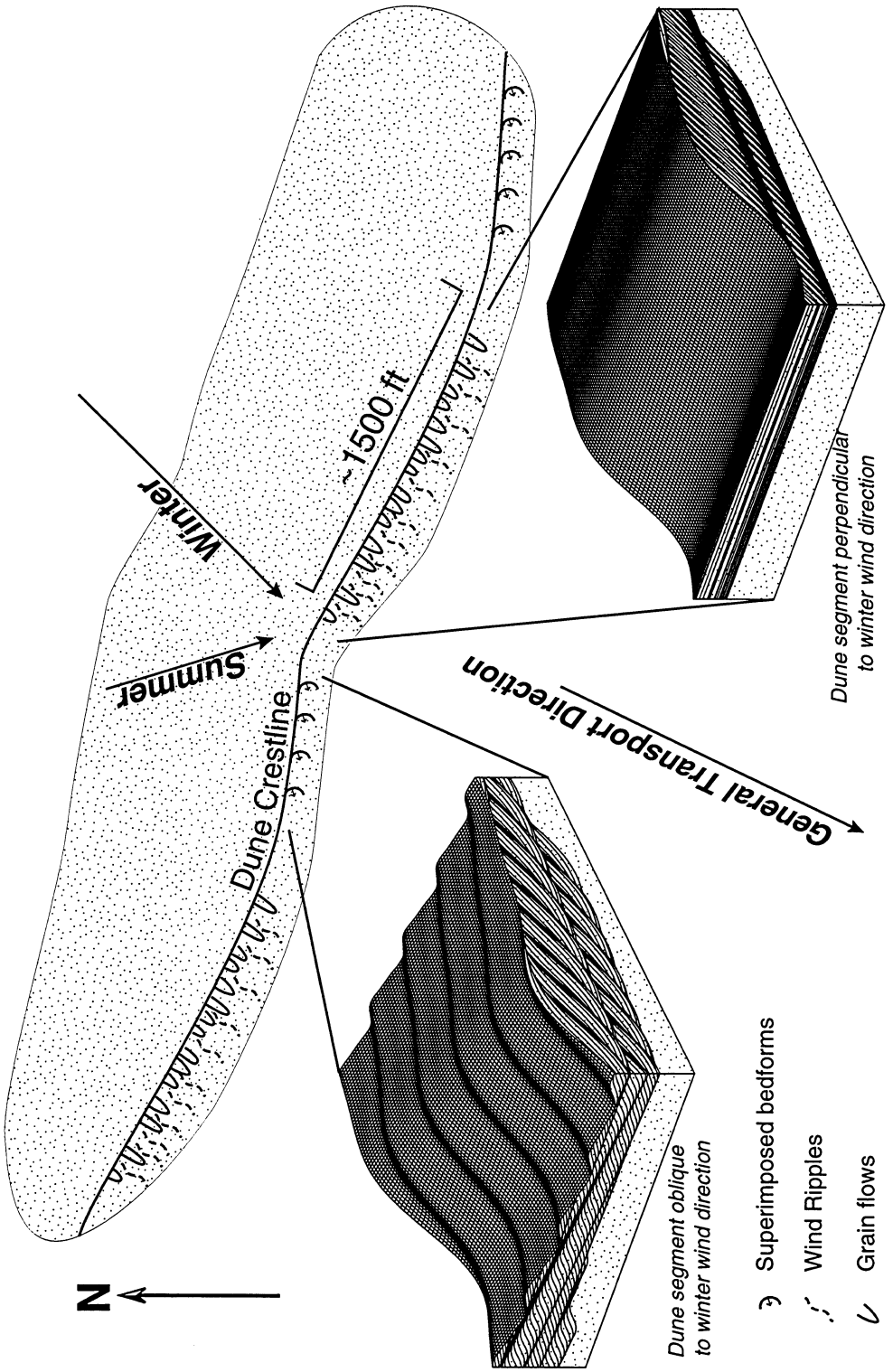

Figure 1.13. Idealized compound crescentic bedform, Tensleep Sandstone. Bedform reconstruction made using the program developed by Rubin (1987). Bounding surface and stratification orientations were determined and used in conjunction with the method of Rubin and Hunter (1983) to determine orientations of superimposed bedforms. The main bedform is migrating to the south-southwest, and the superimposed bedforms are migrating to the west along the arms of the main bedform oriented more oblique to the dominant winter wind.

surface orientations. These reconstructions reflect the complexity of the cross-strata observed in outcrop.

The bedform reconstruction indicates that northeast winds were responsible for most of the processes taking place on the Tensleep bedforms. This would correspond well with the winter winds predicted by Parrish and Peterson (1988) (Fig. 1.5). During the winter, the more transverse portions of the lee face were subject to grainflow deposition as well as reworking of the lee face by wind ripples. The combined presence of grainflow and wind ripple laminae suggests that flow separation was occurring on the upper portions of the lee face while, simultaneously, along-slope transport and resulting traction deposits prevailed on the lower lee face. This would indicate the winds were not perfectly transverse. Those portions of the crestline oblique to the winter winds had superimposed bedforms migrating to the west as a result of along-slope flow.

The bedform reconstruction shows that summer winds had a less significant impact than winter winds on Tensleep bedform morphology, suggesting a less vigorous wind system. The cyclic presence of third-order bounding surfaces indicates that the bedform lee faces were eroded by along-slope windflow on a regular basis. One explanation for this cyclic erosion is annual reworking of the lee face by oblique summer winds. This would suggest that the summer winds were more out of the northwest than shown in Figure 1.5. The paleoclimatic reconstructions of Parrish and Peterson (1988) predicted that this area could be effected by alternate summer winds out of the northwest.

A modern analog of the type of bedform that dominated the Tensleep is shown in Figure 1.14, a Landsat image of a portion of the Cherchen Desert, northern Takla Makan Desert, northwestern China. The image is dominated by compound crescentic bedforms separated by discontinuous interdune areas. These large bedforms are 260 to 98m (320ft) high and average 2253m (1.4 miles) from base of stoss to base of lee. The distance along their lee face from horn to horn averages 3219m (2.0 miles) (Breed et al., 1979). The interdune areas, like those postulated for the Tensleep, are laterally discontinuous. Parallel to the crestline of the bedforms, the interdune areas average 1609m (1.0 miles)and across the interdune areas the average distance is 1207m (0.75 mile).

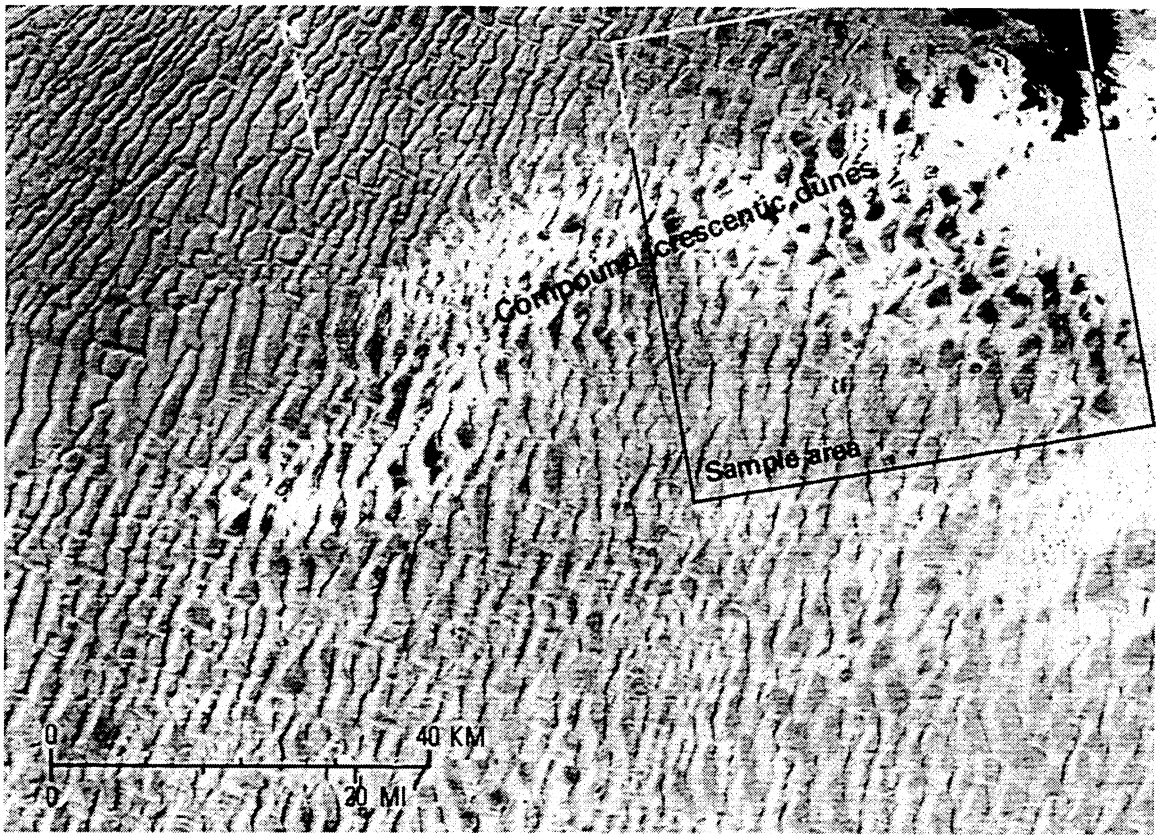

Figure 1.14. Landsat image of a portion of the Cherchen Desert, northern Takla Makan Desert, northwestern China. The bedforms in this area are suggested as modern analogs of Tensleep bedforms. Dune dimensions given in text were taken from the sample area.

Effects of Accumulation Processes on Reservoir Heterogeneity. The Tensleep eolian units are composed primarily of wind-ripple laminae with lesser amounts of grainflow laminae. Wind-ripples migrating across a lee face are formed by saltation processes that result in very tightly packed sand grains within each coarsening-upward, wind-ripple lamina. In contrast, grainflow laminae result from avalanching on the lee face of the bedform, and are less tightly packed, coarsening-upward laminae. This grain packing difference results in wind-ripple laminae being less porous than grainflow laminae (Goggin et al., 1988; Chandler et al., 1989).

This difference in packing affects fluid flow through Tensleep reservoirs. Recent work has documented the relative permeability anisotropy associated with accumulation-related structures (Dunn, 1994, 1995; Iverson et al., 1996).

Across stratification, a more piston-like displacement is observed, with reduced recovery after breakthrough (Iverson et al., 1996).

There are several indications in outcrop and in core that the bounding surfaces in the Tensleep serve as barriers to fluid flow. In outcrop, the occurrence of different color strata on either side of a bounding surface suggests that the two areas have experienced somewhat different diagenetic histories (Fig. 1.15a). Increased carbonate and anhydrite cementation is also noted along bounding surfaces in Tensleep cores and outcrops (Fig. 1.15b); presumably as a result of greater fluid flow parallel to the bounding surfaces than across them.

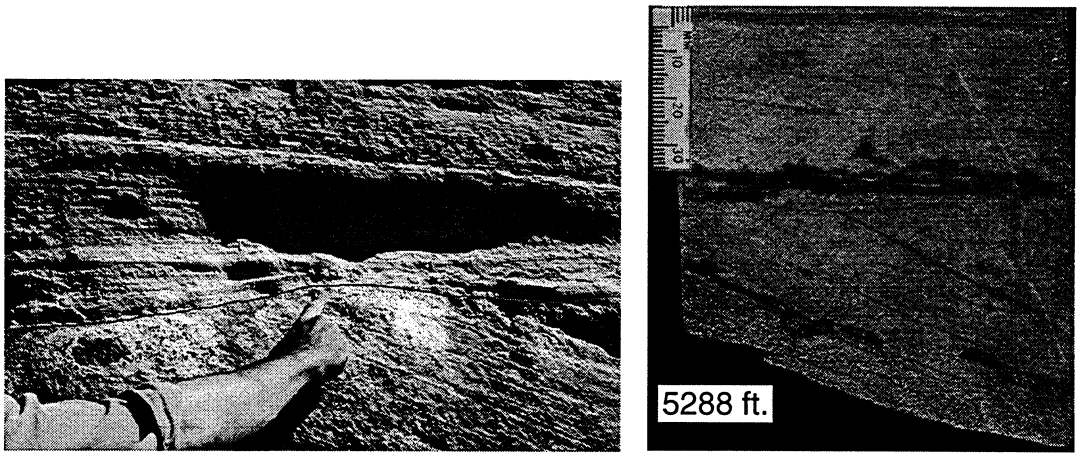

Figure 1.15. Diagenetic features associated with bounding surfaces. a. Outcrop photo from the Medicine Lodge section (ML on Fig.1.1). Note color change across a first-order bounding surface with low-angle wind-ripple laminae above the surface and higher-angle grainflow and wind-ripple laminae below. b. Incrased cementation along a first-order bounding surface in a core sample from the EBET #217 well located in the Elk Basin field, northwestern Bighorn Basin. Scale bar in millimiters.

A number of authors have documented that the permeability along bedding planes is greater than across bedding planes in the Tensleep Sandstone (Emmett et al., 1971; Andrews and Higgins, 1984; Shebl, 1996). This difference is related to the contrast in grain-packing across individual laminae as well as across bounding surfaces. First-, second-, and third-order bounding surfaces are all capped by thin, tightly packed wind-ripple laminae and overlie grainflow laminae and thicker, less tightly packed wind-ripple laminae (Fig. 1.10). The

contrast in packing across a bounding surface tends to inhibit fluid flow across the surface; instead, fluids tend to move parallel to the bounding surface. Figure 1.10 illustrates the general geometry of the internal erosional bounding surfaces and the flow-units they define. Figure 1.16a illustrates the general dimensions of the flow units perpendicular to the crestline of the Tensleep bedforms. The third dimension, parallel to the crestline of the bedforms, is much more difficult to measure because of the paucity of plan-view outcrop exposures of the Tensleep crossstrata. However, using the computer program of Rubin (1987), it is possible to reconstruct the bedforms and their internal geometries and to estimate the third dimension of these flow units (Fig. 1.16b). Improved definition of these units should result in improved strategies for waterflood recovery in Tensleep reservoirs.

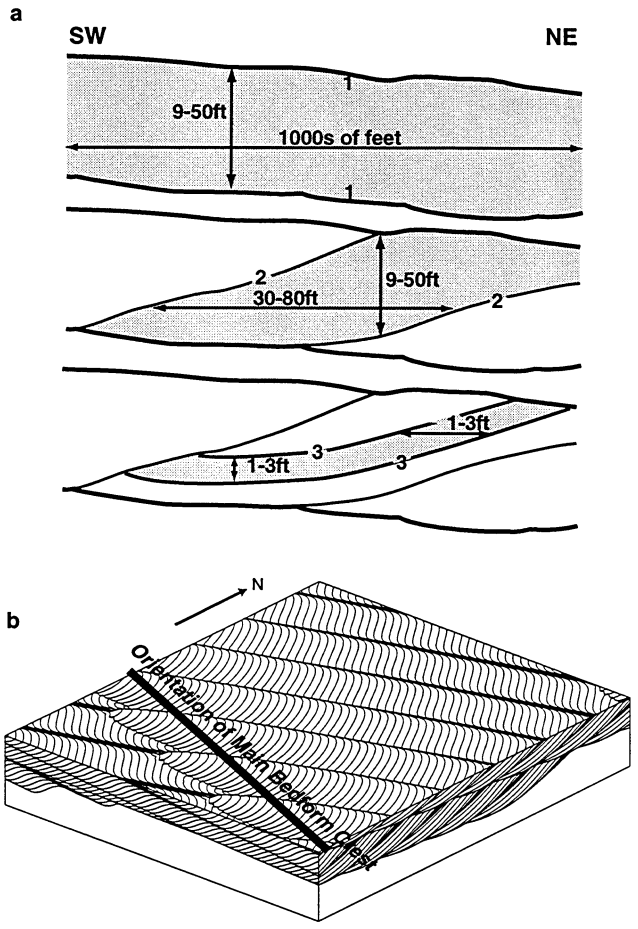

Figure 1.16. a. Dimensions of first-, second-, and third-order bounded flow units perpendicular to main bedform crestline. b. Bedform reconstruction using the program of Rubin (1987) shows plan-view appearance of flow units. This view allows estimates of flow-unit geometry generally parallel to main bedform crestline.

Preservation Processes

In order for sediments to be preserved in the rock record, the sediments must be placed below some base-level of erosion. In the case of the Tensleep, this occurred through cyclic relative sea-level rises probably related to glacial activity in the southern hemisphere (Wanless and Shepard, 1936; Crowell and Frakes, 1972; Ramsbottom, 1979). As

the sea transgressed, the low interdune areas were inundated first, and eventually the entire dune field was flooded (Time 2 and 3, Fig. 1.6). Marine flooding commonly resulted in large-scale soft-sediment deformation of the upper portion of the eolian units. With complete flooding, the uppermost eolian sediments were reworked into burrowed, dolomitic sandstones; culminating in open-marine deposition of sandy, fossiliferous carbonates (Time 3, Fig. 1.6).

Figure 1.3 illustrates the distribution and continuity of the six eolian-marine sequences identified in the Bighorn Basin. The continuity of individual marine dolomitic units was controlled by both depositional and postdepositional processes. The rates of relative sea-level rise versus sediment supply controlled how far inland, or to the east, individual marine dolomitic units extended. If the rate of sediment supply outpaced the rate of sea-level rise, then the marine units were restricted to the western portions of the basin. Conversely, if the rate of sea-level rise was significantly greater than the rate of sediment supply, then the marine incursion extended far to the east. Postdepositional fluvial valley incision across the top of the Tensleep resulted in localized erosion of the upper eolian-marine sequences. The upper eolian-marine sequences were only preserved in the southeast portion of the Bighorn Basin (Kerr et al., 1986; Wheeler, 1986; Kerr, 1989). The higher frequency of marine incursions on the western side of the Bighorn Basin resulted in thinner individual sequences on average, which are more dominated by interdune accumulations than the equivalent strata in the southeastern Bighorn Basin.

Effects of Preservation Processes on Reservoir Heterogeneity. It has been recognized for some time that the heavily cemented marine dolomitic units can contribute to compartmentalization in the Tensleep by acting as vertical barriers to fluid flow between the eolian cross-stratified sandstones. However, fracturing of the dolomitic units, which is common along the axes of structures, does allow fluid communication between the eolian sandstones (Emmett, 1971). Well-log crosssections show that the marine dolomitic units are present over large areas (Fig. 1.3). Individual dolostone-bounded eolian units generally thicken to the west and show significant local variation in thickness across the basin. These local thickness variations may be caused by subtle differences in local subsidence

rates. The same local variations in subsidence affected the thickness of the dolomitic units and, ultimately, the degree of differential erosion into the dolomites and sandstones during lowstand exposure.

Preliminary results indicate that soft-sediment deformation, interpreted to result from relative sea-level rise, has had an impact on permeability distribution in the Tensleep Sandstones. Comparison of core descriptions with core analyses (porosity and permeability measurements) reveals an increase in permeability associated with the uppermost portions of individual eolian units, and in particular within the soft-sediment disturbed zones (Fig. 1.17). Disturbed

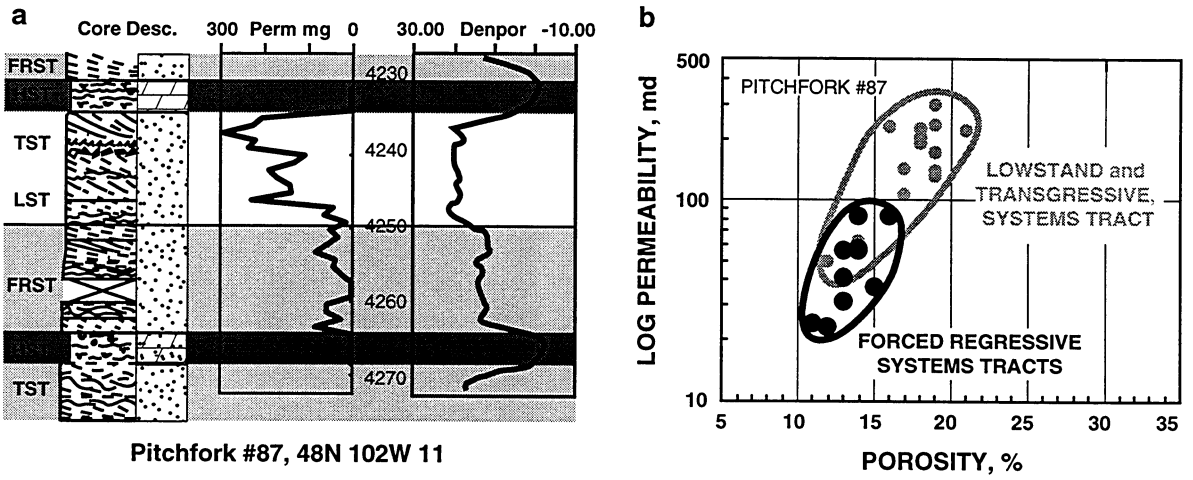

Figure 1.17. a. Comparison of Pitchfork #87 (Pitchfork Field, sec.11, T48N, R102W) core description with its permeability and density porosity log, showing an increase in permeability and porosity in the lowstand and transgressive systems tracts (LST, TST; Fig. 1.7). b. Log permeability v. percent porosity for the same sandstone-dolomite cycle in the Pitchfork #87 well. Note that permeability and porosity are higher for the lowstand and transgressive systems tracts than for the forced regressive systems tracts (FRST).

zones generally occur toward the top of individual eolian units and are associated with sea-level transgression (Fig. 1.6). This increase in permeability associated with softsediment deformation is postulated to result from a change in pore geometry. The homogenization of the strata caused by the soft-sediment deformation would also tend to lessen the effects of compartmentalization formed by the erosional bounding surfaces. However, more core descriptions and

core analyses must be acquired in order to statistically determine if these transgressive deposits can be consistently recognized in well logs.

Conclusions

1) Reservoir heterogeneity in the Tensleep Sandstone is primarily controlled by the processes taking place during both accumulation and preservation of the eolian system. Accumulation-related small-scale heterogeneity is caused by grain-packing variation associated with stratification types and erosional bounding surfaces within the eolian units. Laterally extensive marine dolomitic units form the large-scale heterogeneities; they result from fluctuations in relative sea level, which cause preservation of the eolian units.

2) A hierarchy of flow-units exists within the Tensleep eolian units. These flow-units are defined by erosional bounding surfaces formed by bedform surface processes during accumulation of the eolian sediments. The erosional bounding surfaces commonly separate tightly packed wind-ripple laminae above the surface from more loosely packed wind-ripple and grainflow laminae below. This results in fluid flow being greater parallel to the boundaries than across the boundaries.

3) Bedform reconstructions utilizing outcrop foreset orientation and outcrop photomosaics indicate that the compound cross-strata of the Tensleep were produced by compound crescentic bedforms migrating to the southsouthwest, with superimposed bedforms on some portions of the lee face migrating to the west.

4) Well-log cross sections were used to correlate six eolian-marine sequences across the Bighorn Basin. Individual sequences tend to thicken to the west, but they show localized variations in thickness related to local subsidence changes.

5) The Tensleep is placed into a sequence stratigraphic framework such that the erosional bounding surfaces capping the marine dolomitic units are equivalent to sequence boundaries. Correlation to a relative sea-level curve suggests that the sequence boundary and the eolian accumulation formed during the time of falling relative sea level.

Acknowledgements

This work was funded by the Department of Energy under Contract No. DE-AC22-93BC14897. Field assistance was provided by Lauren Personette, Jeff Crabaugh, Jack Deibert, John Humphreys and Robert Bruner. The paper was considerably improved through reviews by Gary Kocurek, David Copeland, David M. Wheeler, Michael H. Gardner, and Mark Sonnenfeld.

INTERPRETING EOLIAN RESERVOIR ARCHITECTURE USING BOREHOLE IMAGES*

MARY CARR-CRABAUGH[1,3], NEIL F. HURLEY[2,3] & JANINE CARLSON[2]

[1] Institute for Energy Research
University of Wyoming
P.O. Box 4068
Laramie, Wyoming 82071

[3] Marathon Oil Co.
Petroleum Technology Center
Littleton, CO 80160

[2] Current Address:
Colorado School of Mines
Department of Geology and Geological Engineering
Golden, CO 80401-1887

Abstract

Eolian reservoirs exhibit significant compartmentalization and directional permeability caused by the processes taking place during accumulation of sediments within an eolian system. The contrast in grain packing across erosional bounding surfaces is one of the primary controls of fluid-flow patterns within eolian reservoirs. Better prediction of the geometry of flow units bounded by erosional surfaces can be made by reconstructing the type of bedform that formed the accumulation. Subsurface study of the occurrence and the frequency of erosional bounding surfaces has been limited by the availability and quality of core data. However, using borehole images, specifically FMI and FMS logs, the orientation of stratification can be resolved, and the cross-cutting relationships produced by erosional bounding surfaces can be identified. Comparison of the stratification orientation above and below an erosional bounding surface makes it possible to classify the erosional bounding surface within a process-oriented

* Proceedings of the Gulf Coast Section SEPM Foundation 17th Annual Research Conference on Stratigraphic Analysis, December 8-11, 1996, Houston.

hierarchy. Using the foreset and bounding surface orientations gathered from the FMI and FMS log data, and using computer simulation methods for bedform reconstruction, a bedform that reflects the observed variations in stratification can be constructed. An integrated study of FMS logs, FMI logs, and cores from the Tensleep Sandstone in the Oregon Basin Field, Bighorn Basin, Wyoming indicates that erosional bounding surfaces can be identified and classified. The FMI and FMS logs also allow delineation of eolian facies such as interdune accumulations.

Introduction

In today's drive for increased cost-effectiveness, it has become increasingly important to construct accurate and detailed reservoir models to plan enhanced oil recovery programs. One of the major stumbling blocks to accurate reservoir modeling is reservoir heterogeneity at all scales (Weber, 1986). Within the Tensleep Sandstone, a hierarchy of heterogeneity types that influence fluid migration has been identified in outcrop and core (Carr-Crabaugh and Dunn, 1996) (Fig. 1.18). The large-scale heterogeneity within the Tensleep, defined by sandstone-dolomite sequences, is easily recognized using conventional log suites. According to the hierarchy of heterogeneity types discussed by

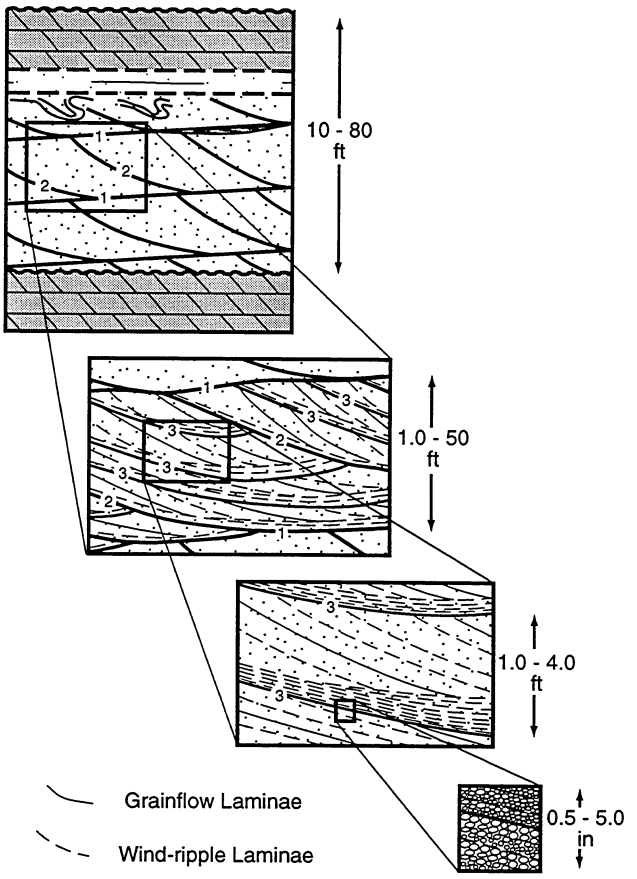

Figure 1.18. Illustration of different scales of reservoir heterogeneity in the Tensleep Sandstone. The largest scale of heterogeneity is defined by the marine dolomitic units, which subdivide the cross-stratified eolian sandstones. The smaller-scale heterogeneities are defined by first-, second-, and third-order erosional bounding surfaces indicated by 1,2, and 3. Commonly, tightly-packed wind-ripple laminae overlie the erosional bounding surfaces (Carr-Crabaugh and Dunn, 1996). The tight packing results in low permeability and inhibits fluid-flow across the erosional bounding surfaces.

Weber (1986), this large-scale heterogeneity influences reservoir continuity as well as sweep efficiency. The smaller-scale heterogeneity packages, defined by erosional bounding surfaces and cross-stratification type, affect sweep efficiency and residual oil saturation. These small-scale features, which have a significant impact on enhanced oil recovery programs, are not definable using conventional log suites. However, in areas where outcrop and core data are limited, the erosional surfaces that delineate small-scale heterogeneities can be clearly defined using electrical or acoustic borehole-imaging logs. In this study, Schlumberger's FMS (Formation MicroScanner) and FMI (Formation MicroImager) logs were used.

Previous studies have demonstrated that fluid flow in eolian reservoirs is significantly influenced by the stratification type and erosional bounding surfaces inherent in the system (Weber, 1987; Goggin et al., 1988; Chandler et al., 1989; Lindquist, 1988). In the Nugget Sandstone, Nelson (1985) demonstrated an order of magnitude higher permeability, at a given porosity, in samples measured parallel to bedding than in samples measured perpendicular to bedding. It has also been documented in the Tensleep Sandstone that permeability along bedding planes is greater than across bedding planes (Emmett et al., 1971; Andrews and Higgins, 1984; Shebl, 1995). Using FMI and FMS logs, it is possible to quantify the attitude of strata in eolian reservoirs, and to create a three-dimensional model in order to better predict fluid-flow patterns.

Study Area

The Oregon Basin Field is an elongate, doubly plunging, asymmetric anticline located on the western side of the Bighorn Basin in Park County, Wyoming. Oil was initially discovered on the North Dome of Oregon Basin in 1927 and on the South Dome in 1928 (Cordiner and Livingston, 1977; Morgan et al., 1977).

The present study was initially undertaken as part of a larger study funded by the Department of Energy (D.O.E. Contract No. DE-AC22-93BC 14897) studying Tensleep Sandstone relative permeability in the Bighorn and Wind River Basins of western Wyoming (Dunn, 1994, 1995; Carr-Crabaugh and

Dunn, 1996; Iverson et al., 1996). Marathon Oil Company is a cost-share partner on the project and provided data on the North Oregon Basin Field in proximity to recently drilled horizontal well completions (Fig. 1.19). Marathon Oil Co. was interested in a more detailed study of the reservoir compartmentalization affecting the horizontal well completions. An integrated study of three cores, two FMS logs, and one FMI log was undertaken to assess the feasibility of identifying flow-units delimited by erosional bounding surfaces within the eolian portions of the Tensleep Sandstone.

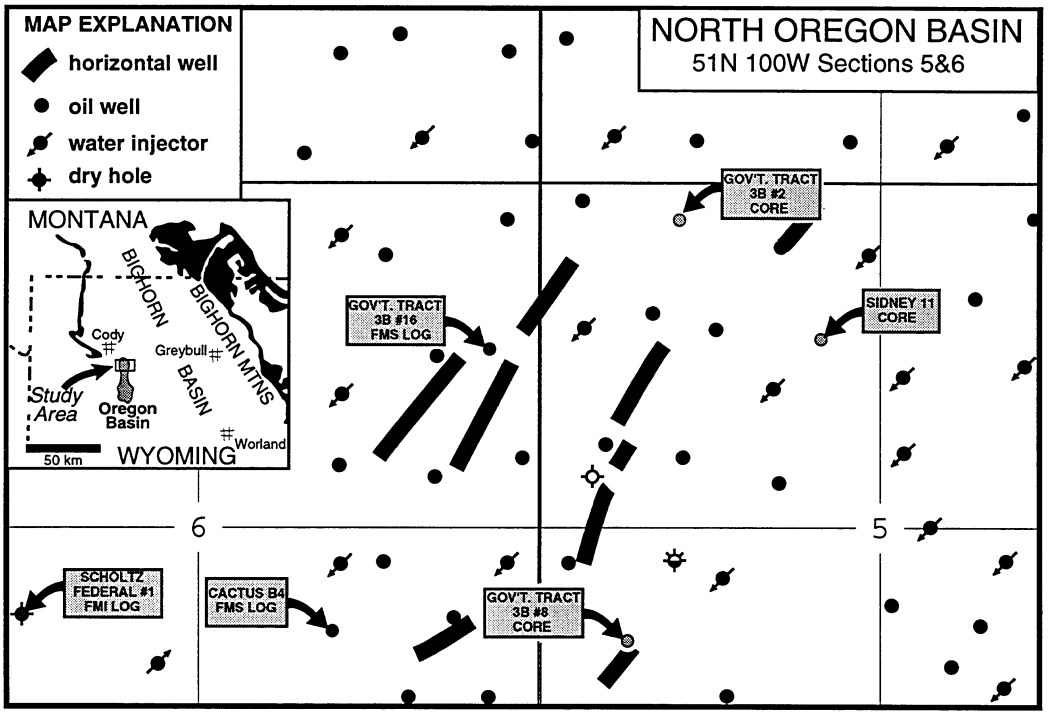

Figure 1.19. Map of core and well log locations in North Oregon Basin field study area. Sections are one mile on a side; quarter sections are delineated.

Stratigraphic And Paleogeographic Background

The Tensleep Sandstone has been assigned a Middle Pennsylvanian (Desmoinesian) to Lower Permian (Wolfcampian) age, primarily on the basis of fusulinid data (Branson, 1939; Henbest, 1954, 1956; Verville, 1957) supported by brachiopod (Brainerd and Keyte, 1927; Hoare and Burgess, 1960) and conodont studies (Rhodes, 1963) (Fig. 1.2). Differential truncation of the Tensleep

Sandstone in the Bighorn Basin, resulting in significant variations in unit thickness, has been demonstrated with both faunal evidence (Verville et al., 1970) and physical stratigraphic relationships (Wheeler, 1986; Kerr et al., 1986; Kerr, 1989).

The Tensleep Sandstone is composed of a series of eolian sandstones and marine dolomitic sandstones, reflecting the cyclic nature of relative sea-level change during Tensleep time. This relative sea-level fluctuation was probably related to glacial activity in the southern hemisphere (Wanless and Shepard, 1936; Crowell and Frakes, 1972; Ramsbottom, 1979). Correlation of the dolostones across the Bighorn Basin shows that the marine incursions that formed the dolostones migrated generally from west to east across the basin (Fig. 1.3). These eolian-marine cycles are composed of compound sets of eolian cross-strata gradationally overlain by sandy to fossiliferous dolostones capped by sharp to erosional contacts (Fig. 1.4). The Tensleep eolian units of the Bighorn Basin are characterized by very-fine to fine sandstones with varying amounts of quartz, dolomite, and anhydrite cements.

The study area was at approximately 10° north latitude during accumulation of the Tensleep Sandstone during the Late Pennsylvanian to Early Permian (Fig. 1.5) (Scotese et al., 1979). Paleocurrent measurements from Tensleep outcrop exposures on the eastern side of the Bighorn Basin indicate a predominance of south-southwest dips (Wheeler, 1986; Peterson, 1988; Kerr, 1989). This trend corresponds to paleowind flow reconstructions for this time period shown in Figure 1.5, which indicate that winds out of the present-day north and northeast were dominant (Parrish and Peterson, 1988; Peterson, 1988). The global circulation models of Parrish and Peterson (1988) indicate a monsoonal climate with annual fluctuations between northerly summer winds and northeasterly winter winds.

Tensleep Depositional Model

A depositional model developed for the Tensleep Sandstone by CarrCrabaugh and Dunn (1996) takes into account both the accumulation dynamics of the eolian system and the preservation processes associated with

relative sealevel rise. Accumulation represents net deposition of sediment through time, and results in a three-dimensional body of sediment (Kocurek and Havholm, 1993). Preservation refers to the placing of an accumulation below some regional baselevel of erosion. Kocurek and Havholm (1993) identified a spectrum of eolian systems as dry, wet, and stabilized, depending on the geological processes affecting accumulation. A dry eolian system is one in which the water table is at a depth below the sediment surface, such that it has no stabilizing influence on the sediment, and in which accumulation takes place strictly for aerodynamic reasons (Kocurek and Havholm, 1993). The Tensleep eolian units are considered characteristic of a dry eolian system because of a lack of sedimentary structures normally indicative of a high water table and a paucity of interdune accumulations. Regional relative sea-level rise caused flooding of this area and the formation of marine carbonates. This placed the Tensleep eolian system below the regional base-level of erosion, resulting in its preservation. Figure 1.6 illustrates the accumulation and preservation processes that have been inferred in the Tensleep Sandstone. Depositional fabrics that resulted from these processes influenced fluid migration patterns in subsurface Tensleep Sandstone reservoirs.

Analysis Of Bedding-Plane Orientation

Dipmeters have been used for many years to help determine paleocurrent directions in sandstones. Using the conventional approach, an operator computes dips using various correlation algorithms, then examines the "tadpoles" to look for patterns in the computed dips (Gilreath, 1987; Höcker et al., 1990). Various facies models are applied to these patterns, and inferences are made about paleocurrent directions.

The introduction of modern borehole-imaging logs (Bourke et al., 1989; Luthi and Banavar, 1988) has increased our ability to detect bed boundaries in subsurface formations. These tools provide electrical or acoustic images of much of the borehole wall. Examples of such tools are Schlumberger's FMS (Formation MicroScanner) and FMI (Formation MicroImager), Haliburton's EMI (Electrical MicroImager) and CAST (Circumferential Acoustic Scanning Tool),

and Western Atlas' CBIL (Circumferential Borehole Imaging Log). With software available from a number of vendors, conventional dipmeter devices such as the 4-, 6-, and 8electrode tools can be made to emulate more advanced borehole-imaging logs such as the FMI and EMI logs. Conventional dipmeters can then be used as data sources for modern stratigraphic and sedimentologic interpretations.

A traditional problem in dipmeter analysis has been the poor quality of the computed dips. With borehole images, one no longer needs to depend entirely on dips calculated by a correlation algorithm. The technique presented here depends heavily on hand-picked dips in borehole images. A second problem, which has been the removal of structural dip, has been solved with techniques discussed in the following three-step process.

Step 1: Dip Determination

The first step in paleocurrent orientation is to obtain a dipmeter log in digital form. We have loaded the data onto a SGI (Silicon Graphics) workstation and interpreted the logs using REVIEW/RECALL software from Z&S Consultants, Inc. Comparable software is available from Schlumberger, Halliburton, Western Atlas, and other logging companies.

Once the raw data are loaded, magnetic-declination and accelerometer corrections are applied. Accelerometer correction compensates for the irregular speed at which the sonde moves up the hole. Azimuthal images are then generated. Figure 1.20 shows an example of Tensleep bedding planes observed in FMI images. At this point, the interpreter can choose to pick dips on the screen or to use a set of computed dips. For the present study, we chose to rely on handpicked dips to accurately reflect the subtle cross-cutting relationships of the bedding planes. An ASCII file of the dips is then transferred to a spreadsheet package such as EXCEL for further analysis.

Step 2: Lithology Determination

When dip directions and dip magnitudes for the various bedding surfaces imaged by the FMI and FMS logs have been collected, it is necessary to classify individual bedding planes by lithology type. Three lithology types are delineated

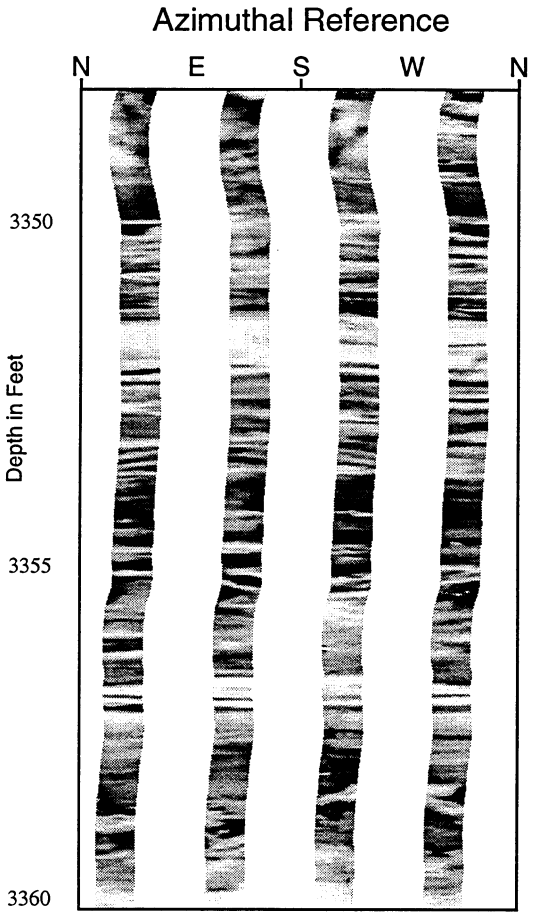

Figure 1.20. Uninterpreted dynamic image from the Gov't. Tract 3B #16 FMS log.

within the Tensleep: marine dolomitic sandstones and dolomites, interdune accumulations, and eolian cross-strata. These were determined on the basis of inclination and character of the bedding surfaces, and the associated gamma ray and porosity logs.

Structural dips should be determined in lithologies that were likely to be flat-lying upon deposition. Outcrop and core studies indicate that within the Tensleep, two facies are expected to contain flat-lying lithologies: the interdune accumulations and marine dolomitic sandstones. The dolomitic sandstones are distinguished using gamma-ray, density, and neutron logs. Interdune accumulations can be identified in high-quality FMI and FMS images by the wavybedded nature of the individual laminae. The dips of the interdune accumulations and the marine dolomitic sandstones are combined to form a structural dataset.

Step 3: Determination and Removal of Structural Dip

The dip and dip direction of individual bedding planes represents a combination of original bedding-plane orientation and generations of structural overprinting. Hurley (1994) demonstrated that borehole-imaging logs are particular useful for dividing long sections into unconformity-bounded and faultbounded dip domains through the use of dip-domain analysis. Analysis of the Tensleep Sandstone bedding-plane orientations indicates that the Tensleep

represents a single dip domain in the study area. Therefore, a mean bedding-plane orientation was determined using the interdune stratification and the marine dolomitic sandstones for each FMS and FMI log. Once a structural dip is determined for each log, the entire dataset is rotated to compensate for the structural dip, using the Z&S software.

Description Of Stratification

As discussed previously, the Tensleep Sandstone is composed of a series of interbedded eolian sandstone and marine dolostone sequences (Fig. 1.4). Tensleep eolian units are composed of one to several sets of compound cross-strata. Each set is bounded by first-order bounding surfaces and represents the deposits of a single bedform as it migrates and climbs through time.

Figure 1.10 illustrates the hierarchy of erosional bounding surfaces observed in the Tensleep Sandstone outcrops and cores (Carr-Crabaugh and Dunn, 1996). These erosional bounding surfaces reflect the depositional processes occurring in the dune field. First-order surfaces separate one set of cross-strata from another, and are produced by erosional processes within the interdune area between large bedforms (Fig. 1.10) (Brookfield, 1977; Kocurek, 1981; Rubin and Hunter, 1982). Second-order surfaces are erosional surfaces that form as small superimposed bedforms migrate across the lee face of a larger bedform (Rubin and Hunter, 1983). Third-order or reactivation surfaces form as a result of shifting winds that change bedform morphology and produce relatively synchronous bounding surfaces. A detailed description of Tensleep cross-stratification and a discussion of erosional bounding surface formation can be found in Carr-Crabaugh and Dunn (1996).

Oregon Basin Stratification

Previous descriptions of the Tensleep eolian units have relied heavily on laterally extensive outcrops along the eastern side of the Bighorn Basin (Wheeler, 1986; Kerr et al., 1986; Kerr, 1989; Carr-Crabaugh and Dunn, 1996). Tensleep exposures are very limited along the western side of the Bighorn Basin, and are not of the quality that would allow detailed examination of the eolian

stratification. However, borehole imaging logs have made it possible to identify the same hierarchy of erosional bounding surfaces in the subsurface Tensleep Sandstone as that observed in Tensleep outcrops.

Bounding surfaces are identified in the FMI and FMS logs by erosional truncation of laminae as well as by abrupt changes in foreset orientation. Criteria for classifying the erosional bounding surfaces were established through outcrop and core study. Figure 1.21 illustrates the expected progression of foreset tadpoles associated with each type of erosional bounding surface. Using these criteria, erosional bounding surfaces in three borehole-image logs were identified and classified according to this process-oriented hierarchy. Figure 1.22 illustrates a series of bounding surfaces identified in the Government Tract 3B #16 well.

The FMS and FMI log data indicate that all types of bounding surfaces identified in surface outcrops are also present in the subsurface. Set thickness, as defined by first-order surfaces, varies from 0.3 to 4m (1.0 to 13ft) and has a geometric mean thickness of 1.1m (3.5ft) in the Oregon Basin Field. The set thickness in outcrop along the eastern side of the basin varies from 1 to 18m (3.2 to 60ft) with a geometric mean thickness

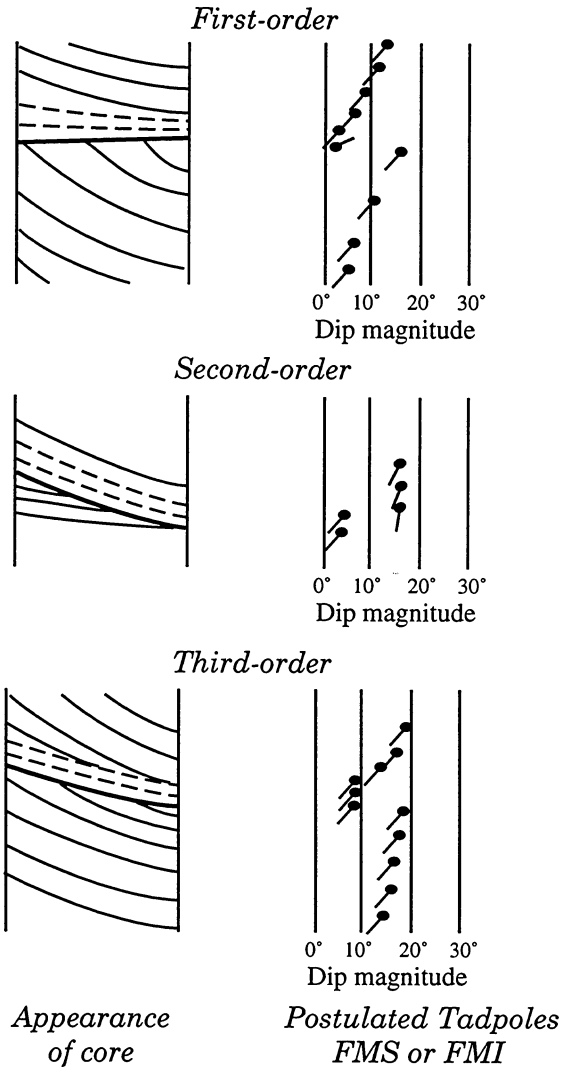

Figure 1.21. Comparison of types of erosional bounding surfaces observed in core and outcrop with the expected FMS or FMI tadpole arrangement. The tadpoles reflect the dip direction and dip magnitude of the associated laminae after structural dip has been removed. Dashed lines are wind-ripple laminae, and solid lines are grainflow laminations.

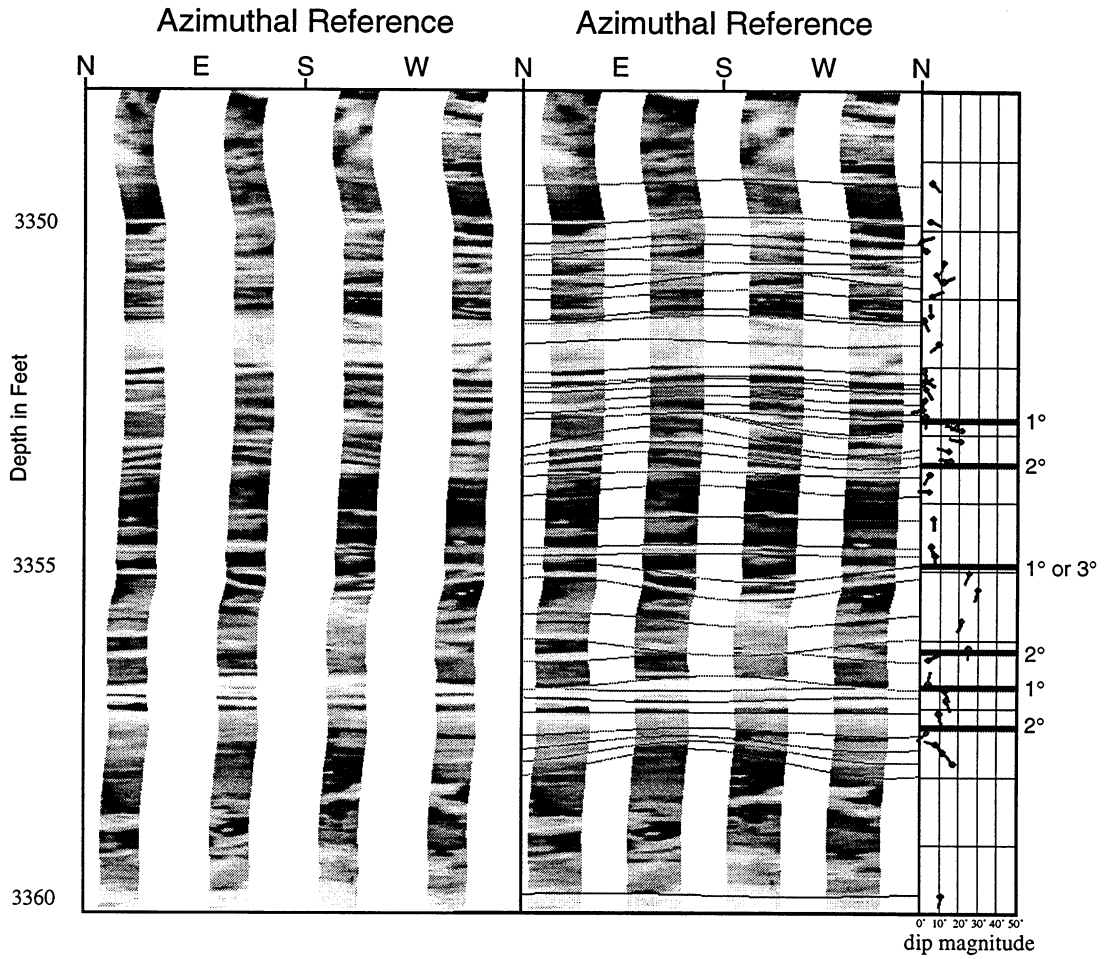

Figure 1.22. Interpreted dynamic image from the Gov't. Tract 3B #16 well. Lines trace the intersection of forsets and the borehole. The tadoles indicate the dip magnitude of the foresets and point in the dip direction. Structural dip has been removed from these images. 1º, 2º, and 3º indicate first-, second-, and third-order erosional bounding surfaces.

of 2.9m (9.1ft). In outcrop, the firstorder bounding surfaces are undulatory in nature and show up to 8.5m (28ft) of relief. This relief results in significant lateral variability in set thickness. Firstorder surfaces are expected to be undulatory on the western side the basin, as well.

Second-order surfaces are less common than first-order surfaces in the Oregon Basin Field, probably for two reasons. Because second-order surfaces form an arc across a set of cross-strata, and are distributed at irregular intervals

along the set of cross-strata, it would be possible to penetrate a set of cross-strata and not encounter a second-order surface. Second, not all sets of cross-strata necessarily contain second-order surfaces. In outcrop, second-order surfaces only occur in approximately thirty percent of the cross-stratified sets.

Bedform Reconstruction Using Subsurface Data

Having classified the erosional bounding surfaces as to their style of formation, it is possible to use these data to recreate the bedforms or dunes that formed these accumulations (Table 1.1). These reconstructions can be used to better model the distribution of heterogeneities within Tensleep reservoirs.

Table 1.1. Erosional bounding surfaces identified in the borehole image logs. Number of surfaces, average dip, and dip direction are indicated.

Well Name	Formation Thickness	First-order Surfaces number & average orientation	Second-order Surfaces number & average orientation	Third-order Surfaces number & average orientation
Gov't Tract 3B #16	167'	6 5.0° at 172°	5 19.9° at 215°	1 7.2° at 180°
Scholtz #1	214'	20 6.6° at 138°	6 20.3° at 200°	4 15.5° at 179°
Cactus B4	213'	4 4.5° at 221°	4 16.9° at 247°	

The occurrence of second-order surfaces indicates that some portions of the Tensleep dunes had superimposed bedforms migrating along the lee face of larger bedforms. Following the techniques outlined by Rubin and Hunter (1983), it was determined that the superimposed bedforms were migrating, on average, to the south-southeast at 145 degrees, and that the larger or main bedforms were migrating to the south-southwest at 208 degrees. Using this data and a computer program developed by Rubin (1987), a three-dimensional model of the dune that formed these accumulations was created (Fig. 1.23). Figures 1.23A and B illustrate the three-dimensional geometries of the erosional bounding surfaces before and after truncation by erosion. The paucity of second-order surfaces suggests that not all of any bedform lee face had superimposed

bedforms. This is also suggested by the average foreset dip direction to the south at 174°. Figure 1.24 illustrates what those portions of the bedform looked like. A large, sinuous, crested bedform would allow for both of these conditions to exist simultaneously along the same dune lee face in response to the same airflow. Those areas oblique to the predominant airflow regime would be dominated by transport of sediment along the lee face and superimposed bedforms would result; those portions perpendicular to the primary airflow would result in more simple stratification dominated by grainflow and wind-ripple laminae (Fig. 1.25).

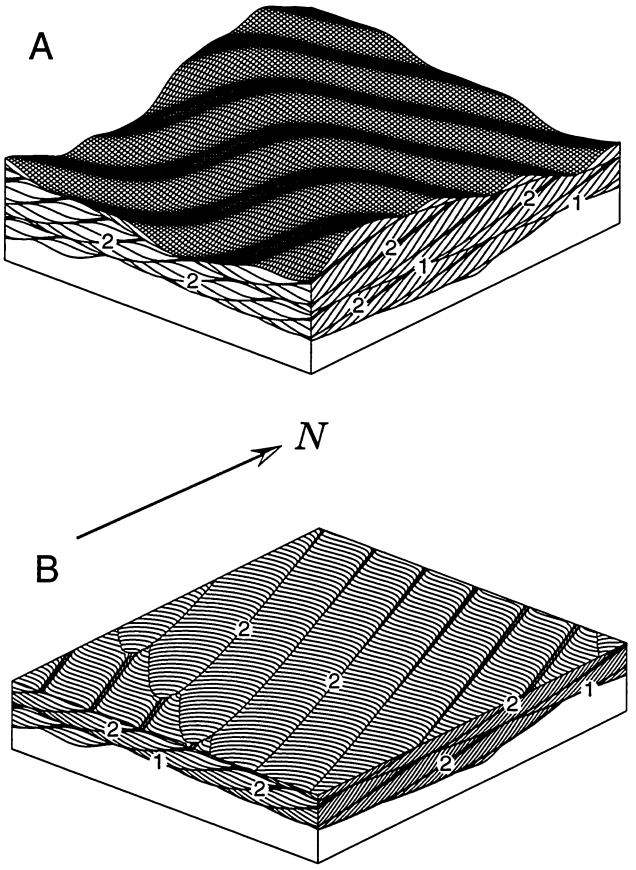

Figure 1.23. Portion of the Tensleep bedform reconstructed using the program developed by Rubin (1987). First-order (1) and second-order (2) bounding surfaces are labeled. A. The main crestline is oriented along a southeast-northwest line at 119º and is migrating to the south-southwest. Along the lee face of the main bedform, superimposed bedforms are migrating to the southeast at 145º. B. Stripping off the surface features allows visualization of the three-dimensional geometry of the flow-units defined by the erosional bounding surfaces.

Implications Of Stratification Style On Reservoir Heterogeneity

Several studies have documented that permeability along bedding planes is greater than across bedding planes (Emmett et al., 1971; Andrews and Higgins, 1984; Shebl, 1995). This variation in permeability is controlled primarily by the depositional processes controlling grain packing in eolian sediments. The most common stratification types in eolian reservoirs are wind-ripple laminae and grainflow laminae. Both stratification types coarsen upward.

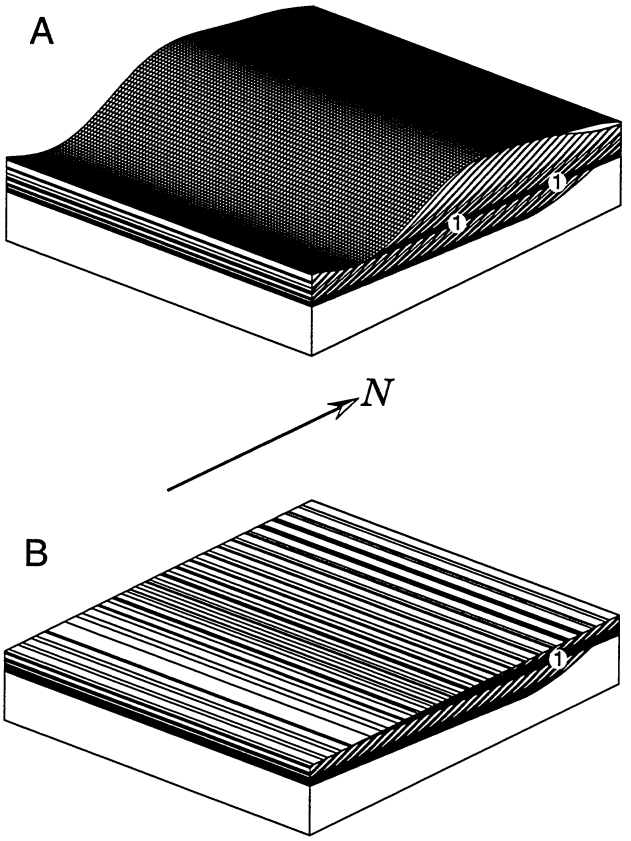

Figure 1.24. Portion of the Tensleep bedform reconstructed using the program developed by Rubin (1987). A. The main crestline is oriented along a south-north line at 90º and is migrating to the south. B. Stripping off the surface features allows visualization of the three-dimensional geometry of the flow-units defined by the erosional bounding surfaces.

However, because wind-ripple laminae form as a result of grain saltation processes, they are much more tightly packed than grainflow laminae. Grainflow laminae form as a result of grain avalanche. This difference in packing results in wind-ripple laminae having significantly lower porosity than grainflow laminae (Goggin et al., 1988; Chandler et al., 1989). Carr-Crabaugh and Dunn (1996) illustrated that first-, second-, and third-order bounding surfaces in the Tensleep Sandstone are all capped by thin, tightly packed wind-ripple laminae and overlie grainflow laminae and thicker, lesstightly packed wind-ripple laminae (Figs. 1.18 and 1.21). The contrast in grainpacking across bounding surfaces would tend to inhibit fluid flow across the surfaces. Instead, fluids would tend to move parallel to bounding surfaces. Figures 1.23 and 1.24 illustrate the distribution of erosional bounding surfaces and the geometry of the units they define. Such models could be used to distribute three-dimensional porosities and permeabilities in reservoir models of eolian sandstones.

Conclusions

1) Borehole images can be used to identify erosional bounding surfaces in eolian cross-strata and classify them according to the depositional processes that formed them.

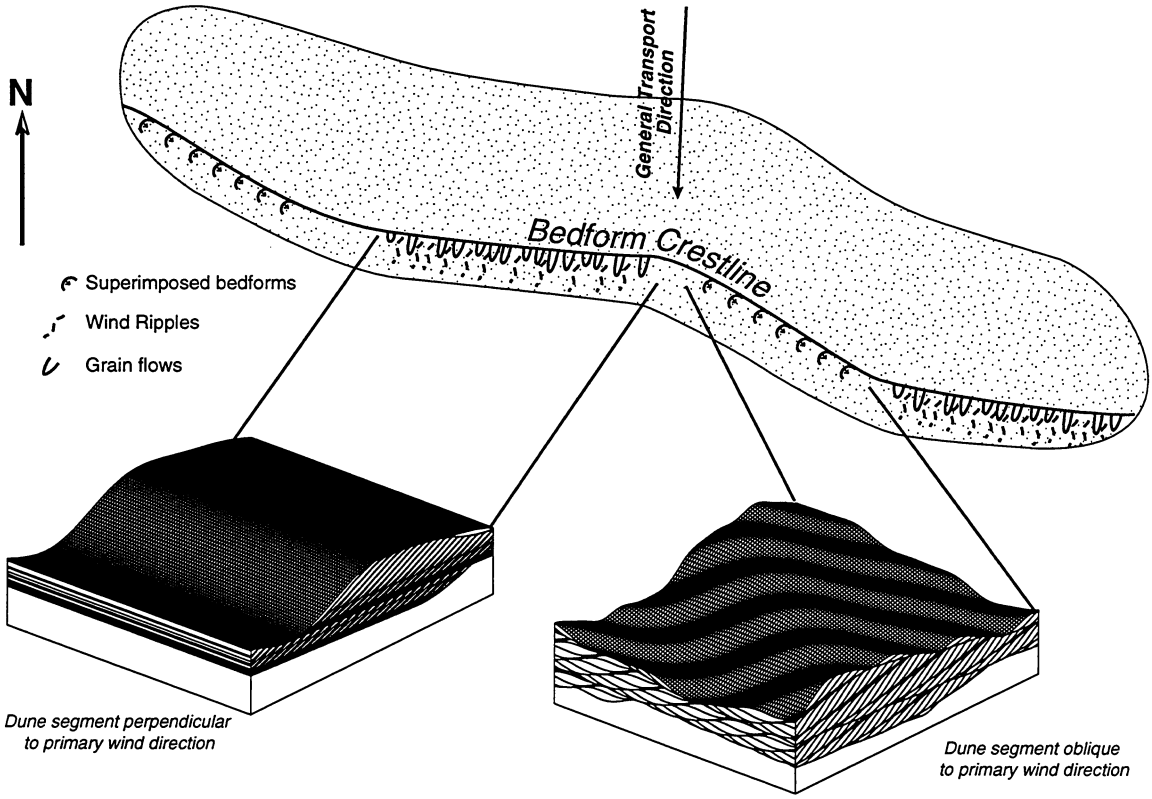

Figure 1.25. Idealized compound crescentic bedform, Tensleep Sandstone. Bounding surface and stratification orientations were determined and used in conjuntion with the method of Rubin and Hunter (1983) to determine orientations of superimposed bedforms. The main bedform is migrating to the south, and the superimposed bedforms are migrating to the south -southeast along the arms of the main bedform oriented obliquely to the dominant wind direction.

2) After structural dip is removed, foreset and bounding surface dip direction and dip orientation data can be used to recreate the configuration of the dunes that formed the Tensleep eolian accumulations.

3) The dunes which formed Tensleep accumulations in Oregon Basin Field in the western Bighorn Basin were large, crescentic bedforms migrating to the southsouthwest with superimposed bedforms migrating to the southeast.

4) Bedform reconstruction can be used to model the three-dimensional geometry of flow-units enclosed by erosional bounding surfaces. Such models can be used to distribute heterogeneous porosities and permeabilities into reservoir flow models.

TASK 2.0: RELATIVE PERMEABILITY ANISOTROPY AND SPATIAL VARIATION

OBJECTIVES

The focus of this task is to obtain quantitative laboratory data on the magnitude and variability of relative permeability anisotropy and spatial variation of the dominant reservoir and boundary surface lithologies of the Tensleep Sandstone. Data are compiled and placed within the regional frameworks constructed in Task 1.0. An additional objective of this study is to provide algorithms for calculating relative permeability from quantitative pore imagery data.

RELATIVE PERMEABILITY MEASUREMENTS

Introduction

Absolute permeability is recognized as an anisotropic quantity (Nelson, 1985). Gas permeability (k_g) is dependent upon the direction of flow, i.e., parallel or across sedimentary bedding surfaces. When bedding surfaces are well defined, the permeability parallel to bedding is consistently higher than that perpendicular to bedding. This intrinsic permeability anisotropy exists regardless of fluid saturations. Data collected during this study for the Tensleep from two basins (Fig. 2.1) and for the Tensleep from a single well (Fig. 2.2) show that permeability anisotropy is most prevalent in the lower permeability samples, and the horizontal permeability is consistently greater than vertical.

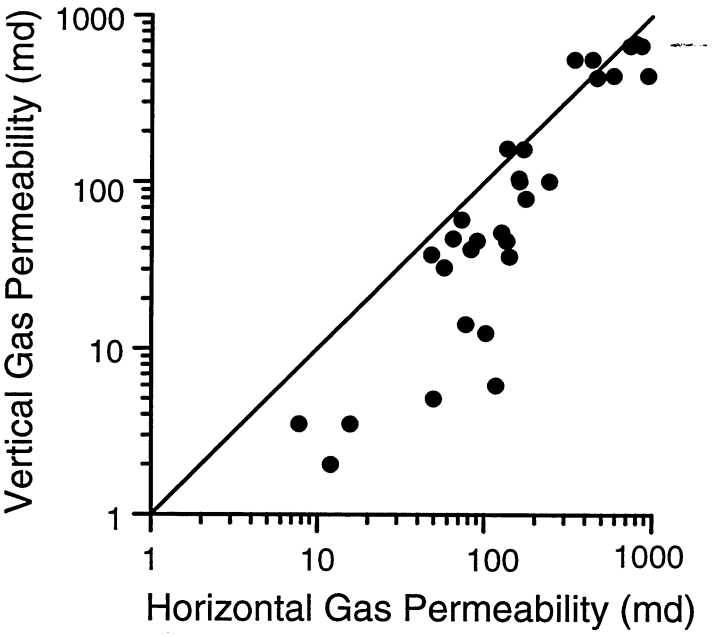

Figure 2.1. Standard gas permeability measurements for Tensleep sandstone cores used in this study. Samples are from various locations in outcrop and subsurface as described by Dunn et al. (1995). Each sample was cleaned, dried, and corrected for Klinkenburg slip.

Relative permeability data are commonly available

(Honarpour et al., 1986), and measurements of absolute permeability anisotropy are routine in the petroleum industry. However, little has been done on relative permeability anisotropy. Corey and Rathjens (1956) show core measurements where relative permeability measured in the vertical direction differ slightly from that measured parallel to bedding (Fig. 2.3). However, the number of measurements presented are insufficient to conclusively determine the characteristics of relative permeability anisotropy. The trends displayed by Corey and Rathjens (1956) for relative permeability anisotropy are a slightly steeper slope and a lower irreducible saturation for the perpendicular-to-bedding relative permeability curve. The first of these trends is verified by this study. However, changes in S_{wi} appear to be isotropic.

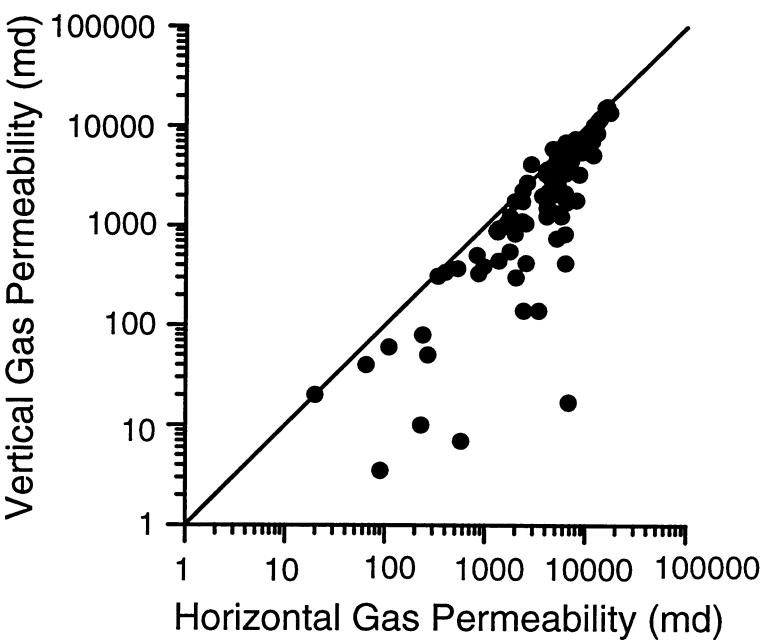

Figure 2.2. Standard gas permeability measurements from a single well drilled through the Tensleep in the southern Wind River Basin by Unocal in the South Casper Creek oil field. Note the similar character of permeability anisotropy as the dataset for this study shown in Figure 2.1.

Kortekaas (1985) used a reservoir simulator to show the effects of relative permeability anisotropy through cross-bedding in sandstones, however, no actual laboratory measurements of relative permeability were included. Willhite (1986) recognized the anisotropy of effective permeability in the equations of flow, noting that k_{ox}, k_{oy}, and k_{oz} are, in general, not equal. However, Willhite assumes that:

$$k_{ox} = k_{ro}\, k_x$$
$$k_{oy} = k_{ro}\, k_y$$
$$k_{oz} = k_{ro}\, k_z$$

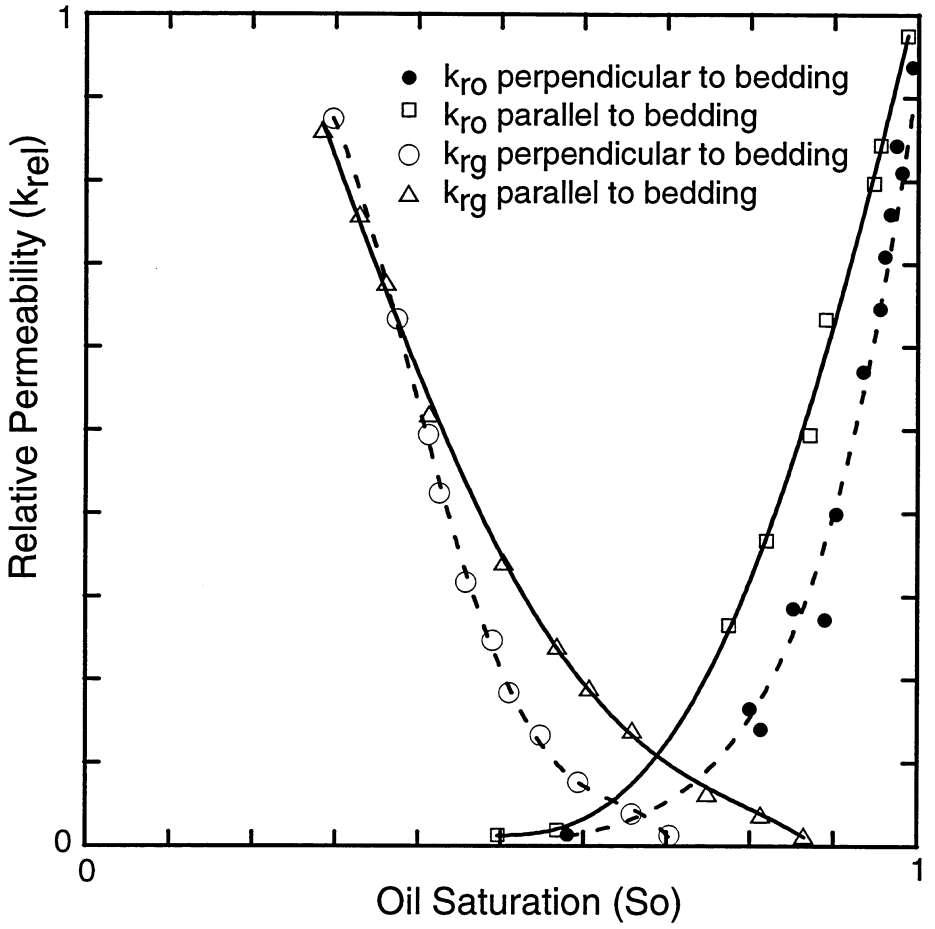

Figure 2.3. Relative permeability curves of Corey and Rathjens (1956) showing their measured steeper curves for perpendicular (vertical) floods. k_{ro} = relative permeability of oil; k_{rg} = relative permeability of gas.

where k_x, k_y, and k_z represent the absolute permeability anisotropy in the two horizontal and the vertical directions respectively. Relative permeability k_{ro} is thus assumed to be a universal function of water saturation alone and to be the same in all directions. This assumption was examined in this study.

Relative permeability by definition, ranges from zero to one: zero is the point where a phase is irreducible, and one is the point where effective permeability equals the base permeability. For this study, the base permeability used was absolute gas permeability. The absolute gas permeability for our sample was consistently higher than the other base permeability that is

commonly used which is the effective permeability to oil at residual water saturation (Fig. 2.4). Regardless of the base permeability used, it is shown in the next section that the base permeability can be divided out by using the ratio of the relative permeability to water (k_w) to the relative permeability to oil (k_o). All of the relative permeability curves are displayed using this quantity.

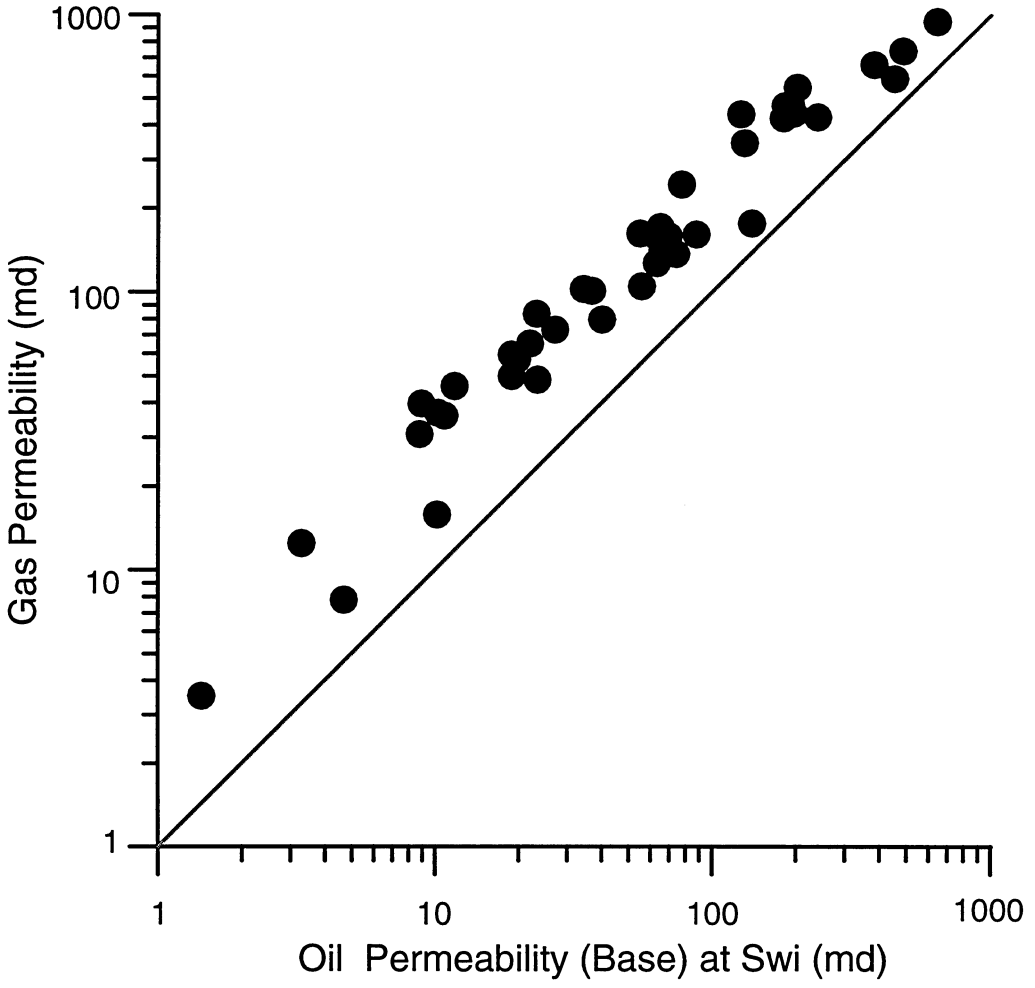

Figure 2.4. Same gas permeability as in Figure 2.1 compared with effective oil permeability at initial water saturation (S_{wi}). After being dried for gas permeability, each sample was saturated with water, then filled with oil to irreducible water saturation (S_{wi}). Oil permeability at S_{wi} is commonly considered the base permeability for subsequent relative permeability measurements.

Efforts were made in this study to hold S_{wi} approximately constant in the measurement of each sample. However, each core has a different porosity and pore structure, yielding required small variations in residual water. Figure 2.5 shows the range of S_{wi} values used in this study. Sandstone samples with high absolute permeability tended to have low S_{wi} whereas the tighter sandstones tended to have slightly higher S_{wi}. Although S_{wi} varies, the variations are consistent between vertical and horizontal core pairs (Fig. 2.5) and has little or no affect on anisotropy measurements.

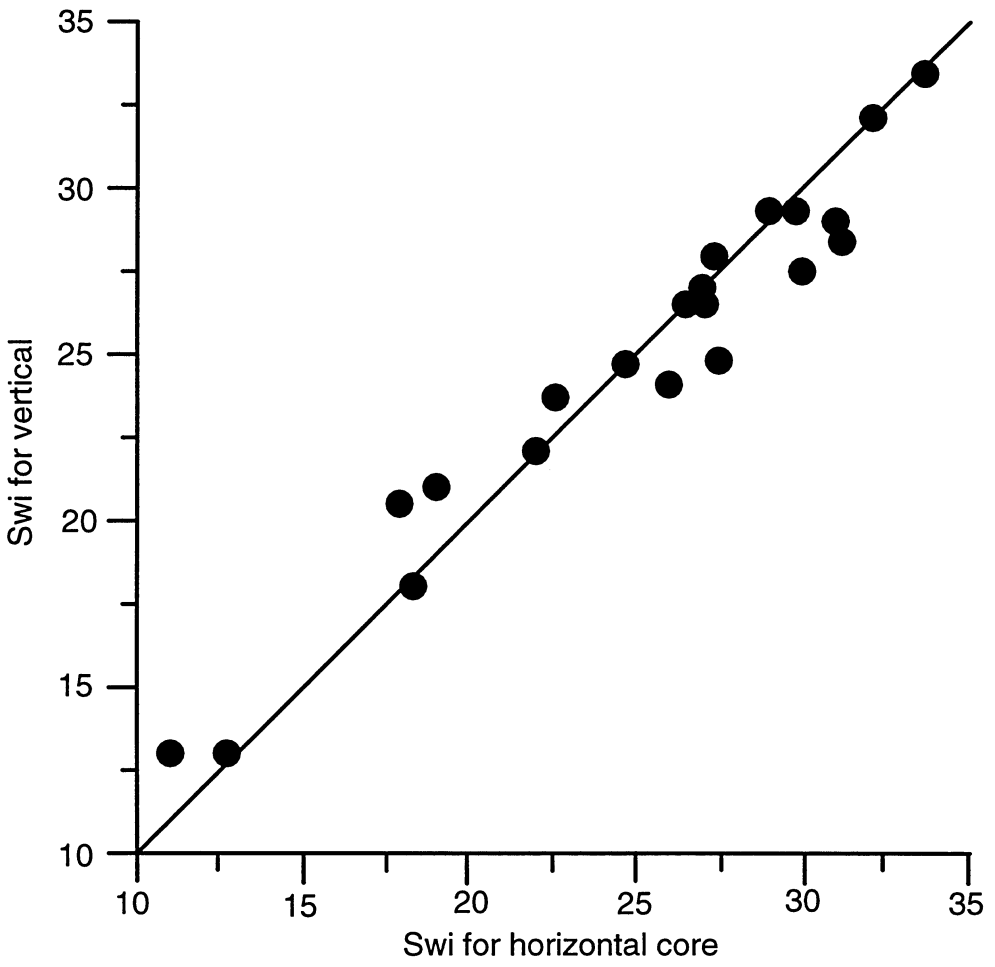

Figure 2.5. Initial water saturations (Swi) reached as described with Figure 2.4. Although an average Swi of 25% water was desired for each core, variations in porosity make it difficult to achieve the same Swi in each core. Most importantly, however, is the fact that Swi is approximately equal in the vertical/horizontal pairs.

Theoretical Basis

The unsteady state technique was used to determine relative permeability. The laboratory apparatus is described in detail by Ajdari (1995) and in prior reports of this study (Dunn, 1994; Dunn, 1995). Some samples were also measured by a commercial laboratory (K&A Labs, Tulsa, OK). The calculations follow a standard procedure (J-B-N technique) published by Johnson, Bossler, and Naumann (1959). Minor modifications and improvements as described by Willhite (1986) have been used in the final calculations.

During the J-B-N laboratory measurement technique, a direct measurement is made of the fraction of water flowing from a core, the water flow divided by the total flow;

$$f_w = q_w / (q_o+q_w), \tag{2.1}$$

where f_w is the fractional flow (of water), q_w is the volume rate of water flowing at a given time during the experiment, and q_o is the rate of oil flowing at the same time. By Darcy's rule for permeability:

$$q_w = \Delta P\,(k_w/\mu_w)\,(A/L), \tag{2.2}$$

$$\text{and } q_o = \Delta P\,(k_o/\mu_o)\,(A/L), \tag{2.3}$$

where k_w is the water effective permeability, k_o is the oil effective permeability, μ_w is the viscosity of water, μ_o is the viscosity of oil, A is the cross-sectional area of the core, L is the length of core in the direction of flow, and ΔP is the change in pressure. Substituting Equations 2.2 and 2.3 into the fractional equation (Eqn. 2.1) yields:

$$(1/f_w) = 1 + (k_o/k_w)\,(\mu_w/\mu_o). \tag{2.4}$$

Therefore using the J-B-N technique, a measurement of the fractional flow from a core, and the knowledge of the viscosities of the fluids yields a direct

measurement of the permeability ratio (k_o/k_w). It is this ratio that is the basic laboratory measurement used in this study.

It was noted earlier that most prior work assumes that:

$$k_{ox} = k_{ro}\, k_x \qquad \text{(horizontal direction)}$$

$$k_{oz} = k_{ro}\, k_z \qquad \text{(vertical direction)}$$

where k_{ro} is the assumed universal oil relative permeability function. Similarly for the water phase,

$$k_{wx} = k_{rw}\, k_x$$

$$k_{wz} = k_{rw}\, k_z.$$

where k_{rw} is the presumed universal water relative permeability function (if it exists) that varies only with water saturation. When we make a direct measurement of the effective permeability ratios with the J-B-N technique, then:

$$(k_{wx}/k_{ox}) = (k_{wz}/k_{oz}) = (k_{rw}/k_{ro})\ .$$

The base permeabilities (k_x and k_z) are eliminated from the calculation and therefore are not required to demonstrate relative permeability anisotropy.

In this study, we make explicit measurements of the quantities:

(k_{wx}/k_{ox}) for horizontally oriented cores, and

(k_{wz}/k_{oz}) for vertically oriented cores.

If relative permeability were isotropic, then (k_{wx}/k_{ox}) would equal (k_{wz}/k_{oz}). However, in this study, they are not. There are consistent variations in (k_{ro}/k_{rw}), demonstrating relative permeability anisotropy.

Sample Collection

The previous chapter presented details regarding the geologic considerations of sample collection. Outcrop samples and subsurface cores from the Tensleep sandstones from the Bighorn and Wind River basins in northwest Wyoming were used in this study. Pairs of cylindrical plugs (1 by 3 inch) were cut immediately adjacent to each other, one to two samples parallel and one sample perpendicular to bedding. The plugs cut with the long axis parallel to bedding are herein called the "horizontal" sample, while the "vertical" plug is the one cut perpendicular to bedding. Eighty-four samples were collected and measured for relative permeability.

Laboratory Measurements

The basic measurements of absolute gas permeability, absolute brine permeability, and oil permeability at residual water saturation are presented in Table 2.1. Forty-two of the samples on Table 2.1 were of suitable high quality for reliable comparison between horizontal and vertical measurements to be included in the anisotropy portion of the study. The complete relative permeability curves are plotted on Figures 2.6 through 2.24.

Table 2.1. Relative Permeability Measurements.

Core	Air perm (md)	Brine perm (md)	Oil perm at Swi (md)	Status
1v*	423	190	182	complete, outcrop
1h*	469	405	182	complete, outcrop
2v*	470	368	192	complete, outcrop
2h*	427	127	240	complete, outcrop
3v	0.65			too tight for apparatus, outcrop
4h	155	122	103	no pair orthogonal, outcrop
5h	461	361	196	no pair, outcrop
6h	618	504	264	no pair, outcrop
Ah*	161	114	88	complete, outcrop
Av*	104	89	56	complete, outcrop
Bv	14	7	3	channel of water during flood, outcrop
Bh	78	51	38	channel, outcrop
Cv*	158	136	70	complete, outcrop
Ch*	138	108	74	complete, outcrop
Dv*	101	68	37	complete, outcrop
Dh2*	162	121	55	complete, outcrop
Dh3*	244	205	78	complete, outcrop
Ev*	547	503	203	complete, outcrop
Eh1*	344	256	131	complete, outcrop
Eh2*	443	394	197	complete, outcrop
F&G				core plug shape problems, outcrop
Hv	690			no pair, outcrop
Hh1	795			core plug shape problems, outcrop
Hh2				core plug shape problems, outcrop
Iv*	664	702	383	complete, outcrop
Ih1*	744	898	487	complete, outcrop
Ih2*	863	293		core plug shape problems, outcrop
3248h*	172	152	65	complete, subsurface core
3248v*	158	152	64	complete, subsurface core
4014h*	73	70	27	complete, subsurface core
4014v*	60	41	19	complete, subsurface core
3217v	2			too tight, subsurface core
3217h	12			no pair, subsurface core
3289v*	36	22	11	complete, subsurface core
3289h*	142	92	66	complete, subsurface core
3962v*	31	24	9	complete, subsurface core
3962h*	57	52	20	complete, subsurface core
3980v*	46	37	12	complete, subsurface core
3980h*	65	77	22	complete, subsurface core
3986v*	12	6	3	complete, subsurface core
3986h*	103	93	34	complete, subsurface core
6726v*	37	25	10	complete, subsurface core
6726h*	48	33	24	complete, subsurface core

Table 2.1. (Cont).

Core	Air perm (md)	Brine perm (md)	Oil perm at Swi (md)	Status
6727v*	40	32	9	complete, subsurface core
6727h*	84	89	23	complete, subsurface core
6815v	5	0.3		too tight, subsurface core
6815h	50	40		no pair, subsurface core
6871v	6	4		too tight, subsurface core
6871h	118	101		no pair, subsurface core
6872v*	50	32	19	complete, subsurface core
6872h*	127	94	63	complete, subsurface core
CC-55v*	437	381	127	complete, outcrop, 2nd year
CC-55h*	592	566	454	complete, outcrop, 2nd year
CC-55h2*	947	946	647	complete, outcrop, 2nd year
MB-45v	4	2	1	too tight, outcrop, 2nd year
MB-45h1*	16	12	10	no vertical, outcrop, 2nd year
MB-45h2*	8	6	5	no vertical, outcrop, 2nd year
MB-65A	44	31	30	no horizontal, outcrop, 2nd year
MB-65B	136	114	102	bounding surface, outcrop, 2nd year
MB-65C	91	70	64	bounding surface, outcrop, 2nd year
NNB1-v	0.1	0.01		too tight, outcrop, 2nd year
NNB1-h1	0.1	0.02		too tight, outcrop, 2nd year
NNB1-h2	0.1	0.02		too tight, outcrop, 2nd year
NNB2-v*	80	39	40	complete, outcrop, 2nd year
NNB2-h*	177	152	139	complete, outcrop, 2nd year
NNB3-A	68	31	33	no horizontal, outcrop, 2nd year
NNB3-B	26	12	10	bounding surface, outcrop, 2nd year
NNB3-C	76	53	48	bounding surface, outcrop, 2nd year
3B8A3220	4	15		too tight, outcrop, 2nd year
3B8B3220	28	8	17	no vertical, outcrop, 2nd year
3B8A3250	14	15	7	no horizontal, outcrop, 2nd year
3B8B3250	152	44	89	bounding surface, outcrop, 2nd year
HR75B	2	0.4	0.7	no horizontal, outcrop, 2nd year
HR75C	40	24	27	bounding surface, outcrop, 2nd year
MB20A	29	15	16	no horizontal, outcrop, 2nd year
MB20F	84	54	55	bounding surface, outcrop, 2nd year
MB40A	2			too tight, outcrop, 2nd year
MB40B	0.2			too tight, outcrop, 2nd year
MB60A	11	4	6	no horizontal, outcrop, 2nd year
MB60B	18	6	11	bounding surface, outcrop, 2nd year
SC21.1A	0.02			too tight, outcrop, 2nd year
SC21.1B	0.02			too tight, outcrop, 2nd year
SC22C	52	29	34	no horizontal, outcrop, 2nd year
SC22G	56	24	38	bounding surface, outcrop, 2nd year

*Cores used in relative permeability anistropy

Results

In general, the vertical oil permeability is lower than the horizontal oil relative permeability. This is shown as a higher permeability ratio (k_w/k_o) for the vertical cores on Figures 2.6 through 2.24. The anisotropy that is apparent on these figures is further quantified in Figures 2.25-2.29.

First, the vertical permeability ratio for each sample is plotted against the horizontal permeability ratio. The point chosen from each relative permeability

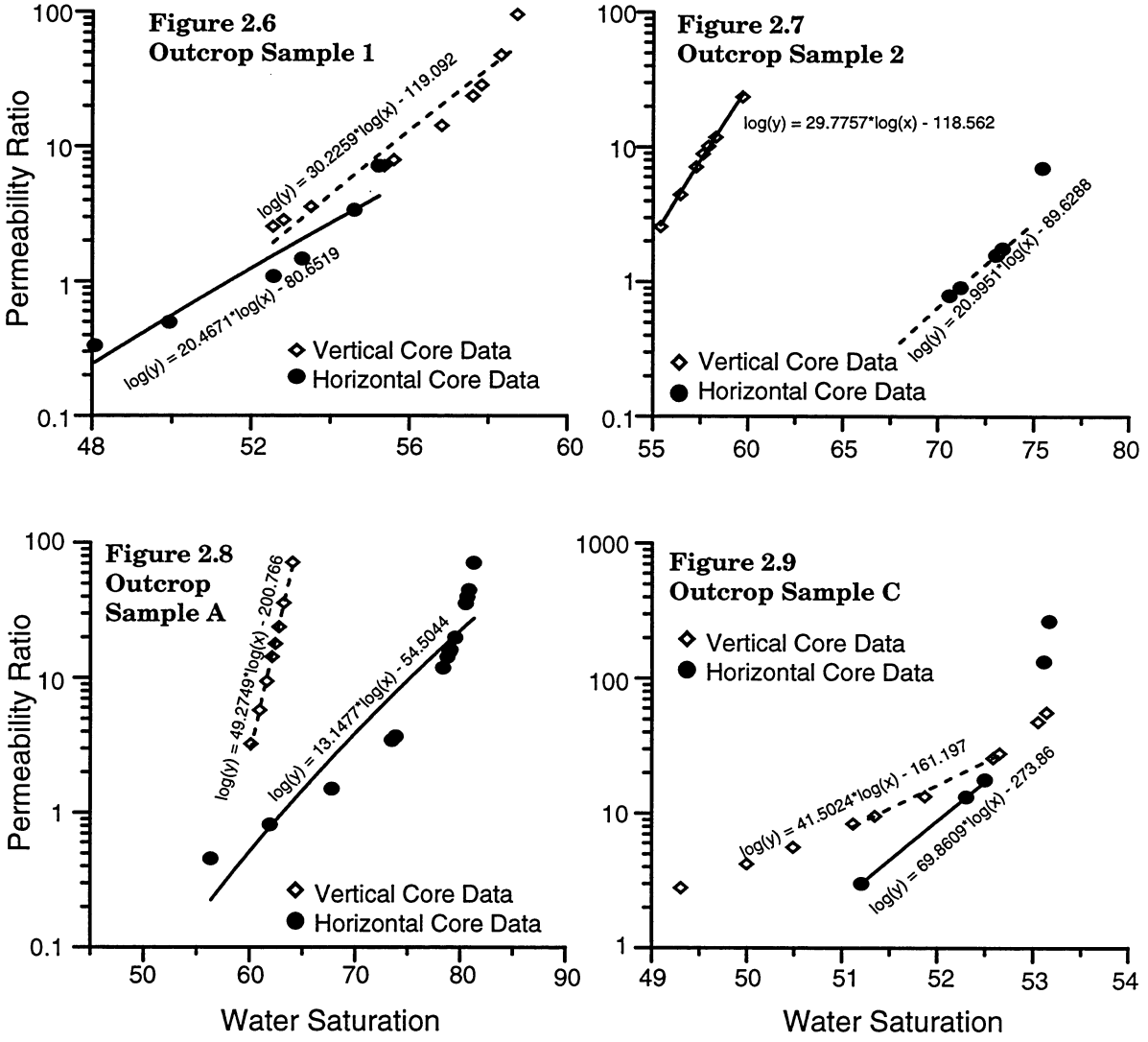

Figures 2.6 through 2.9. Laboratory results from unsteady-state relative permeability measurements of outcrop samples. Fractional flow of water yields a direct measurement of the relative permeability ratio (k_{rw}/k_{ro}). The equation of a best fit line is shown, which is used in future plots to quantify relative permeability anisotropy effects. The vertical core samples were taken perpendicular to bedding; the horizontal cores samples were taken parallel to bedding.

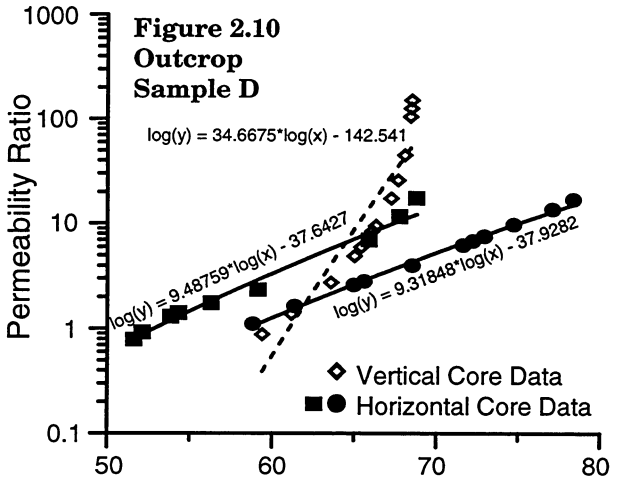

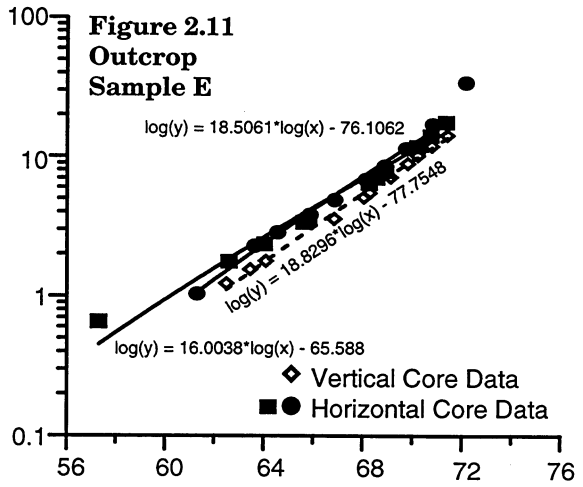

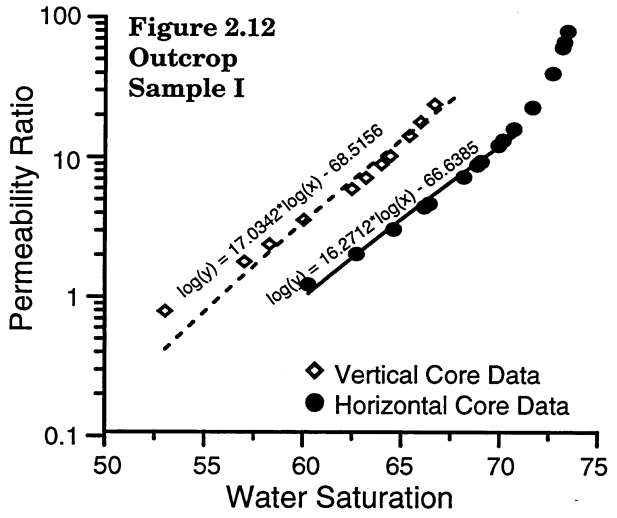

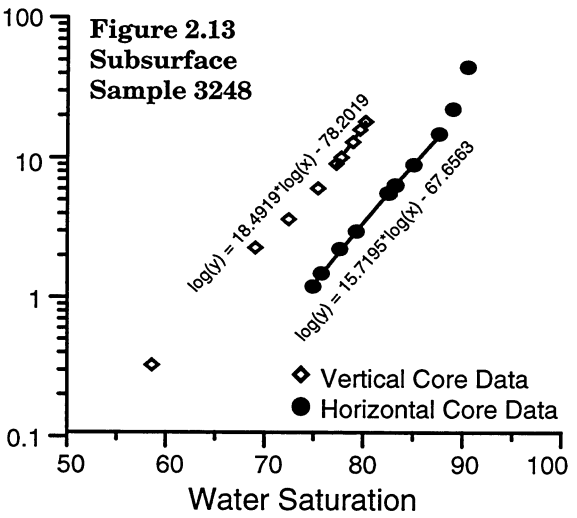

Figures 2.10 through 2.13. Laboratory results from unsteady-state relative permeability measurements of outcrop and subsurface samples. Fractional flow of water yields a direct measurement of the relative permeability ratio (k_{rw}/k_{ro}). The equation of a best fit line is shown, which is used in future plots to quantify relative permeability anisotropy effects. Vertical outcrop core samples were taken perpendicular to bedding; horizontal outcrop core samples were taken parallel to bedding. The subsurface sample pair is from a large diameter core, plugged vertically and horizontally as close together as practically possible. The sample number is the depth where plug was taken.

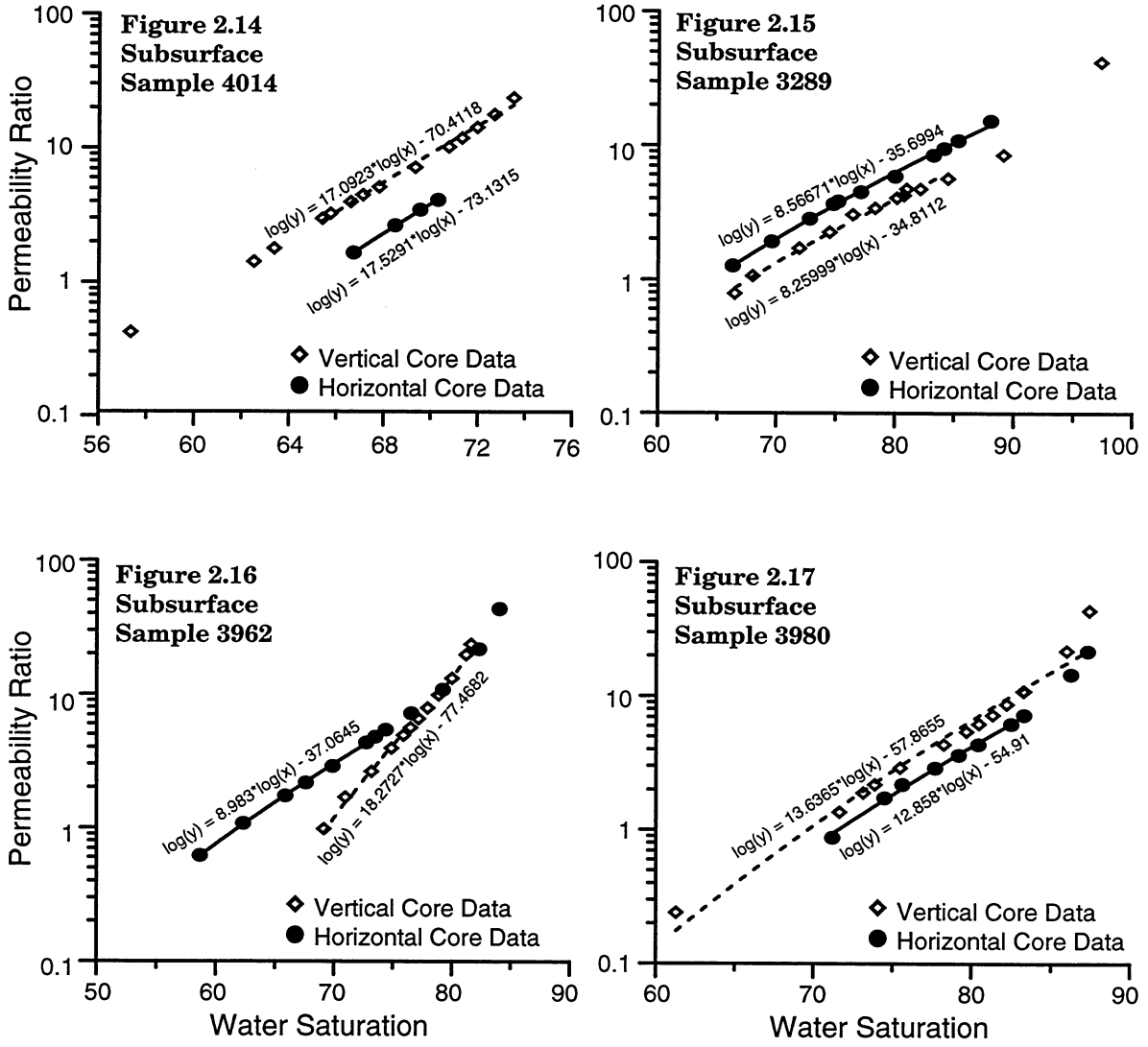

Figures 2.14 through 2.17. Laboratory results from unsteady-state relative permeability measurements of subsurface samples. Fractional flow of water yields a direct measurement of the relative permeability ratio (k_{rw}/k_{ro}). The equation of a best fit line is shown, which is used in future plots to quantify relative permeability anisotropy effects. The subsurface sample pairs are from a large diameter core, plugged vertically and horizontally as close together as practically possible. The sample number is the depth where plug was taken.

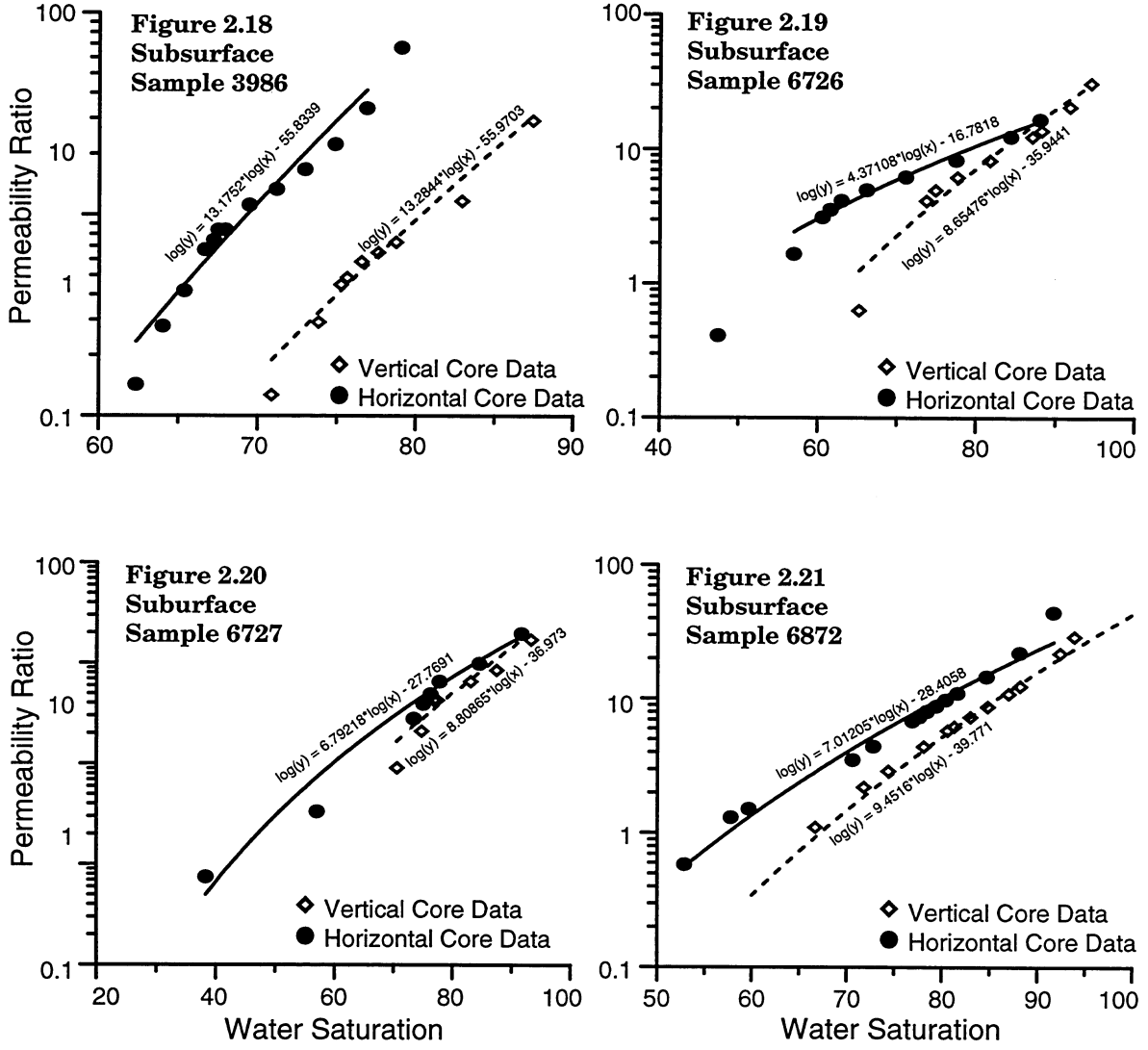

Figures 2.18 through 2.21. Laboratory results from unsteady-state relative permeability measurements of outcrop and subsursface samples. Fractional flow of water yields a direct measurement of the relative permeability ratio (k_{rw}/k_{ro}). The equation of a best fit line is shown, which is used in future plots to quantify relative permeability anisotropy effects. The subsurface sample pairs are from large diameter core, plugged vertically and horizontally as close together as practically possible. The sample number is the depth where plug was taken.

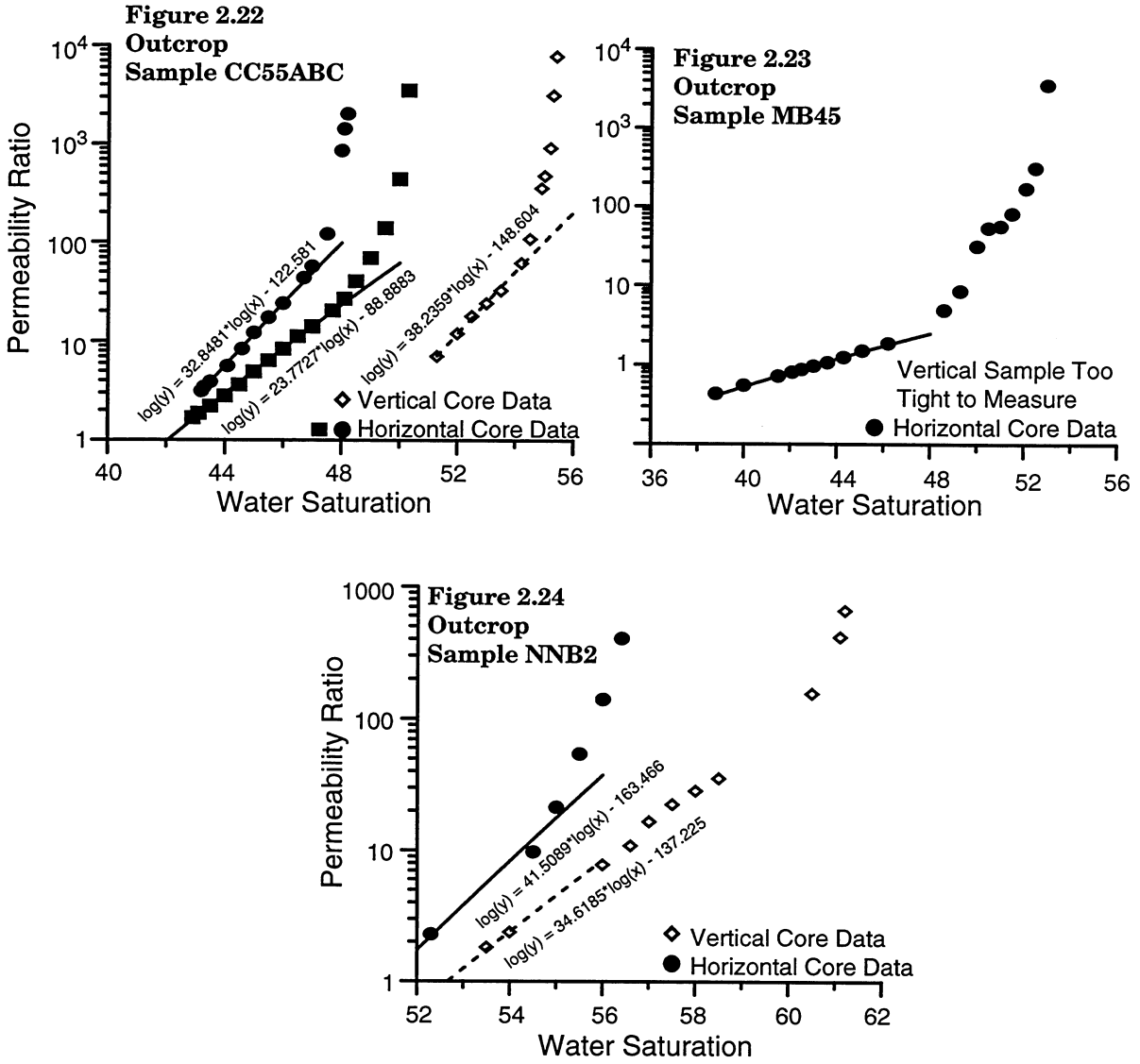

Figures 2.22 through 2.24. Laboratory results from unsteady-state relative permeability measurements of outcrop samples. Fractional flow of water yields a direct measurement of the relative permeability ratio (k_{rw}/k_{ro}). The equation of a best fit line is shown, which is used in future plots to quantify relative permeability anisotropy effects. The vertical core samples were taken perpendicular to bedding; horizontal cores samples were taken parallel to bedding.

curve is the point of minimum water saturation that is common to both the vertical and horizontal permeability ratio curves. These points are tabulated in Table 2.2. There is a distinct anisotropy trend towards a higher permeability ratio in the vertical cores when compared to the horizontal (Fig. 2.25). Because the minimum water saturation common to both vertical and horizontal curves is different for each pair of samples, this plot further demonstrates that the anisotropy exists over a wide range of water saturations.

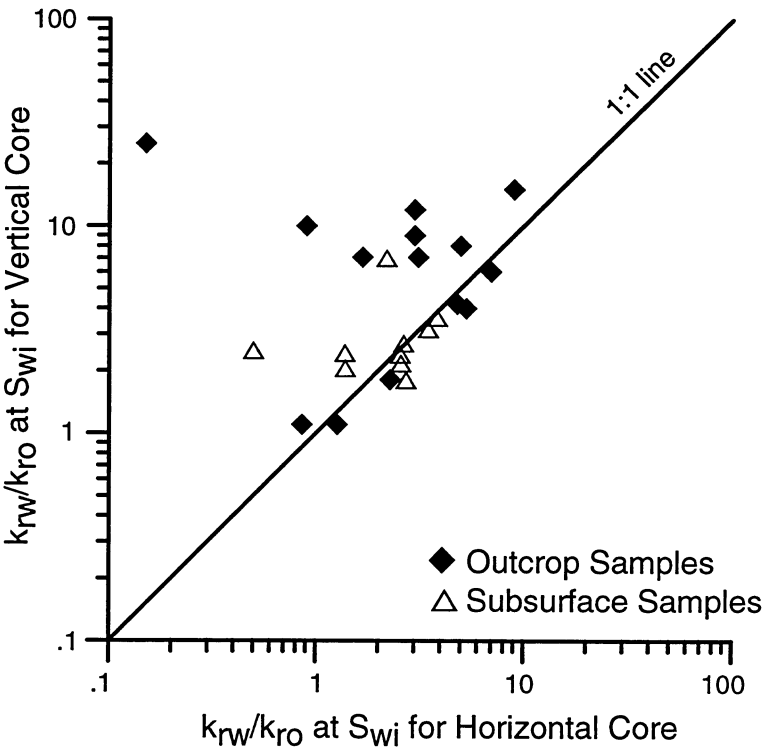

Figure 2.25. Permeability ratio (k_{rw}/k_{ro}) at initial point on displacement curve for vertical core compared against horizontal curve.

Figure 2.26 shows that the relative permeability anisotropy is significantly different than the absolute gas permeability anisotropy. Although there is an overall trend of both oil and gas permeability favored in the horizontal direction (also shown in the next plot), any given pair of points may not follow that trend. Each gas permeability point shifts to a very different direction when connected to the equivalent relative permeability ratio point. For example, some of the gas permeabilities are isotropic (plot on the 1:1 line) whereas the corresponding relative permeability ratio is anisotropic. There are also several pairs of points where the inverse is true — that the relative permeability ratio is isotropic while the gas permeability is anisotropic.

Table 2.2. Permeability ratio points picked from experimental data (Figs. 2.6 through 2.24) and plotted in Figure 2.25. The permeability ratio (k_{rw}/k_{ro}) is visually picked from each curve at the same water saturation for each pair of curves. When the curves occur at different water saturations, the initial (minimum) value is taken from each line.

Sample	Horizontal (k_{rw}/k_{ro})	Vertical (k_{rw}/k_{ro})	Taken from Figure Number:
1	7	6	2.6
2	0.2	25	2.7
A	0.9	10	2.8
C	9	15	2.9
D1	5	8	2.10
D2	3	9	2.10
E1	5	4	2.11
E2	5	4	2.11
I	3	12	2.12
3248	2.2	7	2.13
3289	1.4	2.1	2.15
3962	2.6	2.7	2.16
3980	3.5	3.2	2.17
3986	2.7	1.8	2.18
4014	2.6	2.2	2.14
6726	1.4	2.4	2.19
6727	3.8	3.6	2.20
6872	0.5	3	2.21
CC55C	1.7	7.1	2.22
CC55B	3.1	7.1	2.22
NNB2	2.3	1.8	2.24
MB45B	0.9	1.1	2.23
MB45C	1.3	1.1	2.23

The clearest demonstration of relative permeability anisotropy is given in Figure 2.27 which plots the oil relative permeability (k_{ro}) in the horizontal core against that in the vertical core. In this third plot, the oil relative permeability is the effective permeability of oil at residual water saturation divided by the absolute gas permeability. If the absolute gas permeability were responsible for the anisotropy, then the data would fall on a 1:1 line. However, they do not; the relative permeability of oil is clearly higher in the horizontal cores.

The fourth plot (Fig. 2.28) demonstrates the complete behavior of changing k_{ro} and k_{rw} over a range of water saturations for individual samples. The shape of relative permeability curves (Figs. 2.6-2.24) exhibits anisotropy independent of the k_o and k_g anisotropy shown in Figure 2.26. The slopes of

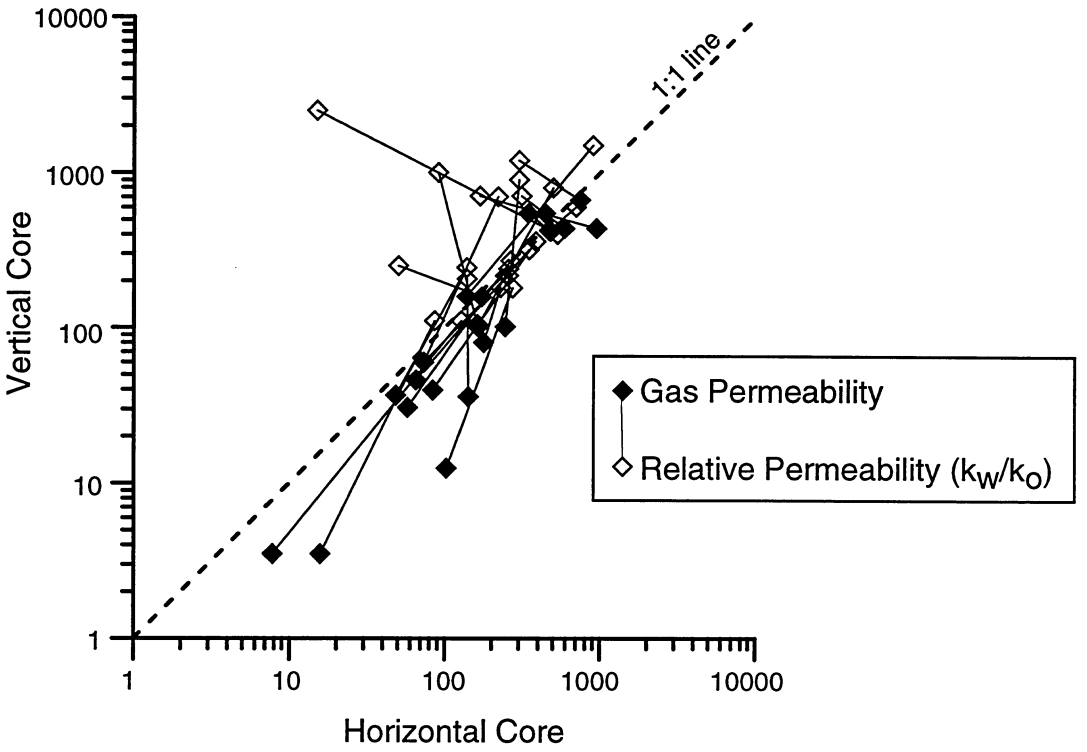

Figure 2.26. Permeability ratio (krw/kro) data points from Figure 2.25 connected to corresponding gas permeability from Figure 2.1. This figure illustrates that points with an anisotropic relative permeability ratio are not necessarily the same as those with an anisotropic gas permeability.

permeability ratio curves are used as another independent measure of relative permeability anisotropy. Each curve in Figures 2.6 through 2.24 was fit with a straight lines and the slopes used to characterize a general shape for each dataset. Figure 2.28 compares the slopes from the vertical core data against those from the horizontal core data. The slopes of the best fit lines for the vertical cores are steeper than those for the horizontal cores — the permeability ratio (k_w/k_o) increases faster with increasing water saturation in the vertical core than in the horizontal core.

Finally, the relative permeability anisotropy is demonstrated by examining the amount of oil produced before water breakthrough for vertical and horizontal cores (Fig. 2.29). The vertical cores produce a greater fraction of their total oil before water breakthrough. Once breakthrough occurs in the experiment, the vertical cores tend to rapidly produce water (steeper slope on the

relative permeability ratio curve on Figure 2.28). The vertical cores tend to start at a lower effective oil permeability, produce a greater fraction of oil before water breakthrough occurs, and exhibit a more rapid decrease in oil relative permeability as a flood proceeds.

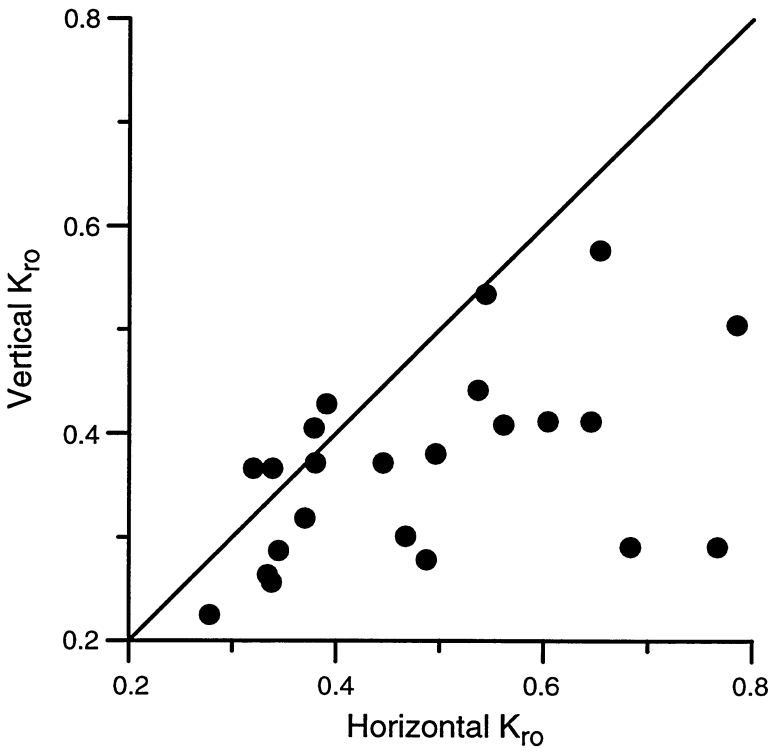

Figure 2.27. Horizontal oil relative permeability vs. vertical oil relative permeability (both at initial water saturation). The base permeability used to calculate relative permeability in this plot is the absolute gas permeability. The complete data are presented in Table 2.1 and plotted in Fig. 2.4. Vertical cores obviously suffer a much greater reduction in oil permeability when compared to the corresponding horizontal core, even when gas permeability is accounted for as it is in this plot.

Interpretation of Measurements

The existence of relative permeability anisotropy was demonstrated above with the trend being towards greater oil relative permeability in the horizontal direction and a larger permeability ratio (k_w/k_o) in the vertical direction. The effects of this on a waterflood can be understood conceptually by examining displacement behavior. Coreflood measurements on the vertical samples are more piston-like in oil displacement behavior, while the horizontal ones tend toward more fractional flow behavior. In true piston-like flow, all oil flows in front of the flood front, and all water flows behind the front — the largest fraction of total recoverable oil produces prior to water breakthrough. This would result in a curve on a permeability ratio plot that had a slope of infinity: ahead of the flood front, the permeability to water would be zero and behind the flood front, the permeability to oil would be zero. While none of the

vertical floods in this study have curves on the permeability ratio plots with infinite slopes, they do have slopes considerably greater than the horizontal floods. Flooding in the horizontal direction tends to bring water through easier, and leave a considerable amount of oil to be displaced after water breakthrough. Horizontal relative permeability anisotropy tends to appear similar to a channeling effect of water.

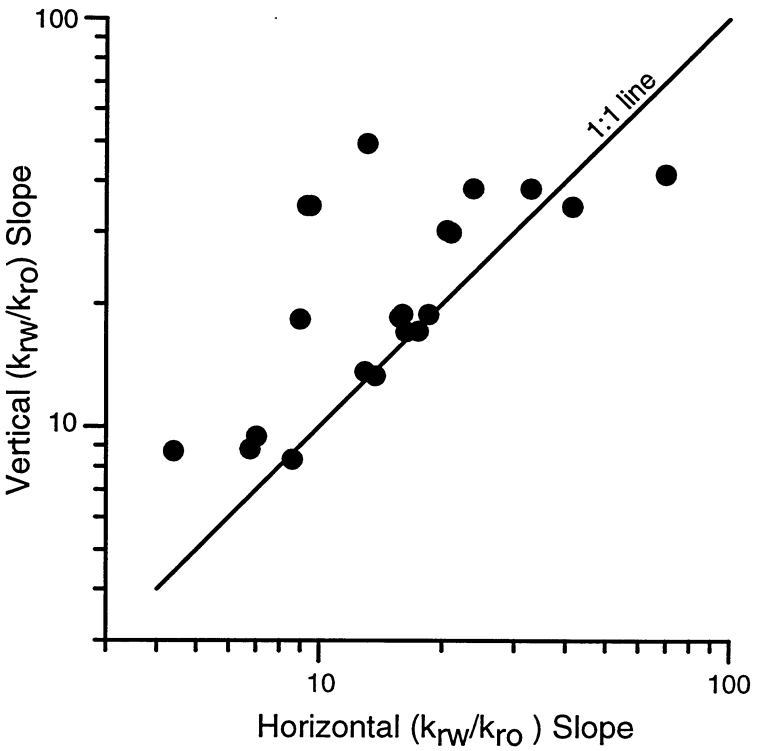

Figure 2.28. Slopes of lines displayed in Figures 2.6 through 2.24. This plot demonstrates the trend towards a slightly steeper relative permeability ratio line for a vertical core as compared with the corresponding horizontal core.

An important concept that follows from the above discussion of relative permeability anisotropy is the prediction of when oil will be produced from an oriented waterflood. If vertical flooding is more similar to piston-like behavior, then we should expect a larger fraction of oil to be produced prior to water breakthrough. Such concepts are supported by the observed data and can also be demonstrated with the use of a two-phase flow reservoir simulator as discussed in the next section on reservoir simulation. Also, field examples, discussed after the simulations, support that relative permeability anisotropy effects are active at the field scale.

RESERVOIR SIMULATION OF RELATIVE PERMEABILITY ANISOTROPY

Reservoir Simulation Using Measured Data

Relative permeability data are applied to a reservoir simulator through the use of an analytic function that provides a "best fit" to the observed range of experimental data. This procedure is described by Willhite (1986) using normalized dimensionless water saturation S_{wd} as the independent variable,

$$S_{wd} = (S_w - S_{wi}) / (1 - S_{or} - S_{wi})$$

where S_w is the core water saturation, S_{wi} is the initial irreducible water saturation, and S_{or} is the residual oil saturation when the experiment ends. In this way, S_{wd} is defined such that it will always range from zero to one during the course of a relative permeability experiment. Figure 2.30 shows the measured relative permeability points for subsurface sample 6872, along with the best-fit power law functions. Previous reports of this study (Dunn, 1995; Iverson et al., 1996) presented a similar analysis of

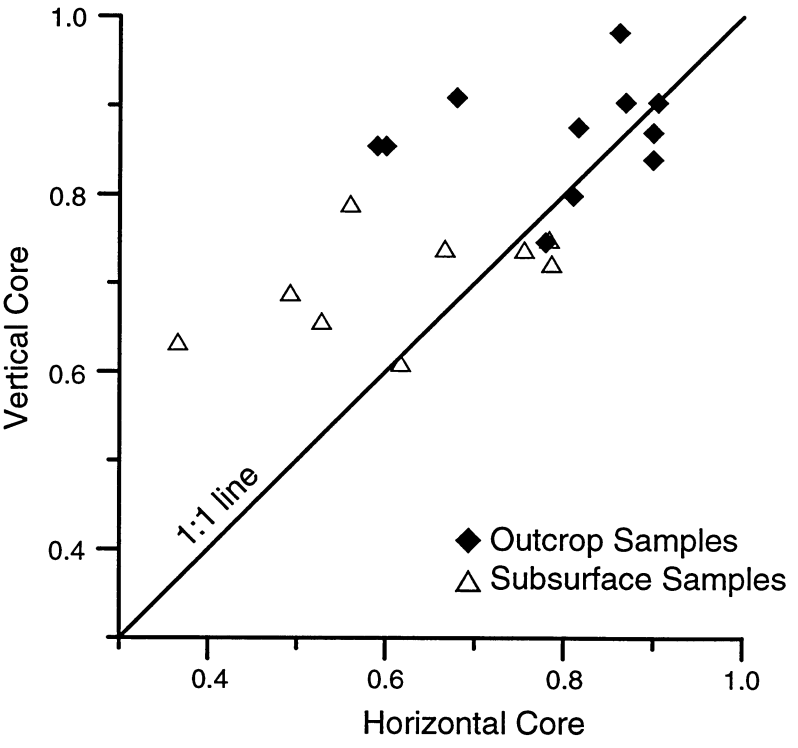

Figure 2.29. Amount of oil produced before water breakthrough divided by the total oil produced until complete flood-out with 100% water flowing. On average, vertical cores produce a greater fraction of their produced oil prior to water breakthrough. Complete "piston-like" displacement would result in a value of 1.0 in this plot.

sample A. It was later found that sample A was the most anisotropic sample of the entire dataset. Sample 6872 is more average and representative of a typical vertical versus horizontal comparison.

The approach for the reservoir simulation for Sample 6872 held most variables constant and varied only the shape of the relative permeability power law function. Oil relative permeability curves (Fig. 2.30) are very similar and will be assumed equal. In prior reports (Dunn, 1995; Iverson et al., 1996)

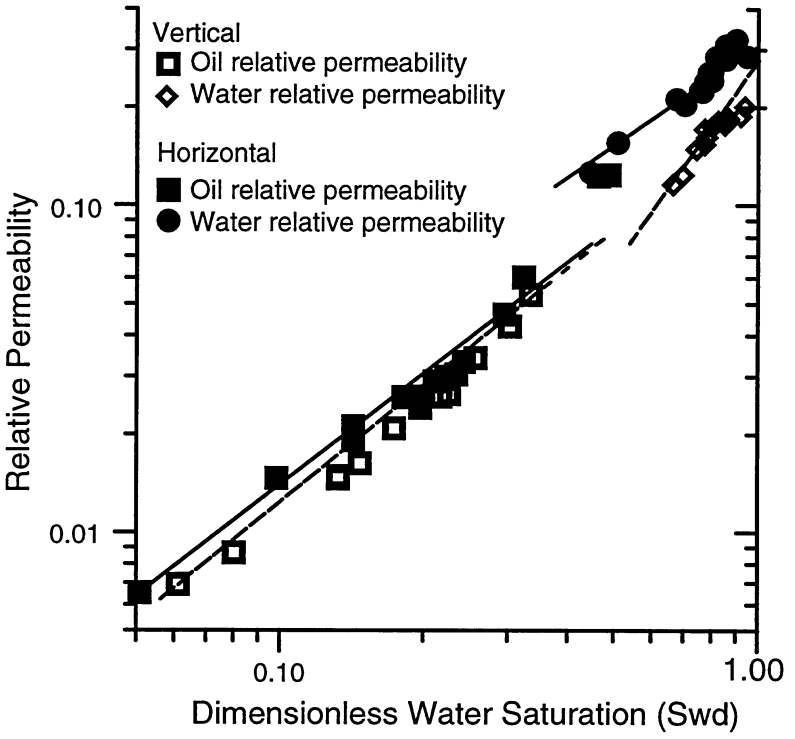

Figure 2.30. Relative permeability data for sample 6872 plotted against dimensionless water saturation (Swd) as defined by Willhite (1986) for fitting a power law function to the observed data.

different slopes for the oil relative permeability curve were used. However, it was subsequently noticed that the oil and water production results did not accurately represent many of the experimental observations. In this report, the steeper (k_{rw}/k_{ro}) observation is simulated by using a steeper water relative permeability function with a lower intercept value. The characteristics of this

representation for relative permeability anisotropy are described in Figure 2.30. Corresponding relative permeability functions are plotted in Figure 2.31.

Relative permeability power law curves (Fig. 2.31) were input to a BuckleyLeverett type simulator. The residual saturations and end-points were held constant so that both vertical and horizontal cores were modeled as having the same initial oil in place, the same irreducible water saturations, and the same residual oil saturations. Only the shape of the water relative permeability curve was different between the vertical and horizontal case. For the vertical water relative permeability, the assumed function is,

$$k_{rw} = 0.6\ (S_{wd})^3\ ,$$

while the horizontal water relative permeability function is,

$$k_{rw} = 1.0\ (S_{wd})^2\ .$$

Oil relative permeability is assumed identical for both vertical and horizontal cases:

$$k_{ro} = 1.0\ (1\text{-}S_{wd})^2\ .$$

A Buckley-Leverett computer program was used to model simple onedimensional displacement of oil by water given the observed relative permeability responses. This program is one-dimensional and suitable for this type of simulation because of its adaptability to variable relative permeability characteristics of oil/water systems. The computer program follows the technique outlined by Willhite (1986) and presented by Whitman (1988). A derivative is computed at each water saturation to determine the extrapolation to average water saturation as a function of the pore volumes of water injected.

Two runs through the simulator demonstrate the potential effects of only a small change in the shape of the power law fit. Parameters input to the BuckleyLeverett simulator are listed in Table 2.3 in terms as described by Whitman (1988). By providing a constant pressure drop, absolute permeability, and reservoir geometry, the flow rates were calculated. For the second run, all parameters were held constant and the power law exponent was increased. The results of the two runs are compared in Figure 2.32 which is a plot of oil

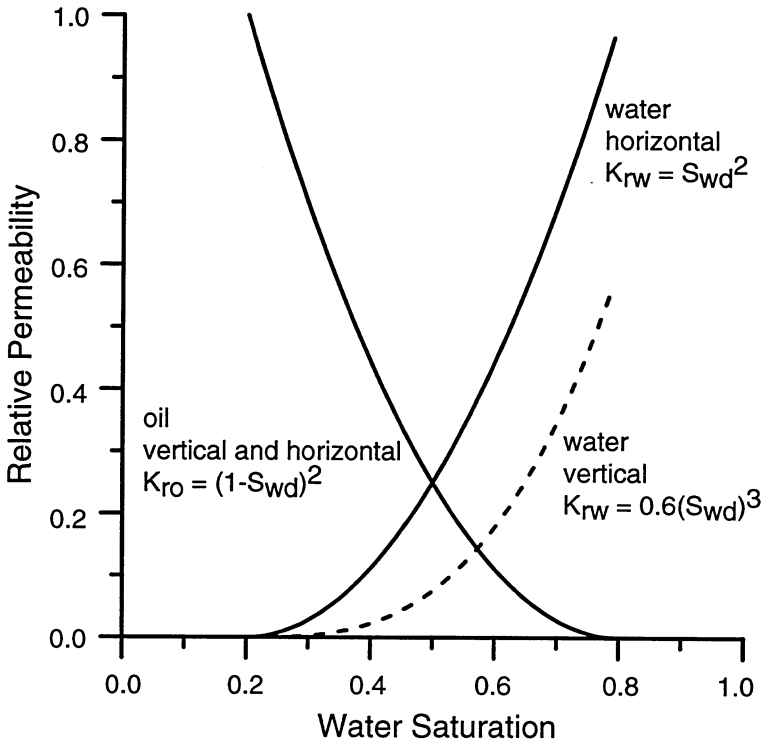

Figure 2.31. Analytic model of relative permeability input to a Buckley-Leverett simulator. The vertical orientation is modeled as simply having a steeper slope (exponent increase from 2 to 3) and a lower constant (decrease from 1.0 to 0.6) compared to the vertical. Shape of oil relative permeability curve is identical in vertical and horizontal simulations runs.

production rate versus time. The major difference between the vertical and horizontal core simulations was the rate at which oil production dropped after water breakthrough. Oil production falls most rapidly in the vertical case as most of the oil production occurs prior to water breakthrough. This observation is consistent with that made with the experimental data (Fig. 2.29) where the vertical core produces more oil early in the waterflood as compared to the horizontal core.

The water-oil-ratio was also very different between the vertical and horizontal displacement simulations (Fig. 2.33). Since the vertical case produced most of the oil prior to water breakthrough, the producing water-oil-ratio rises very rapidly after breakthrough. In the horizontal case, additional oil continued to flow after breakthrough, so the producing water-oil-ratio did not rise as fast.

Table 2.3. Buckley-Leverett simulation parameters. See Willhite (1986) or Whitman (1988) for detailed descriptions of how each parameter is utilized in software.

Horizontal Model

Input Parameters:
width = 30m (100ft)
length = 305m (1000ft)
thickness = 6m (20ft)
porosity = 0.2

S_{wc} = 0.2
S_{wi} = 0.2
S_{or} = 0.3
k_{ro}: alpha1 = 1
m = 2
k_{rw}: alpha2 = 1
n = 2
Oil viscosity = 1 cp
Water viscosity = 1 cp
Oil FVF = 1 bbl/STB
Water FVF = 1 bbl/STB
Constant injection rate case:
rate = 100 b/d
kabs = 200 md.

Calculated Parameters:
pore volume = 71238 bbl

S_{wf} = 0.5535
Swbar = 0.6142
W_{id} @ bt = .4139 PV
N_{pd} @ bt = .4142 PV
initial fw = 0

Msbar = 0.686
Msend = 1

Disp Eff @ bt = 82.83%

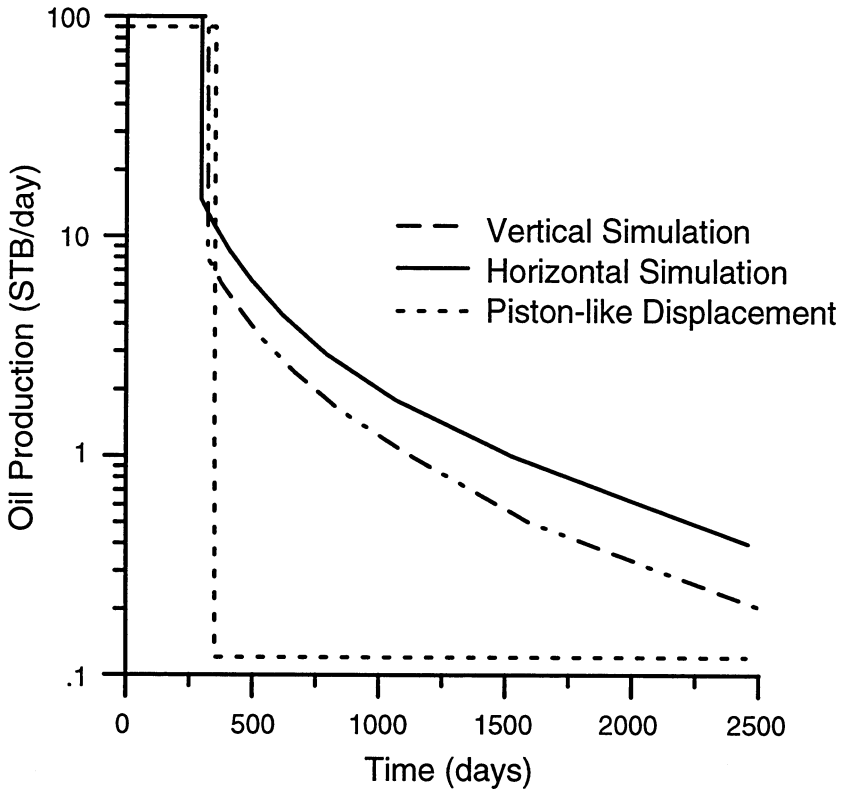

Figure 2.32. Results from two runs through Buckley-Leverett one-dimensional simulator with parameters as described in Table 2.3. Vertical displacement drops oil production more rapidly than horizontal displacement. Piston displacement shown for comparison.

Table 2.3. (Cont)

Vertical Model (all parameters identical to horizontal if not listed below)

Input Parameters:		Calculated Parameters:
		S_{wf} = 0.6145
		S_{wbar} = 0.6499
		W_{id} @ bt = .4498 PV
		N_{pd} @ bt = .4499 PV
kro:	alpha1 = 1.	Msbar = 0.437
	m = 2.	Msend = 0.6
krw:	alpha2 = 0.6	
n = 3.		Disp Eff @ bt = 89.99%

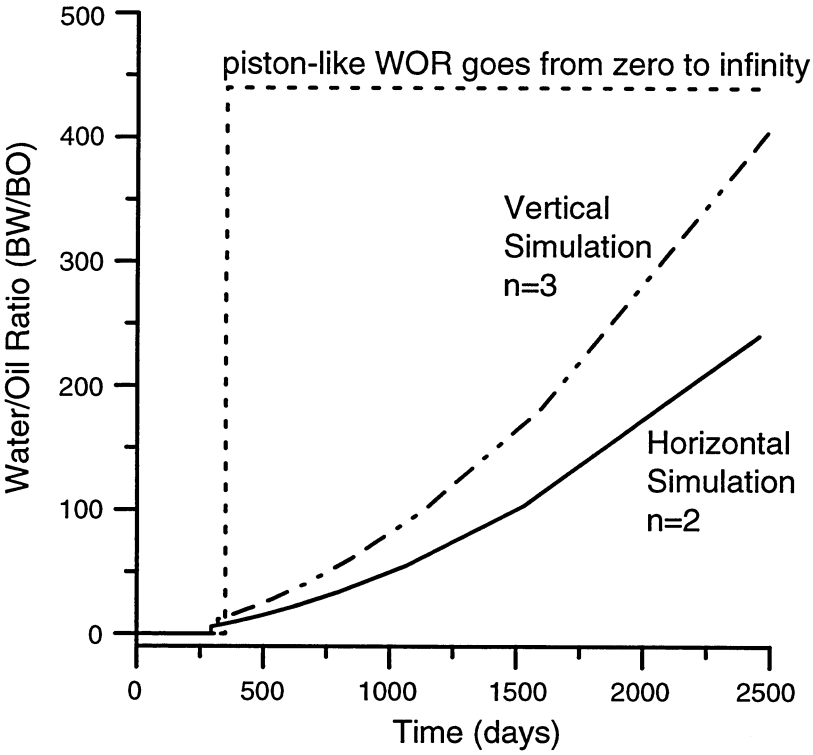

Figure 2.33. Water-oil ratio as a function of time for simulation runs as shown in Figure 2.32 and Table 2.3. Since a greater fraction of oil is produced prior to water breakthrough, the WOR must rise rapidly after breakthrough. In experimental data, this behavior was near "piston-like" (see Figure 2.29) with nearly 100% of the oil recovered prior to breakthrough.

In field practices, the economic limit of production is typically at a cut-off water-oilratio. A vertical waterflood would reach a specified cut-off much sooner.

In practice, however, a vertical waterflood cannot be maintained. The two directions (vertical and horizontal) cannot be confined and flooded separately; flow will simply follow the path of least resistance. Given the relative permeability anisotropy that has been demonstrated, the path of least resistance will be in the horizontal direction. Flooding in the vertical direction cannot be maintained because of the high pressure needed. This is shown with the simulations. Figure 2.34 shows the pressure drop as a function of time given a constant injection rate. This plot demonstrates one of the reasons that waterfloods tend to channel along the horizontal bedding direction. In these simulations, absolute permeability has been set equal in both directions so the anisotropy is only in the relative permeability. Note that the vertical flooding indicates a much higher pressure as a function of time due to the rapid increase in water saturation and the early production of oil. Therefore, two-phase flow requires greater pressure in the vertical direction which, in practice, cannot be maintained.

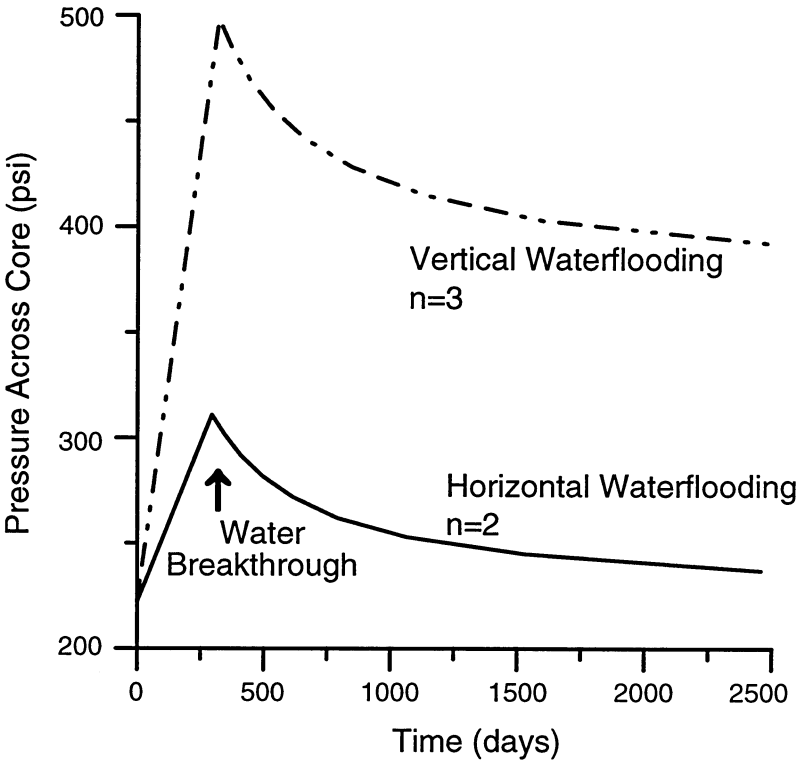

Figure 2.34. Same simulations as in previous figures, showing the significantly higher pressure required to maintain the same flow rate in the vertically oriented core simulation. Such a result explains why two-phase flow will preferentially follow horizontal bedding, even when absolute permeabilities are equal in vertical and horizontal.

Oil Field Comparison

No controlled vertical versus horizontal water flood has ever been accomplished in the field. Sandstone layers are generally horizontal, and there is considerable horizontal distance between injectors and producers. Possibly the best place to look for relative permeability anisotropy effects is the conversion of a mature common waterflood project into production from horizontal wells. The thought is that the original waterflood was dominantly

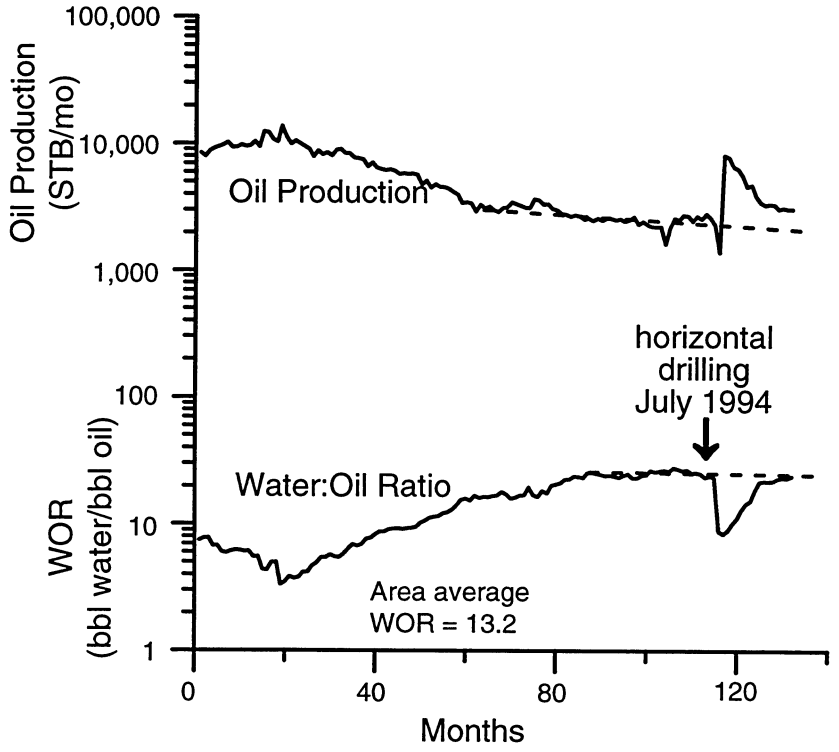

Figure 2.35. Conversion of old vertical wellbore into horizontal drilling project within Tensleep Sandstone in Oregon Basin field, Wyoming. Vertical flow continues for a very brief time after drilling the horizontal, but a dominant horizontal flow regime soon takes over and production increases.

flooding horizontally from vertical injection and production wells. When a horizontal well is drilled, vertical flow is induced where previous flow was restricted to the horizontal orientation.

In 1994, Marathon began a horizontal drilling project in the northern portion of the Oregon Basin Field. Production from the horizontal project in the

Tensleep sandstones at the Gov't 10H well is shown in Figure 2.35. Up to the time of the horizontal drilling in July of 1994, oil production steadily declined and the water-oil-ratio steadily increased. Subsequent to horizontal drilling, oil production increased nearly four-fold. Water production remained fairly constant resulting in a decline in the water-oil-ratio. After 18 months, production rates returned to those typical before the horizontal drilling project. Relative permeability anisotropy best explains the rapid return of production to the pre-horizontal drilling baseline. Relative permeability anisotropy effects determined from the laboratory experiments and simulations predict a brief increase in oil production and a decrease in the water-oil-ratio due to the changing direction of flow through portions of the cross-bedding. Vertical flow cannot be maintained very long due to the high pressure needed in vertical floods. Therefore, flow will eventually return to a horizontal orientation, and oil production will return to the steady decline observed before horizontal drilling.

Three additional examples show similar production patterns. The Sidney 20H (Fig. 2.36), also from Oregon Basin, has shown somewhat sporadic production since conversion from a vertical well to a horizontal wellbore. The horizontal production now appears to be headed back to production levels typical of those before the horizontal

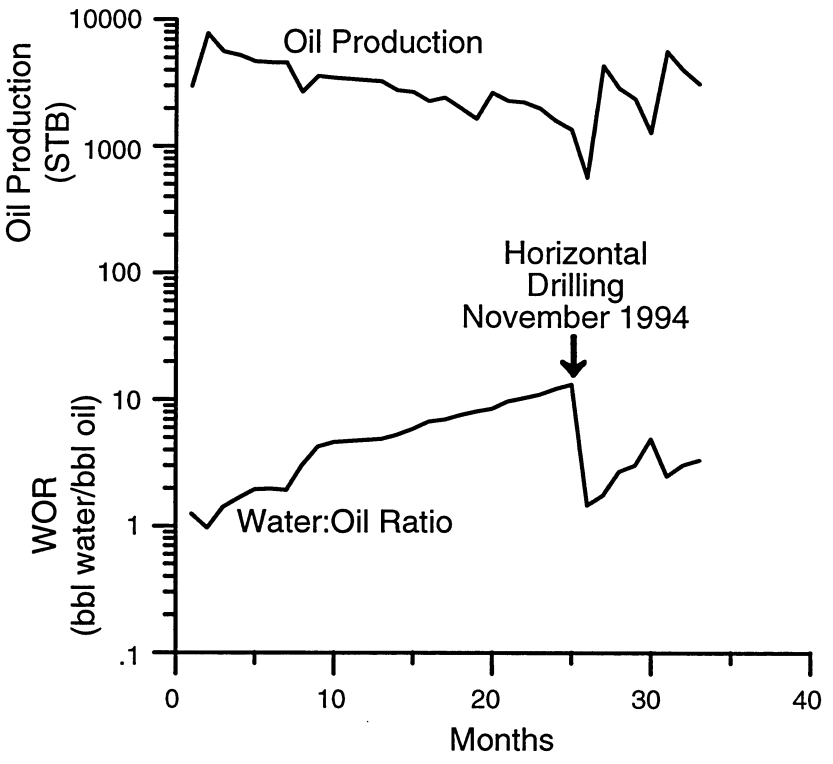

Figure 2.36. Another example of production increase due to conversion of old vertical wellbore into a horizontal in the Tensleep Sandstone at Oregon Basin field, Wyoming.

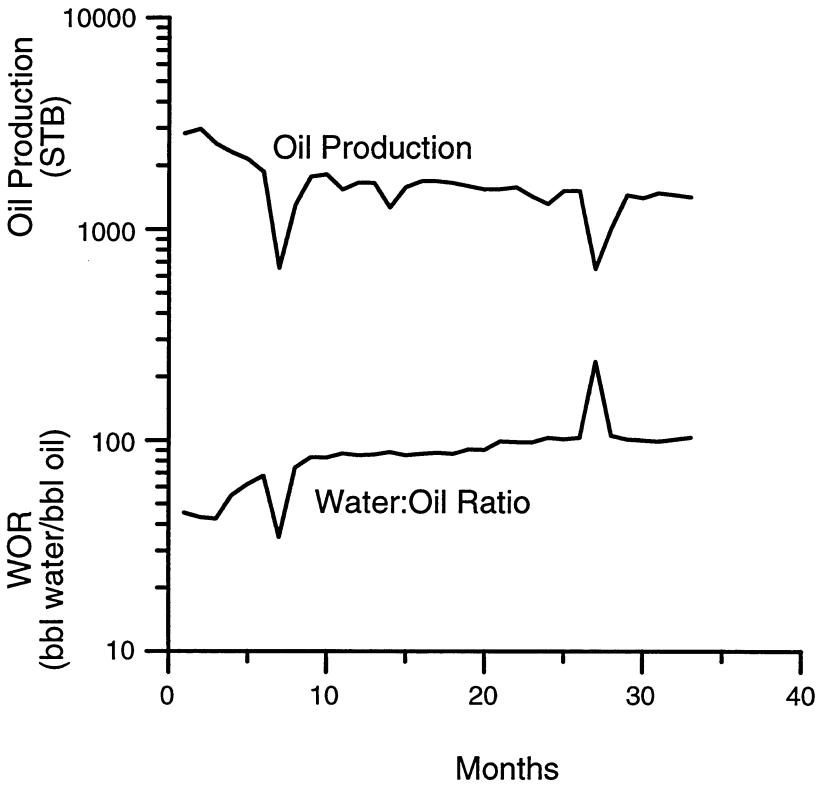

Figure 2.37. Horizontal drilling in Black Mountain oil field of the southern Bighorn Basin. High water:oil ratios have been very detrimental to economics according to Texaco personnel. The well will probably not continue production.

drilling project. A well from the Black Mountain oil field (Fig. 2.37) was drilled from a new well spot location, so pre-horizontal production does not exist. Average production per well in the Black Mountain along with WOR data demonstrate, however, that this horizontal project is similar. Finally, an example from the Pitchfork oil field (Fig. 2.38) shows results similar to Oregon Basin. The horizontal oil production remains relatively high, over a year after horizontal drilling, and the WOR remains low.

PETROGRAPHIC IMAGE ANALYSIS

Purpose

The image analysis task was undertaken in order to create a relatively rapid and less expensive method for estimating relative permeability. Even for unsteady-state measurements, each analysis can cost $900. Using up to three

measurements at each sample point, the cost of any extensive outcrop analog sampling becomes prohibitively expensive.

The approach taken was to quantitatively examine the pore structure between cores taken parallel to and across laminations and bounding surfaces, build a correlation algorithm, and test it.

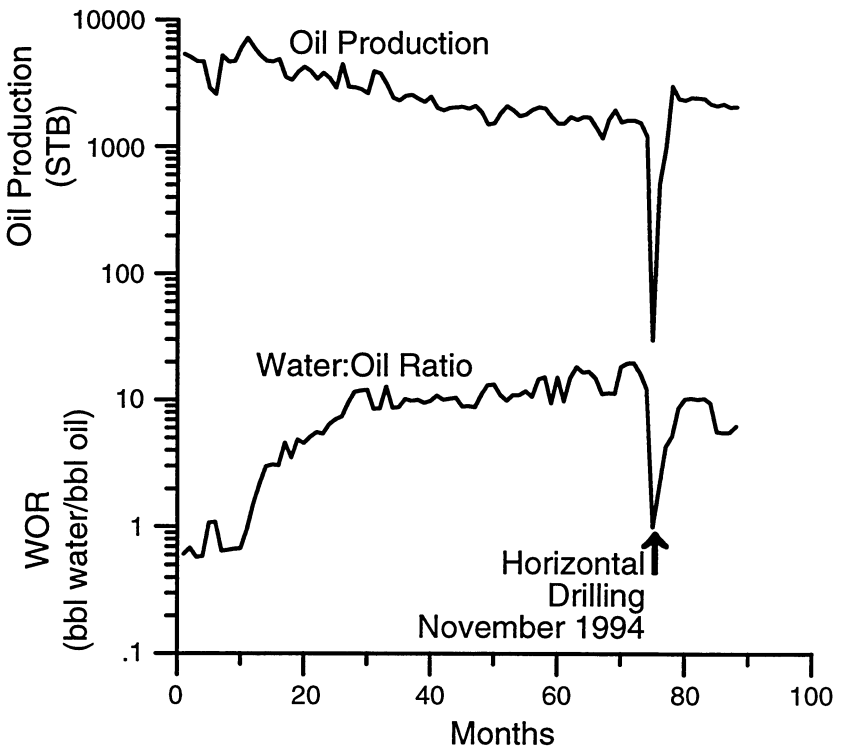

Figure 2.38. Conversion of a vertical wellbore into a horizontal Tensleep producer in the Pitchfork oil field on the southwest side of the Bighorn Basin.

Sample Collection and Preparation

Samples were taken from outcrop and core for use in the image analysis study. The samples were chosen to represent the dominant sedimentary features (including bounding surfaces) of the Tensleep as observed in field and core characterization studies. Rocks selected for image analysis were sampled at orientations near vertical and horizontal with respect to the rock fabric of interest.

Outcrop core samples were collected over two summer field seasons using a chain saw modified to drill 1.5-inch-diameter by 3-inch-long core plugs or were brought back to the laboratory as blocks and drilled in a modified drill press using a core bit with the same specifications as the chain saw's core barrel. Horizontal and vertical samples were taken as close together as physically possible to insure that the measurement of the flow properties through them be

considered orthogonal at one location. Samples taken to study anisotropy were taken in three different directions at right angles to each other to capture maximum differences in the orientation of the stratification within the core samples (Fig. 2.39). This was done to illustrate the effects of stratification on relative permeability anisotropy.

Samples of bounding surfaces were chosen to highlight differences in flow properties between samples. Samples were collected parallel to each other and perpendicular to the bounding surfaces, with one sample above or below the surface and a corresponding sample taken from across the surface (Fig. 2.39). This was done to illustrate the inhibiting nature that bounding surfaces have on two-phase flow properties.

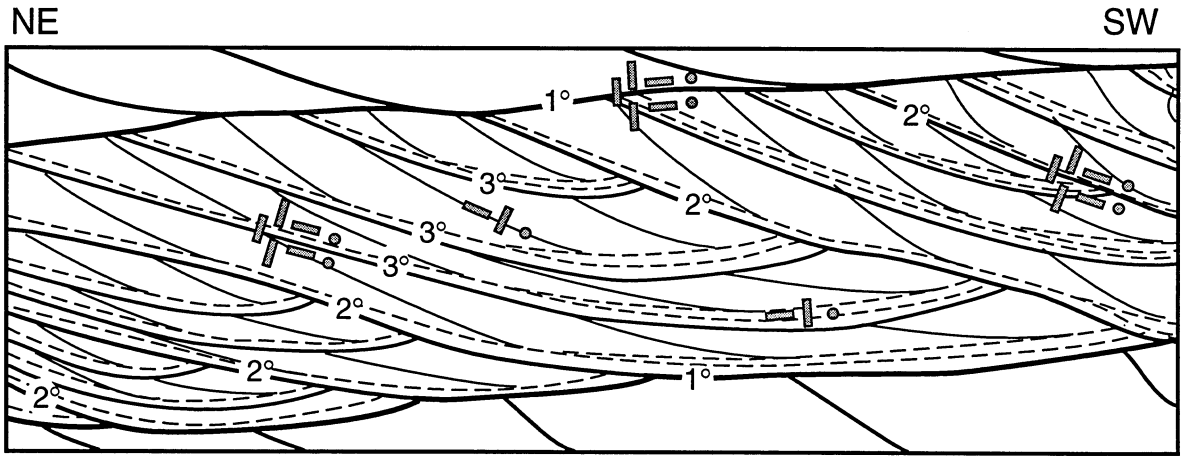

Figure 2.39. Schematic diagram of internal stratification and sampling scheme for the relative permeability and image analysis studies. Sampling concentrated on determining directional differences in the relative permeability of stratification types, such as wind-ripple and grainflow laminae and on determining the ability of different types of erosional bounding surfaces to act as baffles or barriers to fluid flow.

Billets were cut from the core plugs for use in image analysis. All billets were cut perpendicular to the flow direction through the core plug to insure that the conduit pore structure was being analyzed. The billets were then pressure-impregnated with blue-dye epoxy at a minimum pressure of 6.2×10^6Pa (900psi). The epoxy impregnation allows the differentiation between pore structure and rock matrix using backscattered electron (BSE) microscopy.

It was recognized early in the study that plucked grains can greatly change the pore size distribution derived from image analysis (Fig. 2.40). Work by Pittman (1991) points out that during the preparation of thin sections, grains may be plucked from the billet faces during the sawing of the sample. The void left by the plucked grains may later be falsely interpreted as oversized or moldic pores (Fig. 2.41). To minimize this effect, Pittman (1991) recommended that the "damage zone" be removed by grinding away material to a depth greater than roughly one grain diameter. Therefore, after pressure impregnation our samples

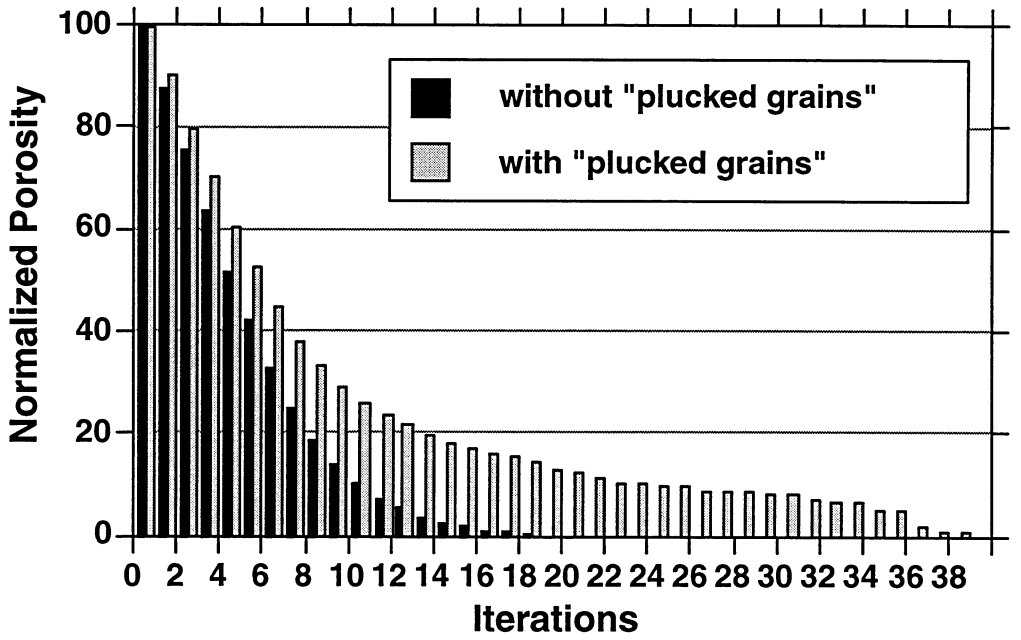

Figure 2.40 Comparison from Wertz 133 horizontal sample 6872H showing the effect of plucked grains on pore-size distribution.

were ground to a depth no less than 0.5 mm to remove any artifact porosity created by the sawing process. This depth is roughly equal to three grain diameters in the Tensleep. After the thin sections were made, any grains plucked during the grinding process are represented by clear pore space while the original pore structure is depicted by the blue color from the dye impregnation. All thin sections were visually inspected to insure any artifact porosity created by cutting the core plugs into billets was removed so that an accurate representation of the pore size distribution could be obtained.

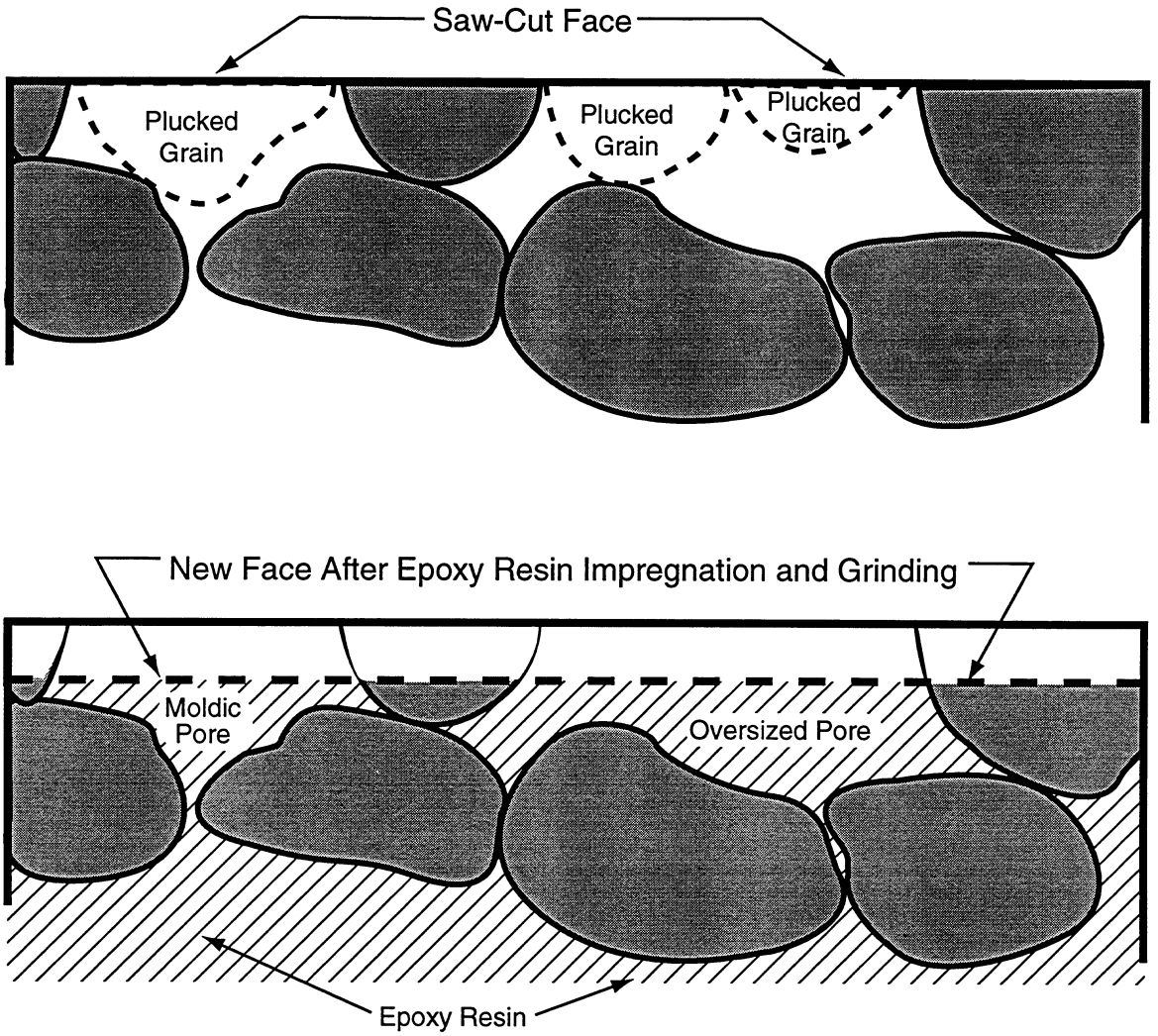

Figure 2.41. Schematic diagrams showing artifact porosity due to grain plucking. The top diagram depicts the plucking of sand grains during the rock saw trimming of a piece of rock to an appropriate size for thin sectioning. The bottom diagram depicts what the rock looks like after epoxy impregnation and grinding. The space once occupied by grains is now filled with epoxy giving the impression of abundant moldic and oversized pores. The rock face that is to be mounted to the thin section glass must by ground at least to the depth of one grain diameter to avoid this artifact porosity. In this study, thin sections were ground to a depth of approximately three grain diameters.

A total of 76 thin sections were utilized for the image analysis portion of the study. Thirty of the thin sections were made from samples that had been measured for relative permeability; the remaining forty-six were from samples that were not measured for relative permeability. Table 2.4 summarizes the samples used.

Table 2.4. Samples collected for scanning electron microscopy image analysis studies. See Tables 2.1 and 2.2 for relative permeability data.

Sample	Surface Type or Stratification	Location Name	Measured Relative Permeability
MB-40a	3° bounding surface	Mahogany Butte	✓
MB-40b	3° bounding surface	Mahogany Butte	✓
MB-20a	3° bounding surface	Mahogany Butte	✓
MB-20f	3° bounding surface	Mahogany Butte	✓
MB-60a	2° bounding surface	Mahogany Butte	✓
MB-60b	2° bounding surface	Mahogany Butte	✓
MB-45a	wind-ripple laminae	Mahogany Butte	
MB-45b	wind-ripple laminae	Mahogany Butte	
MB-45c	wind-ripple laminae	Mahogany Butte	
CC-55a	wind-ripple laminae	Canyon Creek	✓
CC-55b	wind-ripple laminae	Canyon Creek	✓
CC-55c	wind-ripple laminae	Canyon Creek	✓
MB-65a	2° bounding surface	Mahogany Butte	✓
MB-65b	2° bounding surface	Mahogany Butte	✓
MB-65c	2° bounding surface	Mahogany Butte	✓
Gt 3B #8 3220a	3° bounding surface	Oregon Basin	
Gt 3B #8 3220b	3° bounding surface	Oregon Basin	
Bh1	wind ripple laminae	Tensleep Canyon	
Bv	wind-ripple laminae	Tensleep Canyon	
MB-70a	3° bounding surface	Mahogany Butte	
MB-70b	3° bounding surface	Mahogany Butte	
HR-75b	1°bounding surface	Holland Ranch	✓
HR-75c	1°bounding surface	Holland Ranch	✓
Gt 3B #8 3217	wind ripple laminae	Oregon Basin	
Gt 3B #8 3217	wind ripple laminae	Oregon Basin	
Wertz 6815	wind ripple laminae	Lost Solider Field	
Wertz 6815	wind ripple laminae	Lost Solider	
Wertz 6871	wind ripple laminae	Lost Solider	
Wertz 6871	wind ripple laminae	Lost Solider	
Dh2	wind ripple laminae	Mahogany Butte	✓
Dh3	wind ripple laminae	Mahogany Butte	✓
Dv	wind-ripple laminae	Mahogany Butte	✓
MB-30a	wind-ripple laminae	Mahogany Butte	
MB-30b	wind-ripple laminae	Mahogany Butte	
MB-30c	wind-ripple laminae	Mahogany Butte	
Ih1	wind-ripple laminae & grainflow	Mayoworth	✓
Iv	WR/ grainflow	Mayoworth	✓
1h	wind ripple laminae	Wind River Canyon	✓
SC-80a	2° bounding surface	Sinks Canyon	
SC-80b	2° bounding surface	Sinks Canyon	
Gh1	wind-ripple laminae	Crooked Creek	
Gh2	wind-ripple laminae	Crooked Creek	
Gv	wind-ripple laminae	Crooked Creek	
Gt 3B #8 3288h	wind ripple laminae	Oregon Basin	✓
Gt 3B #8 3288v	wind ripple laminae	Oregon Basin	✓
Wilson B12 3962h	disturbed wind ripple laminae	Oregon Basin	✓
Wilson B12 3962v	disturbed WR	Oregon Basin	✓
Wilson B12 3979h	wind ripple laminae	Oregon Basin	✓
Wilson B12 3979v	wind ripple laminae	Oregon Basin	✓
Wilson B12 3286h	wind ripple laminae	Oregon Basin	✓

Table 2.4. (Cont.)

Sample	Surface Type or Stratification	Location Name Permeability	Measured Relative
Wilson B12 3286v	wind ripple laminae	Oregon Basin	✓
MB-35a	wind-ripple laminae	Mahogany Butte	
MB-35b	wind-ripple laminae	Mahogany Butte	
MB-35C	wind ripple laminae	Mahogany Butte	
Hh1	wind ripple laminae	Rome Hill Road	
Hh2	wind ripple laminae	Rome Hill Road	
Hv	wind ripple laminae	Rome Hill Road	
CC-45a	1°bounding surface	Canyon Creek	
CC-45b	1°bounding surface	Canyon Creek	
SC-21.1a	3° bounding surface	Sinks Canyon	
SC-21.1b	3° bounding surface	Sinks Canyon	
CC-50h1	wind-ripple laminae	Canyon Creek	
CC-50h2	wind-ripple laminae	Canyon Creek	
CC-50v	wind-ripple laminae	Canyon Creek	
MB-18a	3° bounding surface	Mahogany Butte	
MB-18b	3° bounding surface	Mahogany Butte	
MB-001a	3° bounding surface	Mahogany Butte	
MB-001b	3° bounding surface	Mahogany Butte	
SC-22a	2° bounding surface	Sinks Canyon	✓
SC-22b	2° bounding surface	Sinks Canyon	✓
SR1-1	wind-ripple laminae	Slip Road	
SR1-2	wind-ripple laminae	Slip Road	
SR1-2	wind-ripple laminae	Slip Road	
MB-NNB1a	3° bounding surface	Mahogany Butte	
MB-NNB1b	3° bounding surface	Mahogany Butte	
MB-NNB1c	3° bounding surface	Mahogany Butte	

Image Input Devices, Data Measurement, and Collection

The image acquisition system used consists of a JEOL-35CF scanning electron microscope (SEM) equipped with a Robinson backscattered electron (BSE) detector. The SEM is linked to a Noran Voyager© image analysis system that provides digital processing of the BSE images.

Backscattered electron detection produces images composed of grey-level intensities that are proportional to the average atomic number of the analyzed portion of the sample. Epoxy has a lower average atomic number than Tensleep Sandstone rock-forming minerals thus providing sufficiently strong grey-level contrasts to easily distinguish pore from rock (Fig. 2.42a).

A binary image of the original grey-level image is created in order to quantitatively isolate the porosity from the rock-forming minerals (i.e., grains and cements). This is completed through a process termed segmentation, in

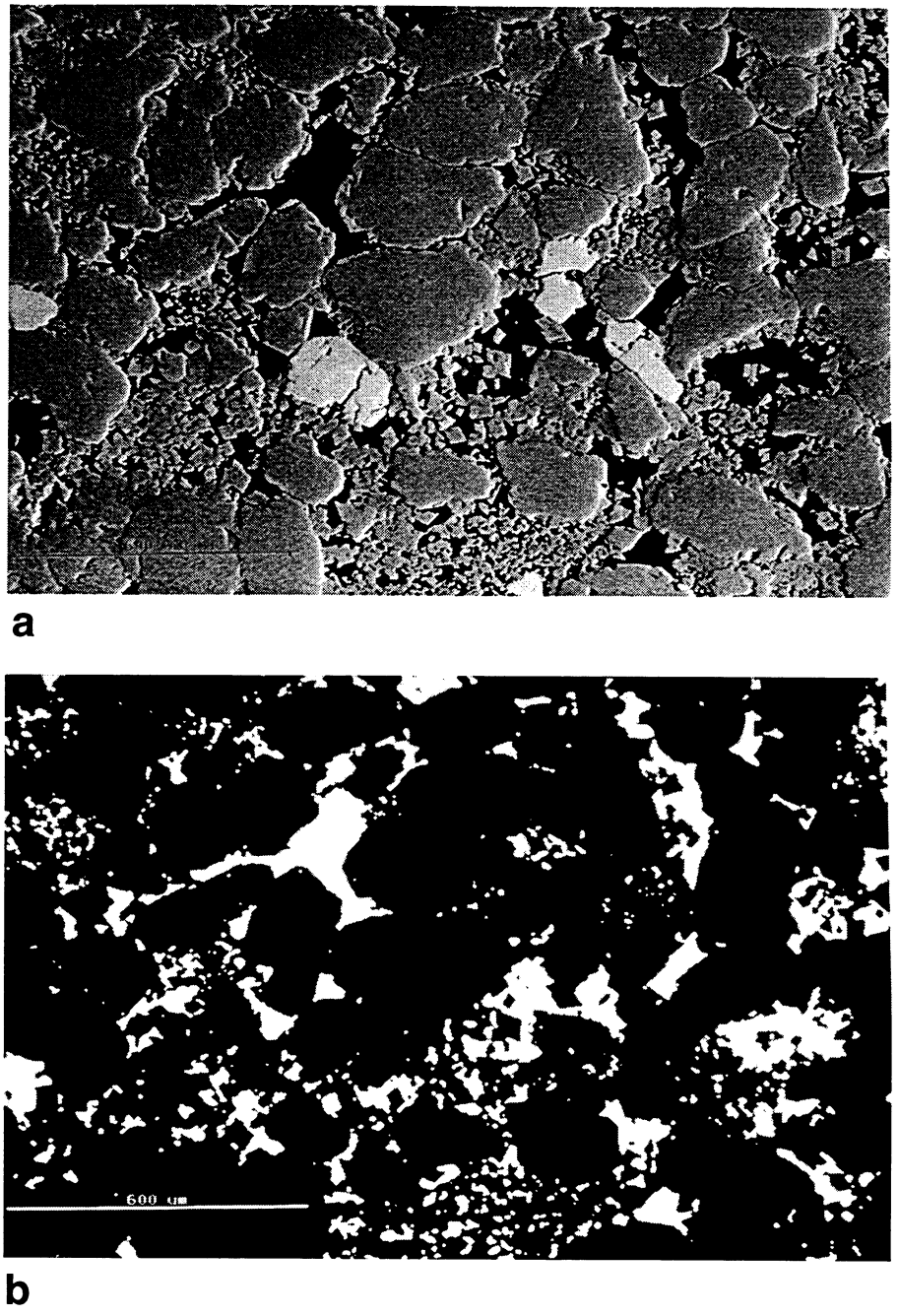

Figure 2.42. Backscattered electron image (BSE) (a) of an analyzed image and the resultant binary image (b) showing the differentiated pore structure. In the BSE image, porosity is black and minerals are varying shades of grey. In the binary image, minerals are black and the porosity is white.

which a histogram of the grey-levels of the image is first created (Fig. 2.43). The grey levels are then partitioned into black and white. The selection is performed manually by using a mouse-controlled sliding grey-level selector. This operation

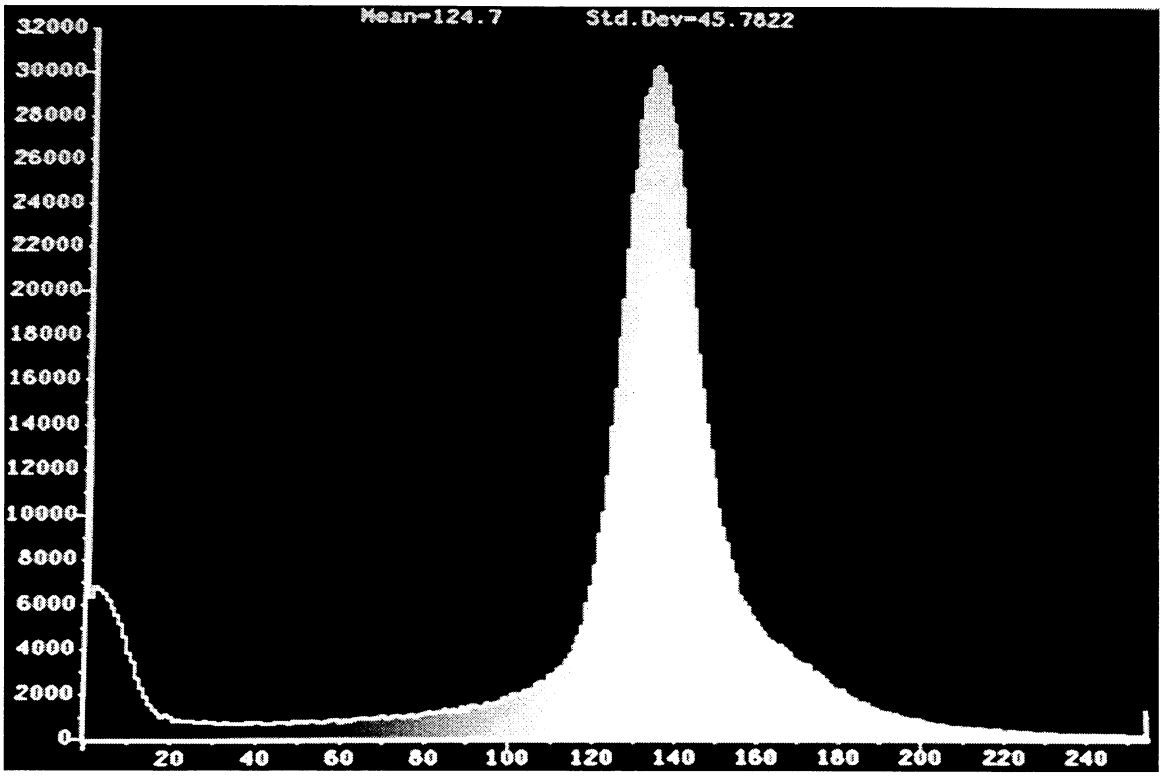

Figure 2.43. Grey level histogram of a typical BSE image used to differentiate porosity from rock matrix.

is one of the most crucial in the image processing sequence, since it defines the pore geometry. Habesch (1990) recommends that the creation of the binary be done manually so that fluctuations in beam intensity, which lead to changes in grey-levels between images, can be recognized and filtered out. The resultant image is a binary of the original image in which porosity is given a value of 255 (white) and the rock matrix is assigned a value of 0 (black) (Fig. 2.42b). The binary image is then processed for pore parameters.

In this study, the binary image was processed using a program modeled after the erosion/dilation algorithms described by Ehrlich et al. (1984) and designed to automatically perform successive and increasing "erosions" and "dilations". Duda and Hart (1973) describe erosion as an operation that strips the outermost layer of pixels from a pore. Conversely, dilation is a process that

adds a layer of pixels to the pore. Erosion followed by dilation does not necessarily restore the object to its original shape (Duda and Hart, 1973). Erosion followed by dilation is called "opening", referring to the ability of this combination of operations to open up spaces or shrink objects radially around a central point (Russ, 1995). The kernel used in most opening algorithms approximates a square and when performed on an image for n iterations, will cause features to shrink by $2n$ pixels. This causes features whose smallest dimensions are less than $2n$ pixels to disappear altogether. Each incremental increase in the degree of opening produces an areal measurement (pixels lost) that represents that fraction of the image porosity that has a dimension equal to the depth of opening. Increasing the number of iterations from zero until all the porosity is removed gives an estimate of the amount of porosity that resides in features of specified sizes (Ehrlich et al., 1984). This is accomplished by keeping track of the number of pixels that have a value of 255 or that remain "on" after each iteration. From those data the porosity at each iteration is calculated and a pore size distribution compiled. Small pore sizes are lost during the initial iterations while the largest pore sizes are lost during the last iterations (Fig. 2.44). Ultimately, the algorithm provides a step-wise breakdown of the pore size distribution of an image. Crabtree et al. (1984) provide a detailed discussion of this method of describing the pore geometry of an image. The distribution of porosity from sequential and increasing erosion/dilation cycles can be directly related to measured relative permeability of the rock through the use of the Kozeny-Carmen equation which is discussed in the next section.

The opening algorithm used in the present study differs slightly from the above described opening algorithm. The reason for this has to do with the fact that in this study we are dealing with a two-phase fluid system rather than a onephase fluid system. In a water-wet two phase system, oil occupies the central portion of the pore and is completely surrounded by water. In cross-section, the distribution of the oil in a pore is approximated by a circle. Therefore, in order to simulate the distribution of the fluids in a two-phase system, an opening algorithm that approximated a circle was needed. This was accomplished by designing a kernel that erodes each individual pore to produce an octagon

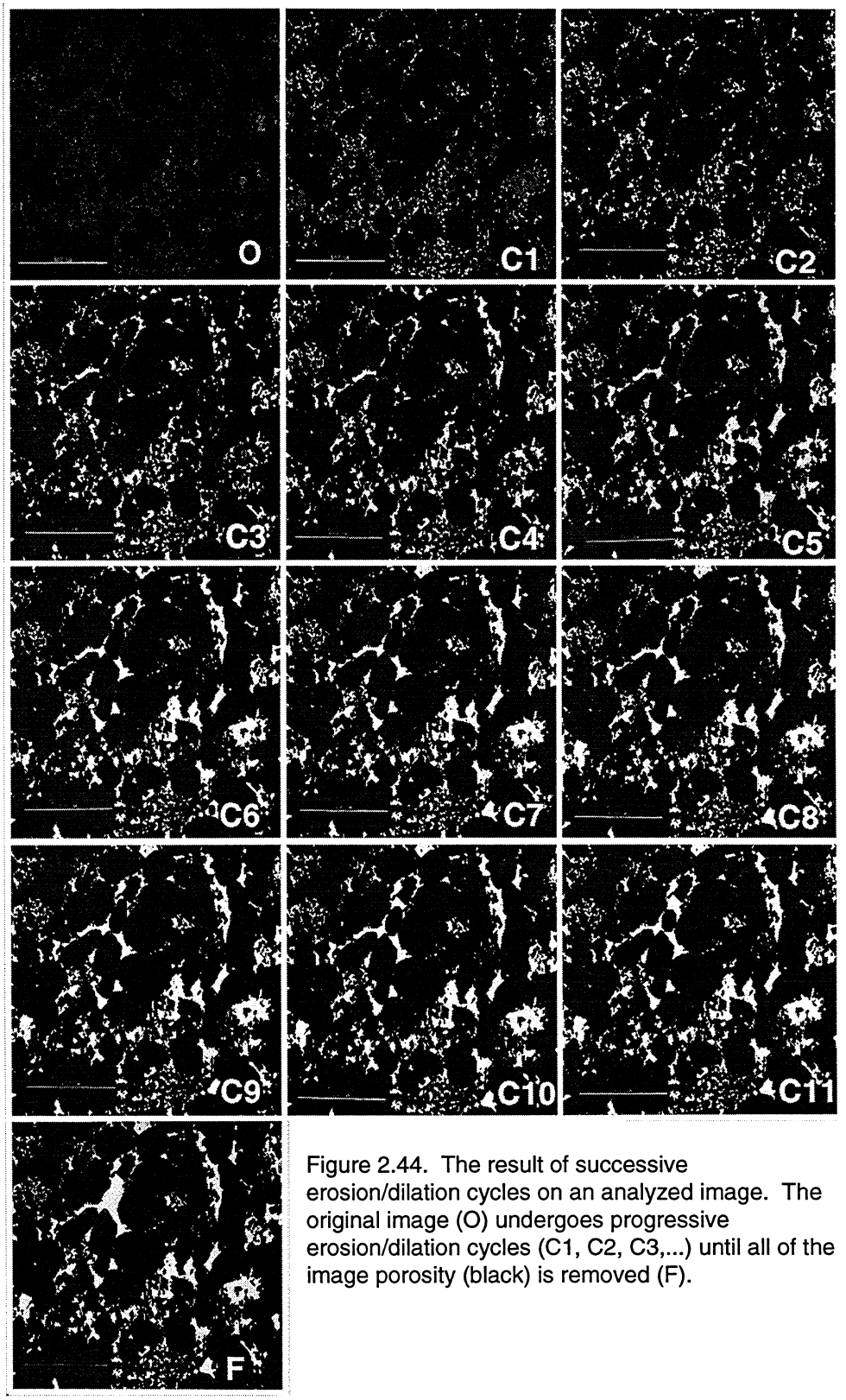

Figure 2.44. The result of successive erosion/dilation cycles on an analyzed image. The original image (O) undergoes progressive erosion/dilation cycles (C1, C2, C3,...) until all of the image porosity (black) is removed (F).

instead of a square. This opening algorithm causes the analyzed features to shrink by $4n$ pixels which means that features whose smallest dimensions are less that $4n$ pixels in width disappear compared to $2n$ pixels in width for the square kernel.

Defining the Pore Image Analysis Algorithms

The equations below are based in part on the Kozeny-Carmen equation (1937) and on generalized formulas for the shape of relative permeability curves. They generate replications of the relative permeability curves derived from measurements of pore geometry in thin sections.

Wyllie and Gardner (1958), in their paper on the use of the Kozeny-Carmen equation to estimate relative permeability, state that when water and oil flow together in a porous medium, each follows a distinct and separate flow path. They also state that the smaller pores initially contain, and are only open to, flow from the water phase, while the larger pores transmit the oil phase. As the water saturation increases, the water phase occupies larger and larger pore sizes and the relative permeability of the water phase increases. Figure 2.45 is a schematic drawing illustrating the effect that increasing water saturation has on reducing the flow paths open to the transmission of oil.

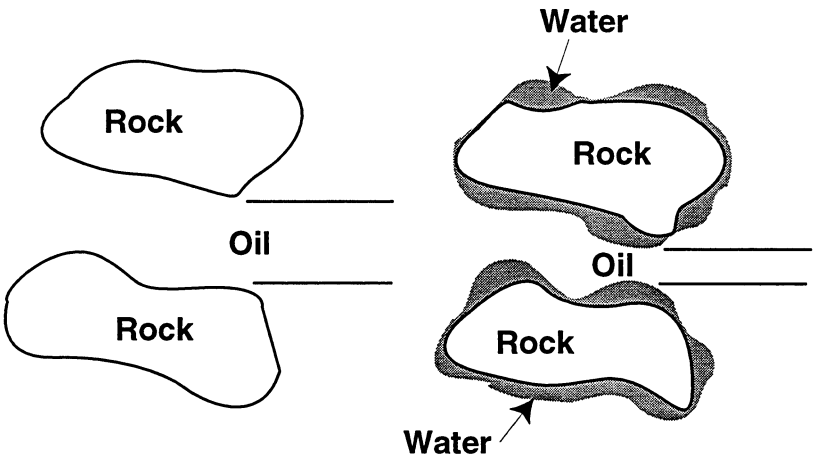

Figure 2.45. Oil flow reduction due to the presence of water (grey areas).

Work by Leverett (1939) and Morgan and Gordan (1970) has indicated that the pore-size distribution directly affects the relative permeability curve of a sample. Leverett (1939) qualitatively tied relative permeability curves to poresize distribution, while Morgan and Gordan (1970) noted how changes in pore-size distribution affect the shape and the location of the curves. Specifically, they noted that rocks with dominantly small pore sizes have higher initial water saturation (Swi) and a limited range of water saturation, while rocks of dominantly large pore sizes have lower initial water saturation and a larger range.

The observations by Leverett (1939) and Morgan and Gordan (1970) can be applied to directional variations in relative permeability as addressed by Corey and Rathjens (1956). These authors investigated how the directional orientation of core plugs with respect to stratification affect relative permeability. They found that at the same water saturation, flow parallel to stratification is greater than flow perpendicular to stratification. While Corey and Rathjens only performed their experiments on one set of core plugs, their study indicates that pore size distribution in the vertical direction is different from pore size distribution parallel to stratification.

The erosion/dilation algorithm provides a technique that can measure these differences in pore size distributions. The algorithm furnishes the operator with a porosity distribution from which permeability may be calculated through the use of the Kozeny-Carmen equation at each step. The Kozeny-Carmen equation ties permeability to the porosity, tortuosity, and specific surface area of a sample. It has long been used in estimating the absolute permeability of samples for which these variables are known. aMore recently it has been applied to pore image analysis techniques to estimate the absolute permeability of samples in which these variables are measured from images. The Kozeny-Carmen equation states:

$$K = \emptyset^3/[Ko(Le/L)^2(1 - \emptyset)^2 * Ss^2], \qquad (2.5)$$

where K is permeability, Ø is porosity of the sample, (Le/L) is tortuosity of the sample, Ss is specific surface area, and Ko is the Kozeny constant. Generally, it

is assumed that $Ko(Le/L)^2 = 5$ (Ruzyla 1986), and the expression may be rewritten:

$$K = Ø^3/[5(1 - Ø)^2 * Ss^2]. \quad (2.6)$$

This equation for absolute permeability is now directly linked to variables that are definable using PIA techniques as has been done by Mowers and Budd (1996), Habesch (1990), and Ruzyla (1986). It is this equation that is the basis for the relative permeability expression.

Relative permeability is the ratio of effective permeability at a specified saturation divided by the effective permeability at 100% saturation. From this we can derive a generalized formula for relative permeability that states:

$$K_{ro} = K_E/K_{B,} \quad (2.7)$$

where K_{ro} is relative permeability of oil, K_E is effective permeability, and K_B is base permeability. From this we can then derive simple equations for both the base permeability and the effective permeability based on the Kozeny-Carmen relationship expressed in Equation 2.6. These equations are

$$K_B = Ø_B^3/[5(1 - Ø)^2 * Ss_B^2], \quad (2.8)$$

and

$$K_E = Ø_E^3/[5(1 - Ø)^2 * Ss_B^2]. \quad (2.9)$$

where $Ø_B$ is the porosity of the initial image, $Ø_E$ is the porosity after each iteration, Ss_B is the specific surface area of the initial image, and Ss_E is the specific surface area after each iteration. A simple expression for relative permeability can then be derived for each individual output from the erosion/ dilation algorithm by dividing the calculated permeability after each iteration of the opening algorithm (Eqn. 2.9) by the calculated permeability of the initial image (Eqn. 2.8). Reducing the equation gives the expression

$$Kro = [Ø_E^3(1 - Ø_B)^2 * Ss_B^2]/[Ø_B^3(1 - Ø_E)^2 * Ss_E^2], \quad (2.10)$$

This is the basic formula from which relative permeability can be calculated from PIA-determined variables which includes the specific surface area as well as the porosity.

The specific surface area of a randomly shaped feature is proportional to the length of a trace around the perimeter of that feature in two dimensions (Weibel, 1979). Perimeter length can be measured by PIA techniques by creating an outline of the image remaining after each iteration, counting the number of pixels that comprised the outline, and multiplying that number by the width of an individual pixel. The specific surface of a rock's pore space is then defined by Equation 2.11:

$$S_s = 4/\prod * P/A_p \tag{2.11}$$

where S_s specific surface, P is the perimeter around the pores, and A_p is the area of the pore.

It was found in this study that the ratio Ss_B/Ss_E was nearly always unity and could therefore be divided out of Eqn 2.10. This leaves the expression

$$Kro = \emptyset_E{}^3(1 - \emptyset_B)^2/\emptyset_B{}^3(1 - \emptyset_E)^2. \tag{2.12}$$

This is the equation used in this study for estimating relative permeability to oil from pore size distribution data derived from thin sections.

In order to create relative permeability curves, water saturation must also be determined. The water saturation data is also calculated from PIA-defined parameters. In relative permeability tests, the water saturation is defined as the amount of water contained in the core divided by the total amount of fluids contained in the system. If a base permeability is chosen at which the initial water saturation is zero, the water saturation could simply be calculated by the expression

$$Sw = 1 - \emptyset_E/\emptyset_B, \tag{2.13}$$

where Sw is water saturation, $\emptyset_B$ is the initial porosity fraction, and $\emptyset_E$ is the porosity fraction after each iteration. While this works when the base permeability used is the oil permeability at zero water saturation, the base

permeability used in this study was the permeability to oil at the initial water saturation which typically was not zero. Therefore, Equation 2.12 can only be used when the system being modeled starts at a water saturation of zero. We modified Equation 2.13 to account for there being some amount of water in the core at the beginning of each test. This equation provides initial water saturations within the range observed in the actual tests. The modified equation is

$$Sw = 1 - \emptyset_E/1.4\ \emptyset_B. \tag{2.14}$$

This is the equation used to estimate water saturation from the thin section PIA data. It best approximated the initial water saturation of the relative permeability tests from the image analysis porosity. Using the values calculated from this expression, an equation can be derived for the relative permeability of water.

The relative permeability of water was determined from an empirical equation that is based on the work of Honarpour et al. (1986). In their chapter on two-phase relative permeability, the authors state that the shape of the water relative permeability curves may be approximated by the general expression

$$Krw = A(Sw)^n, \tag{2.15}$$

where A and n are constants and Sw is the water saturation. We modified this equation to best fit our actual data. The equation used for the relative permeability of water for this study is

$$Krw = (.45Sw)^2. \tag{2.16}$$

Both the equation used for the calculation of the water saturation and the equation for the relative permeability of water are empirical equations derived to best fit our observed data.

Construction of Relative Permeability Curves

Using the expressions above, the relative permeability and corresponding water saturation was calculated using PIA-defined and acquired data. This

procedure was performed on 76 samples from the Tensleep Formation using the PIA technique described above. All the samples were of eolian facies; some were iron stained, and most contained carbonate cement. Thirty of the 76 thin sections had relative permeability measurements made on the core plugs. These were used to test the relative permeability algorithms. For these measured samples, porosity ranged from 9.1 to 28.9%, air permeability ranged from .064 to 962 md, and oil permeability from .023 to 495 md. Eight randomly selected views were digitized from each of 76 thin sections at a magnification of 100X. This provided pixel resolution to a scale of 2.0 microns. The images were analyzed using the aforementioned erosion/dilation algorithm. The resultant pore-size distribution data were compiled and entered into the relative permeability algorithms. An example of the data collected and calculated is given in Table 2.5 for the Wertz 6727V sample.

Table 2.5. Sample table of the measured data (pixels) used to calculate porosity, water saturation, and oil and water relative permeability. Data are from the Wertz 6727V sample.

Iterations	Total pixels	Porosity	Water saturation	Oil permeability	Water permeability
0	215458	0.206	0.286	1.0000	0.000
1	189353	0.181	0.372	0.638	0.003
2	156973	0.150	0.480	0.338	0.015
3	125608	0.120	0.584	0.161	0.035
4	95759	0.091	0.683	0.067	0.063
5	69509	0.066	0.770	0.024	0.093
6	48260	0.046	0.840	0.008	0.122
7	32778	0.031	0.891	0.002	0.146
8	20794	0.020	0.931	0.001	0.165
9	12981	0.012	0.957	0.000	0.179
10	7191	0.007	0.976	0.000	0.189
11	3038	0.003	0.989	0.000	0.197
12	1075	0.001	0.996	0.000	0.201
13	0	0.000	1.000	0.000	0.203

Results

Graphs of the predicted relative permeability values from Table 2.5 plotted with the measured values illustrate that the predicted values closely match the measured values. Five other examples of measured vs. calculated plots are also shown on Figure 2.46.

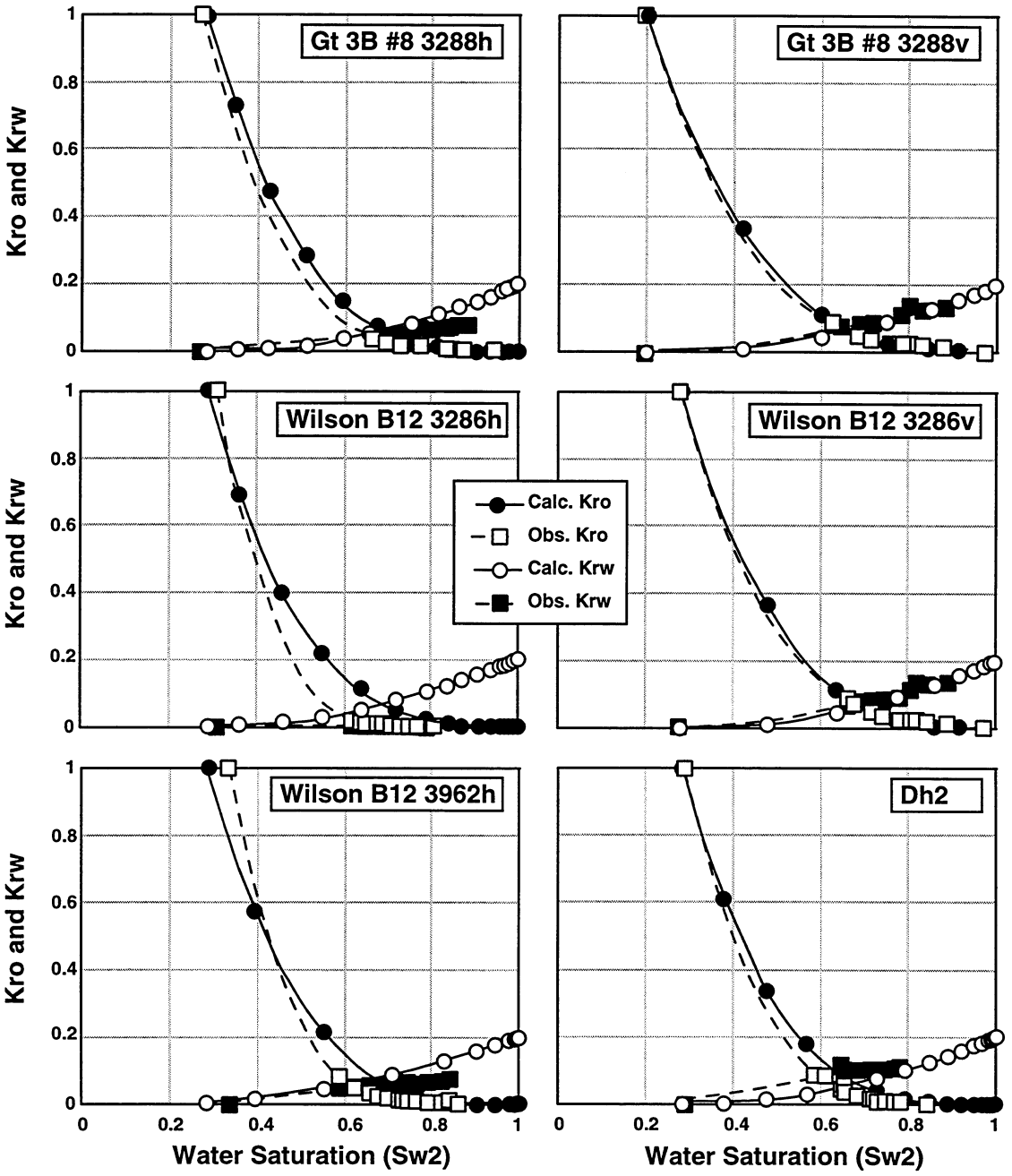

Figure 2.46 Predicted (calculated) and observed relative permeabilities vs. water saturation (Sw2) for both oil (Kro) and water (Krw). Sample numbers are in the upper-right corner of each plot.

Relative permeability anisotropy predicted from image analysis techniques were less than the observed relative permeability anisotropy (Fig. 2.47). This may be the result of slight imperfections in the orientation or

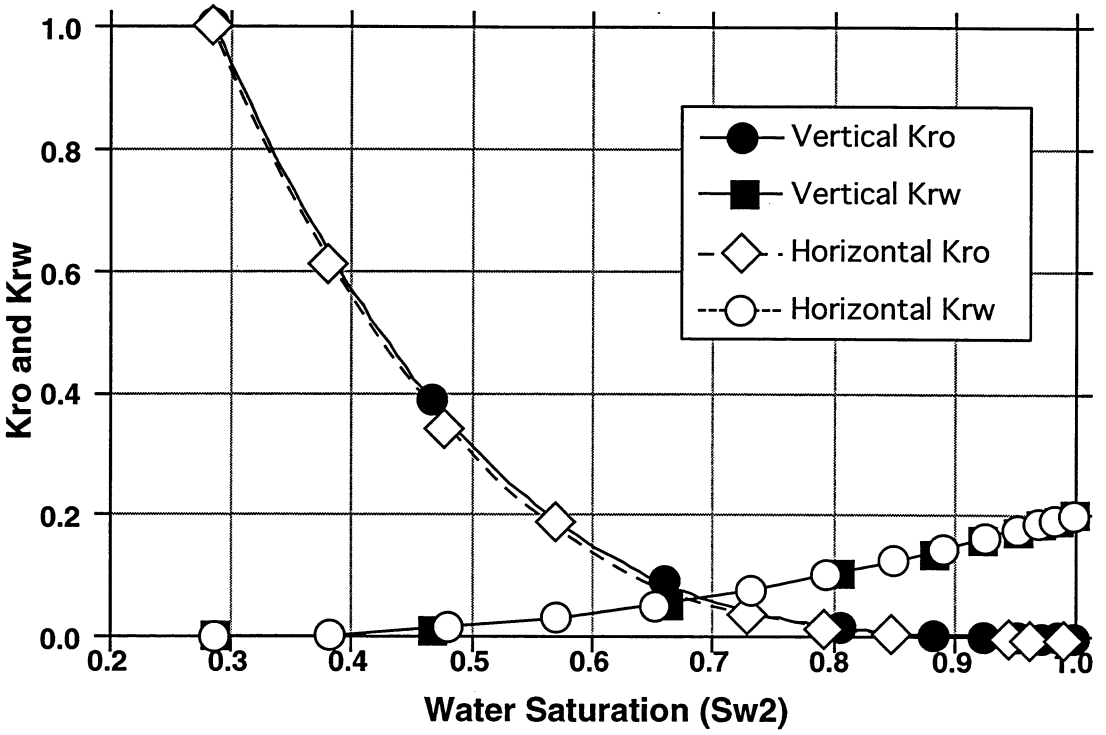

Figure 2.47 Horizontal and vertical calculated relative permeability curves vs. water saturation for both oil (Kro) and water (Krw). Note the small offset between the vertical and the hroizontal oil relative permeability curves.

positioning of the thin section with respect to stratification causing similar pore structures to be analyzed between a sample pair. More likely the lack of separation of the relative permeability curves between an orthogonal set of samples reflects the sensitivity of the image analysis algorithms. In samples in which the analyzed pore structures did not differ greatly from one sample to the next, the estimated relative permeability curves were very close together and did not show the separation in relative permeability that was seen in the measured relative permeability data. Samples in which the pore structure differed widely from one sample to another showed a separation between the different orientations of the samples in the set.

The sensitivity of the image analysis algorithms may be improved by increasing the magnification used to analyze the samples, increasing the number of images collected and analyzed, or even changing/redesigning the erosion/

dilation kernel. The developed algorithms provide generalized relative permeability data that responds to major changes in the pore structure of the analyzed sample. These algorithms provide a method whereby much larger sample sets can be evaluated for relative permeability and a more detailed characterization and understanding of relative permeability heterogeneities across a reservoir can be achieved

Discussion

With recent advances in image analysis, it has become possible to quickly and cheaply measure and quantify the pore structure variables that control the petrophysical properties of rocks. The opening method of estimating pore size distribution without actually measuring individual features is useful when many features in the image have to be measured, and the technique has been applied to studies measuring mineral particle sizes, pore distributions, and sediment distributions. Because these measurements are objective and consistently reproducible, these techniques can be used to quantify the long-recognized relationships that exist between a rock's texture or mineralogy and its petrophysical properties. Although prediction of relative permeability anisotropy from thin section measurements still needs some refinement, success in relating relative permeability curves to thin-section measurements indicates that threedimensional information may be obtained from two-dimensional measurements.

From the pore structure of the samples used in this study, water saturation, oil relative permeability, and water relative permeability values were predicted and observed to closely follow measured values. The close fit of predicted and measured relative permeability data implies that there is a strong relationship between porosity as observed in thin section and relative permeability variables. It is not surprising that such a strong relationship between porosity and relative permeability exists. Recent work by Mowers (1996), Ehrlich et al. (1991a & b), Habesch (1990), McCreesh (1987), and Ruzyla (1986) has indicated a strong relationship between petrophysical properties and the pore networks. By increasing the sensitivity of this method, the techniques

developed in this study may be better applied to directional relative permeability variations. More importantly, although the algorithms used were derived for the Tensleep Formation, the methodology of the present study can be directly applied to other formations; employable algorithms may be developed and implemented relatively quickly. This development relating PIA variables to relative permeability will prove useful in understanding in detail how a reservoir will respond to waterflooding, which will lead to improved development strategies once an understanding of how the sedimentologic features respond to waterflooding is placed into a geologic framework.

Putting the results of the relative permeability measurements into a geologic framework outlined by the work completed in Task One, an understanding of two phase fluid flow in Tensleep eolian units has been developed. Figure 2.48 and 2.49 illustrates how the anisotropy and heterogeneity seen during the relative permeability measurements in Task Two fit into the complex interfingering of sedimentologic features outlined in Task One. Figure 2.49 shows that fluid migration across bounding surfaces during two phase flow (especially first- and second-order surfaces) will be greatly hampered by the nature of the surface. The results from Task Two show that relative permeability is anisotropic in eolian wind-ripple deposits. Fluids are observed to flow more easily along stratification in these deposits. Interfingering of grainflow and wind-ripple deposits also leads to an anisotropic deposit of sediments with respect to relative permeability. Deposits of strictly grainflow laminae, on the other hand, appear to be quite isotropic during two phase flow.

By entering these relative permeability results into an overall framework a better understanding of reservoir behavior during waterflooding was constructed. It is observed that the eolian bounding surfaces break up the reservoir into a series of fluid flow compartments with good fluid flow potential corresponding to the eolian stratification within the compartment and poor potential of fluid flow corresponding to the bounding surfaces. In order to increase recovery efficiency of oil in these compartments, as many compartments

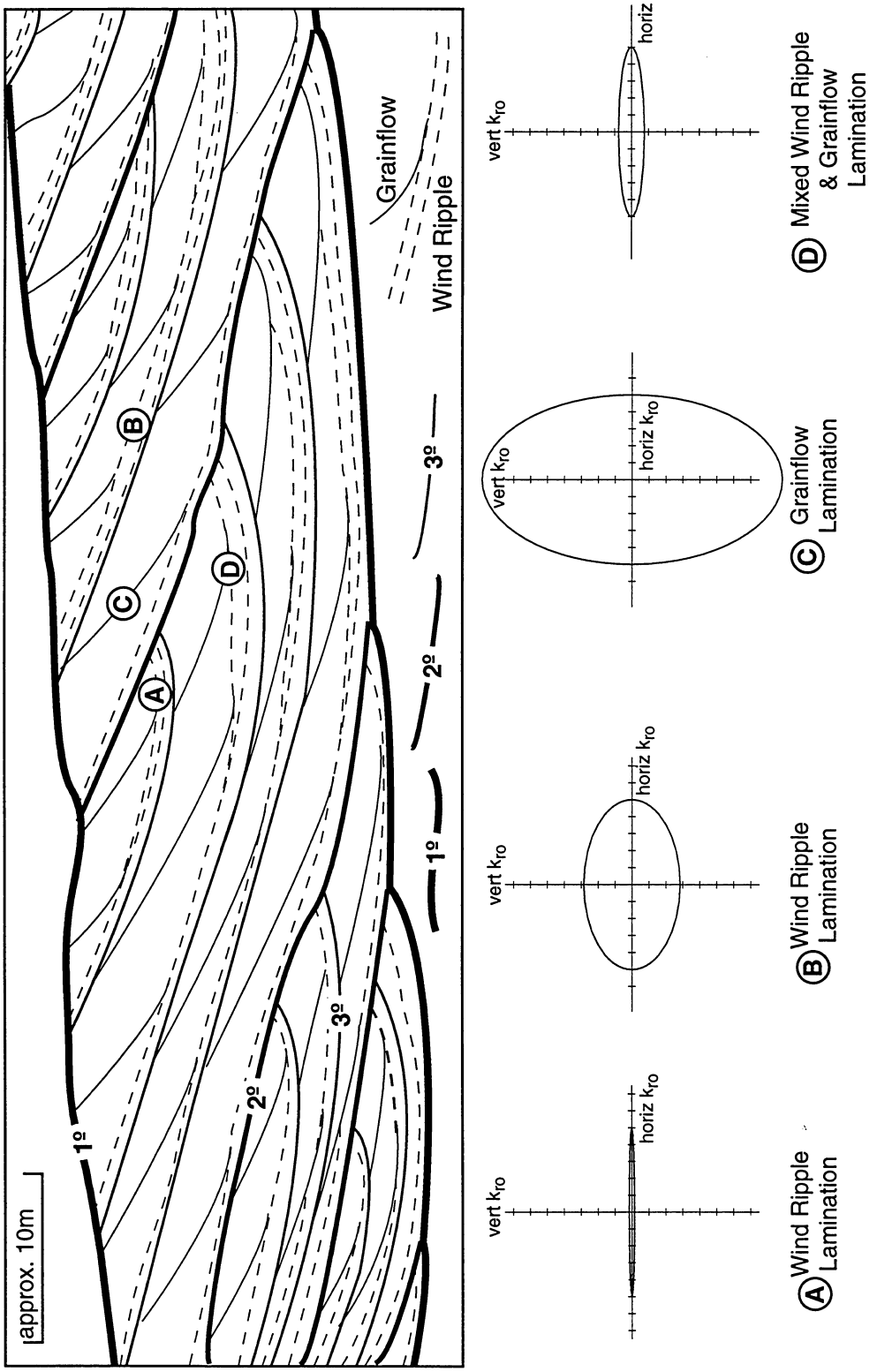

Figure 2.48. Oil relative permeability anisotropy associated with different types of eolian lamination found in the Tensleep. Locations of samples on the schematic drawing of a typical Tensleep outcrop are schematic with respect to types of lamination. Each sample represents a pair of samples - one taken parallel to the lamination and one taken perpendicular to it. The ellipses represent the horizontal and vertical oil relative permeability at each point. A=sample HR75, B=sample NNB3, C= sample MB65, D=sample MB60.

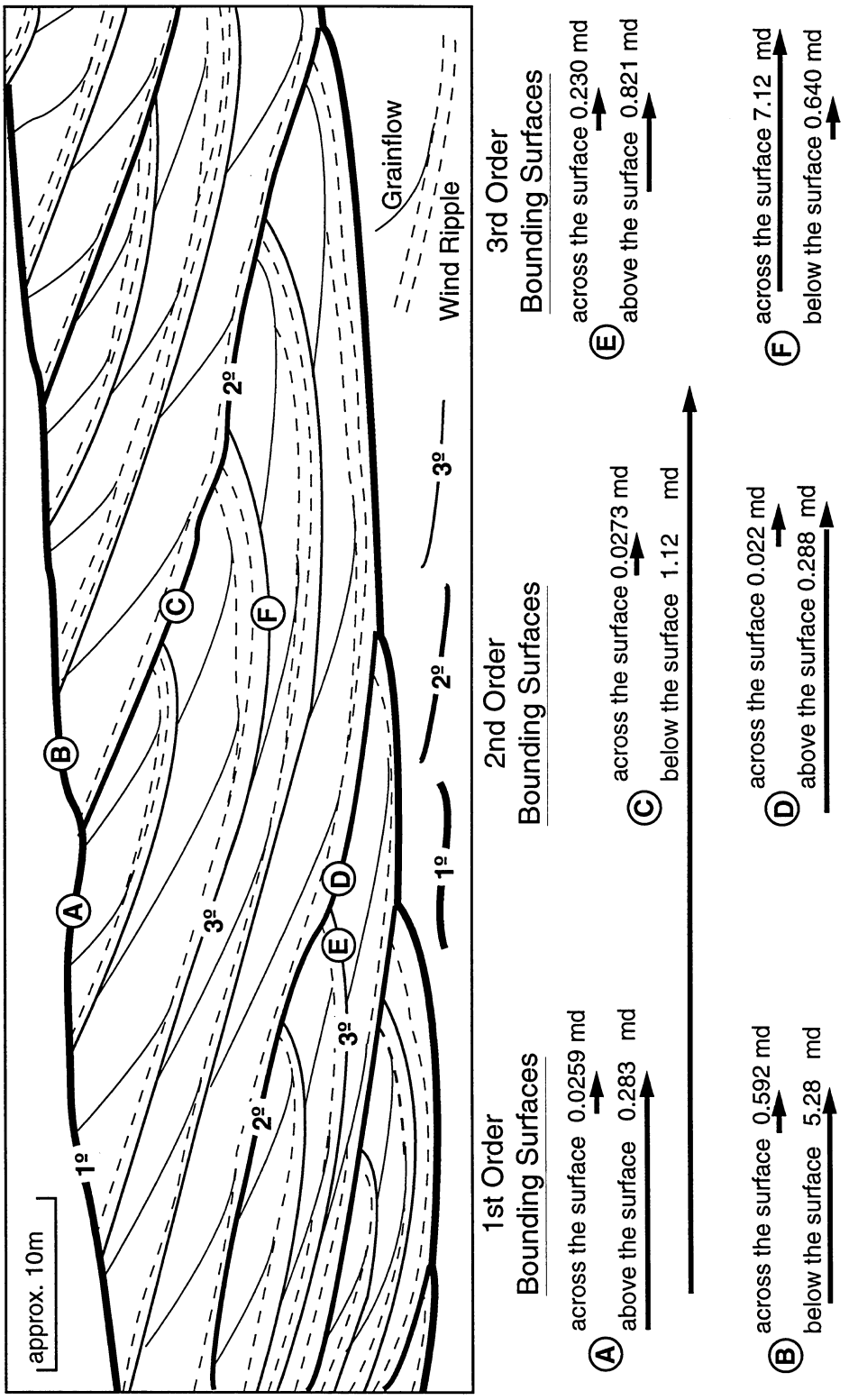

Figure 2.49. Oil relative permeability heterogeneity associated with 1st, 2nd, and 3rd order bounding surfaces. Locations of samples on this schematic drawing of a typical Tensleep outcrop are schematic with respect to types of bounding surfaces. Each sample represents a pair of samples - one taken across the bounding surface and one taken immediately above or below the bounding surface. The length of the arrows are proportional to the differences in the oil relative permeability between the sample pair. A=sample HR75, B=sample NNB3, C=sample MB65, D=sample MB60, E=sample MB20, and F=sample 3B8A.

as possible must be intersected by the wellbore. By drilling into these compartments, production from the zones of good flow potential can be better utilized and a greater percentage of the original oil in place can be recovered.

Oriented drilling can also takes advantage of the anisotropic deposits of wind-ripple laminae and aid in oil production. As previously stated, wind-ripple laminae have a preferential flow direction along stratification. It has also been observed that wind-ripple laminae trend sub-parallel to the second- and third-order bounding surfaces in the Tensleep. By drilling perpendicular to the second- and third-order surfaces of the Tensleep more fluid flow compartments can be perforated and the preferred fluid flow direction of the anisotropic wind-ripple strata can be exploited (Fig. 2.48). These recommendations, based on the observed relative permeability variations, may lead to increased recovery efficiencies in the Tensleep eolian units and have application to other eolian reservoirs.

STATISTICAL ANALYSIS OF PERMEABILITY HETEROGENEITY

Introduction

This study uses semi-variogram analysis to examine permeability heterogeneity in vertical profile in the upper Tensleep. Typically geostatistical studies involve interwell correlations such as the studies by Wolcott and Chopra (1993), Dimitrakopoulos-Roussos (1989), and Tang et al., (1991). This is the first geostatistical study of the Tensleep sandstone in the Bighorn and Wind River Basins and one of only a few using downhole core features for study (Grant et al., 1994 and Prosser, 1993). Both large- and small-scale permeability variations are controlled by processes taking place during accumulation and preservation. Regional thickness variations in the upper Tensleep, on the other hand, are controlled by variations in local subsidence and relative sea-level rise. These were described in Task One. These regional differences are confirmed by the spatial patterns revealed by the variograms. Because the variograms exhibit systematic trends which are related to known characteristics of the Tensleep, the variogram analysis is a valuable tool for predicting reservoir heterogeneity in the upper Tensleep.

Description of Variogram Analyses

The software used for this statistical study is GEO-EAS 1.2.1 issued by the United States Environmental Protection Agency, April 1991.

The semi-variogram, or variogram, is a scattergram of increasing distance between pairs of data points (x-axis) versus the semi-variance between the two data points (y-axis). Semi-variance is half the variance of a pair of points calculated from Equation 2.17,

$$\gamma(\mathbf{h}) = \frac{1}{2N(\mathbf{h})} \sum_{(i,j)\mathbf{h}_{ij}} (v_i - v_j)^2, \tag{2.17}$$

where **h** is the distance between pairs of points, N is the number of pairs that are **h** distance apart, and v_i and v_j are the data values of points i and j.

To construct the semi-variograms in this study, the semi-variance of all pairs of points occurring 0.3m (one foot) apart is calculated first. Next, the semivariance of all pairs of points occurring 0.6m (2ft) apart is calculated, and so on until the only pair left are the two farthest points apart. These distances between pairs of points is referred to as the lag distance (Fig. 2.50). The idea behind the variogram is that for spatially correlated data, the semi-variance value of two points close together in space should be more similar than the value of two points separated by a great distance. In theory, pairs of points closest together should have zero variance. However, when a curve is fit to the dataset, the yintercept of the curve rarely occurs at zero. This is an indication of small scale inaccuracies and is termed the nugget effect (Fig. 2.50).

The range of influence, or range, is the lag distance where there is no more spatial correlation. The sill is the semi-variance at that range. The range is an important feature in this study of permeability variation. At distances beyond the range, the variogram either flattens out, indicating that there is no more spatial relationship, or shows a correlation event of low variance, indicating that permeability values become similar again after a certain distance.

Correlation events in a variogram are not often discussed in geostatistical studies but have proven to be as important as the range in the Tensleep. The

main difference between the range and a correlation event is simply that in a dataset where a correlation event exists, the permeability values tend to be in discrete groups that are relatively evenly spaced. If the variogram produces a range and no correlation event, permeability values never return, with increasing distance, to a level of similarity. Either the permeability values cannot be easily divided into discrete groups of high and low values, or if there are discrete groups, they are so unevenly spaced that the variogram indicates that spatial correlation has ceased all together. A quick comparison of variograms that produce ranges and variograms that produce correlation events can be used as a general indicator of the degree to which the data is spatially compartmentalized.

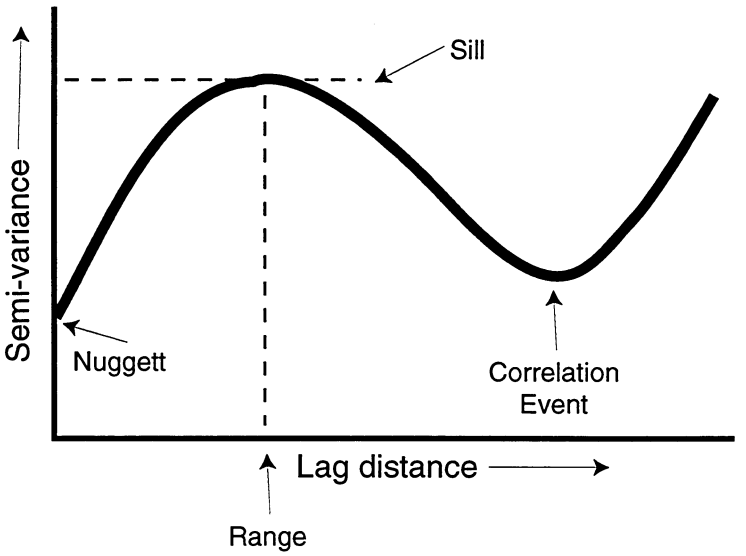

Figure 2.50. Schematic variogram illustratingterminology used.

Synthetic Data Example

To understand the role of stacked marine and eolian facies on the heterogeneity of absolute permeabilities, we constructed a synthetic permeability dataset. The synthetic data, which are similar to but more regular and predictable than the real Tensleep data, demonstrate some of the basic properties of the Tensleep variograms. The synthetic data not only show what type of information is picked up by the variogram, but they also demonstrates the meaning of the "range of influence" in the Tensleep data.

The dataset consisted of three groups of randomly generated numbers. Large numbers were used to represent loosely packed sandstones; moderate numbers represent more tightly packed sands of the bounding surfaces; and low

numbers represent dolomite intervals. A vertical permeability profile of the synthetic data along with the lithology represented is given in Figure 2.51.

The variograms generated from this dataset are shown in Figure 2.52. Notice that in Figure 2.52a, low points in the graph occur at around 11m (35 ft) and at 5.2m (17 ft), indicating low semi-variance and similarity of permeability

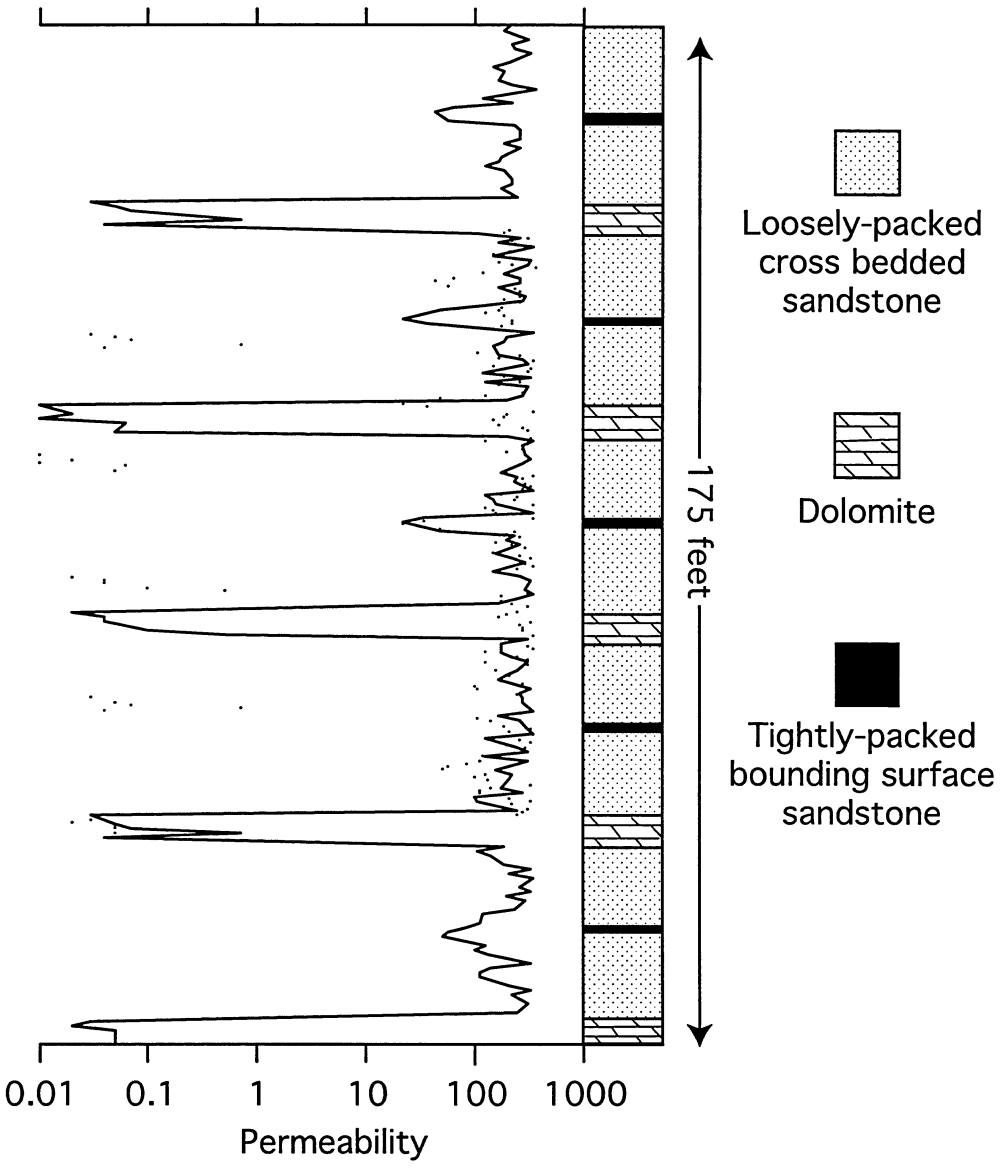

Figure 2.51. Permeability vs. depth plot of the synthetic dataset that was evaulated to aid interpretation of real Tensleep data. Column on the right indicates the type of lithology is represented.

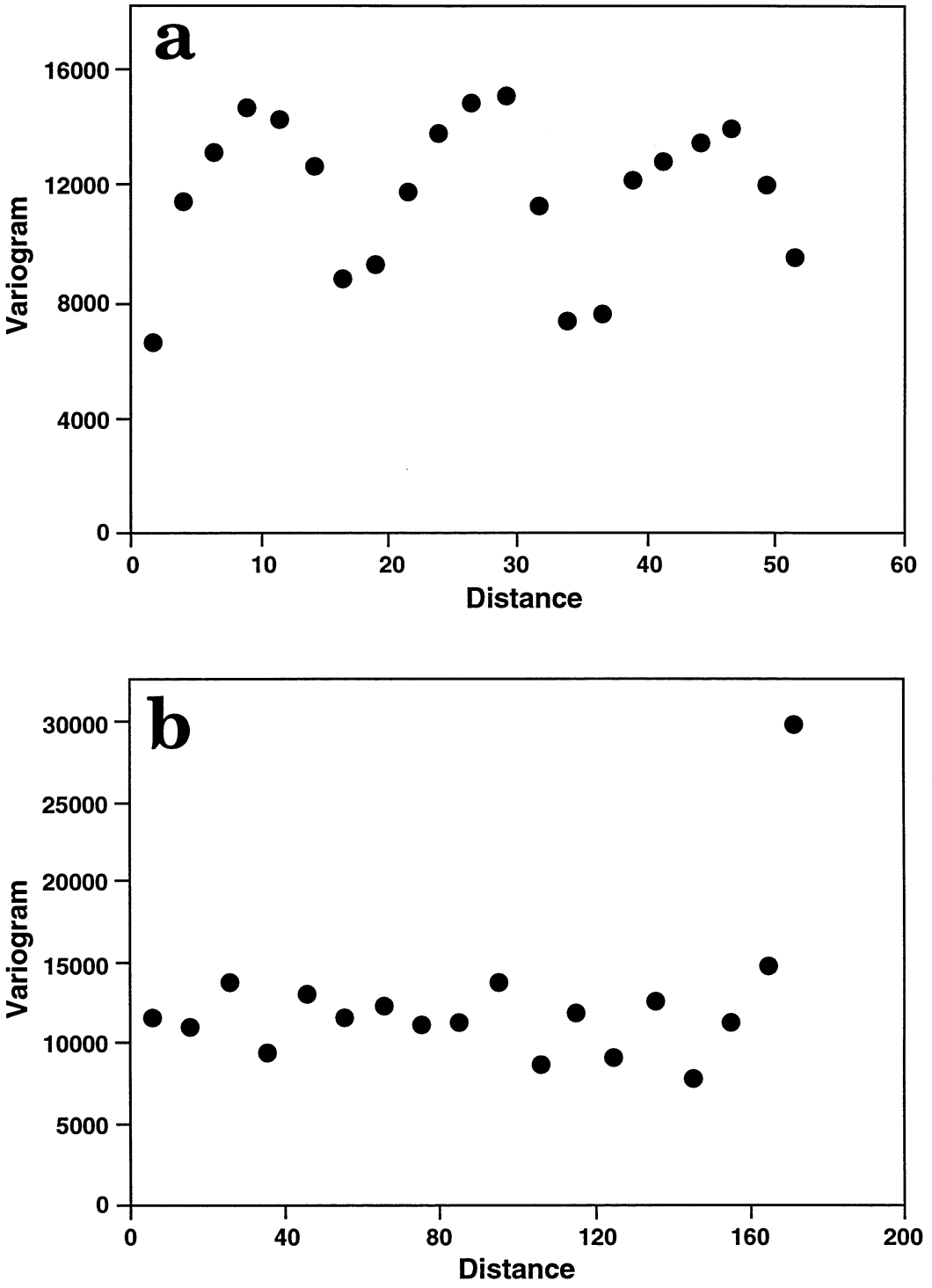

Figure 2.52. Semi-variograms calculated using the synthetic data shown on Figure 2.51. a. Examination of small lag distances shows correlation events at 5.2 and 10.7m (17 and 35 ft.) and ranges at 3 and 8.8m (10 and 29 ft.). b. Examination of large lag distances shows that the larger scale may not be helpful in variogram analysis.

values at those distances between pairs of points. These correlation events show a cyclicity that indicates where permeability values are paired with similar values rather than dissimilar values. Therefore, at both 5.2 and 11m (17 and 35 ft), eolian intervals in the synthetic data are usually paired with other eolian intervals, bounding surface intervals are usually paired with other bounding surface intervals, and marine intervals are usually paired with marine intervals.

At 3.7m (12ft) the variogram produces a small-scale range and at 28m a large-scale range, both represented by high semi-variance. This indicates a point of least similarity between pairs. The significance of these points is that at those distances (3.7 and 8.5m, 12 and 28ft) sandstones are rarely paired with sandstones and marine intervals are rarely paired with marine intervals. At these ranges, a different simulated sedimentation regime begins, whereas at the correlation events, the same simulated sedimentation regime appears again. All of these features are seen in varying degrees in the real Tensleep data.

At very large lag distances the semi-variance rises considerably because the few pairs that are spaced this far apart happen to be very dissimilar (Fig. 2.52b). Issaks and Srivastava (1989) have shown that analyzing beyond a lag distance greater than half the maximum pair distance is not valid because there are so few pairs involved in computing the larger lag distances. It is these large lag distance calculations that are left out of variogram analyses. Figure 2.52b also demonstrates that if the variogram is analyzed at too large a scale, all relevant information is lost.

Another synthetic dataset was generated and variograms made specifically to test the implications of the range of influence that is typically found in variogram data. The dataset consists of groups of 20 points representing 6.1m (20ft) depth intervals; each group of 20 points has a distinct mean and standard deviation. The entire dataset is in successive depths to represent downcore permeability data. In this case no dataset had similar values to other datasets, so no cyclicity was expected.

The range generated by this synthetic semi-variogram was 7m (23ft), indicating that the range of influence can be slightly greater than the thickness of the sets of data (Fig. 2.53). This is because there was some accidental

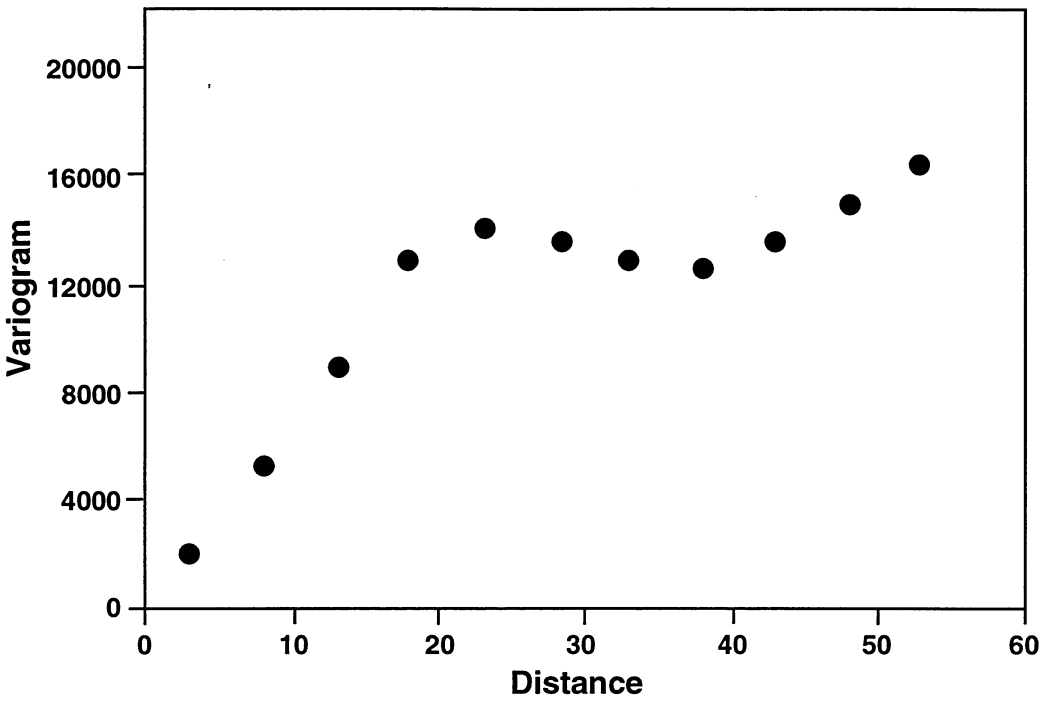

Figure 2.53. Variogram constructed from a second synthetic dataset to test the implications of the range of influence as it relates to Tensleep data. This second synthetic dataset is described in the text. The range of this data set is 7m (23 ft.), and a weak correlation event occurs at 11.6m (38 ft.).

similarity between pairs of data that were separated by more than 6m (20ft). A weak correlation event occurs at 11.6m (38ft), roughly the distance to the next set of data. This is informative in that it shows the possible variability of the range of influence. With Tensleep data, because similar permeability values will never be grouped in exactly evenly spaced packages and because there is not an exact correlation between permeability value and sedimentation type, we can expect the range to give not a precise value representing any one spatial trend, but rather a good indication of the overall trends within the core.

Tensleep Dataset for this Study

This study uses data from six cores in the Bighorn and Wind River Basins (Table 2.6). The data are absolute permeability of horizontal plugs taken from these cores. The plugs are at 0.3m (1.0ft) intervals, and the data are maximum horizontal permeability in millidarcies.

Table 2.6. Tensleep cores used in this semi-variogram study.

Well Name	Core Thickness	Average Permeability	Maximum Permeability
Pitchfork	233	122	680
Gov't Tract	153	98	716
Wertz	380	13	524
Little Buffalo Basin	132	67	329
Neiber Dome	55	2	10
Hamilton Dome	273	135	1466

Two types of variograms were generated for each core dataset. First, a variogram was generated using 1/2 of the maximum pair distance in order to see large-scale spatial relationships. Variograms were also generated using only 3.09.0m (10-30 foot) lag distances to examine small-scale spatial relationships. Each dataset showed distinct spatial relationships at both small and large scales.

The Tensleep permeability data was log normally distributed. Therefore, for the variogram analysis, the log of the permeability value was used so that the data used would be linearly distributed.

Some permeability values were missing from the core analyses. In these instances, the depth values were compressed to make a complete consecutive depth record because it was clear that the variograms were heavily influenced by missing values.

Large-Scale Heterogeneity

The large-scale heterogeneity of the upper Tensleep reflects the thickness of eolian sand packages which are separated by marine dolomite intervals. This heterogeneity is represented in variograms by either a range of influence or by some distance between the range of influence and a correlation event. In general, when a variogram shows a range of influence but no correlation event, there is a good match between the range and the average measured sandstone thickness. When the variogram shows both a range and a correlation event, the average sandstone thickness lies somewhere between the two. Additionally, the correlation event lies at a distance that is slightly larger than the thickness of the thickest sandstone package.

Three of the six studied cores generated variograms that had only ranges (Pitchfork, Gov't. Tract 3B #8, and Wertz 133) and the remaining three generated variograms with both a range and a correlation event (Little Buffalo Basin, Hamilton Dome, and Neiber Dome) (Fig. 2.54). The explanation for these

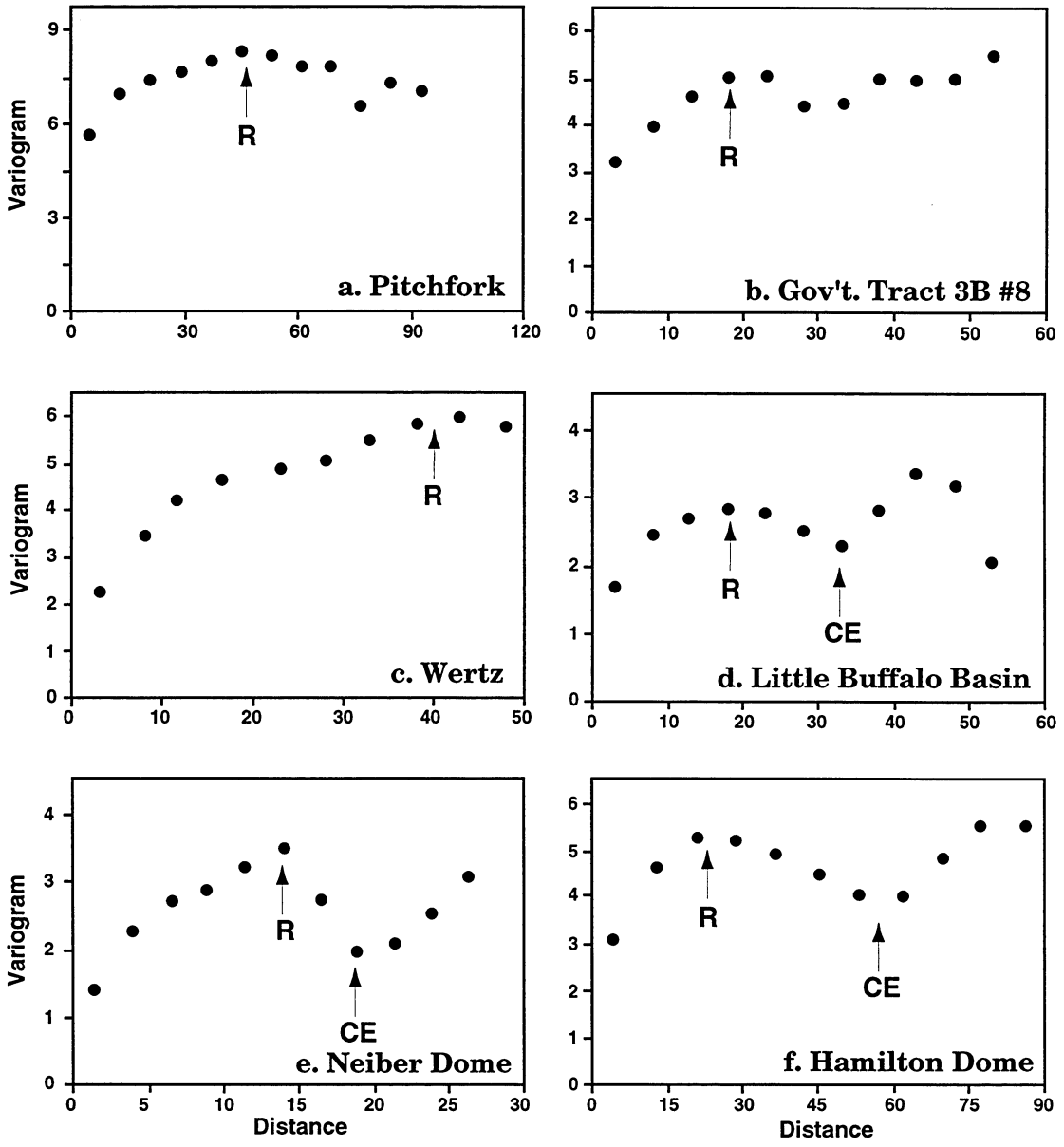

Figure 2.54. Variograms of Tensleep data evaluating large-scale heterogeneity by using large lag distances. Ranges (R) shown on these plots are: (a) Pitchfork 13.7m (45 ft.), (b) Gov't. 3B#8 5.5m (18 ft.), (c) Wertz 12.2m (40 ft.), (d) Little Buffalo Basin 5.5m (18 ft.), (e) Neiber Dome 4.3m (14 ft.), and (f) Hamilton Dome 6.1m (20 ft.). Correlation events (CE) are exhibited only by Little Buffalo Basin (at 9.8m (32 ft.)), Neiber Dome (at 5.8m (19 ft.)), and Hamilton Dome (at 16.8m (55 ft.)).

two types of variograms lies in the fact that datasets that generated correlation events had more evenly spaced sandstone package thickness (Table 2.7). The evenly spaced, closely grouped thickness values are illustrated on Figure 2.55 which is a plot of cumulative frequency of sandstone thickness for each core. Closely grouped values are indicated by steep slopes on Figure 2.55. The core datasets with steep slopes on the cumulative frequency plot are the ones that have correlation events on the semi-variograms.

Table 2.7. Tensleep core large and small scale spatial trends (all numbers in meters).

Well Name	Average Sandstone Thickness	Large-scale Range	Large-scale Correlation Event	Small-scale Range	Small-scale Range with marine units removed
Pitchfork	10.7	13.7		2.4	1.5
Gov't Tract	5.1	5.5		0.9	1.5
Wertz	19.2	12.2		5.2	
Little Buffalo Basin	5.7	5.5	9.8	3.0	3.4
Neiber Dome		4.3	5.8	1.5	
Hamilton Dome	10.1	6.1	16.8	1.8	2.1

For the cores that had only ranges, there is good agreement between the range values and the average sandstone package thickness. For the cores with both ranges and correlation events, the average sandstone package thickness is between the range value and the correlation event, and the correlation event occurs at a distance just beyond the thickest sandstone package. In these cases, the range by itself is not a good indicator of the average sandstone package thickness. However the range, together with the correlation event, gives an indication of the variation in sandstone package thickness and implies that there is compartmentalization.

In addition to its use in evaluating sandstone package thickness, semivariogram analysis has the potential to give an indication of regional and local base level changes. While local subsidence controls accommodation space available for accumulation of eolian sediments, a relative sea-level rise would place the eolian system below a local base-level of erosion, resulting in its preservation. A depositional model was developed for the Tensleep which takes into account both accumulation and preservation dynamics (see Task 1). This

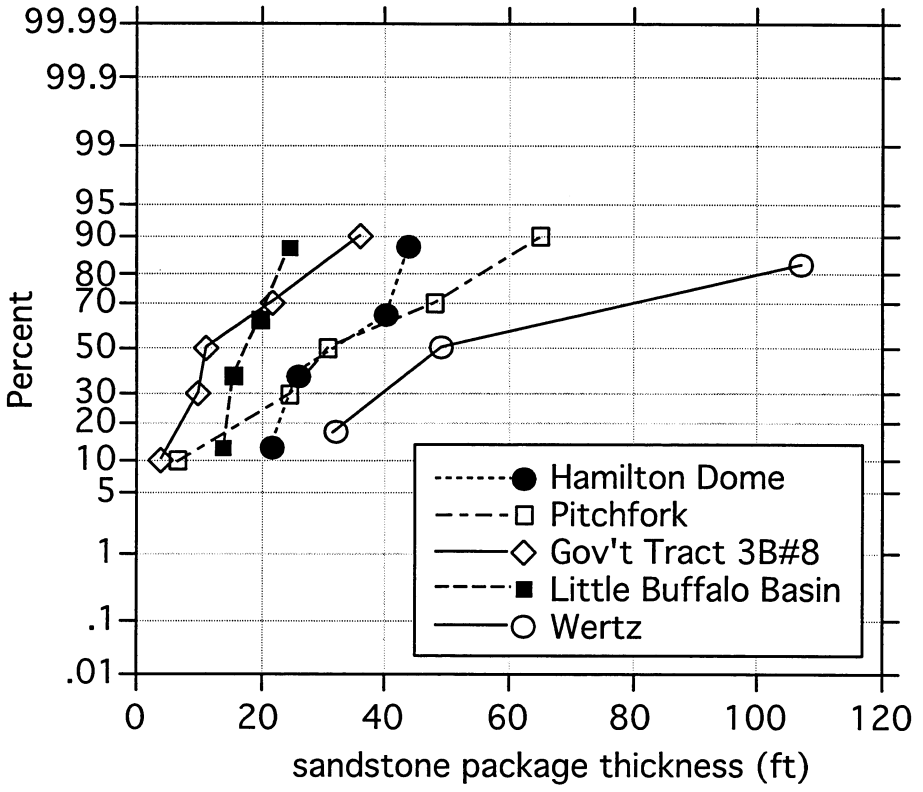

Figure 2.55. Probability plot of sandstone thickness packages in the Tensleep datasets. Datasets with steep slopes on this plot are the ones which have correlation events on the semivariograms.

model suggests local variation in relative sea level rise that is reflected in varying thickness of preserved eolian sand packages.

The sandstone package thickness of the six cores studied reflect this local variation in relative sea level which in turn is reflected in the variograms. The Pitchfork core in the Bighorn Basin and the Wertz core in the Wind River Basin both have anomolously thick average sandstone packages relative to other areas of the Bighorn Basin. The large-scale ranges shown on the semi-variograms of both Pitchfork and Wertz have good agreement with the average sandstone package thickness. In fact, as previously discussed, all of the spatial correlations revealed by variogram analyses are reflected in sandstone package thickness. With more complete regional coverage, a variogram analysis could be an excellent indicator of local base-level histories.

Small-Scale Influences

The synthetic data and the large-scale data have demonstrated that a range of influence, or range, reflects cycle thickness. Also, the distance of the correlation events reflects the distance to the next group of similar data. Smallscale spatial trends in the Tensleep are more difficult to recognize using semivariogram analysis. The large-scale permeability heterogeneities are caused by obvious packages of different lithologies (sandstones vs. dolomites). Small-scale permeability heterogeneities are caused by more subtle differences in eolian sedimentation styles such as grainflow and wind ripple laminae. Studies of permeabilities and eolian sedimentation style have revealed that grainflow laminae have high permeabilities, wind ripple deposits have lower permeabilities and interdune deposits have the lowest (Grant et al., 1994 and Chandler et al., 1989). Disturbed bedding in the Tensleep tends to have relatively high permeability, but more study is needed to determine exactly where it lies in comparison with other eolian sedimentation types (Crabaugh, 1996). Given that these different forms of sedimentation result in different permeabilities, it should be possible to find correlation between sedimentation type and small-scale ranges of influence.

There were no correlation events in the small-scale data, indicating that small-scale permeability variations are not evenly spaced (Fig. 2.56). This contributes to the difficulty of attributing a sedimentological cause to the spatial patterns revealed by the variograms. Table 2.7 shows the small-scale trends for all of the datasets. As with large-scale spatial trends, there is considerable regional variation in the small-scale ranges of influence. However, there is only a weak relationship between the size of large-scale ranges and small-scale ranges. The dataset with the biggest large-scale range, Wertz, also has the biggest smallscale range; the dataset with the smallest large-scale range, Neiber Dome, also has the smallest small-scale range, indicating a very general tendency for smallscale heterogeneities to parallel large-scale heterogeneities. Between these two end members there is little correlation, suggesting that small-scale permeability heterogeneities cannot be reliably predicted based on large-scale permeability heterogeneities.

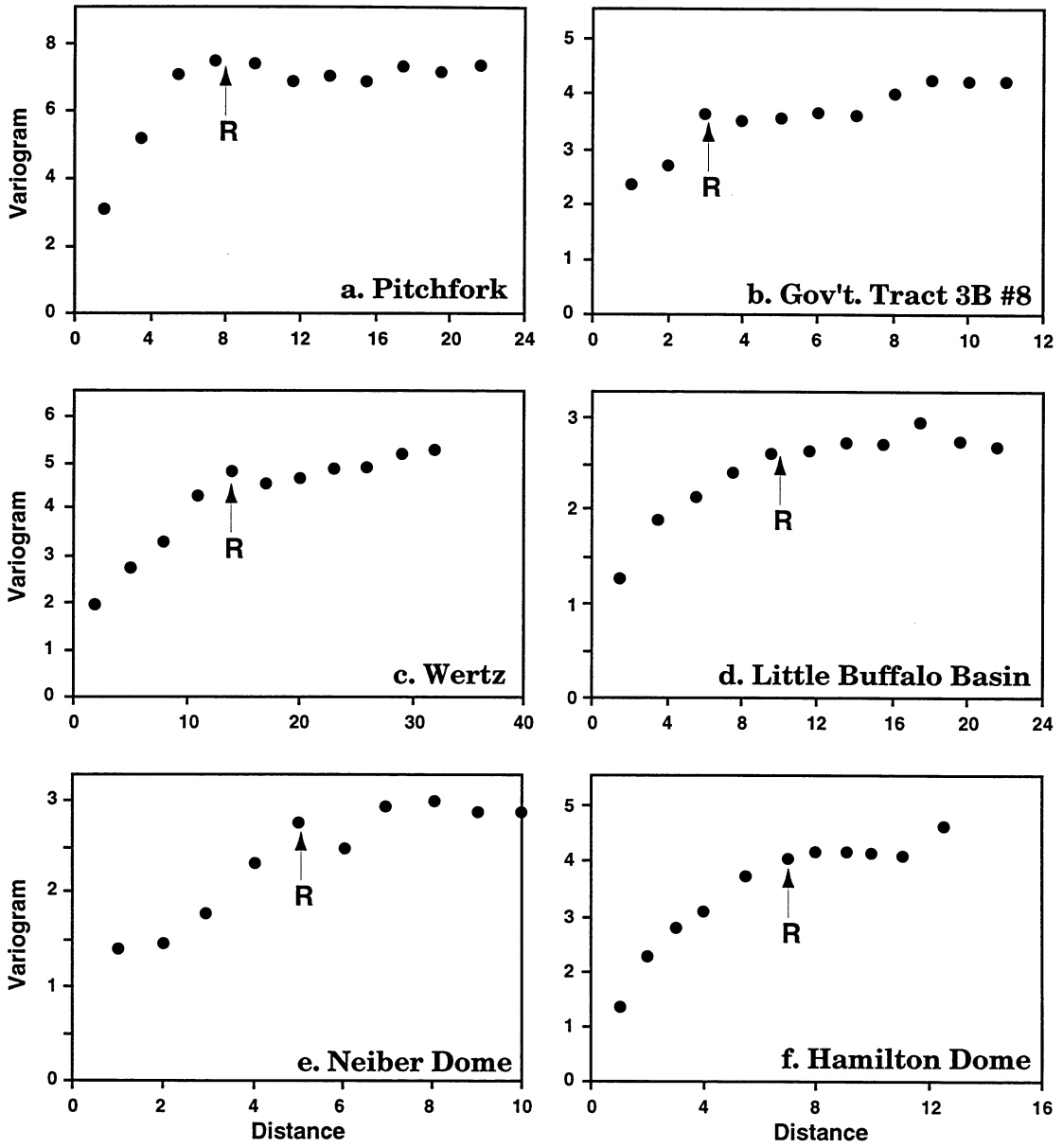

Figure 2.56. Variograms of Tensleep data evaluating small-scale heterogeneity by using small lag distances. Ranges (R) shown on these plots are: Pitchfork (a) 2.4m. (8ft), Gov't. 3B#8 (b) 1m (3 ft.), Wertz (c) 4.3m (14 ft.), Little Buffalo Basin (d) 3m (10 ft.), Neiber Dome (e) 1.5m (5 ft.), and Hamilton Dome (f) 2.1m (7 ft.).

The datasets for which corresponding detailed core descriptions are available are Pitchfork and Gov't. Tract 3B # 8. A close look at the data in Pitchfork revealed that the thickness of disturbed bedding closely approximated the small-scale range of 2.4m (8ft). Zones of disturbed bedding tended to be

groups of relatively large permeability values that were surrounded by relatively small numbers. This is a reasonable hypothesis but certainly not the only possible explanation. For instance, 2.4m (8ft) is a reasonable thickness for first-order bounding surfaces in the upper Tensleep (Crabaugh et al., 1996). There is no doubt that permeability numbers in Pitchfork are clustered in groups of around 2.4m (8ft), but there is not always a clear sedimentological reason.

An explanation for the small range of 0.9m (8ft) in Government Tract 3B #8 was difficult to find. With measurements at only 0.3m (one foot) spacings, a 0.9m (three foot) range is likely insignificant. The geometric mean for first-order bounding surfaces in the upper Tensleep was found to be 1 meter (Crabaugh et al., 1996), so it is possible that the range is meaningful, but more closely spaced measurements would be needed to confirm this.

All of the small-scale spatial correlations found were considerably smaller than the average sand package thickness associated with that dataset. In order to ensure that the small-scale patterns shown in the variogram came from within the sandstone packages and were not reflections of the marine units, variograms were generated without marine data. Permeability values representing marine intervals were removed from the dataset and depth values were compressed so that depth numbers remained consecutive. The variograms without marine intervals always generated a similar small-scale range of influence. Table 2.7 shows the comparison of ranges with marine data and without marine data.

There is no doubt that some spatial correlation exists on a small scale within the eolian units of the Tensleep, otherwise a variogram analysis would have generated a near 100% nugget effect (little difference between the semi-variance at lag = 0.3m (1ft) and the semi-variance at greater lag distances). A comparison with the large-scale investigations suggests that the small-scale ranges are also indicative of permeability heterogeneity within the eolian units of the upper Tensleep. Better coverage in the Bighorn and Wind River Basins will help confirm these potential explanations.

Conclusions of Statistical Analysis of Permeability Heterogeneity

Based on the spatial correlations shown in the geostatistical analyses of the upper Tensleep, the variogram can be viewed as a useful tool in predicting large-scale heterogeneities within the Tensleep Sandstone. These in turn reflect local base-level histories. As with any statistical study, the numbers cannot be interpreted without some knowledge of the dataset. For instance, data from the Pitchfork well indicated a correlation event at 27.4m (90ft), but because examination of the core revealed no sedimentologically significant parameter occurring at 27.4m (90ft) intervals, this correlation event was viewed as fortuitous. Therefore, with a general knowledge of the study area, useful interpretations can be made.

Small-scale heterogeneity, on the order of first- and second-order bounding surfaces, was more difficult to interpret given the information available for this study. A geostatistical study of small-scale heterogeneity is more difficult because of the more subtle differences in sedimentation types within eolian sandstones. Authors who have done similar work on eolian and other types of sediments (Grant et al., 1994 and Prosser and Williams, 1993) have shown that 0.3m (one foot) measurements are sufficiently close to capture small-scale heterogeneities. However, in order to establish patterns that could work as predictive tools in the Tensleep, complete core descriptions and permeability data are required for a larger number of cores.

Variogram shape can also be used to estimate properties of the dataset. Correlation events indicate a relatively high degree of order in a dataset. A range of influence together with a correlation event indicates the variation of eolian sand package thicknesses.

TASK 3.0: CO2 COREFLOOD - FORMATION ALTERATION AND WELLBORE DAMAGE

OBJECTIVES

The work of this task is twofold: establish criteria to determine the susceptibility of Tensleep reservoirs to formation alteration which can cause changes in absolute or relative permeability and establish characterization technology that will be used to optimize recovery efficiency. This task includes: (a) flow experiments on core material to examine the effects of CO_2 flooding on the fluid and rock system; (b) examination of regional trends in water chemistry; (c) examination of local water chemistry trends at field scale; and (d) chemical modeling of both the reservoir and experimental systems in order to scale-up the experiments to reservoir conditions.

CO_2 CORE-FLOODING EXPERIMENTS

Introduction

CO_2 flooding, in which CO_2 gas and brine are injected into reservoirs to produce more oil, has been an important technique for enhanced oil recovery since the 1980s. Through core flooding experiments, studies have demonstrated that one of the advantages of CO_2 flooding is the dissolution of carbonate cements which can increase the permeability of the reservoir rocks (Ross et al., 1981; 1982; Omole and Osoba, 1983; Sayegh et al., 1990). However, carbonate scale formation and corrosion, which accompany CO_2 flooding, are costly. Patterson (1979) reported both scale formation and downhole corrosion after CO_2 injection in the Kelly-Synder oil field, Texas, although he did not specify the type of scale minerals. Bowker and Shuler (1991) reported carbonate scale formation due to CO_2 injection in the Weber sandstone, Rangely oil field, Colorado. The effects of CO_2 injection on hydrocarbons and minerals are other problems which require consideration. Monger and Fu (1987), Monger and Trujillo (1988), Wolcott et al. (1989; 1991) assessed asphaltene precipitation as a by-product of CO_2-oil interaction.

Previous studies on scale formation have mainly been concerned with treatment and prevention (e.g., Patton, 1974; 1986; Jones, 1988). Some recent studies have developed prediction techniques for scale formation based on thermodynamic calculation of changes of mineral saturation when injected and

formation waters are mixed during water injection (e.g, Atkinson et al., 1991; Yuan and Todd, 1991; Mazzolini et al., 1992). The effects of water-rock interaction on scale formation have been neglected in those studies.

This study focuses on predicting scale formation caused by water-rock interaction caused by the addition of CO_2. This is done through core flooding experiments. The Tensleep Formation, which has been one of the biggest oil producers in the State of Wyoming, has great potential for CO_2 flooding to enhance oil recovery. Therefore we conducted the experiments using Tensleep materials so that the results are directly applicable.

Previous Experimental Studies on CO_2 Flooding

Ross et al. (1981, 1982) carried out CO_2 core flooding experiments at 20 and 80°C using calcitic and dolomitic sandstones and oolitic limestone. They injected carbonated brine (chemical composition is not described) and observed increases in permeability in each case, particularly in the oolitic limestone.

Omole and Osoba (1983) carried out three sets of CO_2 flooding experiments at 27°C by injecting CO_2 gas into dolomite cores saturated with 0.1N KCl aqueous solution. They examined the changes in permeability before and after the experiments as it was affected by the amount of CO_2 injected, CO_2 injection pressure, and the pressure gradient across the core. They observed a 64% increase in permeability for the injection of up to 3.28 pore volume of CO_2, a 5 to 22% increase in response to an increase in CO_2 injection pressure (from $7.2x10^6$ to $1.72x10^7$Pa (72 to 172 bars)), and a 22% increase for pressure gradient of up to $7.2x10^6$Pa (72 bars). Assuming that changes in permeability should be due to dissolution or precipitation of carbonate minerals at the pore throats, Omole and Osoba concluded that CO_2 flooding into carbonate reservoirs would result in the dissolution of carbonate minerals near injection wells and precipitation of them at production wells.

Sayegh et al. (1990) carried out CO_2 flooding experiments at 45°C and $1.38x10^7$Pa (138 bars) using sandstone cores from the Pembina Cardium oil field, Alberta, Canada. They observed that the permeability of cores rapidly decreased at the early stage of the experimental runs and then increased

gradually throughout the remainder of the experiment. However, they did not regain the original permeability values during runs of 25 to 50 hours. They also observed dissolution of carbonate cements (calcite and siderite).

Experimental results of Bowker and Shuler (1991), in which Weber sandstone from the Rangely oil field, Colorado was flooded by carbonated water, showed that the permeability of cores did not change substantially throughout the runs. The cores they used contained about 10 vol.% carbonate cements (ferroan calcite and dolomite) as well as about 5 vol.% of illite and mixed-layer illite/smectite. In their experiments, they observed an increase in Ca, Mg, and Fe in the effluent solutions suggesting dissolution of carbonates. However, they observed no increase in permeability during their experiments. They attributed this to fine clays being released from under the carbonate cements which then migrated into and clogged pore throats.

Experimental Set-Up

Two runs (Runs 4 and 5) were carried out during this third year of the contract. Run 4 was a brine-rock only system, and Run 5 was a brine-oil-rock system. Experimental procedures adopted in these experiments were similar to those used in our previous experiments (Dunn, 1994; 1995), except where noted. (see Dunn, 1994 for a complete description of the experimental apparatus).

Materials

Subsurface cores from the Tensleep Formation in the Oregon Basin oil field were used for the experiments. The cores were drilled approximately parallel to lamination. The core dimensions were 0.038m in diameter and 0.062 to 0.075m in length. These cores contained abundant dolomite and anhydrite cement.

The nutrient solution used in both runs was 0.25 mol/L NaCl aqueous solution, which was synthesized by dissolving reagent grade sodium chloride into deionized water. Tensleep crude oil from the Oregon Basin oil field, which was filtered by 0.45μm filter paper was used in Run 5. The API gravity of the oil was 21° (Wyoming Geological Association, 1989).

Apparatus and Run Conditions

In Run 5, each of three cores used during the experiment was saturated with NaCl brine by injecting brine from one end in an stainless steel core holder. This was followed by injection of Tensleep crude oil to oil saturations of 71%, 71%, and 65%, respectively, for the three cores. No preliminary treatments were done for cores used in Run 4.

Core samples wrapped with teflon sheeting were placed into rubber tubing, and both ends of the tubing were attached to stainless steel core-ends with tubing clamps. The total length of the core assemblage was 0.213m in Run 4 and 0.188m in Run 5. This core assemblage was placed in the core holder (high pressure vessel). Free space in the vessel was filled with water and pressurized with N_2 gas to simulate an overburden pressure that was approximately $1x10^7$Pa (100 bars) greater than the internal pressure of the core.

The nutrient solution and CO_2 gas were combined in reservoirs to equilibrium with 80°C and $1.6x10^7$Pa (166 bars). After equilibrium between CO_2 and the nutrient solution was obtained (indicated by a constant CO_2 gas pressure), a Ruska pump sent mineral oil into the upper part of the separator of the reservoirs which displaced the CO_2-nutrient solution into the cores. The flow rate of the nutrient solution was set to $7.5x10^{-3}$L/h in both runs.

Effluent solution was collected into samplers after passing through the back-pressure regulator. Degassed CO_2 from the sample solutions was collected into a gas collector, and the volume was measured. In Run 5, crude oil from the system was not sampled because it remained on the inside wall of the effluent samplers.

Rock and Fluid Analyses

The pH and alkalinity of the sample solutions were measured immediately upon sampling (which was once per day) by combination pH electrode and HCl titration, respectively. Samples in Run 5 were filtered to remove oily materials and fine particulates before pH and alkalinity measurements were made. The samples were then acidified with 1:1 HNO_3 to keep all ions soluble for later analyses. Concentrations of Na, K, Ca, Mg, Fe,

Mn, Al, Sr, Ba, Si were measured by ICP and atomic absorption spectrometry and concentrations of Cl and SO_4 were measured by ion chromatography.

For cores used in Run 4, porosity and air permeability of cores were measured using the Core Laboratories CMS-300, an automated core measurement system. This was done both before and after the experimental run. For cores used in Run 5, porosity and permeabilities were measured only before the experiment. Following the post-experiment porosity and permeability measurements, cores were examined with both standard petrographic and scanning electron microscopes (SEM). Rock fragments obtained when those cores were drilled and trimmed were also examined under SEM to observe the original mineral morphology.

Total and inorganic carbon contents of ground samples and of Tensleep crude oil were measured using a CO_2 coulometer that determined CO_2 gas generated by combustion of the sample at 1200°C (TC, total carbon) and CO_2 gas generated by dissolving the sample into hydrochloric acid (TIC, total inorganic carbon, *i.e.*, carbonate cement). The amount of oil remaining in the core after the run was calculated as the content of TOC (total organic carbon) from measured TC and TIC contents as follows:

$$Oil\ (wt\%) = \frac{TOC_{sample}(wt\%)}{TOC_{oil}(wt\%)} = \frac{(TC - TIC)_{sample}(wt\%)}{TC_{oil}(wt\%)} \tag{3.1}$$

Speciation of Solutions

SOLMINEQ.88 (Kharaka et al., 1988) was used to calculate speciation and mineral saturation indices of the solutions. In those calculations, degassed CO_2 was taken into account to calculate *in-situ* pH values. Using the results of speciation, the saturation index (S.I.) was calculated from the relationship:

$$S.I. = log\left(\frac{IAP}{K_{sp}}\right) \tag{3.2}$$

where IAP and K_{sp} are the ion activity product and the solubility product, respectively. Table 3.1 lists the solubility product of carbonate and sulfate

minerals of interest at the experimental conditions (i.e., 80°C and 1.6x10^{7}Pa (166 bars)). All values except for dolomite were taken from the original database of *SOLMINEQ.88*. The value for dolomite was calculated by using the generally accepted value of $log\ K_{sp}$ = -17.0 at 25°C and 10^{5}Pa (1 bar) (Hsu, 1967; Langmuir, 1971; Busenberg and Plummer, 1982) and the temperature and pressure dependence of $log\ K_{sp}$ used in *SOLMINEQ.88*.

Table 3.1. Solubility product of minerals at 80°C & 1.6x10^{7}Pa (166 bars).

mineral	log K_{sp}
aragonite ($CaCO_3$)	- 8.72
calcite ($CaCO_3$)	- 8.83
dolomite ($CaMg(CO_3)_2$)	- 18.30
strontianite ($SrCO_3$)	- 9.48
witherite ($BaCO_3$)	- 8.95
anhydrite ($CaSO_4$)	- 4.88
gypsum ($CaSO_4\ 2H_2O$)	- 4.77
celestite ($SrSO_4$)	- 6.62
barite ($BaSO_4$)	- 9.45
quartz (SiO_2)	- 3.26
gibbsite ($Al(OH)_3$)	- 31.74

Results of Coreflood Experiments

Two experiments (Runs 4 and 5) were run at 80°C and 1.6x10^{7}Pa (166 bars) for 168 and 143 hrs, respectively. In Run 4, the injection of nutrient solution was interrupted for 44.9 hours due to a malfunction in the autosampler that began at 21.3 hrs. The reaction time after the interruption was counted by neglecting this time interval. The total amount of solution injected was 1.220L (43 pore volumes) in Run 4 and 1.024L (34 pore volumes) in Run 5.

Solution Chemistry

Figure 3.1 shows the change in alkalinity, *in situ* pH, and concentration of Ca and Mg with reaction time during Runs 4 and 5. A vertical line at t = 21.3 (hrs) in the top figure (and the top figure in Figures 3.2 through 3.5) shows the time when the interruption of nutrient solution occurred in Run 4. In Run 4, pH and alkalinity show a complex v-shape pattern at the early stage of the run,

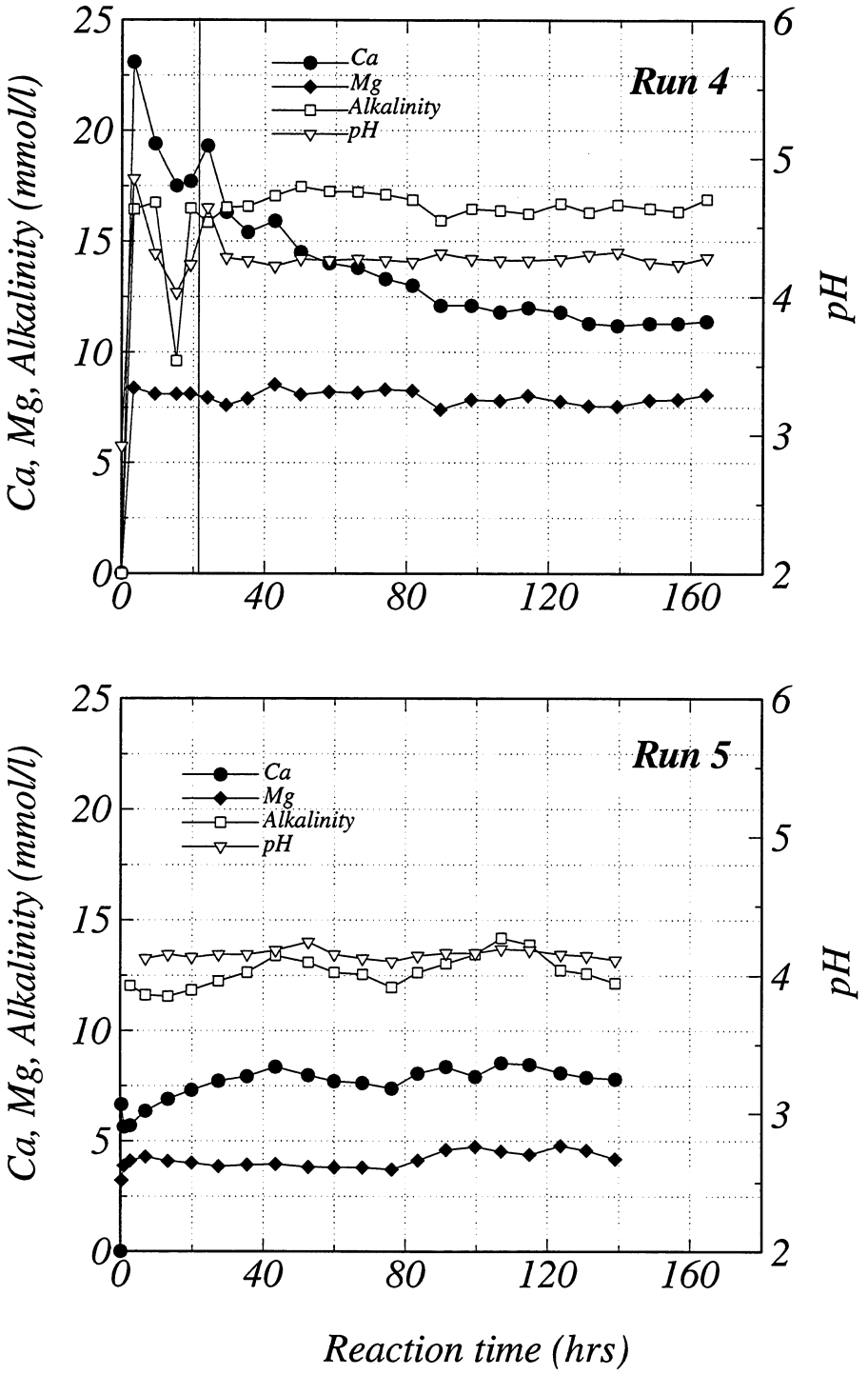

Figure 3.1. Solution pH, and concentrations of Ca and Mg vs. reaction time of CO_2 core flooding experiments (top: Run 4, bottom: Run 5).

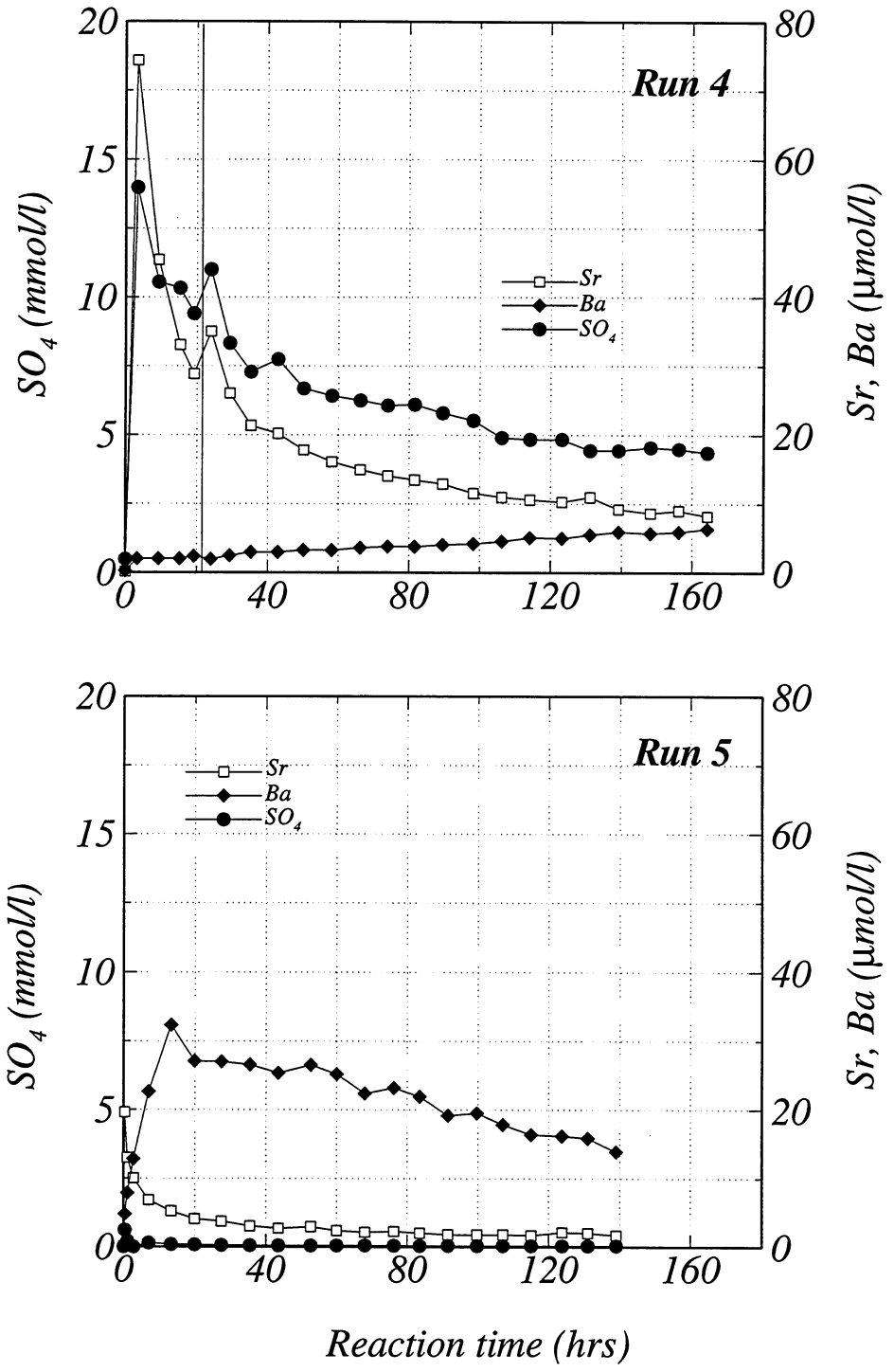

Figure 3.2. Concentrations of SO_4, Sr, and Ba vs. reaction time of CO_2 core flooding experiments (top: Run 4, bottom: Run 5).

whereas they became constant after the reaction time of 30 hrs. Ca concentration decreased continuously throughout the experiment except the sample taken just after the interruption, whereas Mg concentration remained constant throughout the run. Unlike Run 4, the change in concentration of Ca was small in Run 5. Concentrations of Ca, Mg and alkalinity remained smaller in Run 5 than in Run 4.

Figure 3.2 shows the concentration change with reaction time for SO_4, Sr, and Ba during Runs 4 and 5. In Run 4, the concentration of SO_4 and Sr first increased to 14×10^{-3} mol/L and 74.3×10^{-6} mol/L, respectively, and then decreased by the end of the experiment to 4.4×10^{-3} mol/L and 8.22×10^{-6} mol/L. Like the Ca shown in Figure 3.1, the sample taken after the interruption in Run 4 showed a slight increase of SO_4 and Sr. The concentration of Ba, on the other hand, continuously increased to a concentration of 6.41×10^{-6} mol/L by the end of the run. In Run 5, the concentration of SO_4 remained very low (less than 0.62×10^{-3} mol/L) throughout the experiment. The concentration of Ba increased rapidly with the first 5 samples, reaching a concentration of 32.3×10^{-6} mol/L. This was followed by continuously decreasing concentrations reaching 13.9×10^{-6} mol/L by the end of the run.

Figure 3.3 shows the concentration change with reaction time for K, Al, and SiO_2. Unlike the other elements, these three constituents showed quite similar patterns in both runs. The concentration of these elements increased in the first sample then continuously decreased throughout the remainder of the experiment.

Mineral Saturation

Figure 3.4 shows the change in the saturation index of sulfate minerals with reaction time during Runs 4 and 5. In Run 4, the effluent solution was saturated with respect to barite throughout the run. The first solution was nearly saturated with respect to anhydrite (S.I. = - 0.43), however, the saturation index decreased with reaction time to -1.18. The saturation index of celestite showed a similar pattern to those of anhydrite and gypsum, although the S.I. values were smaller. In Run 5, the saturation indices of these four sulfate

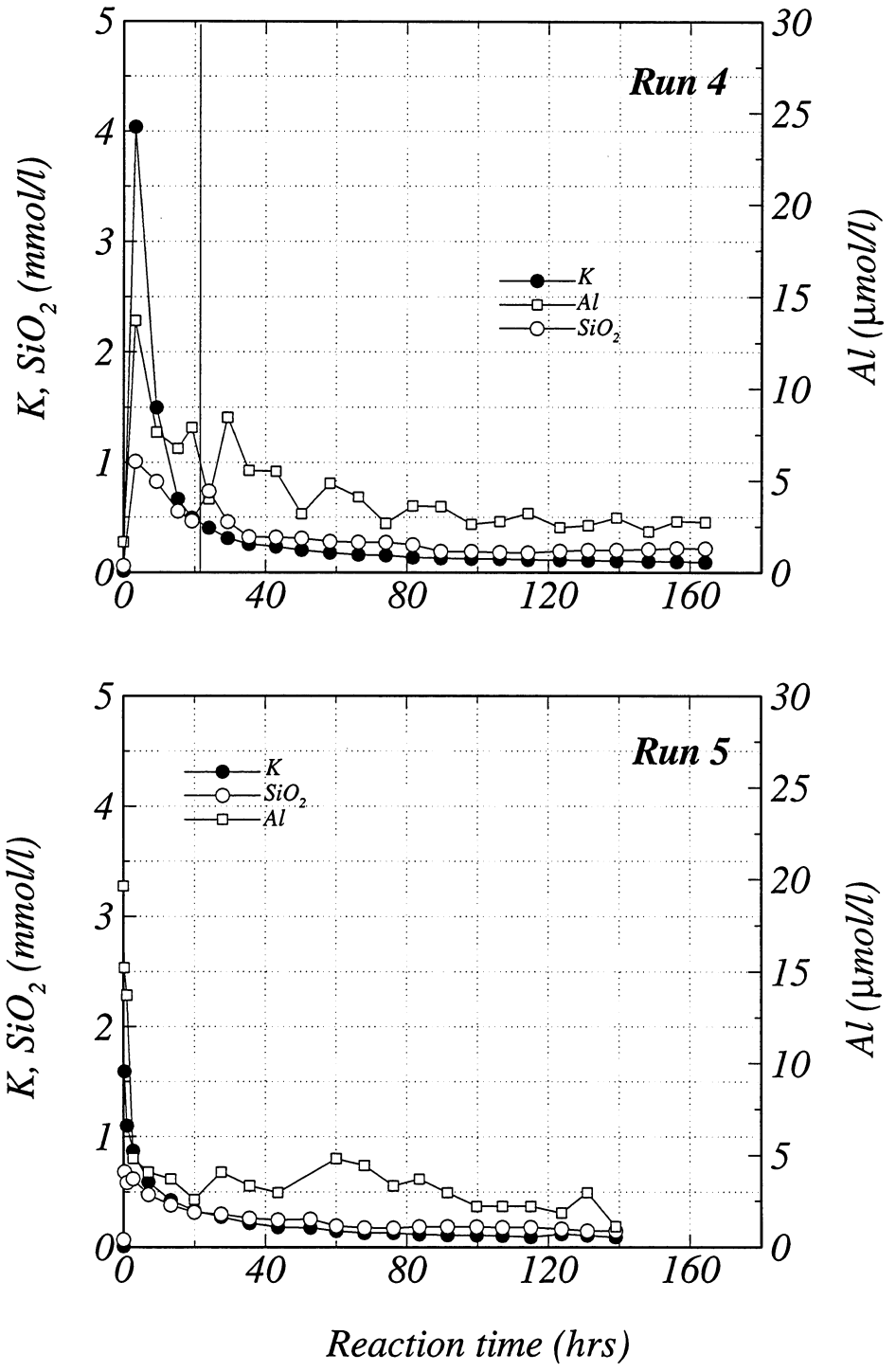

Figure 3.3. Concentrations of SiO_2, K,and Al vs. reaction time of CO_2 core flooding experiments (top: Run 4, bottom: run 5).

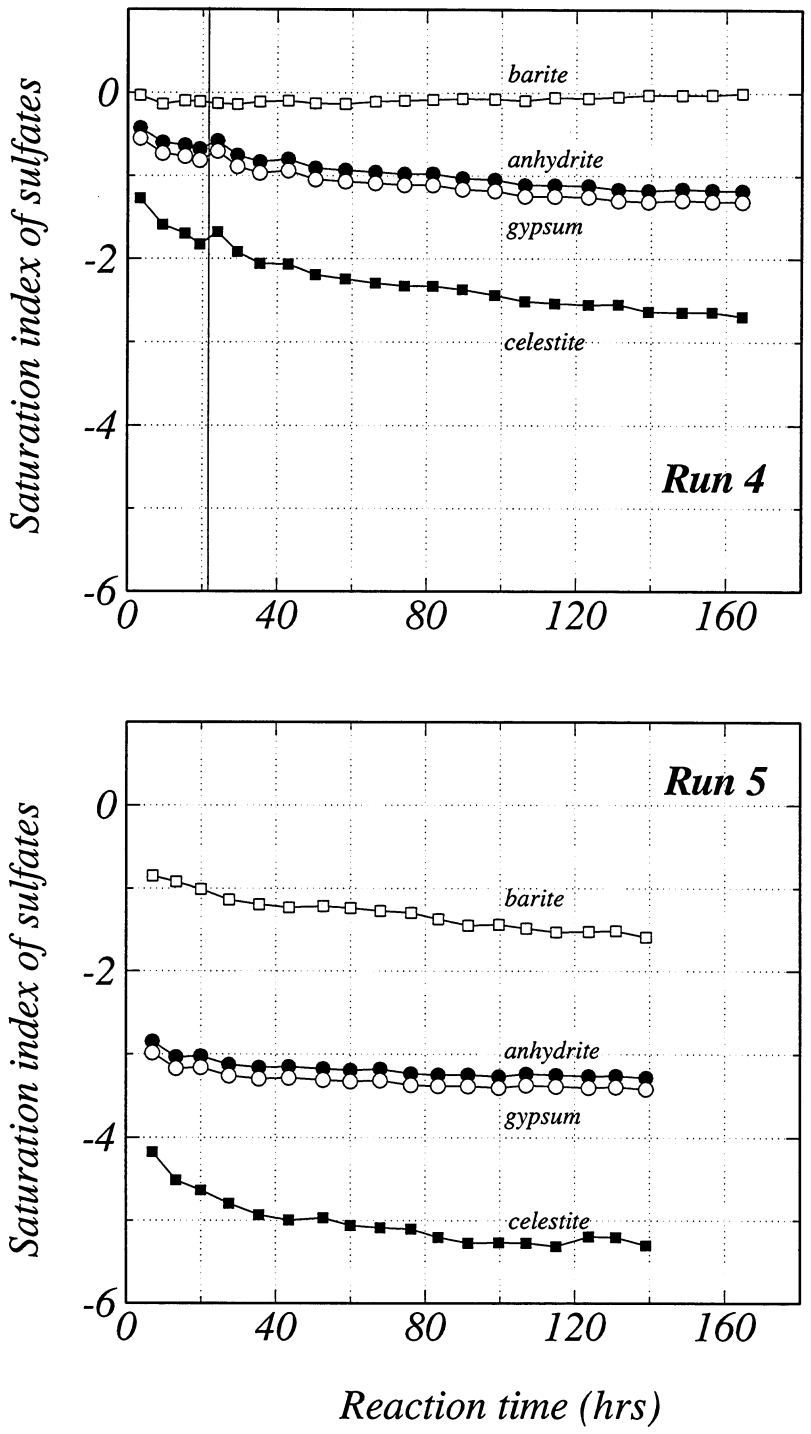

Figure 3.4. Saturation indices of sulfates vs. reaction time of CO_2 core flooding experiments (top: Run 4, bottom: Run 5).

minerals showed the same pattern as in Run 4, but the values were much smaller.

Figure 3.5 shows the change of saturation index of carbonate minerals with reaction time during Runs 4 and 5. In both runs, all solutions remained undersaturated with respect to all the carbonate minerals considered. In Run 4, the saturation indices of all carbonate minerals decrease at the early stage of the run, following the pattern of pH and alkalinity (Fig. 3.1). After the interruption in Run 4, the saturation indices of dolomite, calcite, and aragonite were approximately constant, whereas those of strontianite and witherite decreased then increased slightly. In Run 5, the degrees of undersaturation for dolomite, calcite, and aragonite were higher than in Run 4, whereas those of strontianite and witherite were reversed.

Rock phase

Table 3.2 lists the results of porosity and air permeability measurements of cores used in Run 4. Porosity increased in the top (injection end) and middle cores by 9% and 2% respectively. The porosity of the bottom core (effluent end) did not change. Even though the porosity of the top core increased, its permeability decreased by 31%. The middle core is the only one that experienced an increase in permeability. Its permeability increased by 27%. The permeability of the bottom core decreased (by 44%) even though its porosity was unchanged.

Table 3.2. Change in pore volume, porosity and air permeability of cores in Run 4.

Core	Increase in pore volume (m^3) (after/before)	Change in porosity (after/before)	Change in air permeability
top (injection side)	7×10^{-7}	1.09	0.69
middle	2×10^{-7}	1.02	1.27
bottom (effluent side)	0.0	1.00	0.56

Figures 3.6 through 3.11 show scanning electron photomicrographs of core material used in Run 4. Figures 3.6-3.8 are of fragments obtained from the drilling and trimming of the cores and thus represent the unaltered rock before

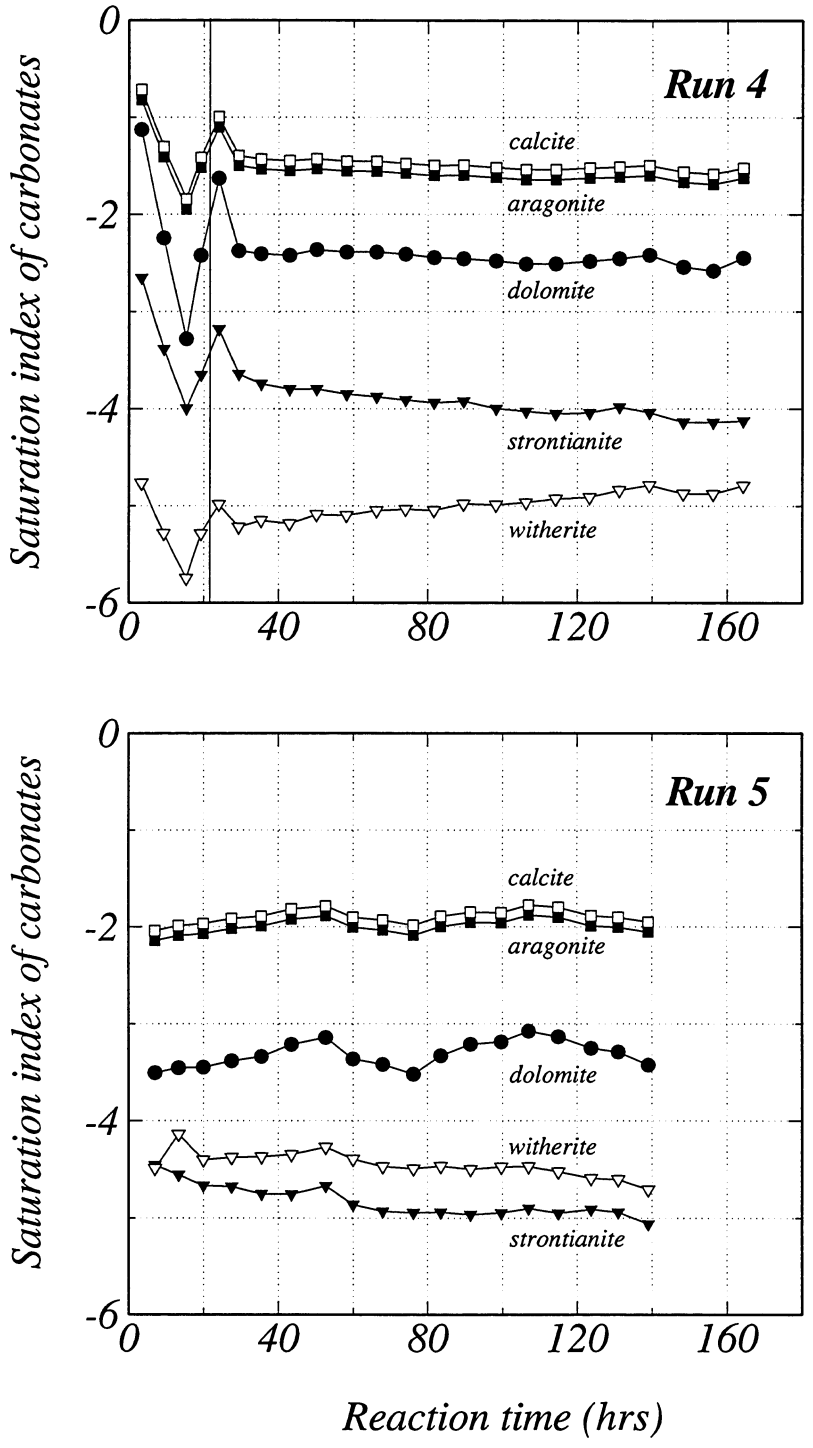

Figure 3.5. Saturation indices of carbonates vs. reaction time of CO_2 core flooding experiments (top: Run 4, bottom: Run 5).

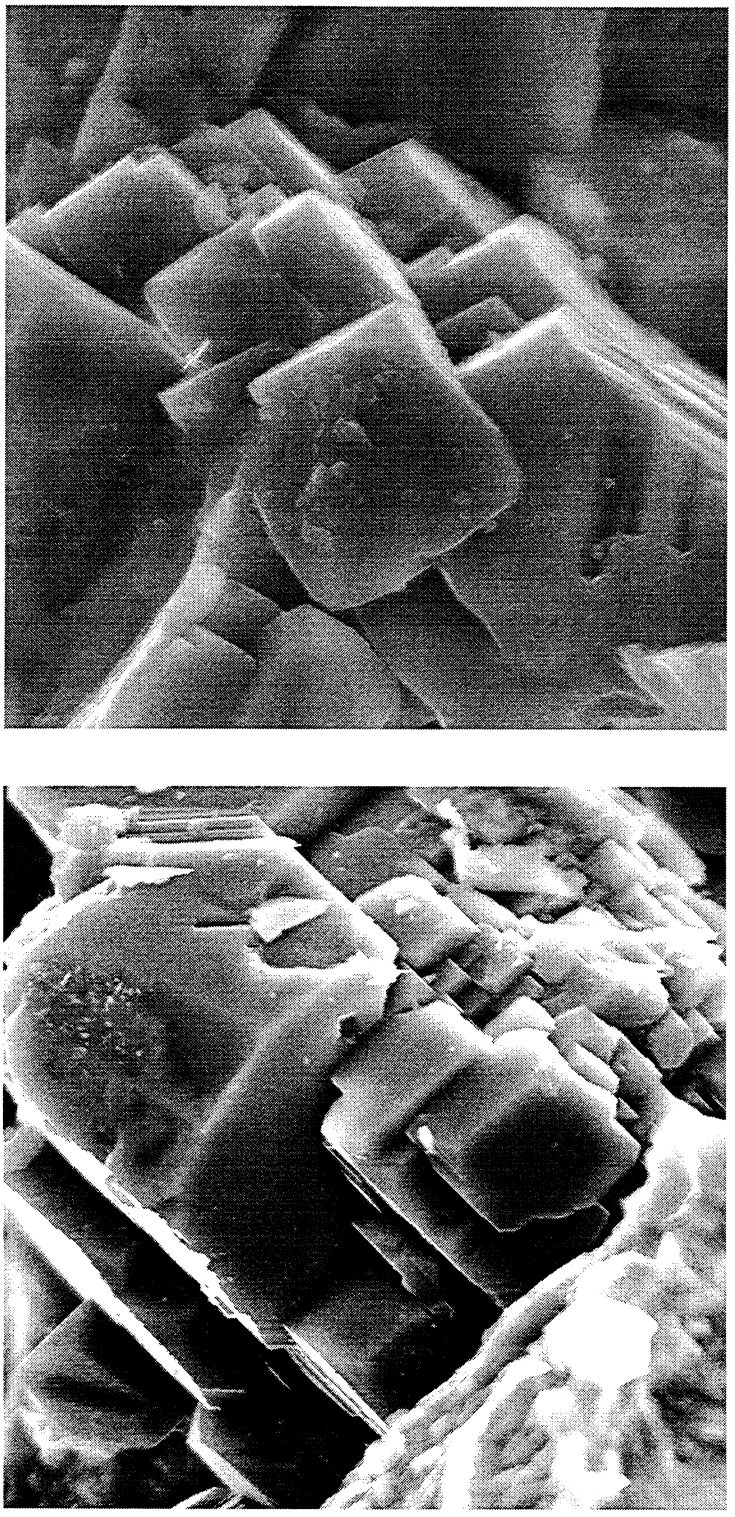

Figure 3.6. Scanning electron photographs of dolomite in Tensleep Formation that was not flooded by carbonated water.

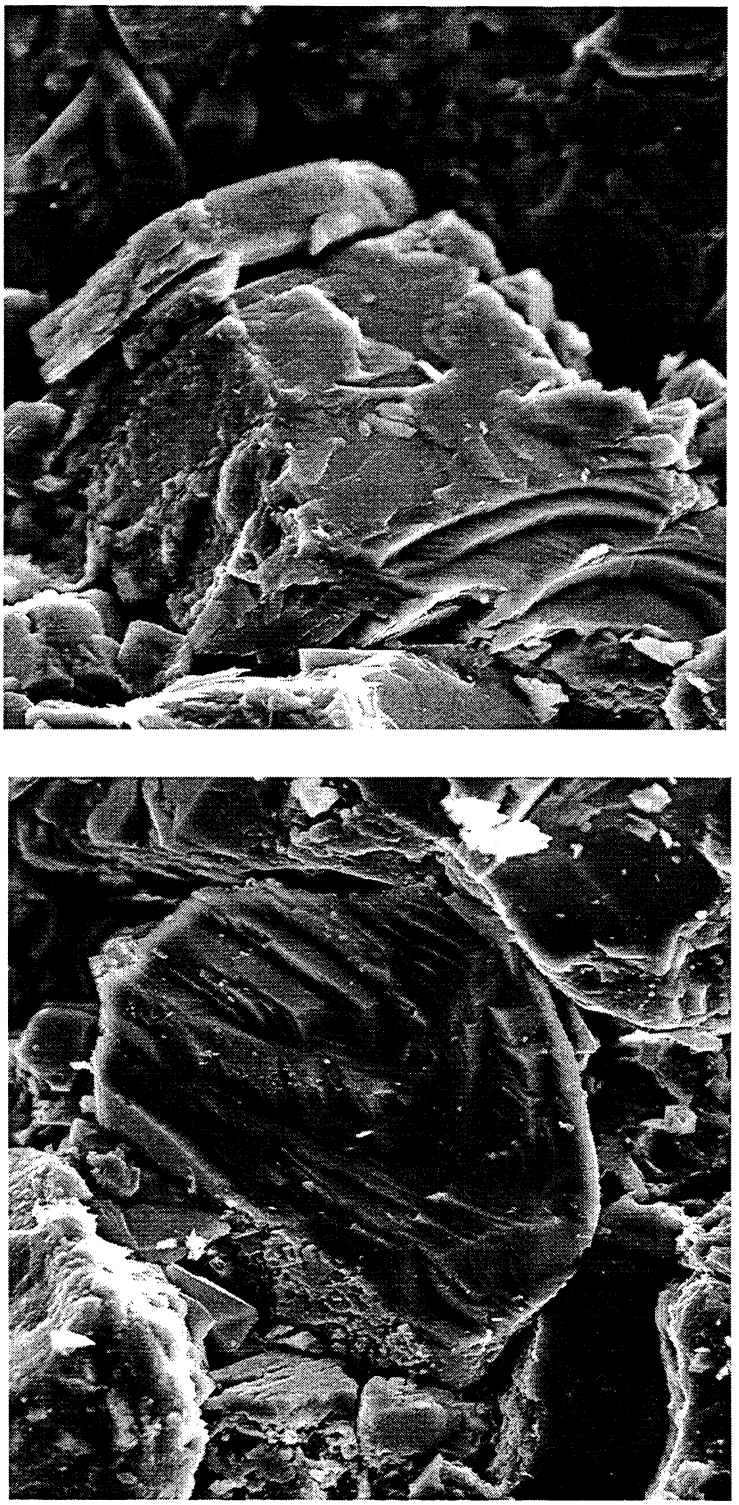

Figure 3.7. Scanning electron photographs of potassium feldspar in Tensleep Formation that was not flooded by carbonated water.

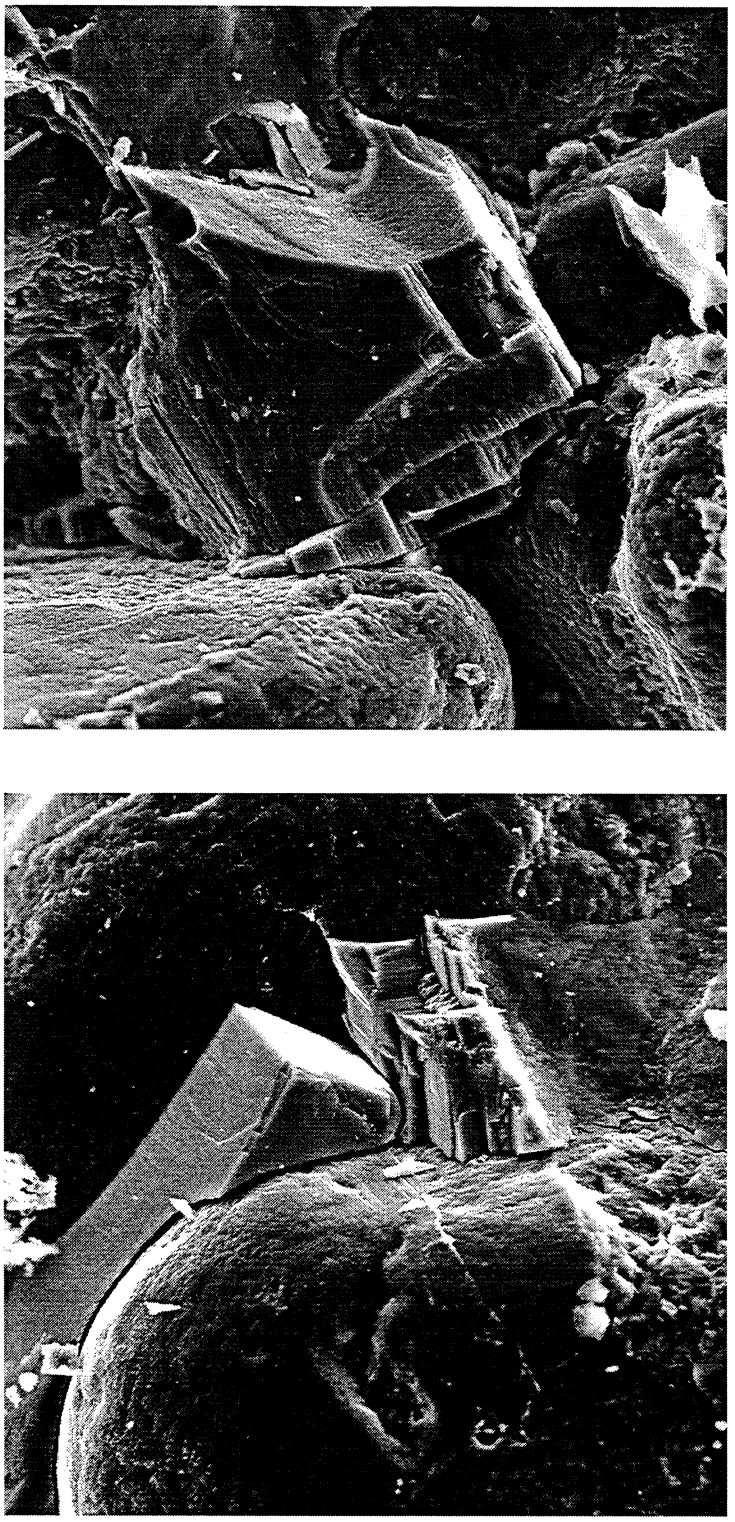

Figure 3.8. Scanning electron photographs of anhydrite in Tensleep Formation that was not flooded by carbonated water.

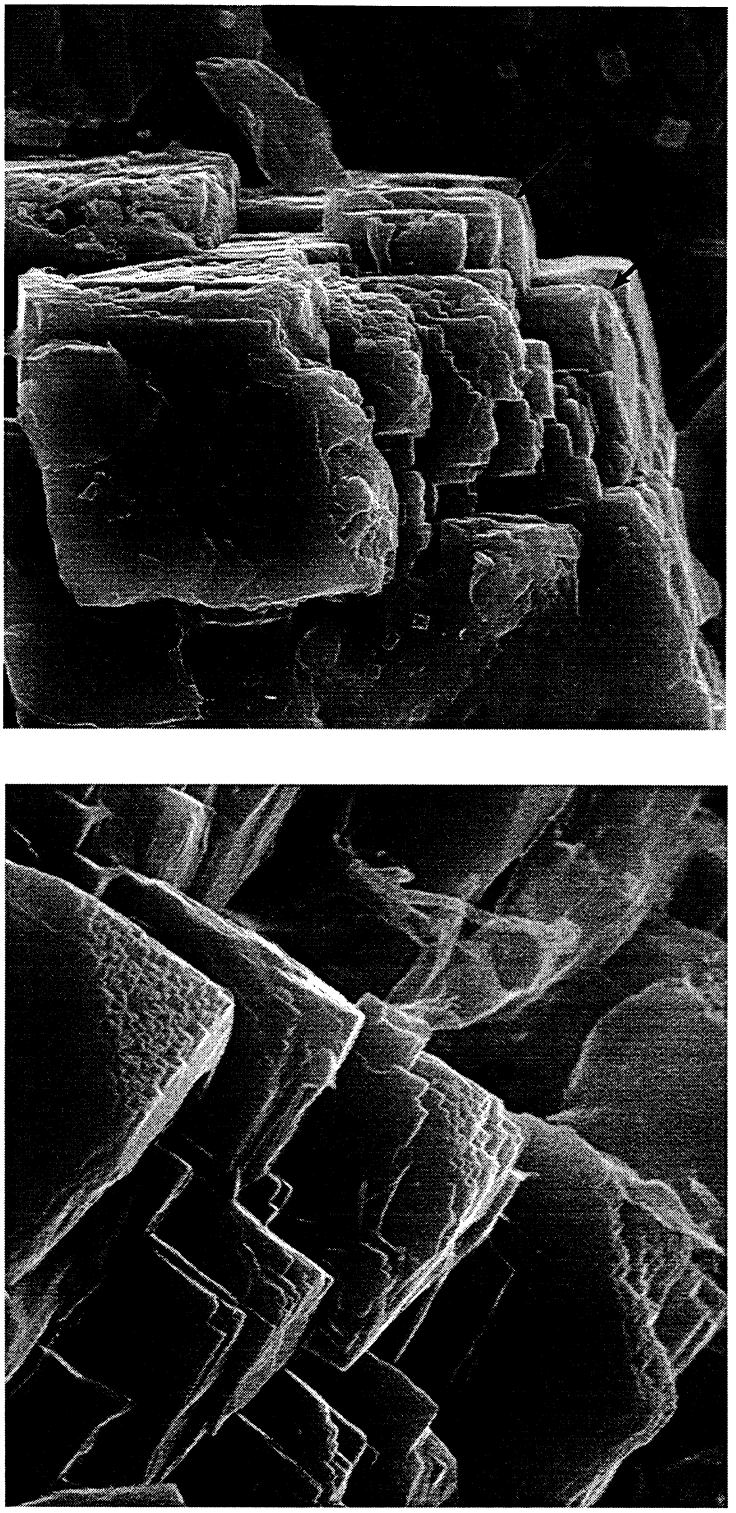

Figure 3.9. Scanning electron photographs of dolomite showing dissolution textures that developed during the CO_2 core flooding experiment (Run 4). Arrows show rounded corners (see text for details).

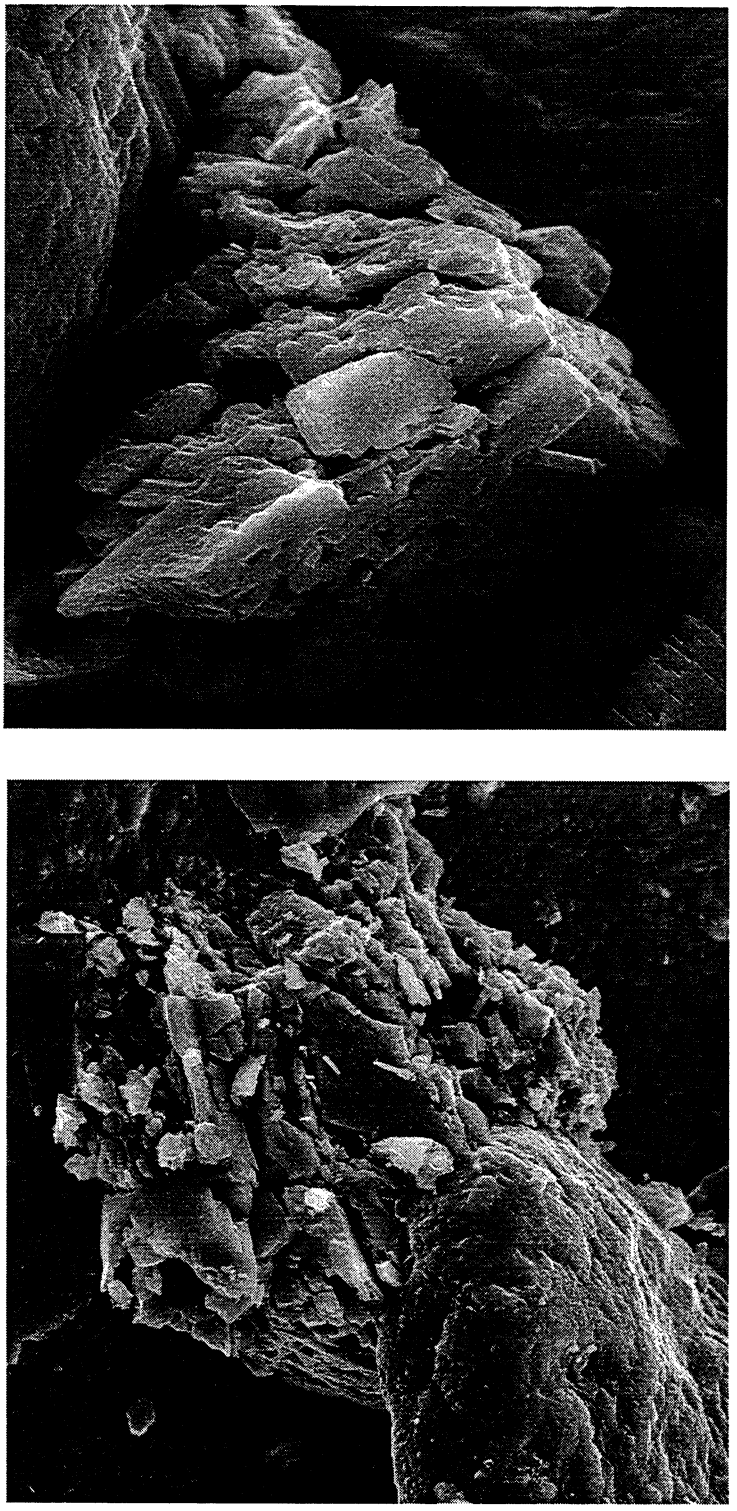

Figure 3.10. Scanning electron photographs of potassium feldspar showing dissolution texture that developed during the CO_2 core flooding experiment (Run 4).

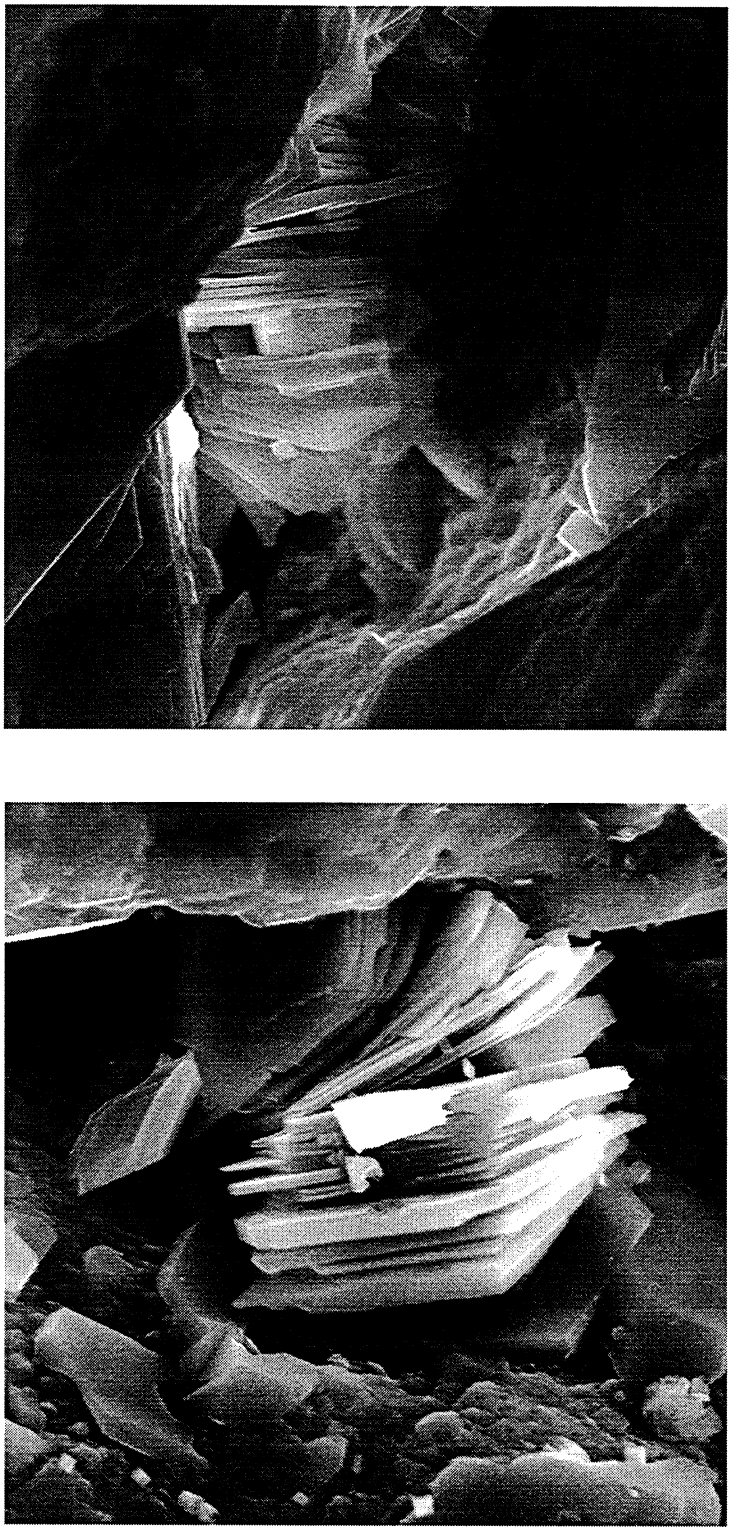

Figure 3.11. Scanning electron photographs of kaolinite that grew during the CO_2 core flooding experiment (Run 4).

the experiment. Specifically, these figures show the original, pre-CO_2 morphology of dolomite, K-feldspar, and anhydrite, respectively. Note in these figures the sharp euhedral crystal forms. Figures 3.9-3.11 are of pieces of the core taken after the experiment. Figure 3.9 shows dissolution textures of dolomite in cores after being flooded by carbonated water. Many step structures, which are not seen in fresh dolomite (Fig. 3.6), developed on the surface of dolomite crystals. Some rounded structures are also observed (shown by arrows in Fig. 3.9 (top)). Figure 3.10 shows dissolution textures of K-feldspar. These are sponge-like frameworks not seen in the fresh unaltered crystals (Fig. 3.7). Figure 3.11 shows kaolinite crystals, which were not observed in core pieces prior to flooding. The platy crystals of kaolinite grew in the pore spaces.

Oil Phase

The oil remaining in the cores after Run 5 was 1.30 wt% for the top core (injection side), 1.74 wt% for the middle core, and 1.95 wt% for the bottom core (effluent side). Oil saturations calculated from those numbers are 31%, 38%, and 56% for the top, middle, and bottom cores, respectively. This compares with oil saturations of 71%, 71%, and 65% at the start of the experiment. Results indicate that oil has moved toward the end of the core assemblage by the injection of the carbonated water and that some oil was produced from the core assemblage.

Discussion

Water-rock interaction

In both Runs 4 and 5, concentration changes of SiO_2, K, and Al with reaction time were quite similar, suggesting that concentration of these constituents were controlled by the same reaction involving the dominant feldspar species of the Tensleep Formation which is potassium feldspar (Todd, 1964; Mankiewicz and Steidtmann, 1979 and this study). Scanning electron microscopy revealed that potassium feldspar was altered and kaolinite crystals were newly formed during the experiment (Run 4, Figs. 3.10 and 3.11). Figures 3.12 and 3.13 show that all sample solutions of both Runs 4 and 5 fall in the

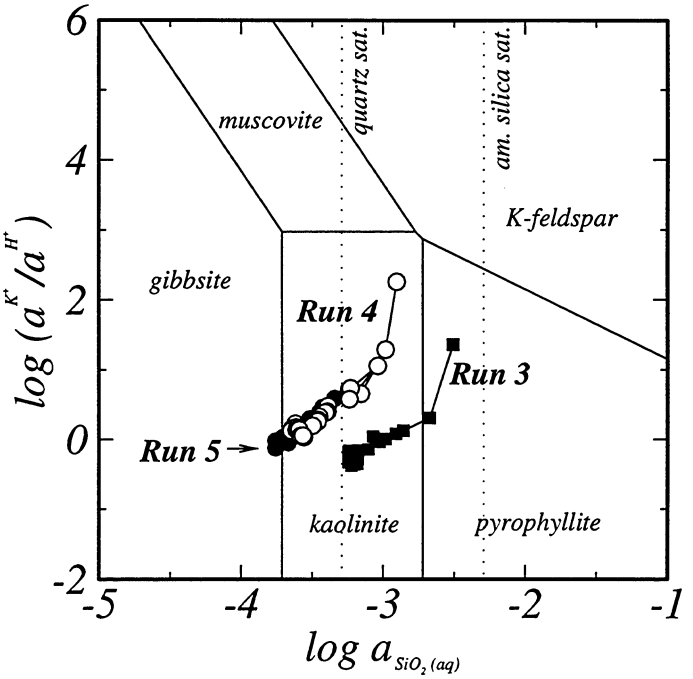

Figure 3.12. Logarithmic activity diagram for the system K_2O-Al_2O_3-SiO_2-HCl-H_2O at 80ºC and 166 bars. The stability boundaries were calculated using thermodynamic data given by Helgeson et al. (1978, 1981).

kaolinite stability field in the activity diagrams for the Na_2O-Al_2O_3-SiO_2-HCl-H_2O and the $K_2OAl_2O_3$-SiO_2-HCl-H_2O systems at 80°C and 1.6x10^{7}Pa (166 bars). Data of Run 3, which were reported in the 2nd Annual Progress Report (Dunn, 1995), are also plotted in those figures for comparison. These facts strongly suggest that concentrations of SiO_2, K, and Al are mainly controlled by hydrolysis reaction of potassium feldspar to form kaolinite, which is given by:

$$2KAlSi_3O_8 + 2H^+ + 9H_2O \rightarrow Al_2Si_2O_5(OH)_4 + 2K^+ + 4H_4SiO_4 \qquad (3.3)$$

The changing patterns of concentration of these constituents (i.e., jump up in the first sample and subsequent monotonous decrease, Fig. 3.3) suggest that the rate of this hydrolysis reaction (Reaction 3.3) is faster at the early stage of the runs and becomes slower with time (see the following section).

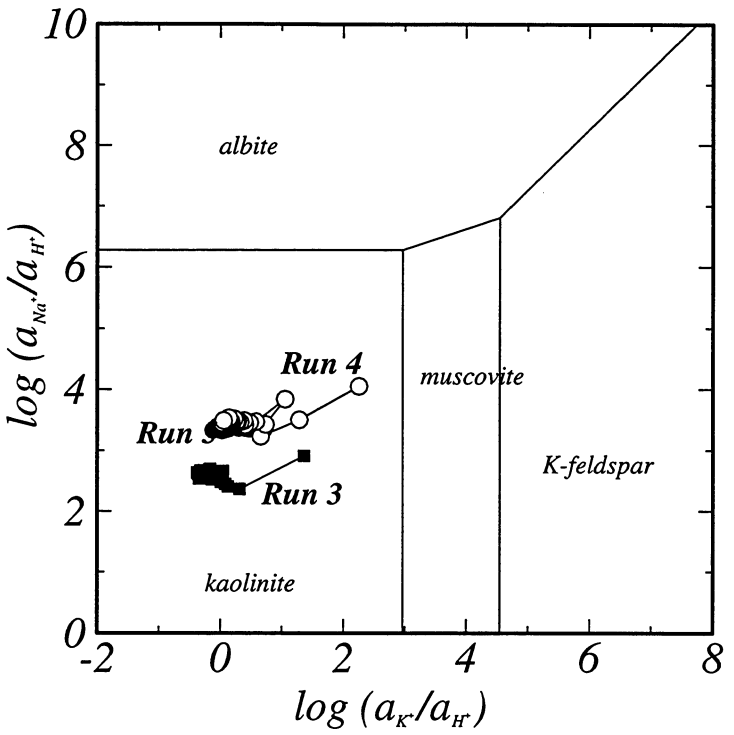

Figure 3.13. Logarithmic activity diagram for the system Na_2O-K_2O-Al_2O_3-SiO_2-HCl-H_2O at 80ºC and 166 bars. The stability boundaries were calculated at quartz saturation using thermodynamic data given by Helgeson et al. (1978, 1981).

The increase in Ca, Mg and alkalinity should be due to dissolution of dolomite. According to Busenberg and Plummer (1982), dissolution of dolomite is controlled by the following three reactions:

$$CaMg(CO_3)_{2(s)} + 2H^+ \rightarrow Ca^{2+} + Mg^{2+} + 2HCO_3^- \quad (3.4)$$

$$CaMg(CO_3)_{2(s)} + 2H_2CO_3^0 \rightarrow Ca^{2+} + Mg^{2+} + 4HCO_3^- \quad (3.5)$$

$$CaMg(CO_3)_{2(s)} + 2H_2O \rightarrow Ca^{2+} + Mg^{2+} + 2HCO_3^- + 2OH^- \quad (3.6)$$

They observed that the dissolution rate was proportional to the activity of H^+ below pH 6, whereas it is independent of the activity of H^+ above pH 8 in the absence of CO_2. In the presence of CO_2 (0 to 0.96 atm), the dissolution rate was proportional to the square root of P_{CO2} (i.e., equivalent to a_{H2CO3}) below pH 5.

They also observed that the reverse reaction becomes dominant in proportion to the activity of HCO_3^-. As the pH range of our solution was 4.03 to 4.85, Reaction 3.4 must be the dominant mechanism of dolomite dissolution in CO_2 flooding. The range of P_{CO2}, however, was much higher than those of Busenberg and Plummer (1982) (0 to 0.97 atm), so that the dominance of Reaction 3.5 and the reduction of the dissolution rate due to the reverse reaction are not clear in this study.

Another reaction important in these experiments was dissolution of anhydrite, which released Ca and SO_4 into solution (Figs. 3.1 and 3.2). A quite similar change in the Sr concentration was observed in Run 4 (Fig. 3.2, top) suggesting that this element was also released by dissolution of anhydrite. As shown in the following section, differences in concentrations between Ca and SO_4 (i.e., $C_{Ca} - C_{SO4}$; C is the molar concentration), which may be an indication of the amount of Ca released by dolomite dissolution, is in good agreement with the Mg increase, supporting dolomite and anhydrite as sources of Ca in the run. In a similar way, $C_{Ca} - C_{Mg}$ (calculated) in Run 5, which should give the net SO_4 released due to dissolution of anhydrite, is plotted against reaction time as well as measured concentration of Ca, Mg, and SO_4 in Figure 3.14. As seen in the figure, SO_4 concentration in Run 5 was much lower than expected from $C_{Ca} - C_{Mg}$. Crude oil was present in Run 5, and since crude oil is a strong reducing agent (e.g., Hunt, 1979), sulfate may be reduced and dissolved into the oil.

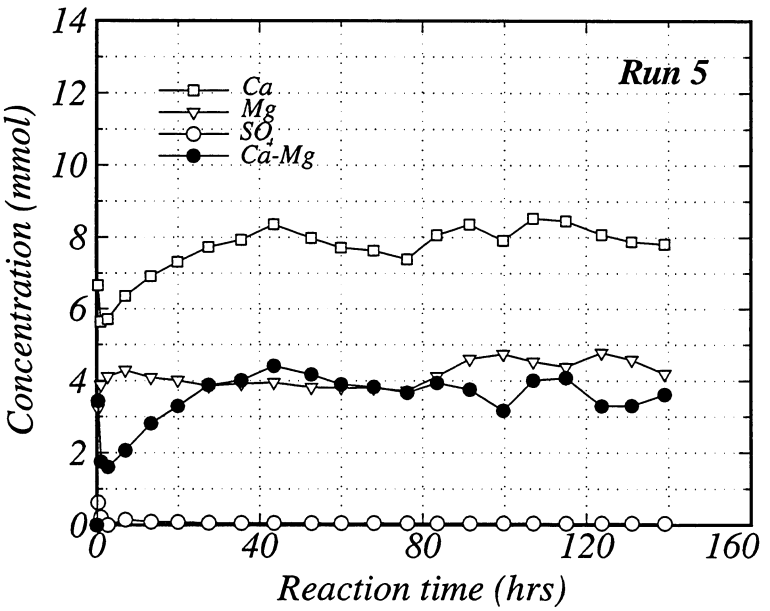

Figure 3.14. $C_{Ca} - C_{Mg}$ vs. reaction time in Run 5. Concentration of Ca, Mg, and SO_4 is also plotted.

The other difference in solution

chemistry between the two runs was the concentration change of Ba with reaction time (Fig. 3.2). In Run 4, it increased as the concentration of SO_4 decreased. As the solution in Run 4 was saturated with respect to barite throughout run, the concentration of Ba had to have been controlled by the solubility product of barite. However, in Run 5, the concentration of Ba first increased then decreased after 13.3 hrs., and the solution was undersaturated with respect to barite throughout the experiment. Also in Run 5, the SO_4 concentration was low throughout the experiment. This would cause an initial rapid dissolution rate for any barium-bearing minerals present which is indicated by the increase in barium concentration. Dissolution then results in less surface area being exposed to the carbonated water solution. Therefore, the Ba concentration in Run 5 had to have been controlled by mineral surface area not the barite solubility product.

Dissolution/Precipitation Rate of Minerals

Figures 3.15 and 3.16 show the relationship between the sum of the three minerals dissolved or precipitated (*e.g.*, dolomite, anhydrite, and potassium feldspar) and the volume of solution injected. The amount was calculated by multiplying the concentration of mineral constituents (Mg for dolomite, SO_4 for anhydrite, and K for potassium feldspar) by the volume of solution injected for each sample and summing them. The amount of dolomite dissolved in Run 4 was calculated from C_{Ca} - C_{SO4} as well as from Mg and they are in good agreement within errors (± 10%; 5% for both C_{Ca} and C_{SO4}). Note that linear trends suggest constant dissolution (positive slope) and precipitation (negative slope) rates. Also, the steeper the slope, the greater the dissolution/precipitation rate. These figures also show the results of Run 3 for comparison. The dissolution/precipitation rate of each mineral was calculated from the slope of the plot in Figures 3.15 and 3.16 for regions with constant slope; the results of the regression are listed in Table 3.3 (Note that the calculated rates are not normalized by the surface area of each mineral because of the lack of such data). Along with this calculation, the volume of mineral dissolved or precipitated was calculated by multiplying the amount of the index species by the molar volume of each mineral ($64.34 \times 10^{-6} m^3$/mole for dolomite, $45.94 \times 10^{-6} m^3$/mole for anhydrite,

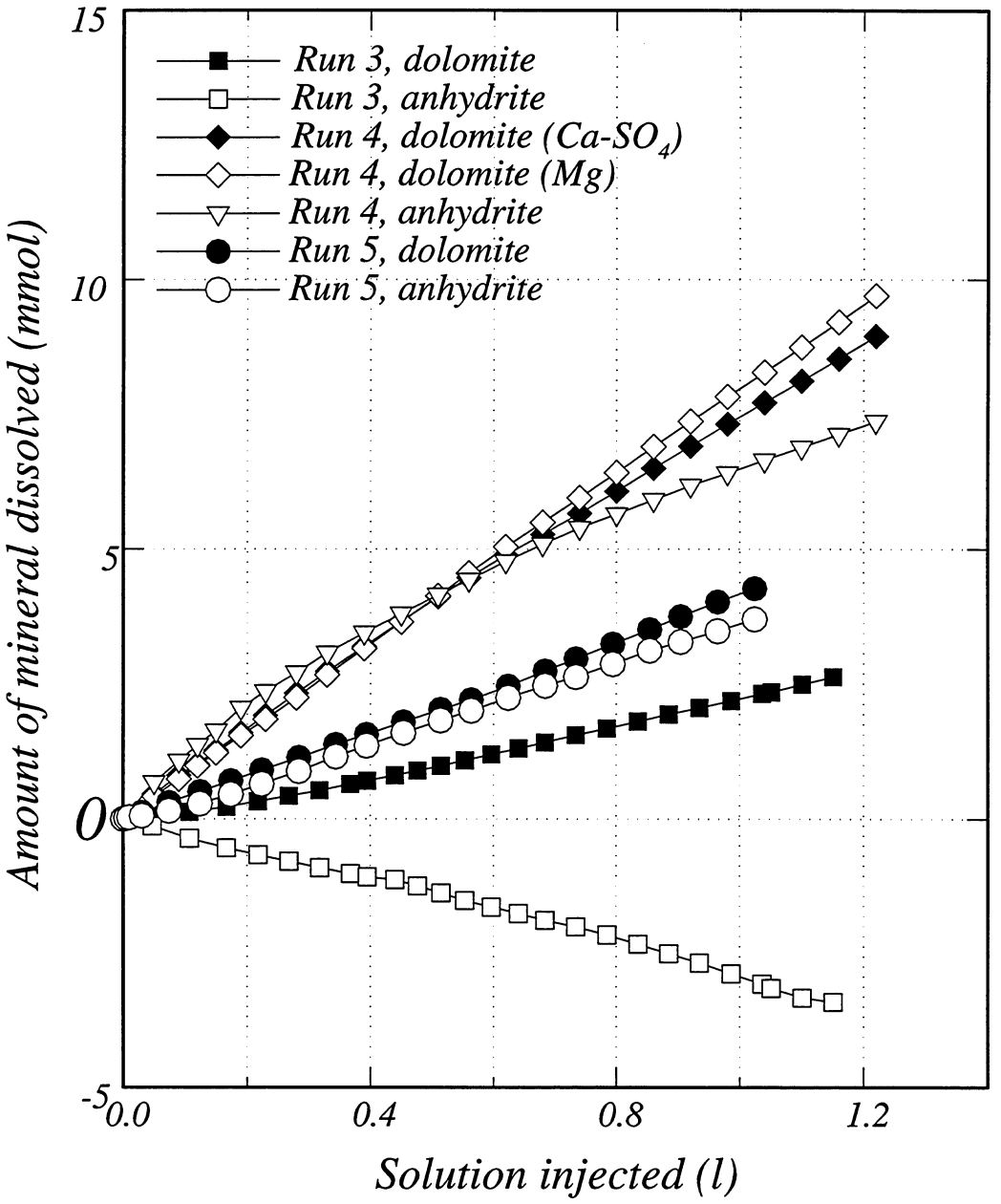

Figure 3.15. Total amount of dolomite and anhydrite dissolved or precipitated during CO_2 core flooding experiments, which is a function of the volume of solution injected.

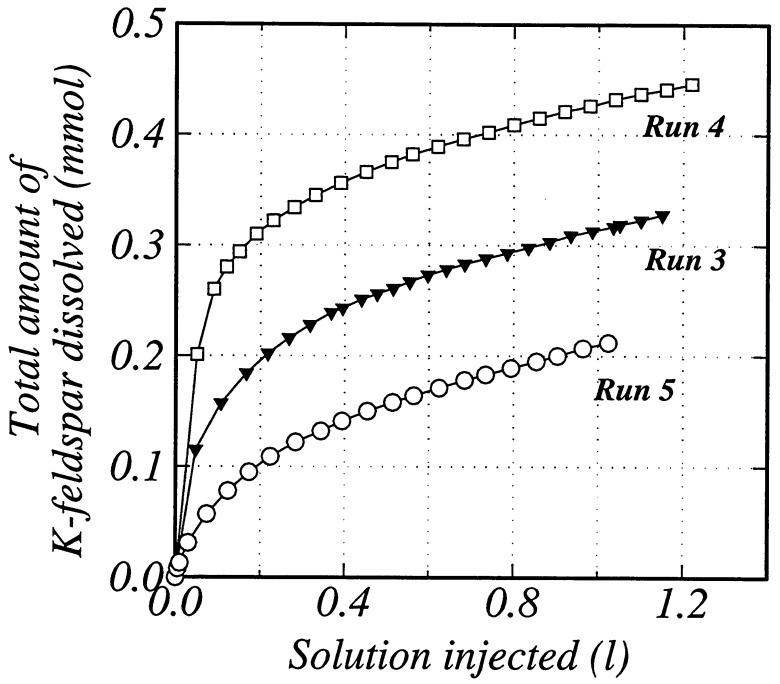

Figure 3.16. Total amount of K-feldspar dissolved during CO_2 core flooding experiments, which is a function of the volume of solution injected.

$108.9 \times 10^{-6} m^3$/mole for potassium feldspar; Robie, et al., 1978; Helgeson et al., 1981). The number of moles of kaolinite precipitated was calculated as half that of potassium feldspar by assuming the stoichiometry of Equation 3.3.

In general, the dissolution and precipitation rate of a mineral is given by:

$$R_{net} = -k_+ \prod_j a_j^{mj} \left[1 - exp\left(\frac{\Delta G_r}{RT} \right) \right]^n \tag{3.7}$$

Where R_{net} is the net rate of reaction determined by forward rate minus backward rate, and $-k_+$ is the rate constant of the forward reaction, a is the activity of species j in the rate-determining reaction, and ΔG_r is the chemical affinity of the reaction (e.g., Nagy et al., 1990, 1991; Nagy and Lasaga, 1992; Burch et al. 1993). By neglecting the effect of a_j on rate, Equation 3.7 can be simplified to the following form which is a function of chemical affinity (ΔG_r) only:

$$R_{net} = -k_+ \left[1 - exp\left(\frac{\Delta G_r}{RT} \right) \right]^n \tag{3.8}$$

Table 3.3: Results of calculation of volume of minerals dissolved or precipitated and rate of dissolution/precipitation.

Minerals	Run 3		Run 4		Run 5	
	volume (m^3)	*rate (mol/L)*	*volume (m^3)*	*rate (mol/L)*	*volume (m^3)*	*rate (mol/L)*
dolomite (*Mg*)	$1.7x10^{-7}$	$2.37x10^{-3}$	$6.2x10^{-7}$	$7.94x10^{-3}$	$2.7x10^{-7}$	$4.12x10^{-3}$
anhydrite (SO_4)	$-1.6x10^{-7}$	$-2.93x10^{-3}$	$3.4x10^{-7}$	$4.27x10^{-3}$*	$1.7x10^{-7}$	$3.7x10^{-3}$
potassium feldspar (*K*)	4.0x10-8	$0.102x10^{-3}$**	$5.0x10^{-8}$	$0.10x10^{-3}$ **	$2.0x10^{-8}$	$0.12x10^{-3}$ **
kaolinite (*0.5K*)	$-2.0x10^{-8}$		$-2.0x10^{-8}$		$-1.0x10^{-8}$	
total volume change	*$3.0x10^{-8}$*		*$9.9x10^{-7}$*		*$4.5x10^{-7}$*	

Positive and negative numbers represent dissolution and precipitation, respectively. Volume of kaolinite precipitated was calculated based on the stoichiometry of Equation 3.2. Dissolution and precipitation rates were calculated by regression of data of linear parts shown in Figure 4, that is, values with * and ** were calculated for the range of the injected solution of > 0.60L and > 0.550L, respectively, whereas others were done for full range.

Figure 3.17 shows, schematically, the relationship between R_{net} and ΔG_r with n = 1 and n = 2. The chemical affinity for the dolomite dissolution reaction was calculated and determined to be 5.80, - 3.96, and - 5.53 kcal/mole, respectively, for the last stages of Runs 3, 4, and 5. These values mean that the dissolution rate of dolomite for the three runs are on the *dissolution plateau,* at which the dissolution rate becomes independent of ΔG_r (see Fig. 3.17).

Lund et al. (1973) showed that dissolution of dolomite in HCl solution is controlled by diffusion at 100°C. Busenberg and Plummer (1982) suggested that the mechanism of dolomite dissolution may shift from surface-reaction control to diffusion-control between 50°C and 100°C. Therefore, dolomite dissolution may be controlled by diffusion partly (*i.e.*, mixed control) under the conditions of these experiments (80°C). The rounded dissolution textures seen in Figure 3.9 supports this point. The difference in hydrodynamic conditions among the three runs were, however, too small to explain the large differences in dissolution rates among the three runs. The factor most likely to have caused the differences in dissolution rates is differences in the mineral surface area exposed to the carbonated solution. Microscopic observation showed that cores used in Run 4 included much larger amounts of dolomite cement compared to those used in

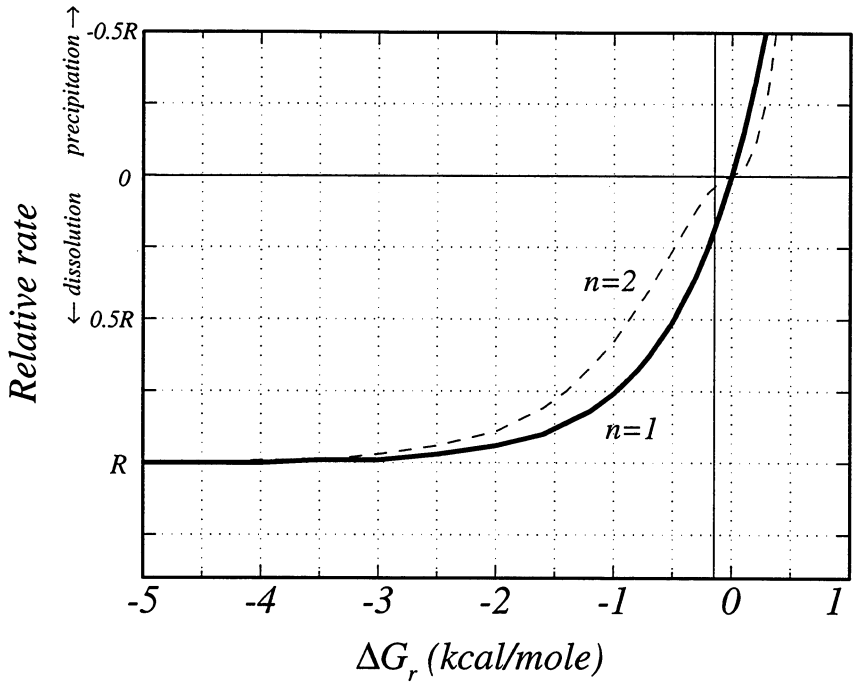

Figure 3.17. Relative dissolution/precipitation rate as a function of ΔG_r. Rate (R) is calculated by the model: $R = k(1-exp(\Delta Gr/RT))^n$.

Run 3. Cores used in Run 5 were not examined under an optical microscope, but oil used in the experiment would have effectively reduced the surface area of the mineral exposed to the carbonated water.

As seen in Figure 3.16, potassium feldspar dissolved at a rapid rate in the early stages of all three runs with that of Run 4 being the largest. The dissolution rate gradually decreased in all three runs becoming constant after the injection of 0.3L of solution. The calculated dissolution rates per volume of solution greater than 0.500L are similar in the three runs (Table 3.3). The pattern seen on Figure 3.16 is similar to the parabolic rate law, in which the dissolution rate of a mineral is proportional to the square of time, which was observed in early studies on feldspar dissolution by Wollast (1967), Helgeson (1971), and Busenberg and Clemency (1976). However, a subsequent study by Holdren and Berner (1979) showed that feldspar etched by hydrofluoric acid does not follow the parabolic rate law. They attributed the kinetic pattern to dissolution, at the early stage of the experiment, of very fine grains and strained particles. These formed during the grinding of material for the experiment, and they have a high surface energy. The cores used in the present study were not

treated with acid, and thus a higher dissolution rate at the early stage of the runs is probably due to dissolution of smaller grains and portions of crystals having higher lattice energy such as crystal defects. SEM observation of the altered potassium feldspars (Fig. 3.7) supports this interpretation. The dissolution of anhydrite in Run 4 showed a similar pattern of the parabolic rate law with smaller extent.

Porosity and Permeability Change

The total volume change due to mineral dissolution and precipitation was calculated to be $3x10^{-8}$ and $9.9x10^{-7}m^3$ in Runs 3 and 4, respectively (Table 3.2). The pore volume was measured after the experiment. The change in the pore volume determined by subtracting the pre- and post-experiment pore volume measurements was determined to be $1x10^{-7}m^3$ in Run 3 and $9x10^{-7}m^3$ in Run 4, respectively. Thus, numbers obtained by the two methods are in good agreement. The increase in pore volume in Run 4 was the largest in the top core, followed by the middle core. The bottom core showed no significant change in pore volume. Thus, more mineral dissolution took place at the injection end than at the effluent end.

The change in permeability for the three cores used in Run 4 did not follow the same pattern as the porosity. Both the injection and effluent ends showed decreases in permeability whereas the middle core showed an increase in permeability. The decrease in permeability is best explained by the precipitation of kaolinite. As seen in Figure 3.11, this mineral precipitated in pore spaces. Even though the volume precipitated is small, its crystal morphology is such that it reduces fluid flow.

Application to CO_2 Flooding in Tensleep Oil Reservoirs

We carried out simulations of mineral dissolution/precipitation to examine the effect of water-rock interaction during CO_2-flooding. The purpose of the simulations was to examine the potential for carbonate wellbore scale in Tensleep oil reservoirs. The simulations used results from our CO_2 core flooding experiments. The results from the experiments that were used in the

simulations include two parameters. We included the chemical evolution of the injected brines due to dissolution of dolomite and anhydrite. We also included the change in the aragonite saturation index as a function of decreasing pressure, in particular, the partial pressure of carbon dioxide. We carried out two simulations. One was for a brine-rock system based on the results of Runs 3 and 4 to estimate the effect of the original brine composition on the potential. A second simulation was for a brine-oil-rock system based on the results of Run 5 to evaluate the effect of oil on the potential for wellbore scale.

Simulation for Brine-Rock Systems

Figure 3.18 summarizes the procedures of the simulation. First, we assume that all cores were mineralogically homogenous. The dissolution rate per unit length of core was calculated for dolomite and anhydrite. This was done by dividing the dissolution rate from Table 3.3 by the full length of the core assemblages (0.225m and 0.213m for Runs 3 and 4, respectively). The calculated rate has units of mole L^{-1} m^{-1}. Simulation of chemical evolution was then carried out as follows: speciation of solution at Δx (Δx is the distance from the injection site) was calculated using *SOLMINEQ.88* after adding mineral constituents of $[R \times \Delta x]$ (mole L^{-1}) into two types of injection solution. Based on the speciation obtained, the dissolution rate for the next Δx was calculated by adopting the rate model $R = k[1\text{-}exp(\Delta G/RT)]$, which is shown in Figure 3.17 with n = 1. These procedures were repeated until the solution obtained saturation with respect to both dolomite and anhydrite. Temperature was kept constant at 80°C. The pressure gradient was set to 10^5Pa/m, and the relationship $P_{total} = P_{CO2}$ was maintained. The chemical composition of the solutions adopted in these simulations are listed in Table 3.4.

Table 3.4. Chemical composition of the injection solution used in simulations.

Constituents (mol/kg)	[A]	[B, C]
Na	90.0×10^{-3}	2.50×10^{-1}
Ca	16.3x10-3	0
Mg	16.3×10^{-3}	0
SO_4	32.5×10^{-3}	0
Cl	90.0×10^{-3}	2.50×10^{-1}

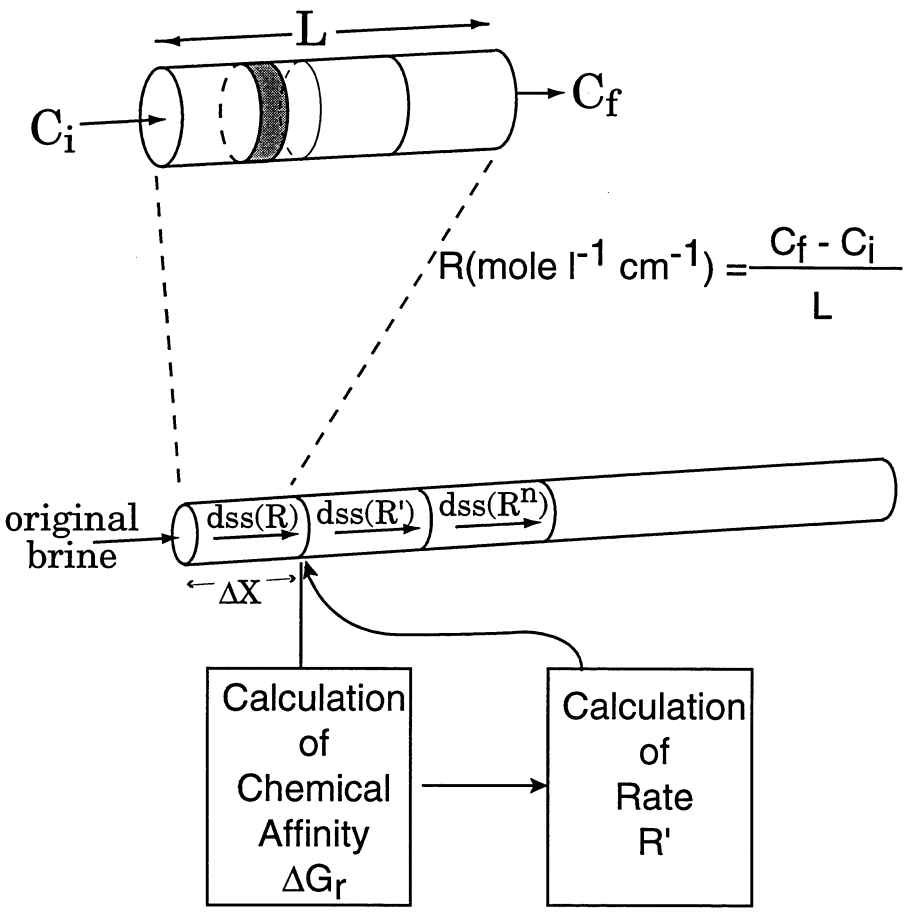

Figure 3.18. Procedures of simulation on dolomite and anhydrite dissolution.

Figures 3.19 and 3.20 show the results of the simulations using the dissolution rates and chemistry of injection water used in Run 3 (Simulation 1A) and Run 4 (Simulation 1B). As seen in these figures, the solution obtains saturation with respect to dolomite at a distance of 3m from the injection well in simulation 1A. Simulation 1A used the smallest dolomite dissolution rate of three obtained from the flooding experiments. In this simulation, the solution was originally saturated with respect to anhydrite, and the saturation index for anhydrite did not change with distance. In the case of Simulation 1B, the solution obtains saturation with dolomite after migrating a distance of only 1m (Fig. 3.20). Figure 3.20 also shows that the saturation state of dolomite is not affected by anhydrite dissolution. Figures 3.19 and 3.20 also show that the

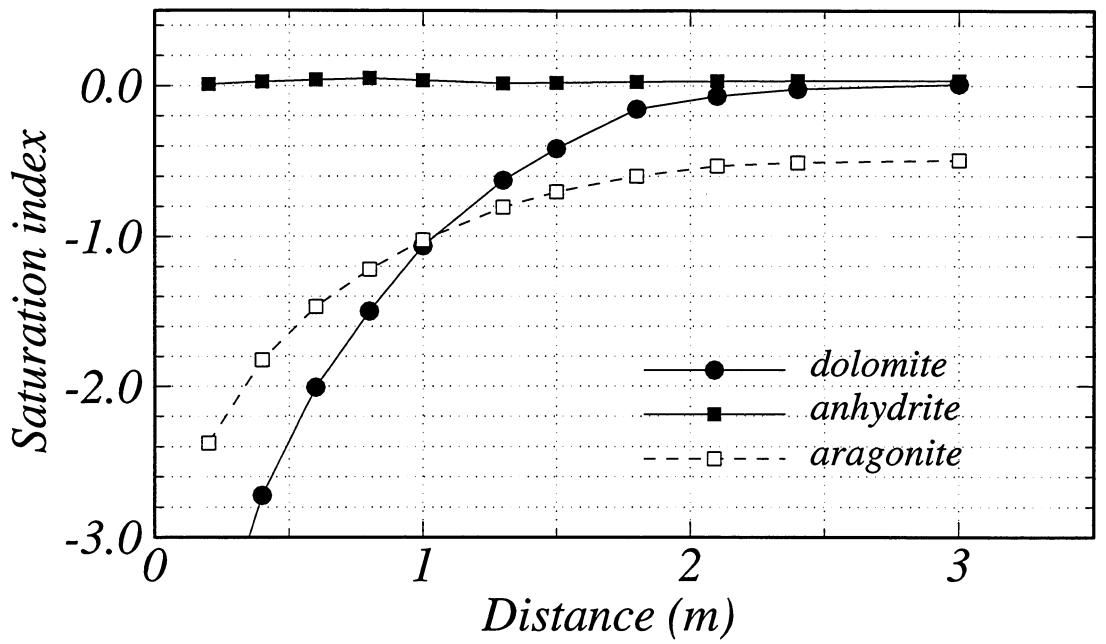

Figure 3.19. Change in saturation index of dolomite, anhydrite, and aragonite in Simulation A using experimental results of Run 3.

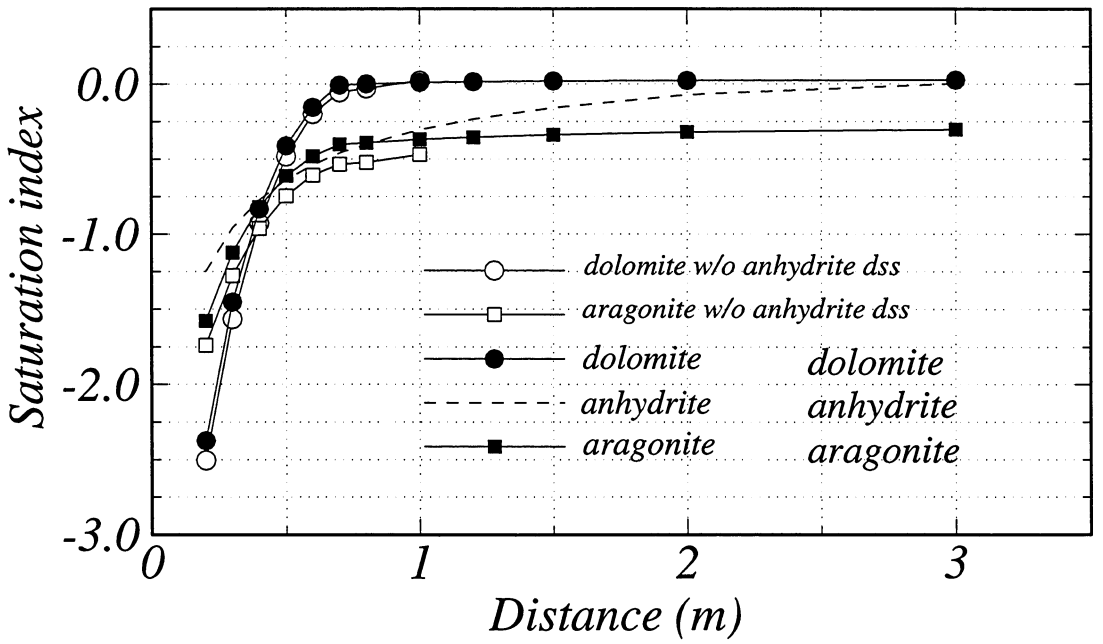

Figure 3.20. Change in saturation index of dolomite, anhydrite, and aragonite in Simulation B using experimental results of Run 4.

solution remains undersaturated with respect to aragonite even after the solution becomes saturated with respect to dolomite. These simulations demonstrate that injection solutions of water and CO_2 will become saturated with dolomite within very small distances from the injection well in real CO_2-flooding in dolomite bearing formations like the Tensleep Formation. Beyond that distance, no more dissolution of dolomite will take place.

The second part of the simulation was to calculate the amount of aragonite scale that would precipitate. The simulation allowed aragonite to precipitate until the solution was no longer oversaturated with respect to aragonite. These simulations specifically examined the effects of different changes in pressure. This simulates the field situation of a pressure drop (reduced P_{CO2}) as the injected solution flows into the production wellbore. Evolved brine solutions (due to mineral dissolution) obtained in the first part of the simulations were used. The results are shown in Figure 3.21. In Simulation B, the solution will be saturated with respect to aragonite at about 10^7Pa (100 bars). If the pressure in the production wellbore is 10^6Pa (10 bars) or less, then $28x10^{-3}$ mol/L of aragonite could precipitate. This indicates a high potential for

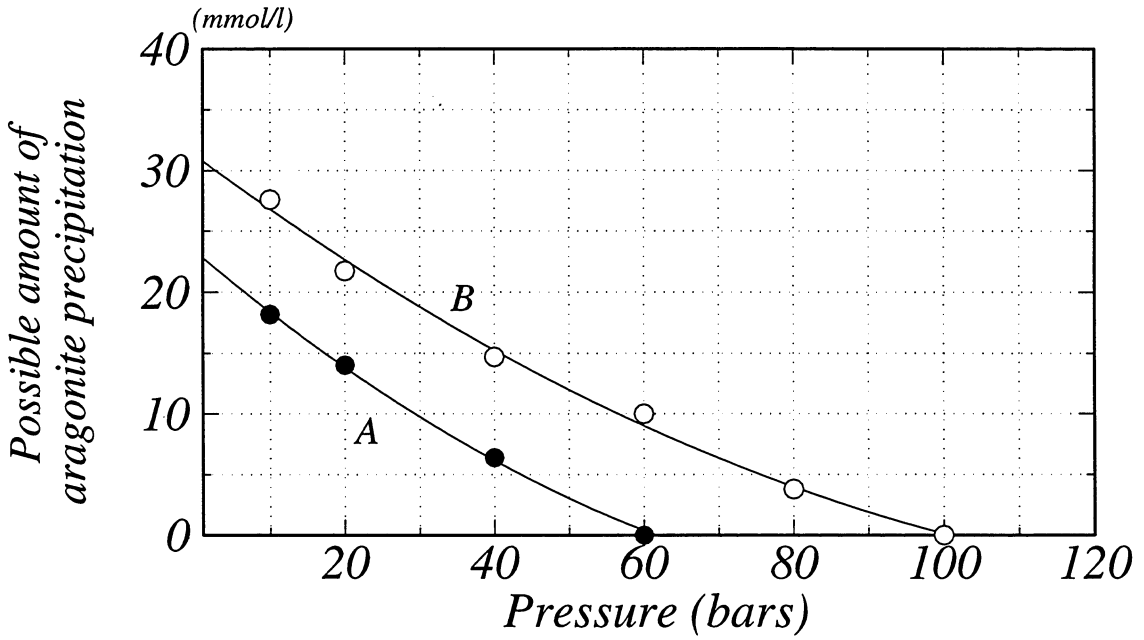

Figure 3.21. Potential aragonite scale formation as a function of pressure in Simulations A and B.

scale formation. Similarly, in Simulation A , the solution will be saturated with respect to aragonite at about $6x10^6$Pa (60 bars). If the pressure in the production wellbore is 10^6Pa (10 bars) or less, then $18x10^{-3}$ mol/L of aragonite could precipitate.

Before solutions reached equilibrium with dolomite and anhydrite at Δx = 3 m, 18.7 mol/L dolomite dissolved into solution A and $21.7x10^{-3}$ mol/L of dolomite and $28.4x10^{-3}$ mol/L of anhydrite dissolved into the solution B. Figure 3.22 shows the change in the activities of Ca^{2+}, Mg^{2+}, and CO_3^{2-} during the whole simulation process. In simulation A, $aCa2+$ increased from 3.68x10-3 to $5.33x10^{-3}$ (45% increase) due to the dissolution of dolomite. In contrast, in simulation B, $a_{Ca^{2+}}$ increased to $7.65x10^{-3}$ due to dissolution of dolomite and anhydrite in solution B. The value of $a_{CO_3^{2-}}$ of solution B was only 7% larger than that of solution A. Thus, the product of $a_{Ca^{2+}}a_{CO_3^{2-}}$ of solution A became smaller than that of solution B, whereas the product of $a_{Ca^{2+}}a_{Mg^{2+}}(a_{CO_3^{2-}})^2$ was equal to that of solution B. As is seen in Figure 3.22, this situation does not change with any drop in pressure. Thus, solution B should have a higher potential for aragonite scale formation at all pressures.

Simulation in Brine-Oil-Rock System

One simulation was carried out for the brine-oil-rock system using results from Run 5. This simulation is referred to as Simulation C. In this simulation, the original brine composition was the same as that used in Simulation B. During the first part of the simulation, the SO_4 concentration was kept at $0.45x10^{-3}$ mol/L. This is the value observed at a steady state in Run 5, despite anhydrite dissolution. As noted in the results section above, this constant sulfate concentration was probably due to reduction of SO_4 by oil. The effect of P_{CO2} on the dissolution of dolomite was also checked in this simulation. In Simulations A and B, the relation of $P_{total} = P_{CO2}$ was held. Crude oil, however, has a high solubility of CO_2 gas. A calculation of the amount of CO_2 dissolved in Tensleep crude oil (based on the method of ASTM, 1985) yields 1.02 wt% CO_2 at 80°C and P_{CO2}=$1.66x10^7$Pa (166 bars) which were the P-T conditions used in Run 5. Therefore, the injected CO_2 gas could dissolve completely into the oil and

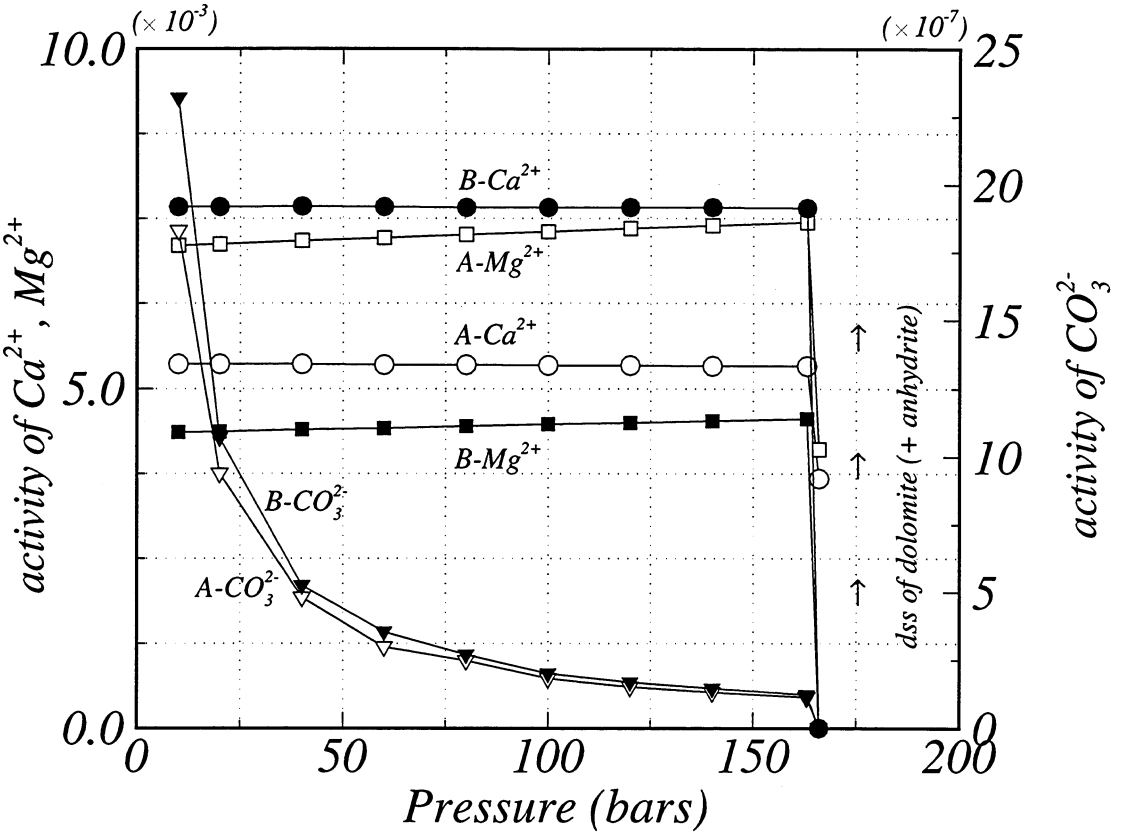

Figure 3.22. Change in a_{Ca2+}, a_{Mg2+}, and a_{CO32-} during Simulations A and B.

water phases when the oil/water ratio is high (miscible injection). In this case, the relationship $P_{CO2} < P_{total}$ would be plausible. Note that P_{CO2} in this case will be an imaginary value that is given by $a_{H_2CO_3}{}^{0} / k_H$, where k_H is the Henry's Law constant.

Figure 3.23 shows dolomite dissolution results of Simulation C for four cases of P_{CO2} in relation to P_{total}. The figure demonstrates that the solution will obtain saturation with respect to dolomite before the solution migrates a distance of 2m. As seen in the figure, solutions with lower partial pressures of carbon dioxide become saturated at smaller migration distances.

The potential for aragonite scale formation as a function of pressure was calculated after adding Ca and SO_4 to obtain saturation with respect to anhydrite. This was done because the solution was still highly undersaturated with respect to anhydrite at the point where dolomite saturation was reached.

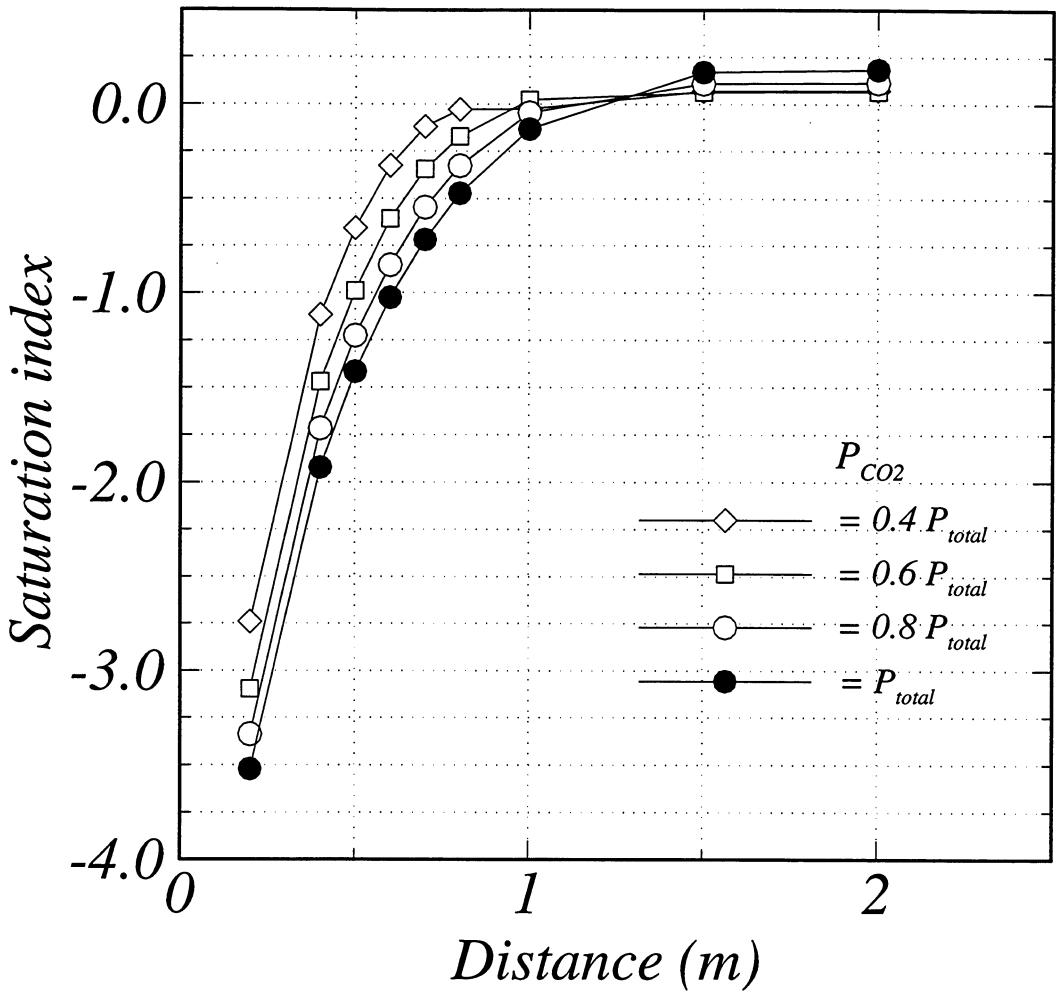

Figure 3.23. Change in saturation index of dolomite, anhydrite, and aragonite in Simulation C using experimental results of run 5.

The results are shown in Figure 3.24. The figure demonstrates that the solution would have high potential for aragonite scale precipitation and that as P_{CO2} becomes lower (*i.e.*, P_{CO2}/P_{total} becomes smaller), the potential for wellbore scale would be reduced. For example, when $P_{CO2} = 0.4P_{total}$, the potential would be reduced 47% compared to the case of $P_{CO2} = P_{total}$ at 10^6Pa (10 bars). The figure shows the results without addition of Ca and SO_4 for the case of $P_{CO2} = 0.4P_{total}$.

Figure 3.25 shows the relationship between amounts of dolomite and anhydrite dissolved before the effect of different pressures was checked (shown on Fig. 3.23). Figure 3.25 indicates that a decrease in P_{CO2} relative to the total

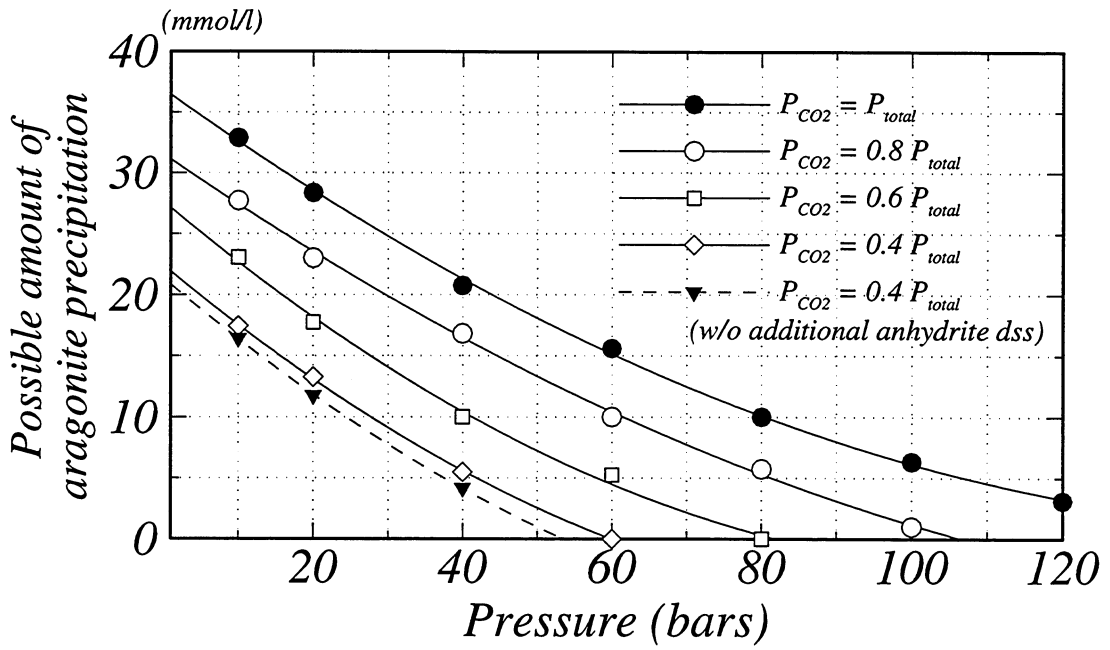

Figure 3.24. Potential aragonite scale formation as a function of pressure in Simulation C.

pressure reduces the amount of dissolution of both minerals. At lower P_{CO2}, the solution pH should be higher than that at higher P_{CO2} and this should raise $a_{CO_3^{2-}}$ to reduce the degree of undersaturation with respect to dolomite, thereby reducing the amount of dolomite that would dissolve.

Factors Affecting Aragonite Scale Formation

The simulations showed that the potential for aragonite scale formation would depend on the amount of dolomite as a source of Ca and alkalinity and on the amount of anhydrite as a source of Ca. The simulations also showed that the amount of dolomite and anhydrite dissolution needed to obtain saturation with aragonite depends upon two parameters. First, the chemistry of the injected solution is important; solutions containing abundant Mg and SO_4 will have lower risk of carbonate scale formation compared to solutions that are poor in those constituents. Second, the P_{CO2} of the system is important; a lower P_{CO2} during a CO_2 flood would help reduce the potential of scale formation. Third, oil reservoirs having higher oil:brine ratios will have lower potential of carbonate scale formation.

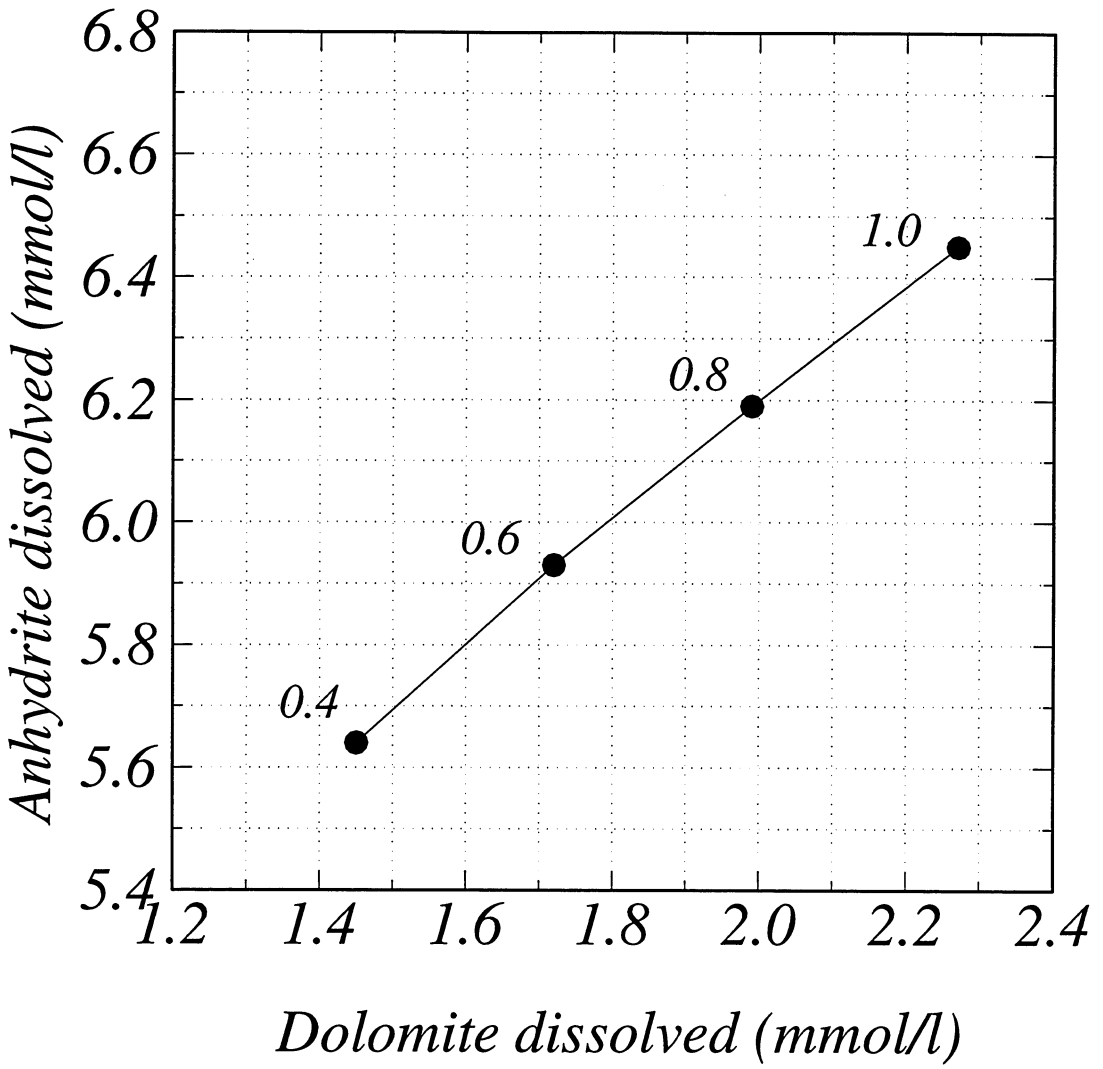

Figure 3.25. Dolomite dissolved vs. anhydrite dissolved in Simulation C.

In the first and second annual reports, Tensleep Formation waters were classified into four types, that is, Type A1- Ca-Mg-HCO_3 type, Type A2: Ca-$MgSO_4$ type, Type A3: Ca-Na-SO_4 type, and Type B: Na-SO_4-Cl type (Dunn, 1994, 1995). From the viewpoints of solution chemistry, Type A2 waters would be the most suitable for the injection water of CO_2 flooding. Type B waters could cause the highest potential of scale formation, so Tensleep oil fields on the western side of the Bighorn Basin may have higher susceptibility to formation damage and scale formation than those on the eastern side (Fig. 3.26).

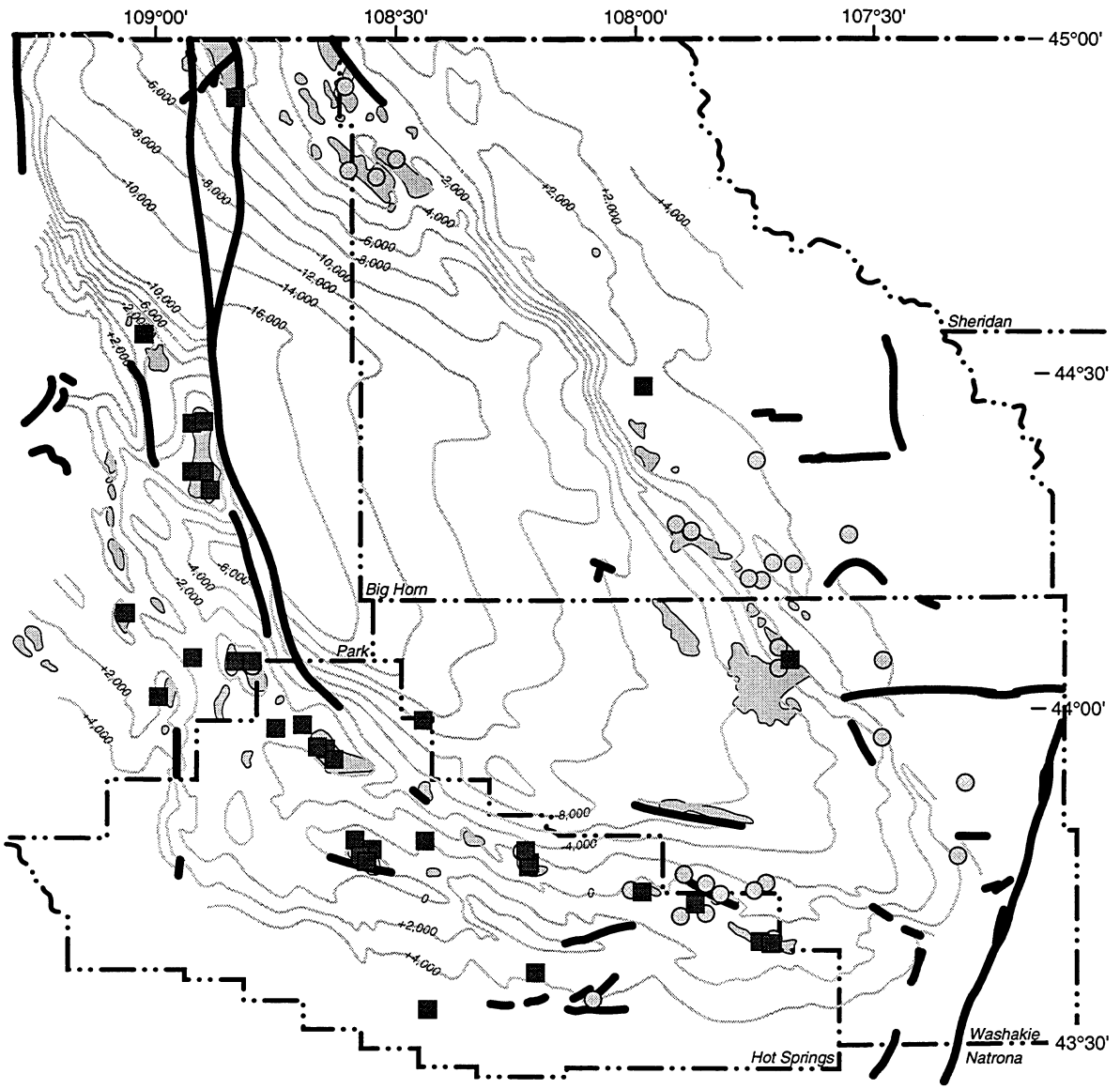

Figure 3.26. Map of the Bighorn Basin showing Tensleep Formation brine susceptibility to scale formation when those waters are used as injection water during CO2 enhanced oil recovery.

Conclusions of CO_2 Coreflood Experiments and Simulations

Experiments on CO_2 core flooding using cores and crude oil from the Tensleep Sandstone and using synthetic aqueous solutions, which were run under typical Tensleep oil reservoir conditions in the Bighorn Basin, Wyoming (*i.e.*, 80°C and 1.66×10^7Pa (166 bars)), clarified the nature of water-rock interaction under high partial pressure of carbon dioxide.

Dissolution of dolomite and anhydrite and hydrolysis of potassium feldspar to form kaolinite were three major reactions that determined the final solution chemistry. The formation of kaolinite in pore spaces probably resulted in a decrease in the permeability of the cores despite a porosity increase from dissolution of cement minerals. In the experiment in which crude oil was used, SO_4 released from anhydrite was reduced by crude oil and remained low in concentration throughout the run. The low concentration of SO_4 resulted in high concentrations of Ba. Dolomite dissolved into the solutions at a rapid dissolution rate, whereas all effluent solutions remained undersaturated with respect to this mineral. The dissolution rate (defined as concentration change in mineral constituents per migration distance) of the two runs were 7.94×10^{-1} and 4.12×10^{-1} mol L^{-1} m^{-1}, respectively (the rate of Run 3 that was run in the second year was 2.37).

Simulations using these rate data, as well as the model given by $R = k[1 \exp(\Delta G / RT)]$, showed that the injected solution will obtain saturation with dolomite near the injection well (within several meters), and thus no further dissolution will take place. Simulation on the pressure dependence of the saturation of aragonite in the evolved solution showed that the solution would have a high potential for aragonite scale formation at pressures $\leq 10^7$Pa (100 bars). Results also indicate that solutions containing Mg and SO_4 dissolve less dolomite and anhydrite compared to solutions that are free of those constituents and that this also reduces the potential for aragonite scale. Based on real formation water chemistry of Tensleep reservoirs as well as these results, oil reservoirs with Type A2 formation water will have the least risk of wellbore scale, whereas oil reservoirs with NaCl type waters will have a higher risk of scale formation.

Results of the experiments and simulations which included crude oil (run 5 and Simulation C) showed that at the injection well, $P_{CO2} < P_{total}$ causes less dolomite and anhydrite dissolution. This, in turn, reduces the potential for aragonite scale in the production wells. Also, CO_2 flooding in reservoirs with higher oil/brine ratios will have a lower risk of wellbore scale formation.

IMPROVED OIL RECOVERY

Introduction

Recent work by Tang and Morrow (1996), Yildiz (1995), and Yildiz and Morrow (in press) has shown that oil recovery from waterflooding is sensitive to the composition of the injected brine. The experiments of Yildiz (1995) and Yildiz and Morrow (in press) use an injected brine of 2% $CaCl_2$ and a connate brine of 4% NaCl + 0.5% $CaCl_2$. Compared to the base case where the injected and connate brines are both the Na-Ca-Cl composition, oil recovery improved by 7.3%. Recovery improved even when the composition of the injected brine was changed after the waterflood was in progress (Fig. 3.27). Tang and Morrow (1996) showed that injected brine that was more dilute than the connate brine resulted in improved recovery (Fig. 3.28). An injected brine with a total dissolved solids (TDS) that was 10% of the connate brine resulted in a 2% improvement in oil recovery compared to the base case of where the injected and connate brine were the same. Diluting the injected brine such that its TDS was

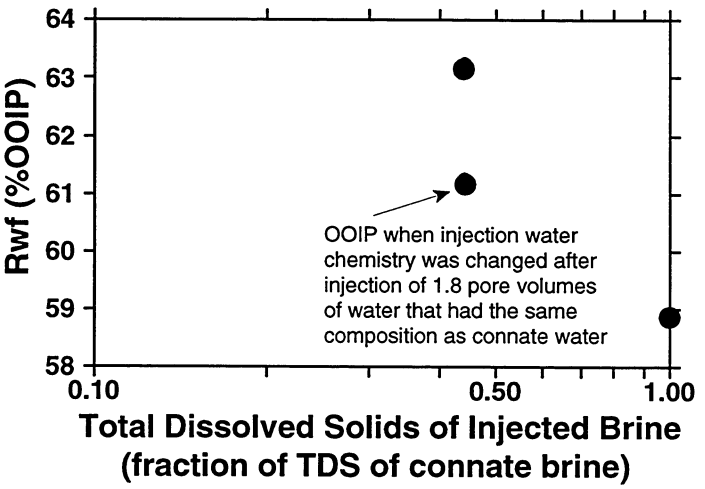

Figure 3.27. Total dissolved solids (TDS) of Injection brine vs. oil recovery (percent of original oil in place). Injection brine composition is reported as a fraction of the total dissolved solids of the connate brine. Data are taken from figures 1a, 2b, and 4a of Yildiz and Morrow (in press) using the values at 4PV. Note the increase in recovery when injection water is more dilute than connate water.

1% of the connate brine improved the oil recovery by 10% compared to the base case. Also, recent results showed increase in recovery of over 10% when dilute brines of either calcium, sodium, aluminum, magnesium, or potassium were injected into a sandstone core containing crude oil composition after injeciton of one pore volume of the formation (N.R. Morrow, pers. comm).

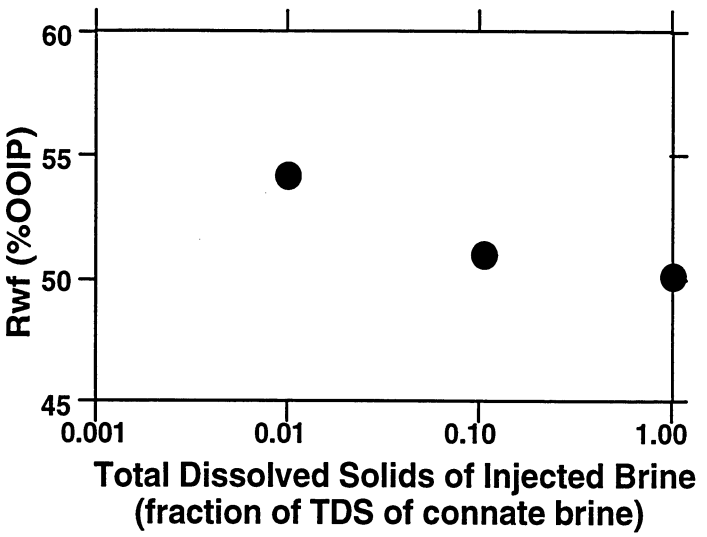

Figure 3.28. Total dissolved solids (TDS) of Injection brine vs. oil recovery (percent of original oil in place). Injection brine composition is reported as a fraction of the total dissolved solids of the connate brine. Data are taken from figures 3b and 4b of Tang and Morrow (1996) using the values at 4PV.

Typically, Tensleep waterflood projects in the Bighorn and Wind River basins re-inject Tensleep produced water. However, the experiments described above indicate that if a different injection water composition was used, recovery would improve. The results of the experiments described above were used along with our work on the distribution of Tensleep Formation water chemistry to estimate potential oil recovery improvement for Tensleep fields in the Bighorn and Wind River basins.

Methodology

Remaining recoverable oil was estimated for all the Tensleep fields in the Bighorn and Wind River basins using the published values for the estimated ultimate recovery (EUR) (Wyoming Geological Assoc., 1989) and subtracting the cumulative production through June 1995. For many of the fields, EUR was not available. However, cumulative production through 1989 closely correlated with the EUR, therefore that relationship was used to estimate EUR for fields where that information was not reported. Remaining recoverable for each field was then increased by different percentages estimated from the formation water

chemistry and the experimental results. Table 3.5 shows the fields, EUR, cumulative production through June 1995, and the remaining recoverable oil prior to any improvements in recovery attributable to changing the chemistry of injected water.

Tensleep fields with the highest TDS (>20,000ppm) were assumed to be able to achieve the greatest improvements in recovery because with these fields, the greatest difference between connate and injection water TDS could be achieved. These were given a value of 10% recovery improvement because this was a reasonable value of percent incrase observed in various experiments. Other fields were assigned lesser values of percent recovery improvement based on the TDS of their produced water: 9% for TDS between 10,000 and 20,000ppm, 6% for TDS between 4,000 and 10,000ppm, 4% for 2,000 - 4,000ppm, and 0% for TDS less than 2,000ppm. Where the water chemistry of a field was not known, we assumed a TDS value between 4,000 and 10,000ppm (and therefore a recovery improvement of 6%) bescause that is the most common TDS range for the other fields. All these percentages are within the range observed by Yildiz (1995), Yildiz and Morrow (in press), and Tang and Morrow (1996). Figure 3.29 shows the Tensleep fields in the Bighorn Basin and the percent recovery improvement that was assumed for each field.

Table 3.5. Fields and Production Data Used in Improved Recovery Calculations.

Field	Total Dissolved Solids (ppm)	Cumulative Production (MMBO) (MMBO)	Estimated Ultimate Recovery (MMBO)	Remaining Recoverable Oil	Incremental Recovery (MMBO)
Alkali Anticline	4506	2.70	3.13	0.432	0.026
Beaver Creek	n/a	81.9	103	20.8	1.249
Big Polecat	3044	6.49	6.70	0.206	0.008
Big Sand Draw	n/a	54.5	67.8	13.2	0.794
Black Mountain	2868	12.7	23.5	10.8	0.430
Bonanza	1834	41.7	43.0	1.34	0.000
Byron	3535	18.6	22.5	3.95	0.158
Casper Creek S	n/a	13.3	22.8	9.49	0.569
Circle Ridge	n/a	12.3	13.1	0.735	0.044
Clark Ranch	n/a	1.64	1.75	0.109	0.007
Cody	n/a	6.01	7.10	1.09	0.066
Cottonwood Creek	4004	1.61	1.80	0.187	0.011
Cowley	2829	0.853	0.964	0.111	0.004
Dallas	n/a	0.426	0.474	0.048	0.003

Table 3.5. (Cont.)

Field	Total Dissolved Solids (ppm)	Cumulative Production (MMBO) (MMBO)	Estimated Ultimate Recovery (MMBO)	Remaining Recoverable Oil	Incremental Recovery (MMBO)
Deaver North	4108	1.43	1.50	0.067	0.003
Derby	n/a	0.201	0.219	0.019	0.001
Elk Basin	11725	187	239	52.0	4.683
Elk Basin South	n/a	14.5	17.5	2.99	0.179
Emerald	n/a	1.42	1.54	0.112	0.007
Ferguson Ranch	n/a	0.487	0.543	0.056	0.003
Fourbear	3132	23.1	28.1	5.04	0.202
Frannie	4164	112	130	17.6	1.054
Garland	3659	93.3	103	9.81	0.392
Gebo	4478	1.91	2.20	0.289	0.017
Gooseberry	5121	0.089	0.095	0.007	0.000
Half Moon	4431	3.98	4.66	0.680	0.041
Hamilton Dome	5495	172	179	6.29	0.377
Hidden Dome	2664	7.25	8.61	1.36	0.054
Homestead	2819	1.53	1.76	0.223	0.009
Lake Creek	8282	7.51	9.13	1.62	0.097
Lamb	n/a	0.579	0.605	0.027	0.002
Lander	n/a	6.73	7.97	1.24	0.075
Little Buffalo Basin	4404	88.6	111	22.7	1.363
Little Polecat	n/a	0.656	0.737	0.081	0.005
Little Sand Draw	3686	1.23	1.40	0.172	0.007
Manderson	4358	1.10	1.26	0.151	0.009
Murphy Dome	2871	38.7	47.7	9.01	0.361
Neiber Dome	n/a	1.38	1.39	0.011	0.001
Notches	n/a	10.8	13.0	2.24	0.135
Nowood Southeast	n/a	0.619	0.637	0.018	0.001
Oil Mountain	n/a	0.189	0.195	0.006	0.000
Oregon Basin	6660	16.3	19.8	3.42	0.205
Pilot Butte	n/a	1.13	1.29	0.155	0.009
Pine Mountain	n/a	0.111	0.119	0.009	0.001
Pitchfork	3814	43.3	57.7	14.4	0.576
Poison Spider	n/a	0.232	0.256	0.024	0.001
Rawhide	3433	0.034	0.036	0.002	0.000
Riverton Dome	n/a	3.02	3.51	0.493	0.030
Sage Creek	4278	12.2	13.8	1.66	0.100
Sage Creek West	3064	1.15	1.30	0.158	0.006
Sand Draw North	n/a	0.271	0.298	0.027	0.002
Sand Draw South	n/a	2.03	2.34	0.310	0.019
Sheldon	n/a	2.04	2.35	0.312	0.019
Sheldon Northwest	n/a	0.800	0.903	0.103	0.006
Shoshone	n/a	0.208	0.227	0.020	0.001
Shoshone North	n/a	0.246	0.270	0.024	0.001
Spring Creek South	3233	15.4	30.2	14.7	0.590
Steamboat Butte	n/a	67.6	70.0	2.42	0.145
Sunshine North	1508	1.96	2.85	0.889	0.000
Torchlight	4283	3.78	3.80	0.017	0.001
Whistle Creek	n/a	4.82	5.67	0.848	0.051
Winkleman	n/a	57.2	71.1	13.9	0.837
Worland	4524	1.58	1.86	0.279	0.017

n/a=not available

Results and Discussion

The calculations show that a waterflood with injection water chemistry that is either more dilute or more concentrated than the formation water for the Tensleep fields listed in Table 3.5 may considerably prolong the life of a field. Total incremental recovery is over 15 MMBO. This would result in over $11 million to the State of Wyoming in severance tax alone assuming a low oil price of $13/bbl. Since many of these fields cover Federal and State lands, the incremental recovery would also result in royalty income for both the state and the federal government. Not all of the Tensleep fields in the two basins are represented in Table 3.5 and in these calculations because production data were not available for all the fields. Also not reflected in these calculations are fields where Tensleep production has been shut-in or abandoned but which may benefit from this technique. Thus these numbers represent conservative estimates for incremental recovery by using injection water that is different from Tensleep connate water in waterflooding projects.

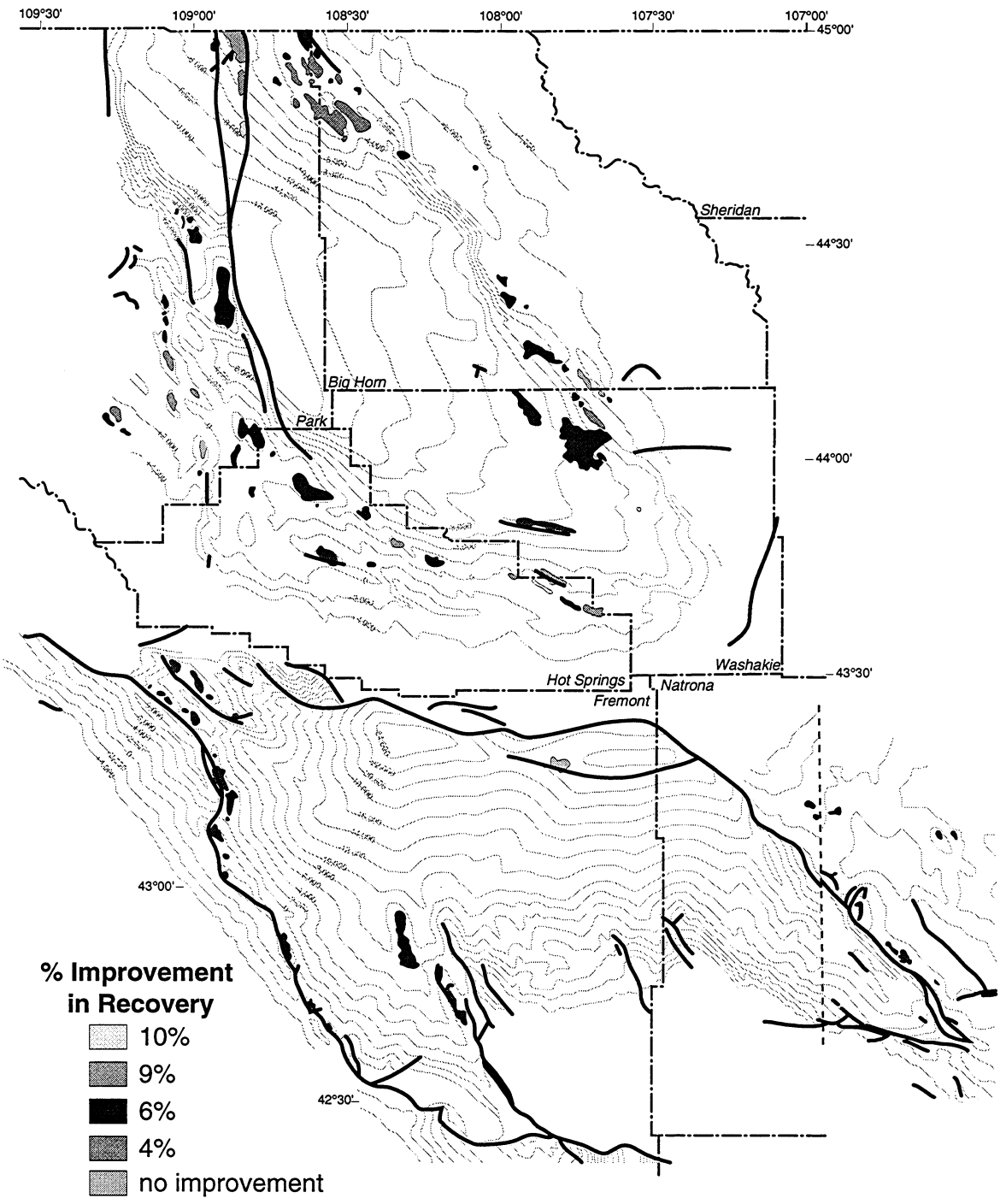

Figure 3.29. Map of Bighorn and Wind River basins showing the anticipated percent increase in oil recovery when waterflood injection water chemistry is different from connate water chemistry. The percent increase is based on the experiments of Tang and Morrow (1996), Yildiz (1995), and Yildiz and Morrow (in press) and on the existing formation water chemistry as described in the text.

REFERENCES

Agatston, R.S., 1952, Tensleep Formation of the Bighorn Basin: Wyoming Geological Association, Seventh Annual Field Conference Guidebook, p. 4448.

Agatston, R.S., 1954, Pennsylvanian and lower Permian of northern and eastern Wyoming: American Association of Petroleum Geologists Bulletin, v. 38, p. 508-583.

Ajdari, I., 1995, Anisotropy of relative permeability within the Tensleep Sandstone: M.S. thesis, University of Wyoming, 106 p.

American Society of Testing and Materials, 1985, Standard method for estimation of solubility of gases in petroleum liquids: Annual Book of ASTM Standards 05-02, 669-673.

Amyx, J.W., Bass, D.M., and Whiting, R.L., 1960, Petroleum Reservoir Engineering, Physical Properties: New York, McGraw-Hill Book Co., 610 p.

Andrews, S., and Higgins, L.S., 1984, Influence of depositional facies on hydrocarbon production in the Tensleep Sandstone, Big Horn Basin, Wyoming; A working hypothesis: Wyoming Geological Association 35th Annual Field Conference Guidebook, p. 183-197.

Atkinson, G., Raju, K., and Howell, R. D. ,1991, The thermodynamics of scale prediction: SPE Paper 21021, Society of Petroleum Engineers International Symposium on Oilfield Chemistry, 209-214, Anaheim, CA.

Bourke, L., Delfiner, P., Trouiller, J.D., Fett, T., Grace, M., Luthi, S., Serra, O., and Standen,E. 1989, Using formation microscanner images: The Technical Review (Schlumberger), v. 37, p. 16-40.

Bowker, K. A. and Shuler, P. J., 1991, Carbon dioxide injection and resultant alteration of the Weber sandstone, Rangely Field, Colorado: American Association Petroleum Geologist Bulletin, v. 75, p. 1489-1499.

Brainerd, A.E., and Keyte, I.A., 1927, New faunal evidence from Tensleep Formation: Journal of Paleontology, v. 1, p. 173-174.

Branson, C.C., 1939, Pennsylvanian formations of central Wyoming: Geological Society of America Bulletin, v. 50, p. 1199-1226.

Breed, C.S., and Grow, T., 1979, Morphology and distribution of dunes in sand seas observed by remote sensing, *in* E. McKee, ed., A Study Of Global

Sand Seas: United States Geological Survey Professional Paper 1052, p. 253302.

Breed, C.S., Fryberger, S.C., Andrews, S., McCauley, C., Lennartz, F., Gebel, D., and Horstman, K., 1979, Regional studies of sand seas using landsat (ERTS) imagery, *in* E. McKee, ed., A study of global sand seas: United States Geological Survey Professional Paper 1052, p. 305-397.

Brookfield, M.E., 1977, The origin of bounding surfaces in ancient eolian sandstones: Sedimentology, v. 24, p. 303-332.

Buckley, S.E., and Leverett, M.C., 1942, Mechanism of fluid displacement in sands, Transactions AIME, v. 146, p. 107-116.

Burch, T. E., Nagy, K. L., and Lasaga, A. C., 1993, Free energy dependence of albite dissolution kinetics at 80°C and pH 8.8: Chemical Geology, v. 105, p. 137-162.

Busenberg, E. and Clemency, C. V., 1976, The dissolution kinetics of feldspars at 25°C and 1 atm CO_2 partial pressure: Geochimica et Cosmochimica Acta, v. 40, p. 41-49.

Busenberg, E. and Plummer, L. N., 1982, The kinetics of dissolution of dolomite in CO_2-H_2O systems at 1.5 to 65°C and 0 to 1 atm P_{CO2}: American Jour. Science v. 282, p. 45-78.

Carmen, P.C., 1937, Fluid flow through granular beds: Transactions in Industrial Chemical Engineering, v. 15, p.150-166.

Carr-Crabaugh, M., and Dunn, T.L., 1996, reservoir heterogeneity as a function of accumulation and preservation dynamics, Tensleep Sandstone, Bighorn and Wind River basins, Wyoming, *in* M. Longman and M. Sonnenfeld, eds., Paleozoic Systems Of The Rocky Mountain Region: Rocky Mountain Section, SEPM, p. 305-320.

Chandler, M. A., Goggin, D.J., and Lake, L.W., 1989. Field measurement of permeability using a minipermeameter: Journal Of Sedimentary Petrology, v. 59, no.4 p. 613-615.

Chandler, M.A., Kocurek, G., Goggin, D.J., and Lake, L.W., 1989, Effects of stratigraphic heterogeneity on permeability in eolian sandstone sequence, Page Sandstone, northern Arizona: American Association Of Petroleum Geologists Bulletin, v. 73, p. 658-668.

Cordiner, F.S., and Livingston, A.R., 1977, Tensleep reservoir study, Oregon Basin Field, Wyoming - engineering plans for development and operation, South Dome: Journal Of Petroleum Technology, v. 29, p. 897-902.

Corey, A.T., and Rathjens, C.H., 1956, Effect of stratification on relative permeability: Transactions AIME, v. 207, p. 358-360.

Crabaugh, M., 1994, Character and controls of the depositional architecture in a wet eolian system, middle Jurassic Entrada Sandstone, eastern Utah: Ph.D. Dissertation, The University Of Texas at Austin, 136pp.

Crabaugh, M., and Kocurek, G., 1993, Entrada Sandstone: An example of a wet aeolian system, *in* K. Pye, ed., The Dynamics and Environmental Context Of Aeolian Sedimentary Systems: Geological Society Special Publication No. 72, p. 103-126.

Crabtree, S.J., Ehrlich, R., and Prince, C., 1984, Evaluation of strategies for segmentation of blue dyed porosity in thin section in reservoir rocks: Computer Vision, Graphics and Image Processing, v.28, p.1-18.

Craig, F.F. Jr., 1971, The Reservoir Engineering Aspects of Waterflooding: SPE Monograph Series, vol. 3, 41 p.

Crowell, J.C., and Frakes, L.A., 1972, Late Paleozoic glaciation: Part V, Karroo Basin, South Africa: Geological Society of America Bulletin, v. 83, p. 2887-2912.

Dimitrakopoulos- Roussos, 1989, Characterization of petroleum reservoirs using geostatistics, *in* M. Armstrong, eds., Geostatistics: Proceedings Of The Third International Geostatistics Congress, v.2, p. 1010.

Duda, R.O., and Hart, P.E., 1973, Pattern classification and scene analysis: New York, John Wiley, 481 p.

Dunn, T. L., 1994, Anisotropy and spatial variation of relative permeability and lithologic character of Tensleep sandstone reservoirs in the Bighorn and Wind River basins, Wyoming: Department of Energy Contract No, DE-AC22-93BC14897: First Annual Progress Report, Bartlesville, OK, 76p.

Dunn, T.L.,1995, Anisotropy and spatial variation of relative permeability and lithologic character of Tensleep sandstone reservoirs in the Bighorn and Wind River basins, Wyoming: Department of Energy, Contract No, DE-AC22-93BC14897, Second Annual Report, 114 p.

Ehrlich, R., Kennedy, S.K., Crabtree, Jr., S.J., and Cannon, R.L., 1984, Petrographic image analysis, I - Analysis of reservoir pore complexes: Journal of Sedimentary Petrology, v. 54, p. 1365-1376.

Ehrlich, R., Crabtree, Jr., S.J., Horkowitz, K.O., and Horkowitz, J.P., 1991a, Petrography and reservoir physics I: Objective classification of reservoir porosity: American Association of Petroleum Geologists Bulletin, v. 75, p. 1547-1562.

Ehrlich, R., Etris, L., Brumfield, D., Yuan, L., and Crabtree, S.J., 1991b, Petrography and reservoir physics III: Physical models for permeability and formation factor: American Association of Petroleum Geologists Bulletin, v.75, p. 1579-1592.

Emmett, W.R., Beaver, K.W., and McCaleb, J.A., 1971, Little Buffalo Basin Tensleep heterogeneity - its influence on drilling and secondary recovery: Journal of Petroleum Technology, v. 23, p. 161-168.

Gilreath, J.A., 1987, Strategies for dipmeter interpretation: Part 1: The Technical Review (Schlumberger), v. 35, p. 28-41.

Goggin, D.J., Chandler, M.A., Kocurek, G., and Lake, L.W., 1988, Patterns of permeability in eolian deposits: Society of Petroleum Engineers, Formation Evaluation, v. 3, p. 532-534.

Grant, C.W., Goggin, D.J., Harris, P.M., 1994, Outcrop analog for cyclic-shelf reservoirs, San Andreas Formation of Permian Basin: stratigraphic framework, permeability distribution, geostatistics, and fluid flow modeling: American Association of Petroleum Bulletin, v. 78, No 1, p. 23-54.

Habesch, S.M., 1990, The evaluation of pore-geometry networks in clastic reservoir lithologies using microcomputer technology *in* J.T. Hanley and D.F. Merriam, eds., Microcomputer applications in geology II: Oxford, England, Pergamon Press, p.91-110.

Havholm, K.G., and Kocurek, G., 1988, A preliminary study of the dynamics of a modern draa, Algodones, southeastern California, U.S.A.: Sedimentology, v. 35, p. 649-669.

Helgeson H. C., 1971, Kinetics of mass transfer among silicates and aqueous solutions: Geochimica et Cosmochimica Acta, v. 35, p. 421-469.

Helgeson H. C., Delany, J. M., Nesbitt, H. W., and Bird, D. K., 1978, Summary and critique of the thermodynamic properties of rock-forming minerals: American Journal of Science, v. 278A, p. 229.

Helgeson, H. C., Kirkham, D. H., and Flowers, G. C., 1981, Theoretical prediction of the thermodynamic behavior of aqueous electrolytes at high pressures and temperatures. VI. Calculation of activity coefficients, osmotic coefficients, and apparent mole and standard and relative partial mole properties to 600°C and 5kb: American Journal of Science 281, 1249-1516.

Holland-Hansen, W., 1995, Sequence stratigraphy theory: remarks and recommendations, *in* R. Steel, V. Felt, E. Johannessen, and C. Mathieu, eds., Sequence Stratigraphy Of The Northwest European Margin: Norwegian Petroleum Society, Special Publication No. 5., p. 13-21.

Henbest, L.G., 1956, Foraminifera and correlation of the Tensleep Sandstone of Pennsylvanian age in Wyoming: Wyoming Geological Association, 11th Annual Field Conference Guidebook, p. 58-63.

Henbest, L.G., 1954, Pennsylvanian foraminifera in Amsden Formation and Tensleep Sandstone, Montana and Wyoming: Billings Geological Society, Fifth Annual Field Conference Guidebook, p. 50-53.

Hoare, R.D., and Burgess, J.D., 1960, Fauna from the Tensleep Sandstone in Wyoming: Journal of Paleontology, v. 34, p. 711-716.

Höcker, C., Eastwood, K.M., Herweijer, J.C., and Adams, J.T., 1990, Use of dipmeter data in clastic sedimentological studies: American Association of Petroleum Geologist Bulletin, v. 74. p. 105-118.

Holdren, Jr., G. R. and Berner, R. A., 1979, Mechanism of feldspar weathering I. Experimental studies: Geochimica et Cosmochimica Acta, v. 43, p. 1161-1171.

Honarpour, M., Koederitz, L., and Harvey, A.H., 1986, Relative permeability of petroleum reservoirs: CRC Press, Boca Raton, 143p.

Hsu, K. I., 1963, Solubility of dolomite and composition of Florida ground waters: Journal of Hydrology, v. 1, p. 288-310.

Hunt, J. M., 1979, Petroleum Geochemistry and Geology: San Francisco, Freeman, 617p.

Hurley, N.F., 1994, Recognition of faults, unconformities, and sequence boundaries using cumulative dip plots: American Association of Petroleum Geologists Bulletin, v. 78, p. 1173-1185.

Isaaks, E. H., and Srivastava, M.R., 1989, An Introduction To Applied Geostatistics: New York, Oxford University Press, 561pp.

Iverson, W.P., Dunn, T.L., and Ajdari, I., 1996, Relative permeability anisotropy measurements in Tensleep Sandstone: Society Of Petroleum Engineers, Paper No. SPE 35435; SPE/DOE Tenth Symposium On Improved Oil Recovery.

Johnson, E.F., Bossler, D.P., and Naumann, V.O., 1959, Calculation of relative permeability from displacement experiments: Transactions AIME, v. 216, p. 370-372.

Jones, L. W., 1988, Corrosion and water technology for petroleum producers: Tulsa, OGCI Publications, 202p.

Kerr, D.R., 1989, Sedimentology and stratigraphy of Pennsylvanian and Lower Permian strata (Upper Amsden Formation and Tensleep Sandstone) in North-Central Wyoming: Ph.D. Dissertation, University of Wisconsin, Madison, 382 p.

Kerr, D.R., and Dott, R.H., 1988, Eolian dune types preserved in the Tensleep Sandstone (Pennsylvanian-Permian), North-Central Wyoming, *in* G. Kocurek, ed., Late Paleozoic and Mesozoic Eolian Deposits Of The Western Interior Of The United States: Sedimentary Geology, v. 56, p. 383-402.

Kerr, D.R., Wheeler, D.M., Rittersbacher, D.J., and Horne, J.C., 1986, Stratigraphy and sedimentology of the Tensleep Sandstone (Pennsylvanian and Permian), Bighorn Mountains, Wyoming: Wyoming Geological Survey, Earth Science Bulletin, v. 19,p. 61-77.

Kharaka, Y.K., Gunter, W.D., Agarwall, P.K., Perkins, E.H., and De Braal, J.D., 1988, SOLMINEQ.88: A computer program code for geochemical modeling of water-rock interactions; USGS Water Resource Investigations Report 88-4227.

Kocurek, G., 1981, Significance of interdune deposits and bounding surfaces in aeolian dune sands: Sedimentology, v. 28, p. 753-780.

Kocurek, G., 1988, First-order and super bounding surfaces in eolian sequences - bounding surfaces revisited, *in* G. Kocurek, ed., Late Paleozoic and Mesozoic eolian deposits of the western interior of the United States: Sedimentary Geology, v. 56, p. 193-206.

Kocurek, G., 1991, Interpretation of ancient eolian sand dunes: Annual Review of Earth and Planetary Sciences, v. 19, p. 43-75.

Kocurek, G., and Havholm, K. 1993, Eolian sequence stratigraphy - a conceptual framework, *in* P. Weimer and H. Posamentier, eds., Recent advances in

and applications of siliciclastic sequence stratigraphy: American Association Of Petroleum Geologists Memoir 58, p. 393-409.

Kortekaas, T.F.M., 1985, Water/oil displacement characteristics in crossbedded reservoir zones: Society of Petroleum Engineering Journal, v. 37, p. 917-26.

Krystinik, L.F., 1990, Early diagenesis in continental eolian deposits, *in* S. Fryberger, L. Krystinik and C. Schenk, eds., Modern and ancient eolian deposits: hydrocarbon exploration and production: Rocky Mountain Section, Society Of Economic Paleontologists and Mineralogists, p. 8: 1-11.

Langmuir, D., 1965, The geochemistry of some carbonate ground waters in central Pennsylvania: Geochimica et Cosmochimica Acta, v. 35, p. 1023-1045.

Leverett, M.C., 1939, Flow of oil-water mixtures through unconsolidated sands: Trans. AIME, v. 132, p. 149-71.

Lindquist, S.J., 1988, Practical characterization of eolian reservoirs for development, Nugget Sandstone, Utah-Wyoming Thrust Belt, *in* G. Kocurek, ed., Late paleozoic and mesozoic eolian deposits of the western interior of The United States: Sedimentary Geology, v. 56, p. 315-339.

Lund K., Fogler H.S., and McCune, C.C., 1973, Acidization I. The dissolution of dolomite in hydrochloric acid: Chemical Engineering Science, v. 28, p. 691700.

Luthi, S.M., and Banavar, J.R., 1988, Application of borehole images to three-dimensional geometric modeling of eolian sandstone reservoirs, Permian Rotliegende, North Sea: American Association of Petroleum Geologists Bulletin, v. 72, p. 1074-1089.

Mankiewicz, D., and Steidtmann, J.R.,1979, Depositional environments and diagenesis of the Tensleep Sandstone, Eastern Bighorn Basin, Wyoming, *in* P. Scholle and P. Schluger, eds., Aspects of Diagenesis: SEPM Special Publication 26, p. 319-336.

Mazzolini, E. I., Bertero, L., and Truefitt, C.S., 1992, Scale prediction and laboratory evaluation of $BaSO_4$ scale inhibitors for seawater flood in a high-barium environment: Society Petroleum Engineers Production Eng., SPE Paper 18063, p. 63-73.

McCreesh, C.A., 1987, Determination of pore type-throat size relationships in sandstones and their implications in terms of diagenesis and petrophysics: Ph.D. dissertation, University of South Carolina, 110 p.

Monger, T.G., and Fu, J.C., 1987, The nature of CO_2-induced organic deposition: Journal of Petroleum Technology, SPE Paper 16713, p. 147-159.

Monger, T.G., and Trujillo, D.E., 1988, Organic deposition during CO_2 and rich gas flooding: Society Petroleum Engineers SPE Paper 18063, p. 63-73.

Morgan, J.T., Cordiner, F.S., and Livingston, A.R., 1977, Tensleep reservoir study, Oregon Basin Field, Wyoming - reservoir characteristics: Journal of Petroleum Technology, v. 30, p. 886-896.

Morgan, J.T., and Gordon, D.T., 1970, Influence of pore geometry on water-oil relative permeability: Journal of Petroleum Technology, October, p.1199-1208.

Mowers, T., and Budd, D.A., 1996, Quantification of porosity and permeability reduction due to calcite cementation using computer-assisted petrographic image analysis techniques: American Association of Petroleum Geologists Bulletin, v. 80, p. 309-322.

Nagy, K.L., Blum, A.E., and Lasaga, A.C., 1991, Dissolution and precipitation kinetics of kaolinite at 80°C and pH 3: The dependence on solution saturation state: American Journal Science, v. 291, p. 649-686.

Nagy, K.L., and Lasaga, A.C., 1992, Dissolution and precipitation kinetics of gibbsite at 80°C and pH 3: The dependence on solution saturation state: Geochimica et Cosmochimica Acta, v. 56, p. 3093-3111.

Nagy, K.L., Steefel, C.I., Blum, A.E., and Lasaga, A.C., 1990, Dissolution and precipitation kinetics of kaolinite: Initial results at 80°C with application to porosity evolution in a sandstone: American Association of Petroleum Geologists Memoir 49, p. 85-101.

Nelson, R.A., 1985, Geologic analysis and naturally fractured reservoirs: Contributions in petroleum geology and engineering No. 1, Houston, Gulf Publishing Co., 320 p.

Omole, O., and Osoba J.S., 1983, Carbon dioxide-dolomite rock interaction during CO_2 flooding processes: Paper 83-34-17 Petroleum Society Canadian Inst. Min. Metal. 1-13, Banff, Alberta.

Paces, 1973, Steady-state kinetics and equilibrium between ground water and granitic rock: Geochimica et Cosmochimica Acta, v. 37, p. 2641-2663.

Parrish, J.T., and Peterson, F., 1988, Wind directions predicted from global circulation models and wind directions determined from eolian sandstones of

the western United States - A Comparison, *in* G. Kocurek, ed., Late Paleozoic and Mesozoic eolian deposits of the western interior of the United States: Sedimentary Geology, v. 56, p. 261-282.

Patterson, K.W., 1979, Fighting downhole corrosion and scale in flood CO_2 at SACROC: Petroleum Engineer International, July, p.36-44.

Patton, C.C., 1974, Oilfield Water Systems: Norman, Oklahoma, Campbell Petroleum Series, 178 pp.

Patton, C. C., 1986, Applied Water Technology: Norman, OK, Campbell Petroleum Series, 364p.

Peterson, F., 1988, Pennsylvanian to Jurassic eolian transportation systems in the western United States, *in* G. Kocurek, ed., Late Paleozoic and Mesozoic eolian deposits of the western interior of the United States: Sedimentary Geology, v. 56, p. 207-260.

Pittman, E.D., 1992, Artifact porosity in thin sections of sandstones: Journal of Sedimentary Geology, v. 62, p. 734-737.

Prosser, D. J., Williams, B.P.J., 1993, Permeability heterogeneity within aeolian sandstones: American Association Of Petroleum Geologists 1993 Annual Convention, Program with Abstracts, p. 168.

Ramsbottom, W.H.C., 1979, Rates of transgression and regression in the Carboniferous of NW Europe: Geological Society Of London Journal, v. 136, p. 147-153.

Rhodes, F.H.T., 1963, Conodonts from the topmost Tensleep Sandstone of the eastern Big Horn Mountains, Wyoming: Journal of Paleontology, v. 37, p. 401-408.

Robie, R.A., Hemingway, B.S., and Fisher, J.R., 1979, Thermodynamic properties of minerals and related substances at 298.15K and 1 bar (105 Pascals) pressure and at higher temperatures: U.S. Geological Survey Bulletin 1452, 456p.

Ross, G.D., Todd, A.C., and Tweedie, J.A., 1981, The effect of simulated CO_2 flooding on the permeability of reservoir rocks, *in* F.J. Fayer, ed., Enhanced oil recovery developments in petroleum science, Number 13: Amsterdam, Elsevier, p. 3351-366.

Ross, G. D., Todd, A.D., Tweedie, J.A., and Will, A.G.S., 1982, The dissolution effects of CO_2-brine systems on the permeability of U.K. and North Sea

calcareous sandstones. Proc. 3rd Joint SPE/DOE Symp. on Enhanced Oil Recovery SPE/DOE-10685, 149-162, Tulsa, OK.

Rubin, D.M., 1987, Cross-bedding, bedforms and paleocurrents: Society Of Economic Paleontologists and Mineralogists, Concepts In Geology, v. 1, 187 p.

Rubin, D.M., and Hunter, R.E., 1982, Bedform climbing in theory and nature: Sedimentology, v. 29, p. 121-138.

Rubin, D.M., and Hunter, R.E., 1983, Reconstructing bedform assemblages from compound cross-bedding, *in* M. Brookfield and T. Ahlbrandt, eds., Eolian sediments and processes: Developments In Sedimentology, v. 38, p. 407-427.

Russ, J.C., 1995, The Image Processing Handbook: Boca Raton, CRC Press, 674p.

Ruzyla, K., 1986, Characterization of pore space by quantitative image analysis: Formation Evaluation, v. 1, p. 389-398.

Sayegh, S.G., Krause, F.F., Girard, M., and DeBree, C., 1990, Rock/fluid interactions of carbonated brines in a sandstone reservoir: Pembina Cardium, Alberta, Canada. Society of Petroleum Engineers, Formation Evaluation, December 399-405.

Scotese, C.R., Bamback, R.K., Barton, C., Van Der Voo, R., and Ziegler, A.M., 1979, Paleozoic base maps: Journal of Geology, v. 87, p. 217-277.

Shebl, M.A., 1995, The impact of reservoir heterogeneity on fluid flow in the Tensleep Sandstone of the Bighorn Basin, *in* R.W. Jones, ed., Resources of Southwestern Wyoming; Wyoming Geological Association, 1995 Field Conference Guidebook, p. 343-359.

Stiles, W.E., 1949, Use of permeability distributions in water-flood calculations: Transactions AIME, v. 186, p. 9-13.

Tang, R. W., Behrens, R.A., Emanuel, A.S., 1991, Reservoir studies with geostatistics to forecast performance: Society of Petroleum Engineers Reservoir Engineering, May 1, v.6, No.2, p. 253.

Tang, G.Q., and Morrow, N.R., 1996, Effect of temperature, salinity and oil composition on wetting behavior and oil recovery by waterflooding: SPE Paper 36680 presented at the Society of Petroleum Engineers Annual Technical Conference and Exhibition, Denver, CO, October 6-9, 1996.

Todd, T. W., 1964, Petrology of Pennsylvanian rocks, Bighorn Basin, Wyoming. American Association of Petroleum Geologists Bulletin, v. 48, p. 1063-1090.

Van Wagoner, J.C., Posamentier, H.W., Mitchum, R.M., Vail, P.R., Sarg, J.F., Loutit, T.S., and Hardenbol, J., 1988, An overview of the fundamentals of sequence stratigraphy and key definitions, in sea-level changes - an integrated approach: SEPM Special Publication No. 42, p. 39-45.

Verville, G.J., 1957, Wolfcampian Fusulinids from the Tensleep Sandstone in the Bighorn Mountains, Wyoming: Journal of Paleontology, v. 31, p. 349-352.

Verville, G.J., Sanderson, G.A., and Rea, B.D., 1970, Missourian Fusulinids from the Tensleep Sandstone, Bighorn Mountains, Wyoming: Journal of Paleontology, v. 44, p. 478-479.

Wollast, 1967, Kinetics of the alteration of K-feldspar in buffered solutions at low temperature: Geochimica et Cosmochimica Acta,v. 31, p. 635-648.

Wanless, H.R., and Shepard, F.P., 1936, Sea level and climatic changes related to Late Paleozoic cycles: Geological Society of America Bulletin, v. 47, p. 1176-1206.

Weber, K.J., 1986, How heterogeneity affects oil recovery, *in* L. Lake and H. Carroll, eds., Reservoir characterization: Austin, Academic Press, Inc., p. 487-544.

Weber, K.J., 1987, Computation of initial well productivities in aeolian sandstone on the basis of a geological model, Leman Gas Field, U.K., *in* R. Tillman and K. Weber, eds., Reservoir Sedimentology: SEPM Special Publication No. 40, p. 333-354.

Weibel, E.R., 1979, Stereological methods, volume 1 - practical methods for biological morphometry: Academic Press Inc., New York City 415p.

Wheeler, D.M., 1986, Stratigraphy and sedimentology of the Tensleep Sandstone, Southeast Bighorn Basin, Wyoming; M.S. Thesis, Colorado School of Mines, Golden, 263 p.

Whitman, D.L., 1988, Use of microcomputer graphics to teach waterflooding concepts: Paper SPE 17785, presented at PIAM conference, San Jose, California.

Willhite, G. Paul, 1986, Waterflooding: Society of Petroleum Engineers Textbook Series, vol. 3, 326 p.

Wolcott, D. S., Chopra, A.K., 1993, Incorporating reservoir heterogeneity with geostatistics to investigate waterflood recoveries: Society of Petroleum Engineers Formation Evaluation, v. 8, p. 26-32.

Wolcott, J.M., Monger, T.G., Sassen, R., and Chinn, E.W., 1989, The effect of CO_2 flooding on reservoir mineral properties: Society Petroleum Engineers SPE Paper 18467.

Wolcott, J.M., Groves, F.R., Trujillo, D.E., and Lee, H.G., 1991, Investigation of crude-oil/mineral interactions: Factors influencing wettability alteration: Society Petroleum Engineers SPE Paper 21042.

Wyckoff, R.D., Botset, H.G., and Muskat, M., 1933, The mechanics of porous flow applied to water-flooding problems: Trans. AIME, v. 103, p. 219-242.

Wyllie, R.M.J., and Gardner, G.H.F., 1958, The generalized Kozeny-Carmen equation, its application to problems of multi-phase flow in porous media: World Oil, v.146, p.121.

Wyoming Oil and Gas Fields Symposium Bighorn and Wind River Basins, 1989, Oil and Gas Field Symposium Conference, Wyoming Geological Association, 555p.

Yildiz, H.O., 1995, Effect of brine composition on oil recovery by waterflooding: Ph.D. Dissertation, New Mexico Institute of Mining and Technology, 140pp.

Yildiz, H.O., and Morrow, N.R., *in press*, Effect of brine composition on recovery of Moutray crude oil by waterflooding: Journal of Petroleum Science and Engineering.

Yuan, M. D., and Todd, A. C., 1991, Prediction of sulfate scaling tendency in oilfield operations. Society of Petroleum Engineers Production Engineering, February 63-72.